UNIVERSITY OF CALIFORNIA, SAN DIEGO

Balancing the Beneficial Contributions of Foundation Rocking and Structural Yielding in Moment-Frame and Frame-Wall Building Systems

A dissertation submitted in partial satisfaction of the

requirements for the degree

Doctor of Philosophy

in

Structural Engineering

by

Weian Liu

Committee in charge:

Professor Tara C. Hutchinson, Chair
Professor Ahmed-Waeil M. Elgamal
Professor William Hodgkiss
Professor Bruce L. Kutter
Professor Pui-Shum Shing

2014

The dissertation of Weian Liu is approved, and it is acceptable in quality and form for publication on microfilm and electronically:

_____

_____

_____

_____

_____
Chair

University of California, San Diego

2014

DEDICATION

To my parents Fufa Liu and Fenlan Li for their everlasting love, encouragement, and support.

EPIGRAPH

Persistent exercises can improve your self-cultivation as an accomplished *Junzi* (superior person).

-Shijing · Guofeng · Weifeng

TABLE OF CONTENTS

LIST OF ACRONYMS

This section provides a list of acronyms which are frequently used in this dissertation in alphabetical order.

Abbreviation	Description
aBD	asymmetric Balanced Design
aFRD	asymmetric Foundation Rocking Dominated
aSHD	asymmetric Structural Hinging Dominated
ASCE	American Society of Civil Engineers
BD	Balanced Design
BNWF	Beam-on-Nonlinear-Winkler-Foundation
BRB	Buckling-Restrained Brace
CGM	Center for Geotechnical Modeling
CL_ftg	Column rocking footing
CL_fuse1	Column fuse at first level
CL_fuse2	Column fuse at second level
CoSSY	Compatible Soil Structure Yielding
CMS	Artificial motion name for “Combined Morgan with Steps”
EDP	Engineering Demand Parameter
EPO	Elastic-Plastic with Overstrength
EPP	Elastic-Perfectly Plastic
ExCL_ftg	Exterior Column Footing
FB	Floor Beam
FF	Free Field
FR	Foundation Rocking
FRD	Foundation Rocking Dominated
GZ	Motion name representing Gazli earthquake in 1976
HDPE	High-density polyethylene
ICP	Integrated Circuit Piezoelectric
InCL_ftg	Interior Column Footing
KB	Motion name representing Kobe earthquake in 1995

Continued on next page

Abbreviation	Description
LP	Linear Potentiometer
MEMS	Microelectromechanical System
MFP	Multiple-Fuse-in-Parallel
MFS	Multiple-Fuse-in-Series
MG	Motion name representing Morgan Hill earthquake in 1984
NEES	Network for Earthquake Engineering Simulation
NSF	National Science Foundation
PI	Principal Investigator
PPT	Pore Pressure Transducers
PT	Post-tensioned
PSD	Power Spectral Density
RC	Reinforced Concrete
RPM	Revolutions Per Minute
RR	Restrained Rocking
sBD	symmetric Balanced Design
sFRD	symmetric Foundation Rocking Dominated
sSHD	symmetric Structural Hinging Dominated
SDOF	Single-Degree-of-Freedom
SDP	Stiffness Degrading and Pinching
SF	Motion name representing San Fernando earthquake in 1976
	or: strip footing
	or: Single-Fuse
SFSI	Soil-Foundation-Structure Interaction
SG	Strain Gauge
SHD	Structural Hinging Dominated
SSI	Soil-Structure Interaction
SW	Shear Wall
SW_ftg	Shear Wall Rocking Footing
SW_fuse	Shear Wall Fuse
TCU	Seismic station in Taiwan
UCD	University of California, Davis
UCSD	University of California, San Diego

LIST OF PARAMETERS

This section provides a list of parameters used in this dissertation in alphabetical order. Note that the base dimensions include, mass (M), force (F), length (L), and time (T).

Parameter	Description	[Base Unit, SI Units]
A_c	Critical contact area required for the footing to support the vertical load	[L^2, m^2]
A_{ftg}	Footing area	[L^2, m^2]
B_{ftg}	Footing width	[L, m]
C_c	Coefficient of curvature of sand	[Dimensionless]
C_r	Foundation rocking yield coefficient	[Dimensionless]
C_s	Base shear coefficient	[Dimensionless]
$C_{s,cor}$	Corrected base shear coefficient	[Dimensionless]
C_y	Structural fuse yield coefficient	[Dimensionless]
C_u	Coefficient of uniformity of sand	[Dimensionless]
D_{ftg}	Footing's depth of embedment	[L, m]
D_r	Relative density of sand	[Dimensionless, %]
DR	Drift Ratio	[Dimensionless, %]
DR_{max}	Maximum Drift Ratio	[Dimensionless, %]
EI	Flexural Stiffness	[FL^2, N-m^2]
f_y	Yield stress	[F/L^2, MPa]
F_y	Yield force of an inelastic element	[F, N]
FS_v	Vertical factor of safety against bearing failure	[Dimensionless]
g	Acceleration due to gravity	[L/T^2, 9.81m/s^2]
G_{max}	Maximum shear modulus of sand	[F/L^2, MPa]
G_s	Specific gravity	[Dimensionless]
H_1	Column height at first story	[L, m]
H_2	Column height at second story	[L, m]
H_A	Hysteretic area of an inelastic element under one full cycle of loading	[FL, J]

Continued on next page

Parameter	Description	[Base Unit, SI Units]
H_{SW}	Shear wall height	[L, m]
k_e	Elastic stiffness of an idealized structural fuse	[F/L, N/m]
k_p	Plastic stiffness of an idealized structural fuse	[F/L, N/m]
k_u	Unloading stiffness of an idealized structural fuse	[F/L, N/m]
K_o	Initial lateral stiffness of a foundation-building system	[F/L, N/m]
K_θ	Elastic rotational stiffness of a rocking footing	[FL, N-m/rad]
L_{cc}	Center-to-center spacing	[L, m]
L_{CLftg}	Column footing length	[L, m]
L_{fuse}	Length of the fuse perpendicular to the bending axis	[L, m]
L_{SWftg}	Shear wall footing length	[L, m]
LL	Liquid Limit of clay	[Dimensionless, %]
M_1	First story mass	[M, kg]
M_2	Second story mass	[M, kg]
M_{y_fuse}	Yield moment of structural fuse	[FL, N-m]
$M_{y\_footing}$	Yield moment of rocking footing	[FL, N-m]
M_{y_st}	Yield moment of rocking footing under static axial load	[FL, N-m]
M_w	Moment magnitude of an earthquake event	[Dimensionless]
OCR	Overconsolidation Ratio of clay	[Dimensionless]
P_{st}	Static axial load on footing	[F, N]
PDR	Peak Drift Ratio	[Dimensionless, %]
PDR_{cor}	Corrected Peak Drift Ratio	[Dimensionless, %]
PFFA	Peak Free Field Acceleration	[L/T^2, g]
PGA	Peak Ground Acceleration	[L/T^2, g]
PGD	Peak Ground Displacement	[L, cm]
PGV	Peak Ground Velocity	[L/T, cm/s]
PI	Plasticity Index of clay	[Dimensionless, %]
PL	Plastic Limit of clay	[Dimensionless, %]
PRA	Peak Roof Acceleration	[L/T^2, g]
PRA_{cor}	Corrected Peak Roof Acceleration	[L/T^2, g]
R_{ED}	Energy Dissipation Ratio	[Dimensionless]
R_{RC}	Re-Centering Ratio	[Dimensionless]
RDR	Residual Drift Ratio	[Dimensionless, %]

Continued on next page

Parameter	Description	[Base Unit, SI Units]
s_u	Undrained shear strength of clay	[F/L^2, MPa]
S_a	Spectral acceleration	[L/T^2, g]
S_d	Spectral displacement	[L, m]
S_{xx}	Spectral density of a signal	[L^2/T^4, g^2]
t_d	Strong duration of an earthquake motion	[T, second]
t_{ftg}	Footing thickness	[L, m]
$\overline{T}_1$	Average period of all symmetric frame-wall-foundation models	[T, second]
T_1	Flexible-base first natural period	[T, second]
T_2	Flexible-base second natural period	[T, second]
T_p	Predominant period of an earthquake motion	[T, second]
V_{total}	Total base shear	[F, N]
W	Building weight	[F, N]
W_{SW}	Shear wall width	[L, m]
ZPA	Zero Period Acceleration	[L/T^2, g]
α	Post-yield stiffness ratio	[Dimensionless]
β	Unloading stiffness parameter	[Dimensionless]
δ_y	Yield displacement of an inelastic component	[L, m]
$\Delta\delta$	Zero force displacement range	[L, m]
θ_y	Yield rotation	[Dimensionless, radium]
κ_d	Displacement pinching factor	[Dimensionless]
κ_f	Strength pinching factor	[Dimensionless]
λ_h	Story height ratio (H_2/H_1)	[Dimensionless]
λ_m	Story mass ratio (M_2/M_1)	[Dimensionless]
λ_s	Ratio of first story height to column spacing	[Dimensionless]
λ_t	Ratio of first two natural periods (T_2/T_1)	[Dimensionless]
μ	Displacement ductility	[Dimensionless]
ρ_d	Mass dry density of sand	[M/L^3, kg/m^3]
ϕ	Friction angle of sand	[Dimensionless, degree]
ω_1	Natural circular frequency of the first mode	[1/T, rad/sec]
ω_2	Natural circular frequency of the second mode	[1/T, rad/sec]
Ω	Acceleration amplification ratio	[Dimensionless]

LIST OF FIGURES

LIST OF TABLES

ACKNOWLEDGEMENTS

The research accomplishment in this dissertation would not have been possible without the support and encouragement from many individuals surrounded in my life.

First of all, I would like to acknowledge the support and guidance of my advisor, Professor Tara Hutchinson, who has never ceased in directing me to become an excellent researcher over the past four years. Immediately when I embarked on this research topic, I realized that it is surely challenging; however, it was her consistent and patient instruction indeed that have made it a true success. Her attitude towards research and dedication to the profession, also, has influenced my academic life in a long term.

I also wish to thank all my dissertation committee members, Professors Ahmed-Waeil M. Elgamal, William Hodgkiss, Bruce L. Kutter, and Pui-Shum Shing for their instrumental comments and suggestions on this dissertation.

The experimental aspects of this research have been conducted in close collaboration with researchers at University of California, Davis (UCD). I am indebted to UCD colleagues, namely; Manny Hakhamaneshi, Andreas Gavras, and Dr. Lijun Deng, for their professional collaboration, companionship, and friendship during the test programs. Student assistants, including Dr. Mark Stringer, Kaijie Huang, and Keisuke Nagaura, also contributed their efforts through this test program. In particular, I would also like to thank Professor Bruce Kutter for his invaluable guidance and motivational discussions during model design, testing, and data processing. As the principal investigator (PI) of this research project, his constructive comments greatly contributed to the research. I would also like to take this opportunity to acknowledge the assistance

provided by the staff members at the centrifuge facility at UCD during the test programs, as well as two other PIs of the primary project that supported this research, namely Professors Mark Aschheim and Sashi Kunnath.

I would like to acknowledge friends at UCSD for their friendship and emotional support, which are truly fundamental elements during my graduate study, including: Dr. Ricky Wood, Dr. Nick Trombetta, Dr. Barbara Chang, Xiang Wang, Saurabh Prasad, Christ Trautner, Christine Wittich, Yong Li, Ning Wang, Hefu Pu, and Dr. Xi Chen from Qualcomm.

Finally, I want to dedicate this dissertation to my parents Fufa Liu and Fenlan Li. This dissertation would have remained a dream had it not been for their everlasting love and support since I was born. I hope that this accomplishment will fulfill a dream of being a solid scholar that they had for me over the years when they tried their best to give me the best education as they could.

The research program reported herein is financially supported by the National Science Foundation through the Network for Earthquake Engineering Simulation (NEES) research program under the award CMMI-0936503. Opinions, findings, and conclusions expressed are those of the author, and do not necessarily reflect the view of the sponsoring agency.

It is noted that sections of this dissertation have (or will shortly) be published in broader technical publications. The author was the primary author of the following:

1. Chapter 3, in full, is a reprint of the material as it appears in the proceedings of 15th World Conference on Earthquake Engineering. Liu, W.; Hutchinson, T. C.; Hakhamaneshi, M.; Kutter, B. L., (2012). “Numerical parametric study on

inelastic foundation-building models with presence of rocking foundation." *15th World Conference on Earthquake Engineering*, Lisbon, Portugal, September 24-28.

2. Chapter 4, in part, is a reprint of the material as it appears in the ASCE Journal of Structural Engineering. Liu, W., Hutchinson, T. C., Kutter, B. L., Hakhamaneshi, M., Aschheim, M., and Kunnath, S. (2013). "Demonstration of Compatible Yielding between Soil-Foundation and Superstructure Components." *ASCE, Journal of Structural Engineering*, 139(8): 1408-1420.
3. Chapters 6, 7, and 8, in part, are currently being prepared for submission to similar technical journals. At completion of this dissertation their final forms were in preparation. However, the dissertation author is the primary investigator and first author of these papers.

VITA

2004	B.S. in Civil Engineering (Minor: Bachelor of Business Administration), Wu Han University of Technology, Wu Han, China
2007	M.S. in Bridge Engineering Tongji University, Shanghai, China
2014	Ph.D. in Structural Engineering University of California, San Diego, La Jolla, CA

PUBLICATIONS

Journal Publications:

Liu, W., Hutchinson, T. C., Gavras, A. G., Kutter, B. L., and Hakhamaneshi, M. (201X). "Seismic Behavior of Frame-Wall-Rocking Foundation Systems. Part I: Test Program and Slow Cyclic Test Results." ASCE, *Journal of Structural Engineering*, (In preparation).

Liu, W., Hutchinson, T. C., Gavras, A. G., Kutter, B. L., and Hakhamaneshi, M. (201X). "Seismic Behavior of Frame-Wall-Rocking Foundation Systems. Part II: Shake Table Testing Results." ASCE, *Journal of Structural Engineering*, (In preparation).

Liu, W., Hutchinson, T. C., Kutter, B. L., Gavras, A. G., and Hakhamaneshi, M. (201X). "Effect of Seismic-Induced Axial Load Fluctuation on Asymmetric Frame-Wall-Rocking Foundation Systems." *Earthquake Engineering and Structural Dynamics* (In preparation).

Liu, W., Hutchinson, T. C., Kutter, B. L., Hakhamaneshi, M., Aschheim, M., and Kunnath, S. (2013). "Demonstration of Compatible Yielding between Soil-Foundation and Superstructure Components." ASCE, *Journal of Structural Engineering*, 139(8): 1408-1420.

Conference Proceedings:

Hakhamaneshi, M., Gavras, A. G., Wilson D. W., Kutter, B. L., **Liu, W.**, and Hutchinson, T. C. (2014). "Effects of footing shape on the settlement of rectangular and I-shaped rocking shallow foundations." *8th International Conference Physical Modelling in Geotechnics*, Perth, Australia, January 14-17.

Liu, W., Hutchinson,T. C., Gavras, A. G., Kutter, B. L., and Hakhamaneshi, M. (2013). "Distribution of Inelastic Seismic Demands in Frame-Wall Structures Assessed in Large-Scale Centrifuge Tests." *6th International Conference on Earthquake Geotechnical Engineering*, Istanbul, Turkey, June 17-19.

Liu, W., Hutchinson, T. C., Kutter, B. L., Hakhamaneshi, M., and Gavras, A. G. (2013). "Balancing the Beneficial Contributions of Foundation Rocking and Structural Yielding to Improve Structural Seismic Resilience." *4th ECCOMAS Thematic Conference on Computational Methods in Structural Dynamics and Earthquake Engineering*, Kos Island, Greece, June 12-14.

Hakhamaneshi, M., Kutter, B. L., Tamura, S., Gavras, A. G., **Liu, W.**, and Deng, L. (2013). "Rocking Foundations with Different Shapes on Different Soils." *10th International Conference on Urban Earthquake Engineering*, Tokyo, Japan, March 1-3.

Liu, W., Hutchinson, T. C., Hakhamaneshi, M., and Kutter, B. L. (2012). "Numerical parametric study on inelastic foundation-building models with presence of rocking foundation." *15th World Conference on Earthquake Engineering*, Lisbon, Portugal, September 24-28.

Hakhamaneshi, M., Kutter, B. L., Hutchinson, T. C. and **Liu, W.** (2012). "Settlement Characterization and Prediction of a Rocking Shallow Foundation subjected to Dynamic and Lateral Cyclic Loads." *15th World Conference on Earthquake Engineering*, Lisbon, Portugal, September 24-28.

Liu, W., Hutchinson, T. C., Hakhamaneshi, M., and Kutter, B. L. (2012). "Centrifuge Testing of Systems with Combined Structural Hinging and Rocking Foundations." *2012 ASCE Structure Congress*, Chicago, March 28-31.

Hakhamaneshi, M., Kutter, B. L., Deng, L., Hutchinson, T. C. and **Liu, W.** (2012). "New findings from centrifuge modeling of rocking shallow foundations in clayey ground." *ASCE 2012 Geo-congress*, Oakland, March 25-29.

ABSTRACT OF THE DISSERTATION

Balancing the Beneficial Contributions of Foundation Rocking and Structural Yielding in Moment-Frame and Frame-Wall Building Systems

by

Weian Liu

Doctor of Philosophy in Structural Engineering

University of California, San Diego, 2014

Professor Tara C. Hutchinson, Chair

To date, experimental studies have illustrated that foundation rocking can advantageously provide an isolation mechanism, dissipating energy, and re-centering of building-foundation systems. It is hypothesized that by balancing the beneficial attributes of foundation rocking and inelastic structural behavior (structural fuse), a building-foundation system's seismic performance can be significantly improved.

This dissertation validates this hypothesis from three distinct, yet complementary aspects. The first two involve a pair of system-level experiments focused on low-rise moment-resisting frame and frame-wall structural systems at centrifuge scale, while the last is completed via numerical analyses. For each of the test programs, three fundamental model configurations were constructed considering the strength difference

between the rocking foundation and the structural fuse, namely; **Structural Hinging Dominated** (SHD), **Foundation Rocking Dominated** (FRD), and **Balanced Design** (BD) models. All model specimens were subjected to a sequence of earthquake loading. Experimental results indicate that the SHD models consistently observe the largest building residual drifts and peak roof accelerations, while the FRD models consistently observe the largest footing settlement. The BD models, however, are able to recover and report negligible residual displacements. Importantly, dissipated energy is well distributed amongst the structural fuses and the rocking footings in the BD systems. The frame-wall system test also highlights the significant impacts of seismic-induced axial load variation and building asymmetry on seismic performance. With the rocking wall placed at the far end of the lateral load resisting path, loading towards the strong (wall) direction dramatically reduces axial load on the interior rocking footing. This reduction leads to a highly asymmetric footing moment-rotation hysteresis with a "bend-over" behavior. Moreover, system-level load-carrying capacity varies significantly between the weak and strong directions.

In the final phase of this research, two parameters, defined as the energy dissipation ratio (R_{ED}) and the re-centering ratio (R_{RC}), are proposed to quantify the ability of an inelastic system to dissipate hysteretic energy and to recover from large amplitude transient displacements, respectively. The relation between the R_{ED} and R_{RC} is investigated by numerically studying a variety of simplified inelastic systems under cyclic loading. Results of these analyses indicate that balancing the strength between the rocking foundation and the structural fuse allows the hybrid system to benefit from the

positive attributes of each inelastic mechanism, further substantiating findings from the test programs.

Chapter 1

Introduction

1.1 Background and Motivation

1.1.1 Background

Overwhelming structural and nonstructural damage, and economic and human losses in recent seismic events continue to raise an increasing awareness to the general public and design community regarding the necessity to develop earthquake-resistant structural systems that minimize the impacts of earthquakes (e.g., 2008 Wenchuan Earthquake, China; 2010 Haiti Earthquake, Haiti; 2010 Maule Earthquake, Chile; 2010 Baja California Earthquake, Mexico; 2011 Tohoku Earthquake, Japan). In recent years, a variety of innovative earthquake-resistant structural configurations have been proposed and developed. Base isolation devices, for example, have been implemented within building and bridge structural systems in an effort to isolate structures from the damaging demands of earthquakes. In the past few decades, they have proven successful in this regard, as they elongate a system's natural period away from the period range where the

largest amplitude of most earthquake motions is (e.g. Buckle and Mayes 1990; Kam et al. 2011; Moroni et al. 2012). Application of post-tensioned tendons in beam-column connections or wall-foundation connections are other examples of favorable design alternatives to resist earthquake demands since they can assist the structure with self-centering and thereby effectively control residual displacements imposed during an earthquake (e.g. Kurama et al. 1999; Ricles et al. 2001). However, these and other design strategies may carry either a larger construction cost or a life-cycle (maintenance) cost. As a case in point, base isolation technology has been available in design guidance form since codes of the 1990s, however, fewer than 5% of the buildings in the United States are constructed with base isolators, despite their demonstrated benefits in the field and laboratory. Indeed, alternative design strategies must also carry minimal price tags so that engineers can convince owners of their low implication on overall construction costs.

1.1.2 Attributes of Foundation Rocking

Rocking behavior was recognized as an important alternative to provide seismic resistance in the 1960s when Housner observed that rocking component can sustain large displacements with minimal damage and residual deformation (Housner 1963). Since then, a number of large-scale experiments have been carried out to evaluate the seismic performance of structural rocking behavior when introduced into frame systems (e.g. Clough and Huckelbridge 1977; Kelley and Tsztoo 1977; Midorikawa et al. 2006; Tremblay et al. 2008; Eatherton et al. 2010; Ma et al. 2010), bridge pier systems (e.g. Pollino and Bruneau 2008), and concrete and masonry wall systems (e.g. Kurama et al. 1999; Restrepo and Rahman 2007; Toranzo et al. 2009). These and other experimental

studies indicate that during seismic loading, rocking systems observe nearly zero residual deformations and reduced peak acceleration demand to structural components when implemented with unbonded post-tensioned tendons and energy dissipaters.

When a foundation is loaded during an earthquake, inertial forces are imposed at an elevation well above the base of the footing. As a result, cyclic moments, and therefore cyclic rotations, are induced. This natural mode of response, if allowed (i.e. if the foundation is not exceedingly rotationally stiff), offers similar beneficial attributes as sought after via the aforementioned structural solutions, at a greatly reduced cost to the system. Experimental studies to understand the mechanism of foundation rocking have been pursued since the 1970s when researchers at the University of Auckland performed a pair of shallow foundation slow cyclic tests to characterize the footings moment-rotation hysteretic behavior (Bartlett 1976; Wiessing 1979). Since then, numerous researchers have performed experimental investigations to study the foundation rocking mechanism under various footing and soil conditions (e.g., Taylor and Crewe, 1996; Negro et al. 2000; Rosebrook and Kutter 2001a-c; Gajan et al. 2005 Paolucci et al. 2008; Shirato et al. 2008; Deng and Kutter 2012; Drosos et al. 2012; Figini et al. 2012; Hakhamaneshi et al. 2012; Hakhamaneshi et al. 2013). Findings from these and other studies indicate that rocking shallow foundations have four primary beneficial attributes:

- **Isolation mechanism.** When a foundation is subjected to horizontal loading above the footing base and the rocking mode is engaged, the superstructure's ductility demand is reduced. As a result, one may observe that the rocking foundation isolates the superstructure from damage due to the earthquake.

- **Energy dissipation capability.** If the moment capacity of the foundation is mobilized, the resulting moment-rotation hysteresis is highly nonlinear and able to sustain large rotations, indicating that energy is dissipated within the soil-foundation interface.
- **Robust hysteresis without strength degradation.** The strength of structural components, such as reinforced concrete (RC) members, usually degrades at large deformations. In contrast, foundations resting on competent soil, that are subjected to moment loading will observe little to no strength degradation.
- **Inherent re-centering capability.** The superstructure dead load typically creates a destabilizing second-order effect (P-Δ effect) to vertical structural components (e.g., columns and walls). However, for a rocking footing, the P-Δ effect is beneficial. This is because at the footing edge where the rocking point occurs, is most often at a distance away from the center of gravity. As a result, the dead load enables the structure to inherently re-center.

Compared with hybrid structural rocking systems with post-tensioned tendons or other technologies geared towards attaining the aforementioned attributes, the foundation rocking system may arguably emerge as the most economical solution. This is because, to achieve the above, the foundation size is actually reduced and overstrength is undesirable. In addition, it does not require supplementary components to dissipate energy or render re-centering behavior.

1.1.3 Motivation for the Present Work

Integrating the abovementioned benefits of a foundation rocking mechanism into any structural systems has obvious potential to improve a system's seismic performance. Importantly however it must be recognized that conventional structural systems already incorporate inelastic component response and a departure from this philosophy may be pragmatically difficult. Indeed, within the framework of performance-based earthquake engineering, structural components are strategically designed to provide ample energy dissipation during seismic excitations. However, designing for yielding rocking foundations and yielding structural components within a system has the potential to optimize the seismic performance of any system. Despite its established benefits, foundation rocking has not been acknowledged as a mainstream inelastic mechanism within the structural engineering community. This is likely due to the following two reasons.

First, there is a general partition between the design of structural and geotechnical components. The behavior of structural members (concrete or steel) is reasonably understood and design codes (e.g. ACI 318-11, 2011; AISC, 2011) have been well established for many years. As a result, structural engineers are more confident when designing for inelastic behavior of structural components. In contrast, soil material properties contain greater uncertainty, which results in foundation designs that are highly conservative with large overstrength, despite the fact that the understanding of foundation behavior has significantly evolved over the past few decades. As a result, foundation rocking behavior is intentionally excluded during seismic design.

Secondly, although numerous isolated rocking footing experiments have been conducted, there remains a lack of experimental data characterizing how a rocking foundation will dynamically interact with structural components, particularly when structural yielding is expected.

1.2 Research Scope

To support the adoption of rocking foundations within structural systems with other yielding components, the present dissertation invokes upon three complementary research tasks:

- An experimental investigation of the seismic performance of moment-resisting frame-foundation building models with varying levels of foundation yield moment;
- An experimental investigation of the seismic performance of frame-wall-foundation building models with varying levels of foundation yield moment;
- A theoretical study of the relation between energy dissipation and re-centering considering various types of inelastic systems constructed of multiple inelastic fuses, including a rocking foundation, placed either in parallel or in series in the system.

The first two research efforts are completed by performing two large-scale laboratory experiments at the Centrifuge Geotechnical Modeling (CGM) facility at the University of California at Davis (UCD), whereas the last step is accomplished via systematic numerical analyses in *OpenSees* (Mazzoni et al. 2009). The two experimental

investigations are part of a unique research program shortnamed *CoSSY*: Compatible Soil Structure Yielding. *CoSSY* is financially supported by the National Science Foundation (NSF) through the George E. Brown, Jr. Network for Earthquake Engineering Simulation (NEES) research program. It consisted of two large-scale system-level and two component-level centrifuge experiments, of which the two system-level tests investigated the seismic response of moment-frame and frame-wall structural systems resting on shallow rocking footings, referred to herein as Test-1 and Test-2, respectively. The two component-level tests were focused on characterizing the rocking response of rectangular shallow footings in clayey soil (Hakhamaneshi et al. 2011) and shallow footings with irregular shapes (Hakhamaneshi et al. 2014). These studies are beyond the scope of the present work.

1.2.1 Building-Foundation Configurations

Three fundamental systems may be realized considering the strength difference between the rocking foundation and the inelastic structural component (i.e., structural fuse), as follows:

- **Structural Hinging Dominated** (SHD) system. In this system, the footing's yield moment is significantly larger than that of the structural fuse. In this regard, the foundation component is intended to be protected during seismic loading, and not mobilize its capacity, while the structural fuse is expected to yield and carry large inelastic demands. Most existing buildings are designed with this philosophy, with the foundations typically over designed.

- **Foundation Rocking Dominated** (FRD) system. In this system, the foundation geometry is intentionally under designed typically by reducing its bearing area. As a result, the structural elements remains elastic. In addition, this type of system has the potential to reduce residual displacement demands on the superstructure due to its inherent re-centering capability. However, depending on the foundation soil stiffness, large amplitude rocking at the footing-soil interface could exacerbate footing absolute or differential settlements.
- **Balanced Design** (BD) system. In this system, both the superstructure and the foundation are designed to yield at the same base shear level. Within the superstructure, this yielding can be realized via moment loading of strategic fuses, such as at beam or column ends, or the bottom of shear walls. Within the foundation, this yielding is envisioned as occurring due to rocking, i.e. mobilization of the footing's moment capacity. It is hypothesized that a BD system provides an initial compromise to demonstrate avoidance of extreme behaviors, which might be expected of the two aforementioned systems. These include significant story drift induced by large amplitude structural hinging or excessive foundation settlement induced by large amplitude foundation rocking. However, the BD design concept may benefit from the positive attributes of both extreme systems. For example, it could have a reasonable energy dissipation capacity available in a SHD system, and at the same time also maintain the self-centering characteristic provided by an FRD system. Therefore, balancing the beneficial attributes of each of these yielding

systems has the potential to optimize the seismic performance and thereby enhance the seismic resilience of the foundation-building system.

1.2.2 Scope of Test-1

Test-1 involved evaluating three different 3-dimensional two-story-one-bay moment-frame-foundation building models at centrifuge scale. Figure 1.1 shows a schematic of the moment-frame-foundation configuration. It is noted that inelastic fuses were designed to occur at the bottom of the second floor columns or the foundations below the first floor columns. Pinned connections are introduced at the top of the first and second floor columns to simplify the measurement of moment at each fuse location and to promote foundation rocking. Three models, conceptually intended to behave as either an FRD, SHD, or BD system, were designed with similar layouts, but different combinations of foundation and structural component yield strengths. All models were supported on overconsolidated clay in a rigid container and were subjected to a similar sequence of earthquake motions while in a 30-g centrifuge environment. The main goal of this test was to experimentally investigate the dynamic interactions between rocking foundations and structural fuses in a frame-type structural system.

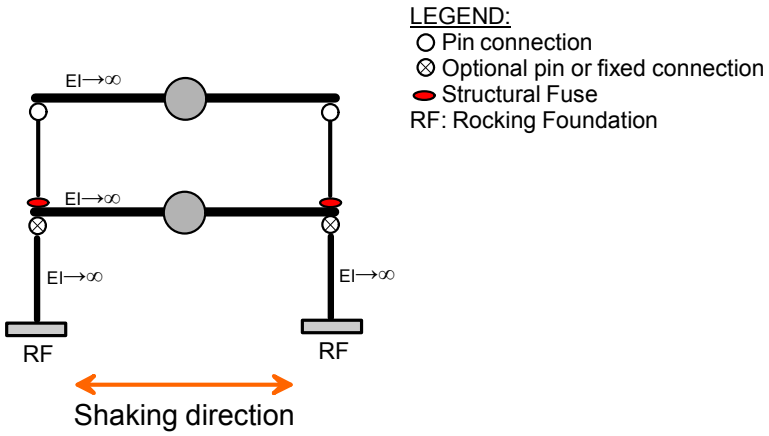

Figure 1.1 Schematic of moment-frame structural configuration (Test-1 concept)

1.2.3 Scope of Test-2

Test-2 was conducted to evaluate the seismic performance of low-rise frame-wall-foundation models. Figure 1.2 schematically depicts the proposed systems, wherein solid ellipses locate the various structural fuse mechanisms. In this test program, 2-dimensional models were constructed and two different layouts were considered, namely; a symmetric system (part a) and a load resisting system with asymmetric geometry (part b). For both scenarios, structural fuses were located at the bottom of columns at each level and at the base of the shear wall (SW).

By varying the strength between the SW fuse and the SW rocking footing, the three types of system behaviors were similarly targeted in this test program, namely SHD, FRD, and BD. Since each of these models were designed with a symmetric and asymmetric layout, six building models were tested in total. These models were supported on dense dry Nevada sand and subjected to a similar sequence of earthquake motions while in a 30-g centrifuge environment. In addition, three models were

additionally subjected to a sequence of quasi-static cyclic loading with increasing amplitude. The objective of this test series was twofold: (1) evaluate dynamic interactions between structural fuses and rocking footings particularly when the structural fuses are located within the SW; (2) investigate the effect of axial load variation induced by seismic action and building asymmetry on the seismic response of the rocking footings and the entire foundation-building system.

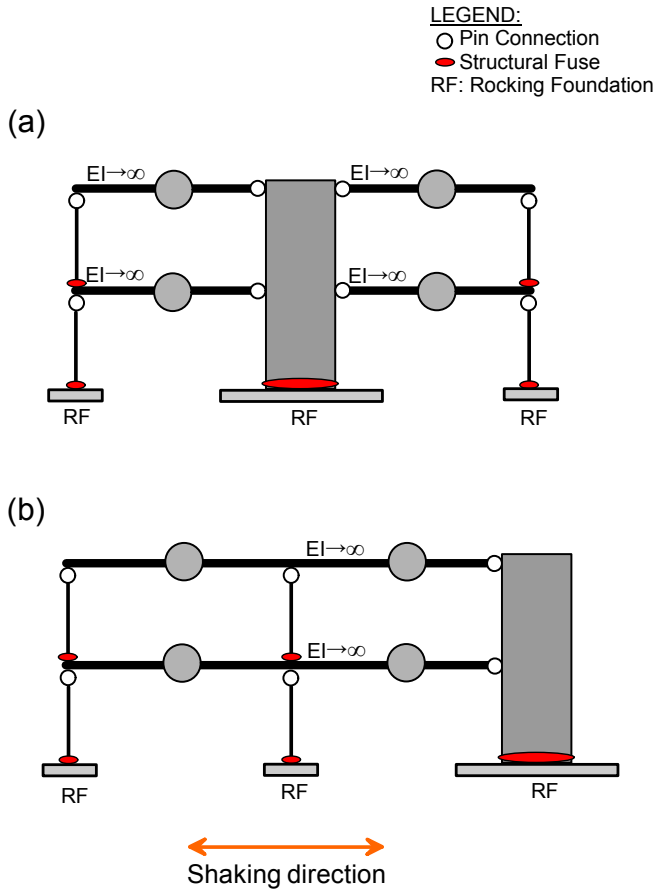

Figure 1.2 Schematics of frame-wall-foundation models: (a) symmetric configuration; (b) asymmetric configuration. (Test-2 concept)

1.2.4 Scope of Numerical Analyses

The goal of the third phase of this research is to investigate the relation between energy dissipation and re-centering of simplified inelastic systems using numerical analyses. In this case, the inelastic systems are constructed by placing multiple fuses, including a rocking foundation, in either parallel or series. Using simplified hysteretic curves, two parameters, namely the energy dissipation ratio (R_{ED}) and re-centering ratio (R_{RC}), are proposed to quantify the seismic performance of the various inelastic systems. These two parameters are not independent, but rather inherently related. As a result, their correlation provides additional perspective regarding the seismic characteristics of foundation-structure systems. The considered inelastic fuse mechanisms in this study include elastic plastic with overstrength (EPO), stiffness degradation and pinching (SDP), and foundation rocking (FR) mechanisms.

1.3 Organization of Dissertation

This dissertation consists of nine chapters organized as follows:

- Chapter 1 introduces the background, motivation, and scope of the present research;
- Chapter 2 provides a comprehensive literature review on the topic of rocking, including structural rocking and foundation rocking.
- Chapter 3 presents numerical parametric studies on simplified frame-type structures during the design stage.

- Chapter 4 provides detailed descriptions of Test-1, discussions of the experimental results, and numerical model validation.
- Chapters 5, 6, and 7 present Test-2 and its findings. In particular, Chapter 5 and 6 focus first on symmetric model results, with emphasis on their cyclic and earthquake response, respectively. Subsequently, Chapter 7 presents the seismic response of the asymmetric model behavior.
- Chapter 8 presents the concept of the energy dissipation ratio and re-centering ratio and correlates them using numerical analysis results of simplified inelastic systems which include rocking foundations as well as the experimental data of Test-2.
- Chapter 9 summarizes the major findings and contributions of the present study and provides recommendations for future work.

Chapter 2

Research Background and Prior Work

Rocking behavior, either within the structural elements of a building or at its foundations, has been highlighted as a promising design solution to minimize earthquake-induced damage. To date, numerous experimental and numerical studies have been performed around the world to investigate the effects of rocking on the seismic performance of a system expecting earthquake loading. This chapter begins by reviewing research related to rocking within structural elements. Subsequently, literature regarding and characterizing rocking at the foundation level is systematically presented.

2.1 Pioneering Efforts on Rocking

Often cited as the earliest, pioneering study identifying the rocking benefit stems from the analytical work conducted by Housner (1963). Field reconnaissance following the 1960 Valdivia earthquake in Chile reported that several lollipop-like water tank structures survived, while modern structures were severely damaged. Motivated by this observation, Housner analytically studied the dynamic response of a rocking block

subjected to three different types of base excitation, including rectangular-type (constant), sinusoidal pulse with constant frequency, and real earthquake motions. He concluded that tall slender rocking blocks, similar to the water tanks, have a greater stability against overturning during earthquake motion excitation, compared to other structures.

Subsequently, Yim et al. (1980) numerically investigated the overturning stability of rocking rigid blocks subjected to horizontal and vertical ground acceleration, considering various conditions in terms of block geometry and ground motion intensity. This study revealed that a rigid rocking block becomes more stable when earthquake motion intensity and slenderness ratio is decreased or the size of the block is increased.

2.2 Previous Studies on Structural Rocking

2.2.1 Rocking Frame System

Motivated by the favorable attributes of rocking behavior, researchers have carried out numerous shaking table tests to better understand the benefits of structural rocking on seismic performance of the structure. One of the earliest experiments in the literature focused on rocking frames was conducted by Clough and Huckelbridge in 1977 at the University of California, Berkeley. Figure 2.1 shows the elevation view of the 3D model specimen, which was a half-scale three-story-one-bay steel frame structure. This model was tested in two different configurations. In one structural system the column base was pin-connected to a block, which was allowed to move vertically by using roller guides on each side, while in another identical structure it was fixed at its base. Comparison of the response results of the two structures demonstrated that by allowing

uplifting of the columns, the system acceleration response and member force demands are greatly reduced in this case by 33%.

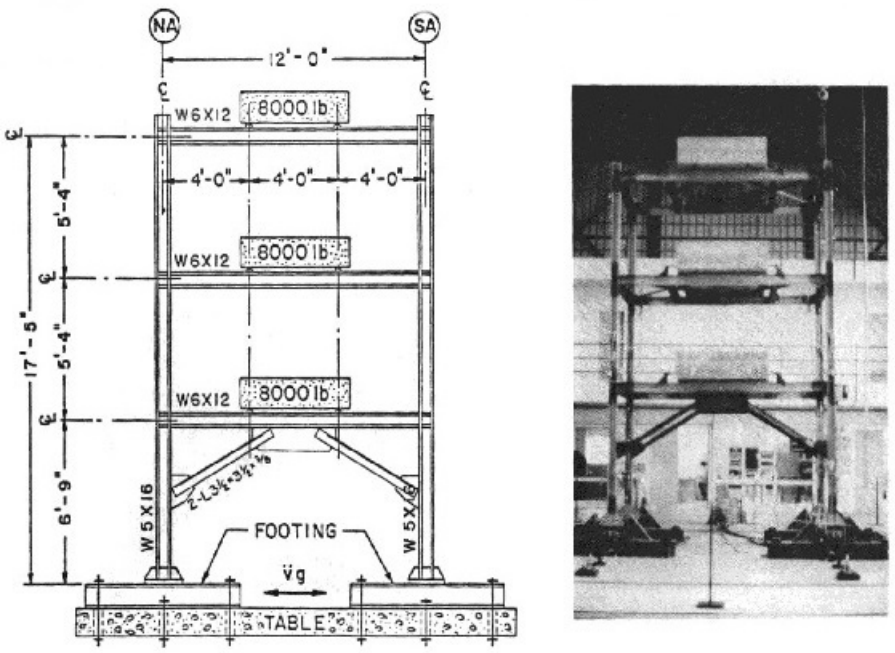

Figure 2.1 Elevation view of a rocking frame structure (from Clough and Huckelbridge 1977)

In a later test program by Midorikawa et al. (2006), a 3D half-scale three-story one by two bay braced steel frames, as shown in Figure 2.2 was tested on a shake table in Japan. In this model, the columns were allowed to uplift and yielding column base plates were installed to dissipate energy.

Shake table tests and numerical analyses were performed to investigate this structure's seismic performance, and in particular, to compare the response with that of a fixed-base configuration. The results showed that the base shear developed in the rocking system were significantly reduced, in this case by 52%, compared with the fixed-base

configuration. The peak displacement, on the other hand, was not significantly amplified in the rocking system, in fact it was almost the same as that of the fixed-base structure.

Figure 2.2 Photograph of a controlled rocking frame structure (from Midorikawa et al. 2006)

In experiments conducted by Pollino and Bruneau (2008) at University of Buffalo, a 3D 1/5-scale four-legged steel bridge pier system was constructed and tested as shown in Figure 2.3. The pier base connection was designed such that sliding along two horizontal directions was restrained while uplift of the pier legs was allowed. Passive energy dissipation devices were implemented at the base of the model to control the rocking response and dissipate seismic energy.

The pier model was subjected to two types of dynamic shaking, uni-directional horizontal base excitation and bi-directional shaking considering simultaneous vertical and horizontal base excitation. The experimental results reveal that the designed

controlled rocking mechanism has an inherent capability to recover from large displacement demands, while at the same time decreasing the base shear demands.

Figure 2.3 Bridge pier model specimen (from Pollino and Bruneau 2008)

Tremblay et al. (2008) implemented viscous dampers into a steel rocking braced frame structure to dissipate seismic energy as well as control peak drift demand. A half-scale two-story braced steel frame was constructed and subjected to earthquake loading at the shake table of Structural Engineering Laboratory at École Polytechnique of Montreal. Figure 2.4 shows a schematic of the test set-up and the constructed model. The test results reveal that the axial load demand imposed on the columns as well as the base

shear is significantly reduced when compared with a traditionally designed braced steel frame structure.

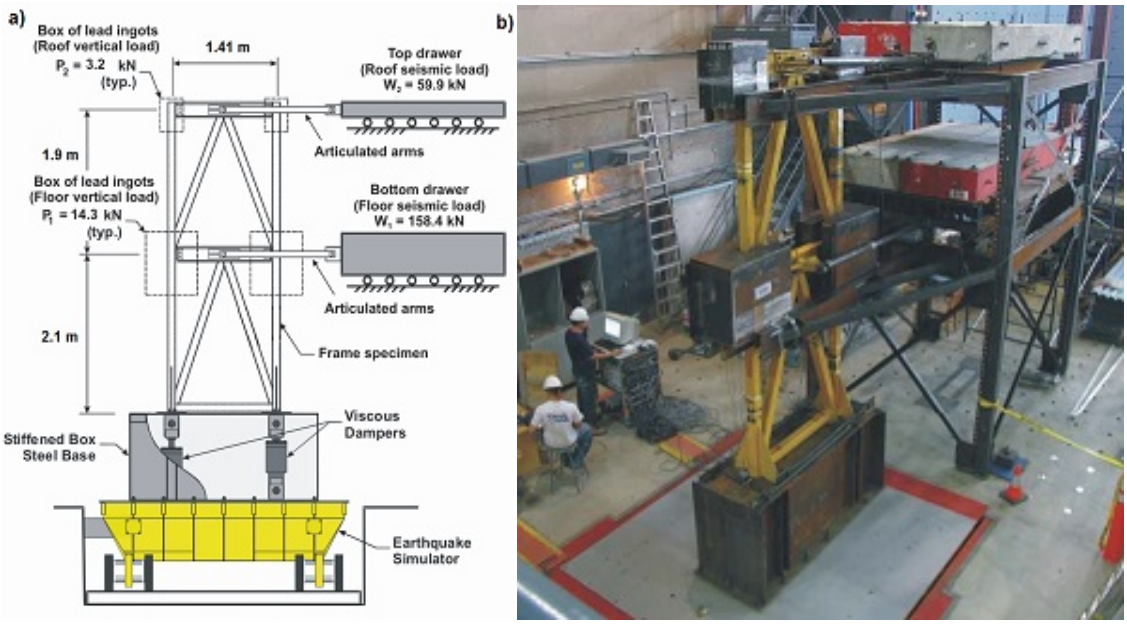

Figure 2.4 Testing of controlled rocking steel frame: (a) schematic of test set-up; (b) photograph of the model specimen (from Tremblay et al. 2008)

Alternative to direct implementation of rocking with concentrically braced or unbraced framing systems, researchers have advanced the rocking idea by incorporating post-tensioned tendons in braced steel frame structural systems (e.g. Eatherton et al. 2010; Ma et al. 2010). Figure 2.5 shows the hybrid rocking frame system tested at University of Illinois. In contrast to previous rocking frame systems, this hybrid system introduces vertical post-tensioning tendons and replaceable structural fuse elements placed between each rocking frame to enhance its re-centering behavior and energy dissipation performance. The test models were subjected to a series of cyclic and dynamic earthquake loads. The model demonstrated a significant re-centering and damage control capability.

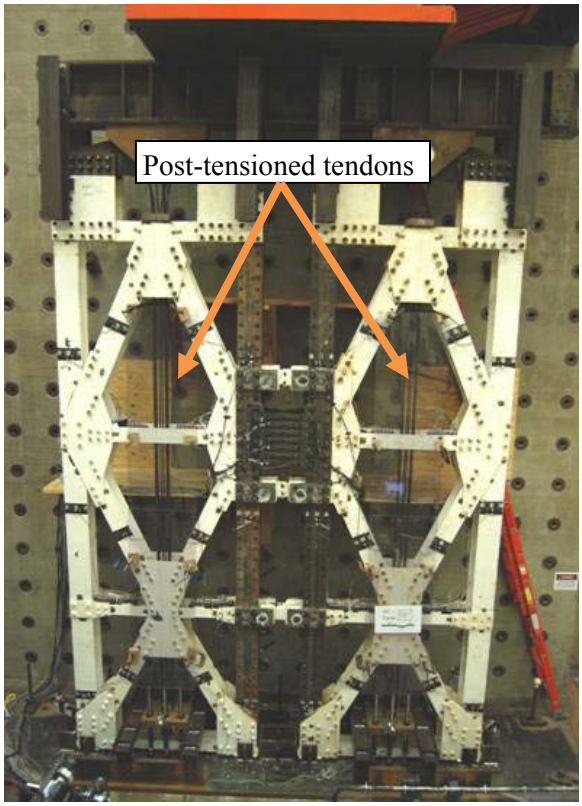

Figure 2.5 Photograph of a model braced frame system, augmented with post-tensioning (from Eatherton et al. 2010)

2.2.2 Rocking Wall System

Researchers have also implemented the rocking concept into wall components and frame-wall structural systems. For example, Kurama et al. (1999) proposed unbonded post-tensioned tendons to connect a precast RC wall and its foundation, as shown in Figure 2.6. In this proposed configuration, the precast wall is allowed to rock around its base, and the lateral force resistance is provided by the post-tensioned tendons. Numerical analyses were then conducted to evaluate its performance under earthquake loading. It is found that although the proposed rocking wall experienced a larger displacement compared with that of a comparable conventionally designed cast-in-place

wall, residual deformations at the end of the dynamic tests were significantly smaller compared to a conventional wall. Ajrab et al. (2004) extended this concept into a frame-wall dual system wherein draped tendons were introduced externally to connect the rocking wall and a rigid foundation. Extensive numerical simulations and parametric studies were carried out to examine the seismic performance of a prototype six-story structure. The authors observed that the floor accelerations and interstory drifts are reduced when supplemental dampers are installed on the test structure.

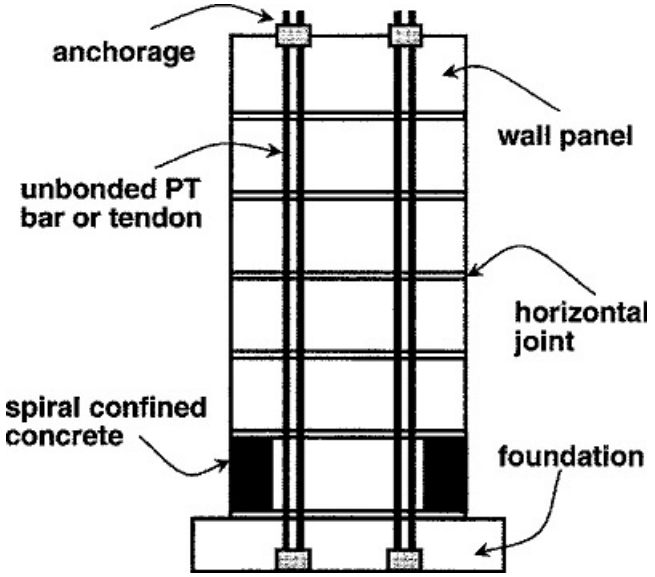

Figure 2.6 Schematic of an unbonded post-tensioned precast wall (from Kurama et al. 1999)

Restrepo and Rahman (2007) performed quasi-static tests on a similar rocking wall component, where unbonded prestressed tendons were installed. Three half-scale precast reinforced concrete walls were constructed at the University of California, San Diego (UCSD), two of which were installed with energy dissipaters. Figure 2.7 shows the reinforcement details of one of these specimens. Upon cyclic loading, all wall units observe no lateral-force capacity degradation, even when the drift ratio attains more than

3%. The wall unit implemented with the energy dissipaters demonstrated a favorable "flag-shape" hysteretic response, with an equivalent viscous damping ratio of 14%.

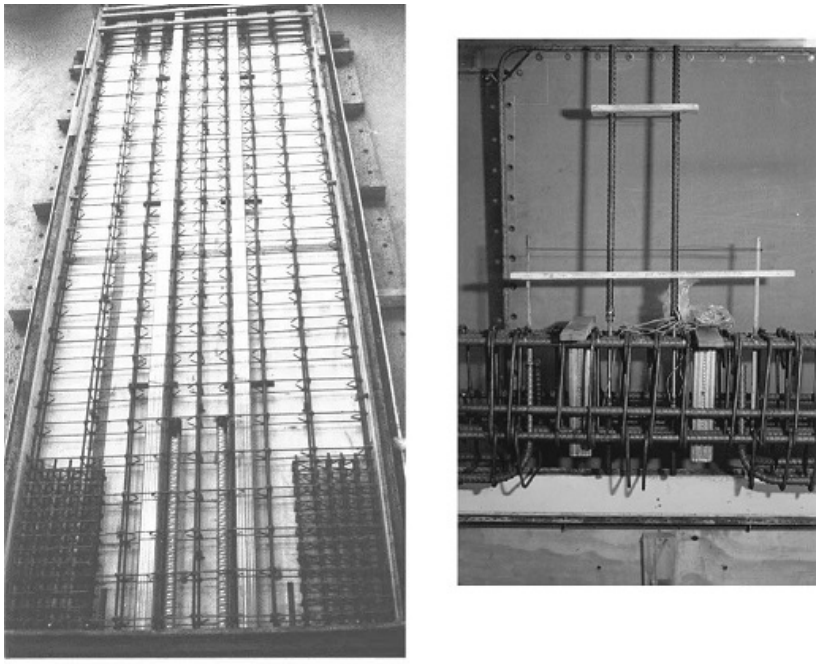

(a) Wall reinforcement (b) Foundation and energy dissipators

Figure 2.7 Reinforcement details of one wall specimen prior to casting of concrete (from Restrepo and Rahman 2007)

Subsequently, Toranzo et al. (2009) designed and tested a 40%-scale rocking wall-frame model. The rocking wall component was constructed of confined masonry, as illustrated in Figure 2.8. In this model, a pair of steel energy dissipating dampers was implemented at the base of the rocking wall in order to absorb additional seismic energy. Upon strong shaking, the hybrid rocking wall system observes no residual deformation, indicating a substantial re-centering characteristic.

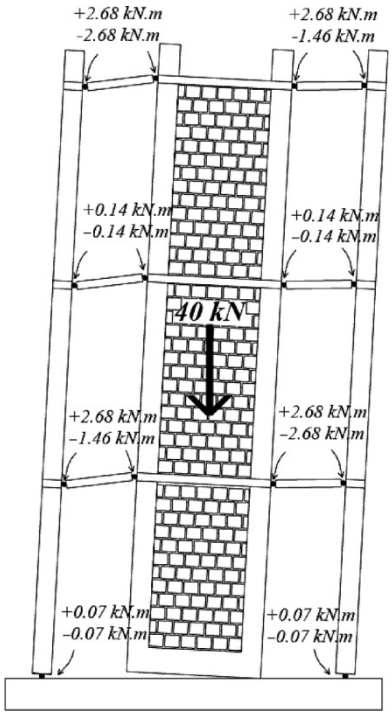

Figure 2.8 Schematics of confined-masonry rocking wall (from Toranzo et al. 2009)

2.3 Previous Studies on Foundation Rocking

Numerous experimental and numerical studies have been conducted to understand the characteristics of a rocking shallow foundation, both as a component and within a system. This section primarily describes the prior work on foundation rocking.

2.3.1 Component-Level Studies

To the authors' knowledge, the earliest experiments on foundation rocking were carried out by researchers in the 1970s at the University of Auckland. These were documented in a pair of Master's thesis by Bartlett (1976) and Weissing (1979). Both test programs were conducted at one-g and focused on understanding the shallow footing's

moment-rotation response. Bartlett (1976) performed cyclic test on a 0.25 × 0.5m shallow foundation resting on the surface of clay. Weissing (1979) used a similar footing, however founded it on dry sand. The obtained moment-rotation hysteretic response at the soil-footing interface was broad, indicating a favorable energy dissipation capability. However, a gradual reduction in the rotational stiffness of the foundation soil is observed. These experimental results reveal the substantial potential of the shallow foundation to dissipate hysteretic energy at the soil-footing interface during rocking. However, progressive permanent settlement is observed in these tests.

Motivated by the aforementioned pioneering work, numerous component-level experimental studies have been performed to characterize foundation rocking response under various soil and footing geometry conditions. In general, the experimental studies are conducted at either 1-g level or with a high-g level via a centrifuge environment.

2.3.1.1 One-g Level Experimental Work

Taylor and Crewe (1996) performed the first dynamic shaking table test on a concrete rocking foundation. A large flexible shear stack of the shake table was designed to replicate soil boundary conditions and produce realistic inelastic soil response, as shown in Figure 2.9. A shallow foundation (0.4m × 0.4m) with 0.1m embedment was placed inside of this designed stack which was filled with sand. An earthquake motion with peak ground acceleration (PGA) of 1.23g was applied at the base of the shake table. The test results reveal a significant permanent settlement of this foundation.

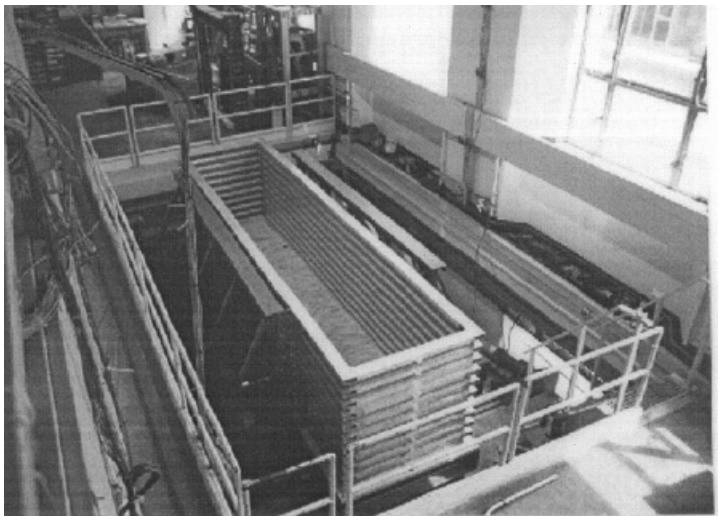

Figure 2.9 Designed shear stack on the shaking table (from Taylor and Crewe 1996)

Negro et al. (2000) carried out large-scale cyclic testing on a rocking shallow foundation. The foundation had a dimension of 1m × 1m in plan view and rested on saturated uniformly distributed Ticino sand (Figure 2.10). Two different soil conditions were considered in this program, loose and dense sand with relative densities (D_r) of 45% and 85%, respectively. Cyclic horizontal force was applied at the top of the foundation to replicate the inertial force transmitted from the superstructure during seismic loading. The experimental results show that the rocking foundation, when resting on low D_r sand, observes a fairly broad moment-rotation hysteretic response; however, it cumulates a significant permanent settlement and rotation at the end of the test program. The foundation founded on a high D_r sand observes significantly smaller peak and permanent settlements.

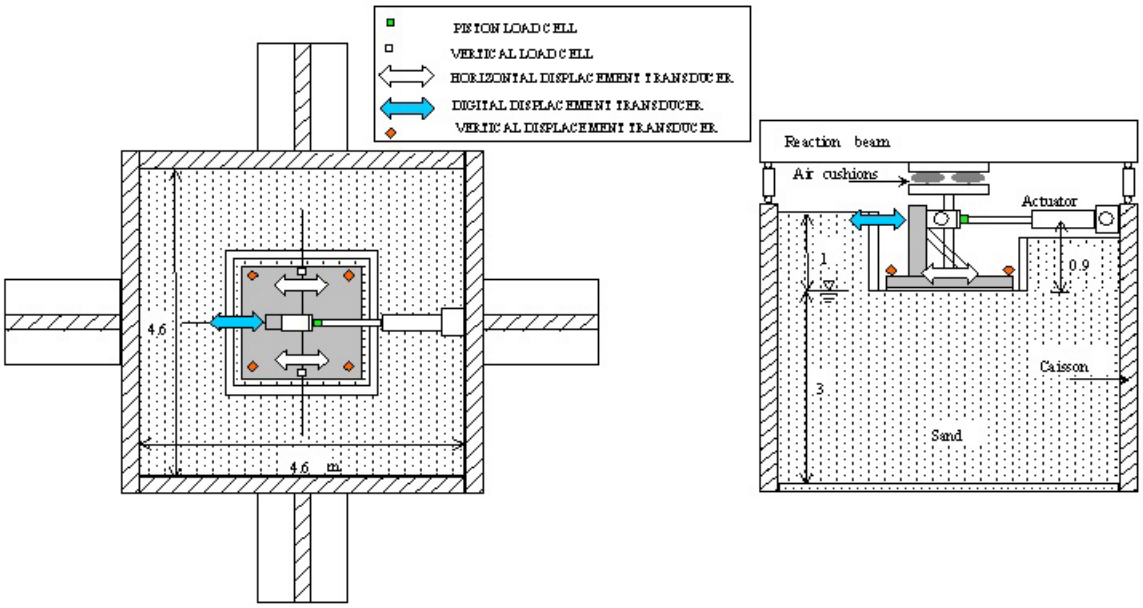

Figure 2.10 Schematic of the experimental set-up (from Negro et al. 2000)

Espinoza and Mahin (2006) performed a series of shaking table tests of 1/4.5-scale lollipop-style concrete bridge structure supported on a spread foundation. As shown in the model schematic (Figure 2.11), the foundation component was resting on a 50-mm-thick layer of neoprene pad used to mimic a competent soil condition. The footing size was significantly reduced when compared with the conventional design followed by Caltrans seismic design criteria to ensure foundation uplift. The experimental results show that the foundation rocking system observes a similar or lower displacement demand compared with a fixed-base design. In the meantime, the column is effectively protected and returns back to its initial position at the end of the shaking due to re-centering.

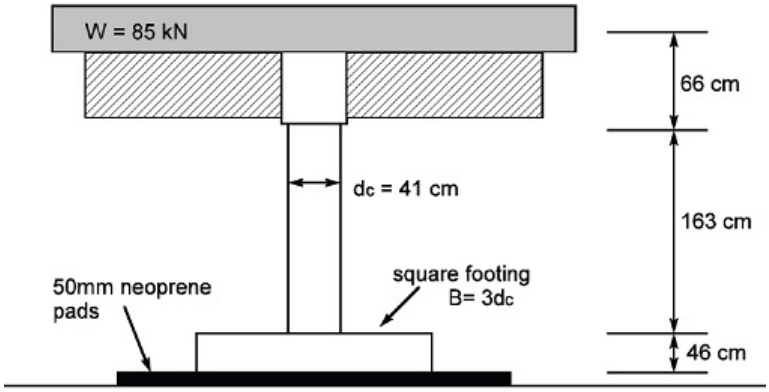

Figure 2.11 Schematic of the tested bridge structure (from Espinoza and Mahin 2006)

Paolucci et al. (2008) and Shirato et al. (2008) jointly performed a series of large-scale 1-g shaking table test to characterize the dynamic behavior of shallow foundations. Figure 2.12 shows a photograph of their test apparatus, which consisted primarily of a laminar box filled with dry Toyoura sand. The sand had a D_r of 80% and an internal friction angle of 42.1º. The footing component (0.5m × 0.5m with a vertical factor of safety FS_v of 29) was placed in the center of the fill surface. The shaking table was then excited by multiple earthquake input motions. The experimental results in terms of the relationship between moment and rotation continue to substantiate the rocking footing's advantageous energy dissipation capacity. However, when the specimen was subjected to a significantly high level of shaking (PGA=8.21 m/s^2), the footing eventually tipped over due to excessive foundation rocking.

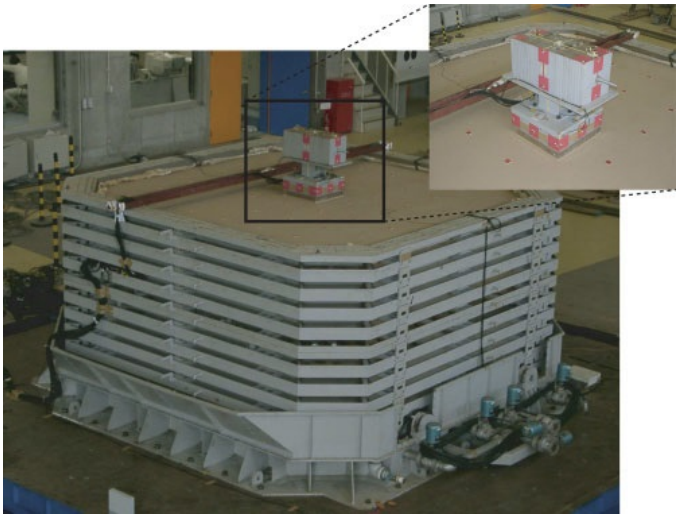

Figure 2.12 Photograph of the experimental set-up and the rocking foundation model (from Paolucci et al. 2008)

Hung et al. (2011) performed pseudo-dynamic tests and slow cyclic testing on several bridge piers to examine effects of foundation rocking on the ductility demand imposed on the bridge column. As shown in Figure 2.13, the bridge pier constructed by circular RC column was considered with two different base conditions, namely fixed-base and rocking-base. The fixed-base condition was created by anchoring the foundation to the rigid floor with four tie-down rods, whereas the rocking-base condition was mimicked by applying a neoprene pad layer underneath the foundation. The experimental results indicate that the rocking-base bridge observes relatively larger deck drift when compared with that of the fixed-base one. However, allowing the foundation to rock provides an isolation mechanism, which greatly limits the moment demand transmitted to the column base and eventually protects the column against failure.

Figure 2.13 Constructed bridge piers under two different conditions: fixed-base (left) and rocking-base (right) (from Hung et al. 2011).

Researchers at the National Technical University of Athens conducted a series of comprehensive experiments on reduced-scale single-degree-of-freedom (SDOF) structures resting on rocking footings (e.g., Anastasopoulos et al. 2012; Anastasopoulos et al. 2013; Drosos et al. 2012). Figure 2.14 provides a photograph of one of the instrumented models in the soil container from these tests. The model specimen consisted of a square shallow footing (15cm × 15cm in plan view), a 45cm-tall rigid column component, and superstructure mass. In these test programs, a variety of soil conditions, including dense (D_r=93%), medium (D_r=65%), and loose sand (D_r=45%), were considered. The vertical factor of safety against bearing failure (FS_v) also varied from 2.6 to 14. The test protocol included both quasi-static cyclic loading and dynamic (earthquake) base excitations. The dynamic testing results indicate that allowing the foundation to rock greatly limits the peak acceleration developed in the superstructure, which effectively protects the superstructure as the inertia force transmitted to the column

base is greatly reduced. In addition, a rocking foundation system with a lower FS_v (3.3) observes a gradually reduced settlement as shaking continues, which is attributed to soil densification after several shaking.

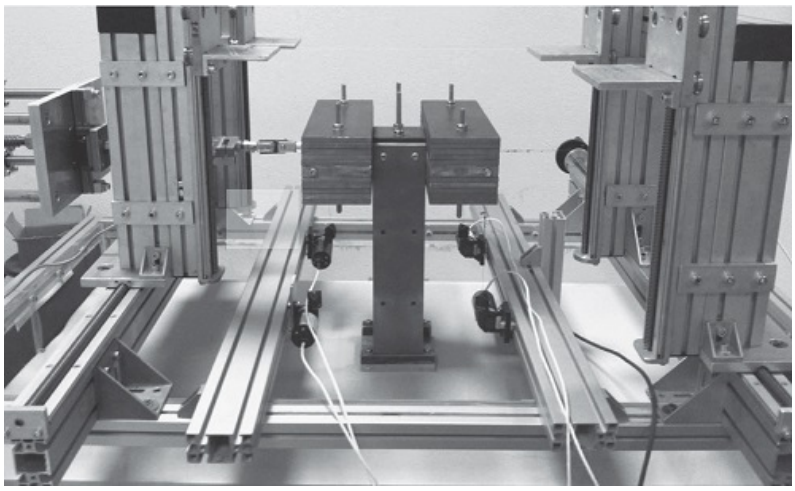

Figure 2.14 SDOF model specimen in soil container (from Anastasopoulos et al. 2012)

2.3.1.2 High-g Level Centrifuge Experimental Efforts

It is generally recognized that the inelastic mechanical characteristics of geotechnical materials are greatly influenced by confining stress. Therefore, to investigate the soil-foundation-structure interaction problem, a replication of prototype stress within the soil specimen is important. The centrifuge environment can impose an amplified gravitational field and therefore has been well known for its utility in the geotechnical field for replicating realistic stress conditions (Schofield 1980; Scott 1983; Kutter 1995).

Since 2000, an experimental program at the University of California, Davis (UCD) has been carried out using centrifuge testing to investigate the mobilization of soil-foundation capacity, allowing nonlinear rocking, sliding, and settling of the footing to

occur (e.g. Roosebrook and Kutter 2001a,b,c; Phalen 2003; Gajan et al. 2005; Thomas et al. 2006). These programs examined several shear wall-footing models typically at 20-g centrifugal acceleration (e.g. see Figure 2.15). Each model was constructed with different footing dimensions, depth of embedment, and initial static FS_v. In addition, a variety of soil conditions, including cohesive (clayey) and cohesionless (medium to dense sandy soil) geotechnical environments were considered. The model specimens were typically subjected to two different loading conditions, namely lateral slow cyclic load and dynamic base excitation. Gajan and Kutter (2008) systematically analyzed and summarized the moment-rotation and settlement-rotation response of the foundations from these test programs. Figure 2.15 (right) shows select hysteretic results from their summary analyses. An important outcome from these tests was the observation that footings with a high FS_v (characterized by Gajan and Kutter as A/A_c, where A is the footing area and A_c is the minimum area to support the vertical load), report a small permanent settlement. These tests also consistently verified the prior re-centering potential of the shallow rocking foundation, since the axial load helps to close the gap between the footing and soil during unloading. Moreover, a favorable amount of moment-rotation energy dissipation is observed for all rocking footings.

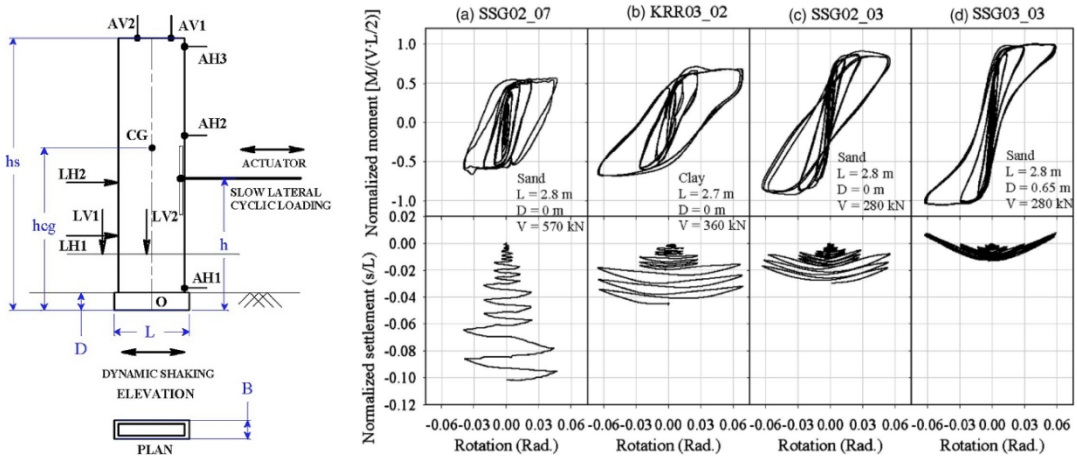

Figure 2.15 Schematic of shear wall-rocking footing and selected hysteretic results in terms of moment-rotation and settlement-rotation relationship (from Gajan and Kutter 2008)

Following these tests, with an emphasis on performance of bridge-foundation systems, Deng and Kutter (2012) implemented concrete pads into the ground to minimize rocking-induced footing settlements. As shown in Figure 2.16, four concrete pads were placed into the ground soil at four edge locations to support the rocking foundation. A reduced-scale SDOF structure was founded on the improved soil condition, and slow cyclic testing and dynamic base shaking was applied. This strategy successfully demonstrated the effectiveness of this treatment in reducing the settlement. It should be noted however, that it did influence the energy dissipated during rocking and the footing's moment capacity.

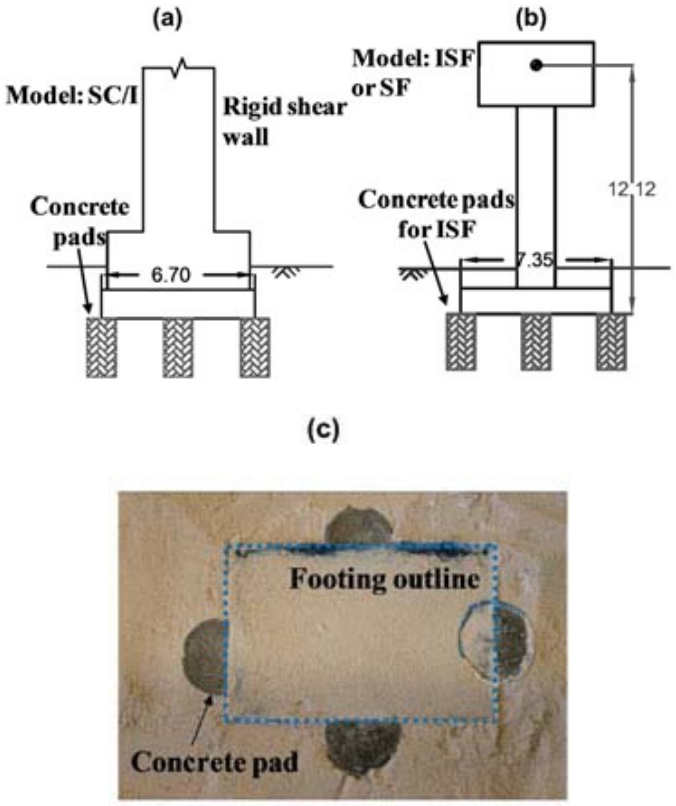

Figure 2.16 Schematics and a photograph of sand with concrete pads (from Deng and Kutter 2012)

Hakhamaneshi et al. (2014) studied the rocking response of I-shaped shallow footings (Figure 2.17). A parameter termed the missing area ratio (MAR) is introduced to characterize the geometry of the I-shaped footing. Several shear wall-I shaped footings with different MARs were constructed and tested via slow cyclic loading in a 35-g centrifuge environment. The experimental results show that a footing with a larger MAR suffers a larger permanent settlement.

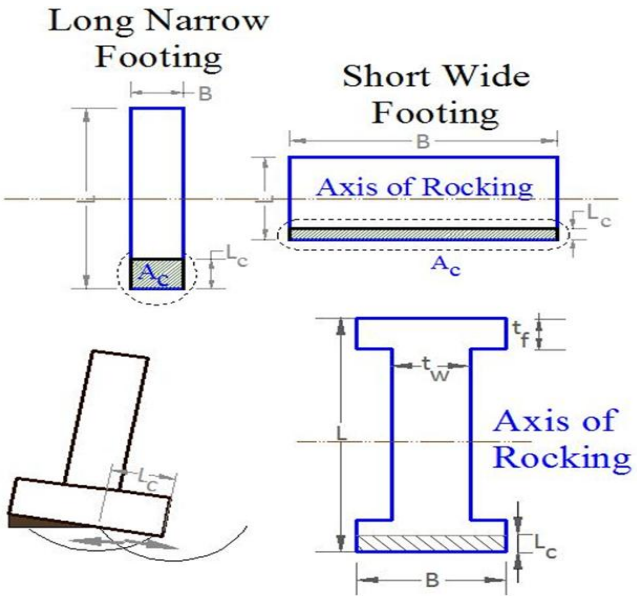

Figure 2.17 Schematics of rectangular and I-shaped rocking footings (from Hakhamaneshi et al. 2014)

2.3.2 System-Level Investigations

Researchers have also performed various system-level characterization whereby the rocking foundation is implemented into a larger structural system. These studies have included a variety of realistic structural configurations, such as bridge structures and frame-type or wall-type buildings.

2.3.2.1 Bridge-Rocking Foundation Systems

Mergos and Kawashima (2005) performed numerical analyses of a bridge structure where foundations were allowed to uplift. Figure 2.18 depicts the elevation view of the five-span continuous reinforced concrete bridge they investigated. In this case, the soil-footing interface was modeled using a distributed array of Winkler-based nonlinear soil spring elements. The results of dynamic analyses indicate that foundation

rocking provides an isolation mechanism, which results in a decrease of the ductility and moment demand on the columns. When the bridge is subjected to biaxial excitation, the isolation mechanism is more pronounced compared with the uniaxial excitation case. However, during a vertical motion excitation, this effect is negligible.

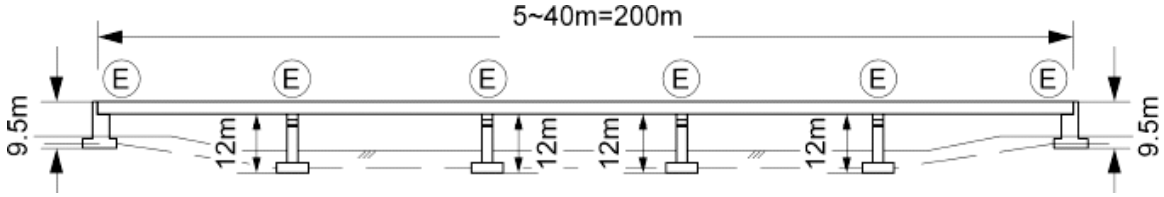

Figure 2.18 Elevation view of the analyzed bridge structure (from Mergos and Kawashima 2005)

Deng et al. (2012a) designed and tested two different centrifuge-scale Single-Degree-of-Freedom (SDOF) bridge system models resting on shallow footings. As shown in Figure 2.19, one model configuration utilizes large elastic footings, which is a representative of a traditionally designed bridge structure, whereas the other model considers much smaller shallow foundations. The geologic medium was constructed by pluviating a uniformly distributed layer of Nevada sand with D_r of 77% in a rigid wall container. The small footing bridge model has FS_v of 29. For both bridge models, the cross-sections of the columns at the base were reduced to effectively mimic the nonlinearity in the superstructure. Upon a sequence of earthquake loading, the foundation rocking system observed less permanent and peak drift demand at the bridge deck compared with the conventional design.

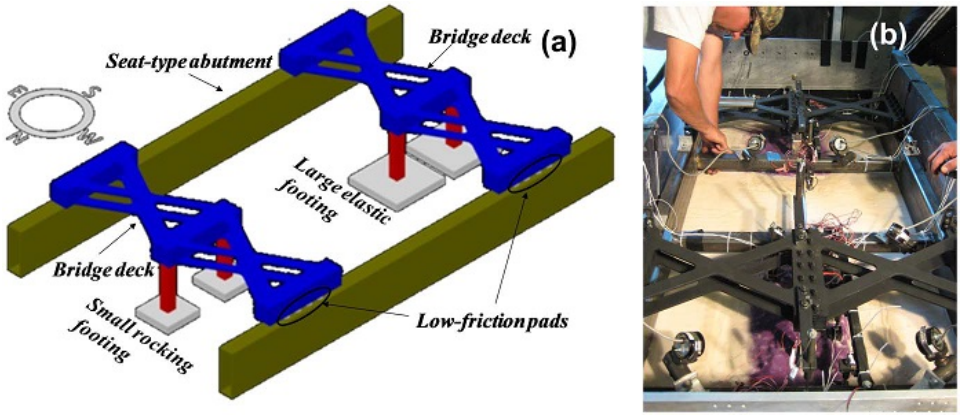

Figure 2.19 Constructed centrifuge-scale bridge-footing models: (a) Model schematic; (b) constructed models in the soil container (from Deng et al. 2012a)

As an extension to the experimental efforts, Deng et al. (2012b) examined the performance difference between a foundation rocking dominated bridge system and a structural hinging dominated system via parametric studies. The foundation rocking mechanism was modeled using Beam-on-Nonlinear-Winkler Foundation (BNWF) approach, as depicted in Figure 2.20. After applying eighty different dynamic ground motions of increasing amplitudes, the results reveal that the rocking dominated system tends to be more stable than the hinging dominated system with similar dynamic properties and system strength. Also, this study continues to substantiate the re-centering benefit of foundation rocking since the rocking system reports significantly smaller residual deformation than that of the hinging system.

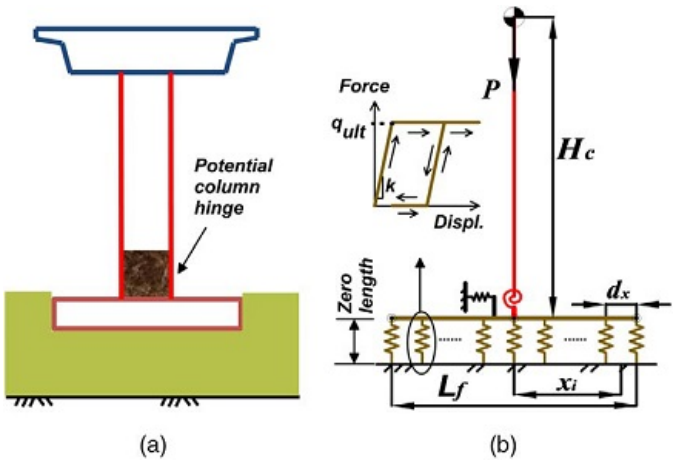

Figure 2.20 Model schematic of simplified bridge structure (from Deng et al. 2012b)

Saad et al. (2012) performed large-scale shaking table tests of a horizontally curved bridge considering rocking foundations at the University of Nevada, Reno (UNR). Figure 2.21 shows a schematic of the tested bridge model and the shaking table facility. The model specimen is a three-span-single-column bent bridge structure with a horizontal curvature of 104º. In this test program, rubber pads were installed around the footing to simulate a realistic soil condition. Numerical simulations have been conducted prior to the test to examine the impact of foundation rocking on the seismic performance of the curved bridge system. Five numerical bridge models with different curvatures were constructed and analyzed in SAP2000 program. The results reveal that allowing the foundation to rock reduced the force demands transmitted to the substructure; however, the deck drift demands were amplified.

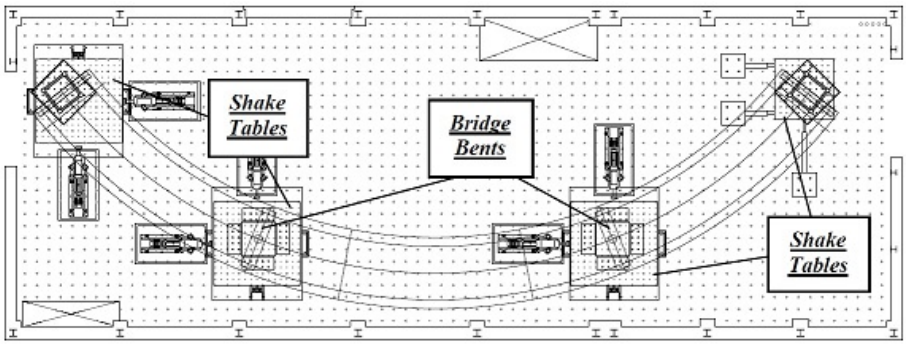

Figure 2.21 Plan view of the test facility and the bridge model at UNR (from Saad et al. 2012)

2.3.2.2 Building-Rocking Foundation Systems

Chang et al. (2007) constructed and tested two reduced-scale 2-D frame-wall building models, namely a one-bay and two-bay models as shown in Figure 2.22, within a 20-g centrifuge environment. Each model was supported on surface shallow footings resting on dry dense sand. In these building models, customized ductile fuse elements were designed and placed at the ends of beam elements to represent nonlinear inelastic behavior of the prototype structure. Upon dynamic shaking and displacement-controlled cyclic loading, it was observed that the rocking footings consistently dissipate more than 65% of the total energy even at large drift demands greater than 2%.

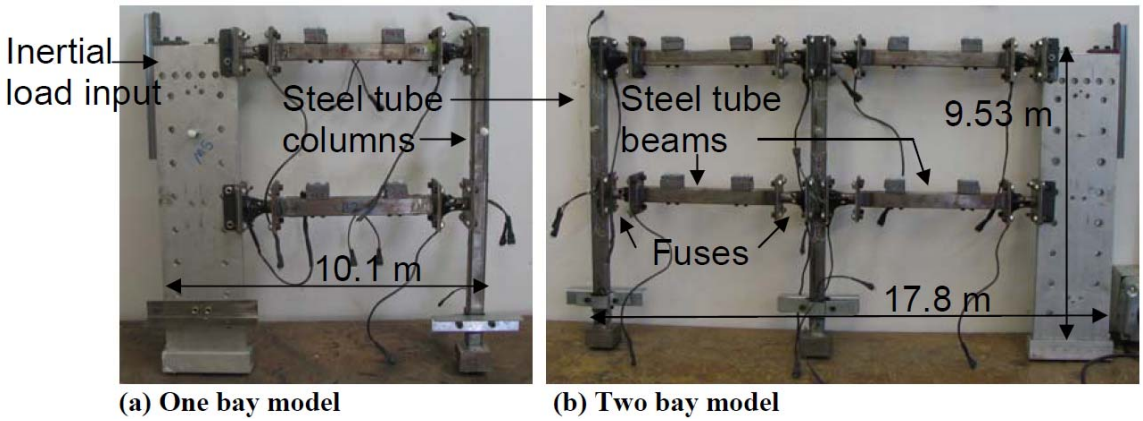

Figure 2.22 Photographs of two constructed centrifuge-scale building models: (a) one-bay model; (b) two-bay model (from Chang et al. 2007)

Raychowdhury and Hutchinson (2011) performed extensive numerical simulations using a Beam-on-Nonlinear-Winkler-Foundation (BNWF) approach to study the effect of inelastic SFSI on the seismic response of shearwall-footing structure systems. The numerical model consisted of an elastic wall element, elastic footing elements, and a distributed array of nonlinear Winkler-based soil spring elements, as shown in Figure 2.23. These spring elements were calibrated against a database of footing experiments (Raychowdhury and Hutchinson 2009). Three different model configurations with various wall heights were considered in this study. Nonlinear time history analyses using earthquake ground motions scaled to different hazard levels were performed. The simulation results continue to substantiate that the foundation rocking is an effective energy dissipation mechanism. It is observed that the moment demand transmitted to the base of the shear wall during an earthquake is reduced by 15-80% compared with that of a fixed-base configuration. In addition, for low-rise buildings energy dissipation is

dominated by nonlinear footing sliding, whereas for medium and high-rise structures, footing rocking contributes more than 80% of the total dissipated energy.

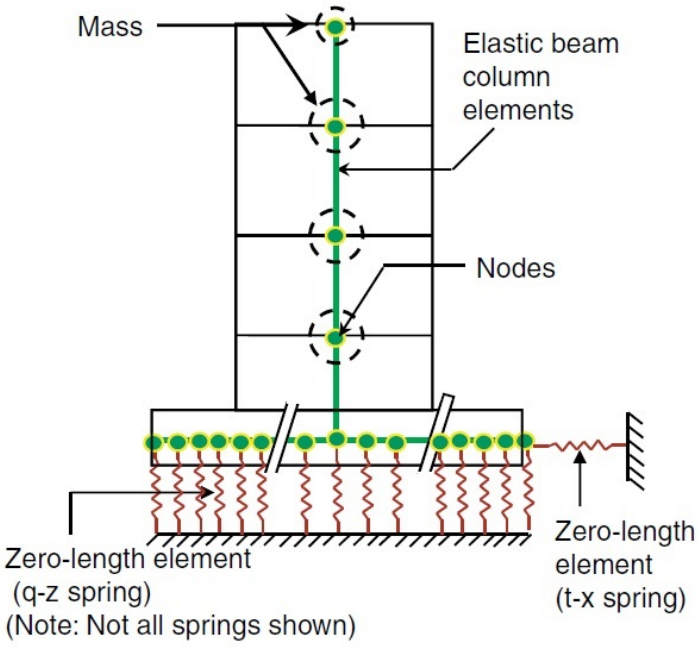

Figure 2.23 Modeling schematic of a shearwall-footing system (from Raychowdhury and Hutchinson 2011)

In parallel, researchers have also performed extensive numerical investigations on frame-type structures implemented with a foundation rocking mechanism (e.g., Gelagoti et al. 2012a; Gelagoti et al. 2012b; Kourkoulis et al. 2012). In these studies, two similar two-story-one-bay RC moment frames were designed following two different strategies, namely, conventional fixed-base design and a rocking footing isolation design, respectively, as shown in Figure 2.24.

The model frames were founded on stiff clay with a undrained shear strength of 150 kPa. The numerical analyses were performed in the ABAQUS program. The results show that during moderate seismic excitation, both frames exhibited similar behavior.

When subjected to significantly strong shaking, the conventionally designed frame observed severe and non-repairable damage in the beams and columns, which could cause a catastrophic collapse; however, the superstructure components of the foundation rocking case experiences negligible but repairable damage.

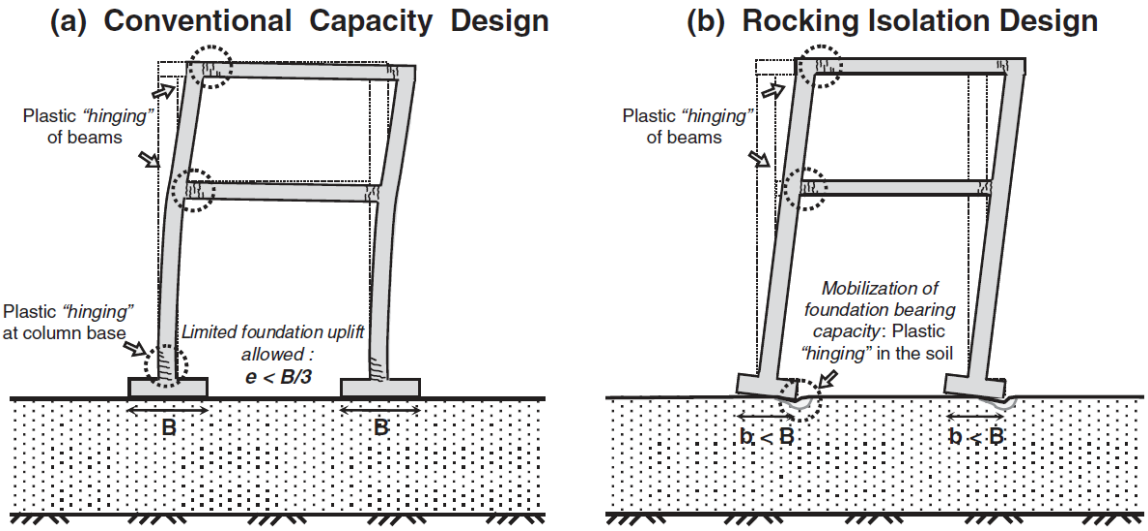

Figure 2.24 Two different frame-type structures: (a) Conventional fixed-base design; (b) Rocking isolation design (from Gelagoti et al. 2012a)

2.4 Summary

This chapter briefly describes and summarizes prior research activities related to structural rocking behavior and the foundation rocking mechanism. It focuses on both component- and system-level experimental and numerical studies.

Largely motivated by the early work of Housner in the 1960s, structural engineers have attempted to allow structural components (e.g., structural wall or lower floor columns) to rock at their bases to protect the structure during seismic events. Due to an

inherent nonlinear elastic behavior of structural rocking, this strategy has a low energy dissipation capacity. However, it has a potentially high re-centering capability. To enhance the energy dissipation capacity, researchers have proposed to implement a variety of external energy dissipaters, such as supplemental dampers, mild steel reinforcement, or other ductile elements, at the base of the rocking component. Meanwhile, unbonded post-tensioned tendons have also been proposed to connect the rocking element to a rigid foundation to help control rocking behavior with a strong re-centering characteristic. Numerous experimental and numerical studies have been performed to examine the seismic performance of this type of hybrid system, and all have demonstrated its effectiveness to reduce residual drift and its ability to dissipate energy. However, these applications have the potential to dramatically increase the construction and maintenance cost and perhaps, as a result may not be cost effective considering the life span of a typical structure.

On the substructure side, however, allowing shallow foundations to rock may provide both benefits concurrently if the geologic media is reasonably competent (e.g., dense sand environment). A number of in-situ field tests and 1-g or high-g level experiments have been carried out to characterize foundation rocking behavior under various soil and footing geometric conditions. These tests generally conclude that foundation rocking can provide a seismic isolation mechanism in which the ductility and acceleration demands imposed on structural components are greatly limited. Additionally, it can assist with dissipating seismic input energy and introduce a self-centering benefit with the assistance of the "P-Δ" effect. Several system-level experimental and numerical studies further substantiate its beneficial contributions to a structure-foundation system as

a whole when subjected to seismic load. In contrast to the structural rocking systems, foundation rocking system is fairly simple as it can be achieved by simply reducing the foundation geometry and allowing it to uplift during shaking. In addition, it does not require any supplemental components to dissipate energy or produce re-centering behavior. As a result, it is generally believed that a foundation rocking strategy would dramatically reduce the total cost, while provide the aforementioned seismic advantages.

Chapter 3

Numerical Analyses to Support Test-1 Design

3.1 Motivation and Scope

Although a handful of experiments have considered the participation of both foundation and structural components to a systems seismic resistance, prior test efforts did not strategically implement a targeted design strategy. To embrace the foundation rocking mechanism within a conventional structural design paradigm, it is useful to systematically consider the systems behavior with varying levels of foundation strength. In parallel, typical earthquake-resistant structural configurations within a building system incorporate structural fuse mechanisms within the superstructure components to dissipate seismic energy; therefore, such a systematic study should similarly embrace this philosophy. The question of how these two inelastic components dynamically interact with each other and share the seismic demand is still unreported and warrants a future investigation. Prior to designing and testing structural models, in this chapter, a numerical

parametric study is conducted on a frame-braced building-foundation system in *OpenSees* (Mazzoni et al. 2009). The primary goal of this study is to investigate the effect of varying the governing parameters on the system's seismic performance and to guide model design for Test-1.

3.2 Proposed Moment Frame-Foundation Building Configuration

In present study, the target structural system is a one-bay-two-story moment-resisting frame-type system. Two types of inelastic *hinging* mechanisms are considered in this system. The first is referred to as a *structural hinging mechanism*, wherein structural components are designed to reach their strength during moderate- or high-intensity earthquake excitation and deform plastically. This inelastic element is termed structural fuse hereafter. The second, referred to as a *foundation rocking mechanism*, is expected to develop at the soil-foundation interface. Figure 3.1a schematically depicts the structural configuration of the target system, wherein the open ellipses located at the bottoms of columns at each level represent the structural hinging and foundation rocking, respectively. The beam elements and the columns at first level are assumed to perform linear-elastic, and therefore the flexural stiffness (EI) is assumed to be theoretically infinite. Therefore, the lateral (elastic) stiffness at the first and second level will be dictated by the foundation rotational stiffness and the second story column flexural stiffness, respectively. As such, it can be considered as a 2 degree-of-freedom (2-DOF) system and its dynamic characteristics, such as natural vibration periods of vibration, can

be analytically determined. In the meantime, pinned connections were introduced at the top of the first and second floor columns for two reasons: (1) to simplify the analysis of moments in the structural fuses and in the rocking foundations; (2) to promote an anticipated foundation rocking mechanism. Part (b) of Figure 3.1 describes an idealized nonlinear load-deformation curve for both the structural fuse and the rocking footing, where k_e, k_p, and k_u denote the elastic stiffness, plastic stiffness, and unloading stiffness, respectively.

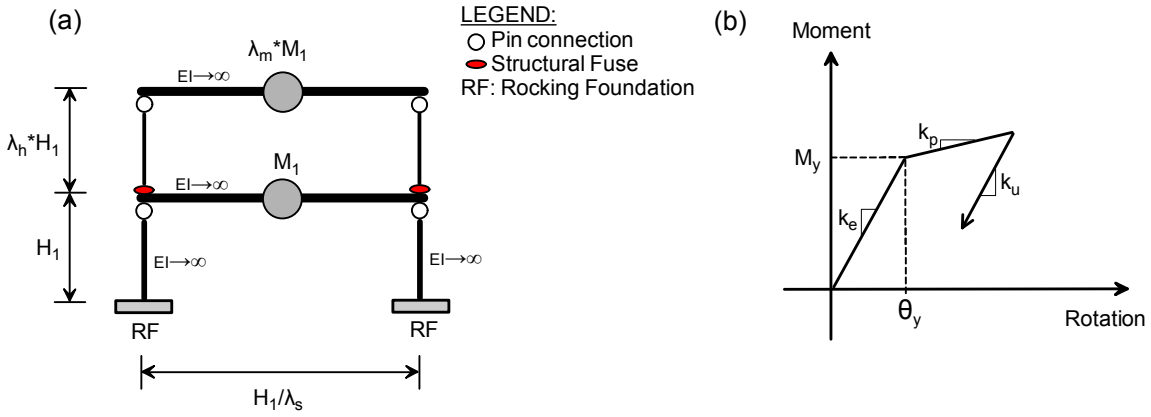

Figure 3.1 (a) Schematic of structure configuration; (b) idealized load-deformation of structural fuse and rocking footing

Table 3.1 identifies several key parameters governing the elastic and inelastic response of the proposed building-foundation system. These parameters include the natural vibrational periods of the system (T_1, T_2), the stiffness hardening and unloading stiffness ratio for structural fuse and rocking footing (k_p/k_e, k_u/k_e), strength parameters for the fuse and footing (C_r, C_y), mass at each level (M_1, M_2), and geometric parameters (H_1, H_2, λ_s).

Table 3.1 System global parameters and their baseline values

Parameter	Parameter Description	Baseline value
M_1	First story mass	1.0
λ_m	Ratio of mass at each level (M_2/M_1)	1.0
T_1	Flexible-base first natural period	0.3 s
λ_t	Ratio of first two natural periods (T_2/T_1)	0.33
H_1	Column height at first story	3
λ_h	Story height ratio (H_2/H_1)	1.0
λ_s	Ratio of first story height to column spacing	0.25
k_p/k_e	Stiffness hardening ratio for fuse and footing	0.01
k_u/k_e	Unloading stiffness ratio for fuse and footing	1
C_y	Structural fuse yield coefficient	0.3
C_r	Foundation rocking yield coefficient	0.3

Two dimensionless parameters, C_y and C_r, are proposed in this study to characterize the yield moment of the structural fuse and rocking footing respectively. The structural fuse yield coefficient C_y is defined as the yield moment of the structural fuse normalized by the inertial weight it must support times the height. Since the upper floor columns cantilever from the second floor level (Figure 3.1a), the yield moment of the structural fuse M_{y_fuse} can be correlated with knowledge of the second story mass M_2 and height of the second floor ($H_2 = \lambda_h \times H_1$), i.e.,

$$M_{y\_fuse} = C_y \times M_2 \times g \times H_2 \tag{3.1}$$

where g = acceleration of gravity.

Similarly, the rocking footing yield coefficient C_r, is defined to characterize the relationship between the moment needed to mobilize the soil-footing capacity ($M_{y\_footing}$) and the superstructure seismic weight. The parameter C_r is effectively the normalized rocking yield capacity of the footing. Considering the effect of the pinned connection at the top of the columns, the yield moment of the rocking footing ($M_{y\_footing}$) may be

correlated to C_r, assuming a uniform seismic lateral force distribution along the building height, as:

$$M_{y\_footing} = C_r \times (M_1 + M_2) \times g \times H_1 \quad (3.2)$$

where M_1 and H_1 = the mass and height of the first story, respectively.

The baseline value of each parameter which is selected based on a review of typical low-rise moment frame-foundation building systems is provided in Table 3.1. It is noted that the mass values are assigned as unity in this study. In addition, the column heights are taken as a length of 3.0. These values do not reflect typical engineering values of a real building, but rather we assigned for simplicity.

3.3 Model Construction and Motion Characteristics

3.3.1 Numerical Model Construction

The numerical model is constructed in *OpenSees* (Mazzoni et al. 2009), wherein elastic beam-column elements and inelastic uniaxial materials are utilized to model structural elastic behavior and inelastic behavior of the fuses, respectively. Figure 3.2a schematically describes the modeling strategy. In this model, the "beam with hinges" (BWH) element (Scott and Fenves, 2006) is utilized to simulate the second story columns with structural fuses, with 10% of the column height defined as the hinge length ((Mazzoni et al. 2009). To model the rocking foundations, a bed-of-spring model, also known as the Beam-on-Nonlinear-Winkler-Foundation (BNWF) approach, is not warranted in the design stage due to lack of underlying soil information and foundation

geometry. Instead, lumped inelastic zero-length spring elements are utilized at the bottom of the first story columns to simulate the footing rocking behavior. In this design stage, it is assumed that the moment-rotation curves of the structural fuses and rocking footings follow an idealized elasto-plastic, e.g. bilinear relationship. In *OpenSees*, these can be realized by using the "Steel01" uniaxial material (Mazzoni et al. 2009), as illustrated in Figure 3.2b. The remaining structural elements of the numerical model, including beam elements and columns at the first floor, are constructed using elastic beam-column elements. In addition, corotational geometric formulation is these analyses to capture second-order effects.

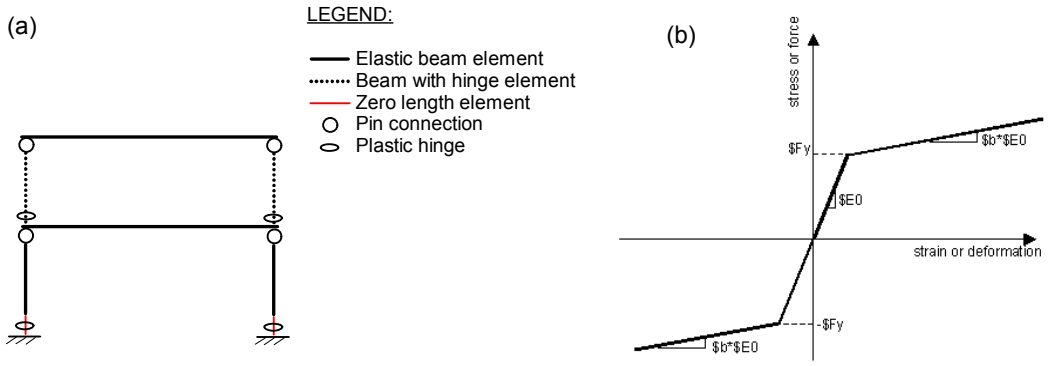

Figure 3.2 Numerical model construction: (a) model construction; (b) Steel-01 elasto-plastic behavior (from Mazzoni et al. 2009)

3.3.2 Input Motions Used in these Analyses

Three recorded ground motions from different seismic events are selected and used to perform dynamic time history analysis. Table 3.2 summarizes the ground motion details and main characteristics of these motions. These motion records are adapted from Pacific Earthquake Engineering Research Center (PEER) motion data base (2012). The

achieved characteristics in Table 3.2 demonstrate varied predominant frequency content of these motions (predominant period T_p ranges from 0.18 to 0.28 sec) as well as varied peak ground acceleration (PGA) (0.59-0.93g). These motions are generally of a short duration with strong duration (t_d) less than 8 seconds.

Figure 3.3a shows the 5% damped elastic spectral acceleration spectrum of each ground motion, overlaid with the target natural periods of the building-foundation system. This plot shows that these motions have a range of dominant frequency content. The Morgan (MG) motion, for example, is dominated by high frequency (low period) component, whereas the Gazli (GZ) motion observes a considerable amount of low frequency components. In addition, two ground motions, GZ and San Fernando (SF), present with descending spectral acceleration demands during period elongation of the system ($>T_1$), while MG presents with ascending demands. The acceleration time history plots of these motions, as provided in part (b), continue to show the diversity of the motion characteristics.

Table 3.2 Motion Source Characteristics

Motion Name	Earthquake Event	Magnitude (M_w)	Recording Station	PGA (g)	T_p (s)	t_d (s)	$S_a(T_1,5\%)$ (g)
GZ	Gazli, USSR, 1976	6.8	Karakyr	0.72	0.28	6.3	0.88
SF	San Fernando, USA, 1971	6.6	Pacoima Dam	0.59	0.24	7.1	0.77
MG	Morgan Hill, USA, 1984	6.2	Coyote Lake Dam (SW Abut)	0.93	0.18	4.5	1.47

Notes: PGA=peak ground acceleration; T_p=predominant period, taken as the period at the peak of the elastic acceleration spectrum; t_d=strong duration is estimated by computing the time difference between 5 and 95% cumulative Arias Intensity.

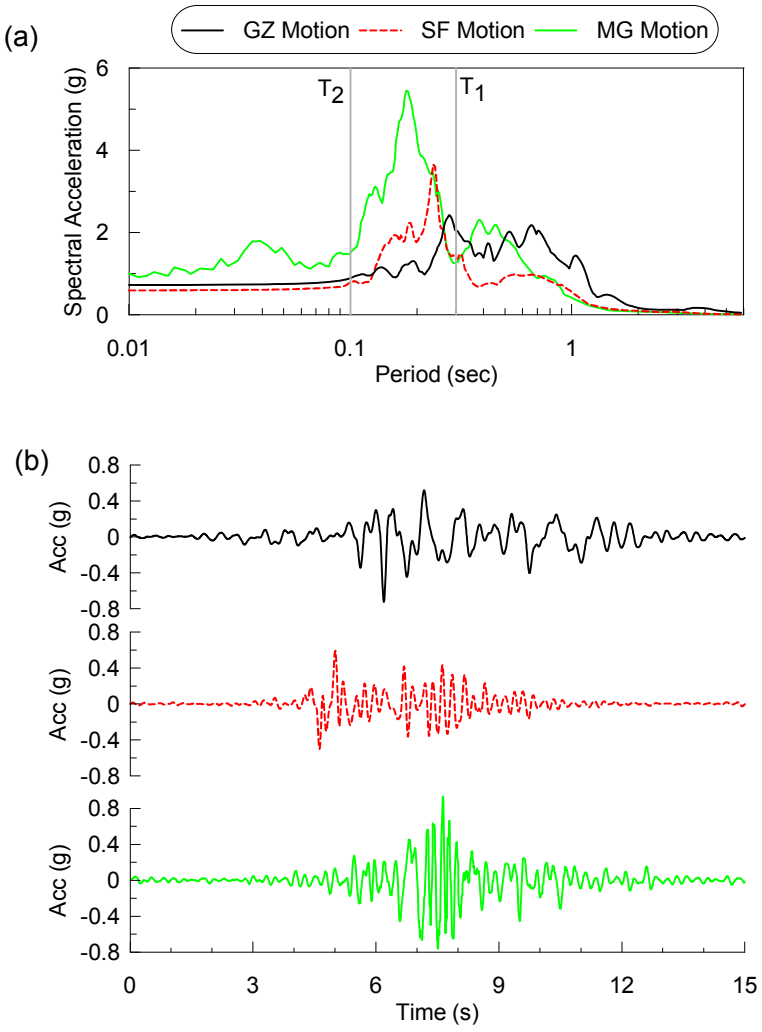

Figure 3.3 Motion Characteristics: (a) 5% damped elastic spectral acceleration spectrum; (b) acceleration time histories

3.3.3 Variables in Parametric Study

Table 3.3 identifies five predominant parameters, the variation of which could significantly influence the inelastic performance of the building-foundation system. The candidate values for each parameter, which are used for sensitivity analysis, are also provided. The strength parameters (C_y and C_r) consider five values ranging from 0.1 to

0.5. The second natural period is considered with three different values, while the story height ratio and mass ratio are selected to vary from 0.5 to 1.5 with an increment of 0.25.

Table 3.3 Predominant parameter and candidate values

Predominant Parameter	Description	Candidate Values	Number of Analyses Performed
C_y	Structural fuse yield coefficient	0.1,0.2,0.3,0.4,0.5	5 × (3motions) = 15
C_r	Foundation rocking yield coefficient	0.1,0.2,0.3,0.4,0.5	5 × (3motions) = 15
λ_t	Ratio of first two natural periods	0.1,0.333,0.4	3 × (3motions) = 9
λ_h	Story height ratio	0.5,0.75,1.0,1.25,1.5	5 × (3motions) = 15
λ_m	Ratio of mass at each level	0.5,0.75,1.0,1.25,1.5	5 × (3motions) = 15

3.4 Numerical Parametric Study

3.4.1 General Scope

The parametric study is performed by varying one parameter at a time, while the remaining parameters are retained of their baseline values (Table 3.1). The goal of this study is to investigate the effect of varying each predominant parameter on the system's seismic performance and further provide guidance for the design of the model in Test-1. Note that the first natural period (T_1) and the mass at the first level (M_1) remain at their baseline values throughout the parametric study. As such, the flexural stiffness (EI) of the elastic structural members is varied to ensure a constant value of T_1 once the predominant parameters are changed. For a 2DOF system, these flexural stiffnesses can be analytically determined with knowledge of the mass at each level and two natural periods based on the fundamental theory of free vibration.

After running motion analyses for different model and motion scenarios, the seismic performance is systematically compared. A number of engineering demand parameters (EDPs) are selected for comparison, including maximum structural fuse rotation normalized by its yield rotation, maximum and residual roof drift normalized by the building height, maximum footing rotation normalized by its yield rotation, and maximum base shear normalized by the superstructure weight. Note that the yield rotation of the structural fuse and rocking footing can be determined by dividing its yield moment (M_y) by its rotational stiffness (k_e), as indicated in Figure 3.1b. It is also noted that the actual value of each EDP does not reflect the performance of a realistic frame-type building structure since the mass is assigned as unity. Instead, the comparison amongst different cases and the ensuing trend is more informative.

3.4.2 Effect of Structural Fuse Yield Coefficient (C_y)

Figure 3.4 shows the effect of varying the structural fuse yield coefficient (C_y) on the system's seismic performance. The plots clearly show that the superstructure seismic displacement demand is reduced as C_y increases for all motion cases. For example, the structural fuse maximum ductility demand, which is defined as the ratio of its maximum rotation (θ_{max}) to its yield rotation (θ_y), is dramatically decreased from 12 to 4 when C_y increases from 0.1 to 0.3. The maximum roof drift and the residual drift observe substantial decrease as well when C_y increases from 0.2 to 0.5, as indicated in Figure 3.4b and c. The rocking footing ductility demand, which is also defined as the ratio of its maximum rotation (θ_{max}) to its yield rotation (θ_y), on the other hand, is significantly amplified as the structural fuse becomes stronger; however, it is not monotonically

increased. Figure 3.4d shows that the rocking footing ductility demand is subjected to reductions when C_y is increased from 0.2 to 0.3 during MG and SF motions. This observation is encouraging that a compatible yield moment between the structural fuse and rocking footing can lead to a decreased ductility demand imposed on the footing. Meanwhile, the maximum base shear demand is less sensitive to C_y variation. Part e shows that, during the SF motion, the normalized maximum base shear remains almost constant (around 32% of the dead weight) even when the C_y is increased by five times. During GZ and MG motions, it is slightly increased from 0.31 to 0.41. These observations conclude that targeting C_y at a range of 0.3-0.4 may produce an optimal seismic performance of the building-foundation system given C_r=0.3.

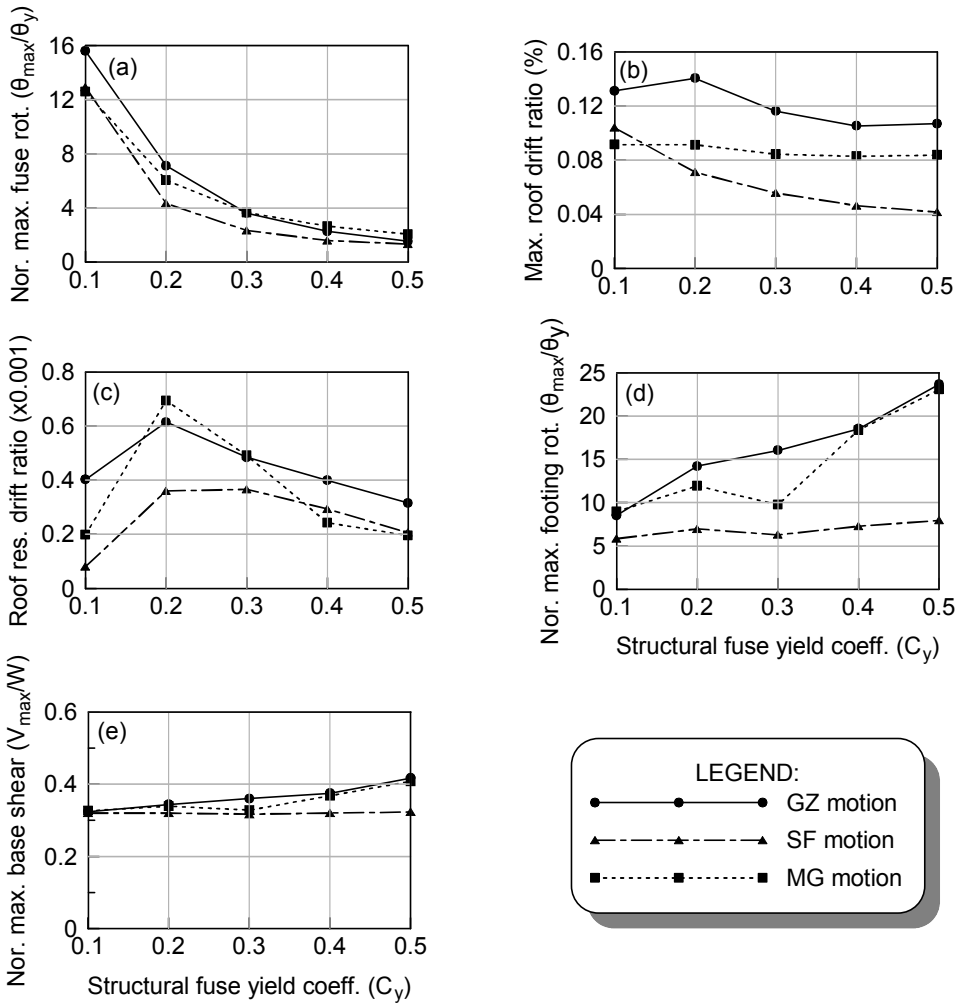

Figure 3.4 Effects of varying C_y on the system's seismic response (C_r=0.3)

3.4.3 Effect of Foundation Rocking Yield Coefficient (C_r)

Similarly, Figure 3.5 examines the effects of the foundation rocking yield coefficient (C_r). The structural fuse observes a substantial increase of ductility demand as rocking foundation becomes stronger. However, the maximum roof drift is gradually reduced when C_r increases for all motion cases. This can be understood by the fact that the maximum roof drift is controlled by the system-level strength. As C_r increases, the

system-level strength is gradually increased; therefore, the maximum roof drift decreases accordingly. The residual response, however, is motion dependent and less sensitive to C_r as it exceeds 0.2 (Figure 3.5c). The ductility demand of rocking footing, as expected, is dramatically reduced as Cr increases. For example, when the footing strength becomes five times stronger, the ductility demand decreases from around 92 to 2.0. On the other hand, the maximum base shear demand is relatively highly sensitive to C_r when it exceeds 0.3. Part (e) indicates that the normalized maximum base shear gradually increases as C_r increases from 0.3 to 0.5 for all motion cases.

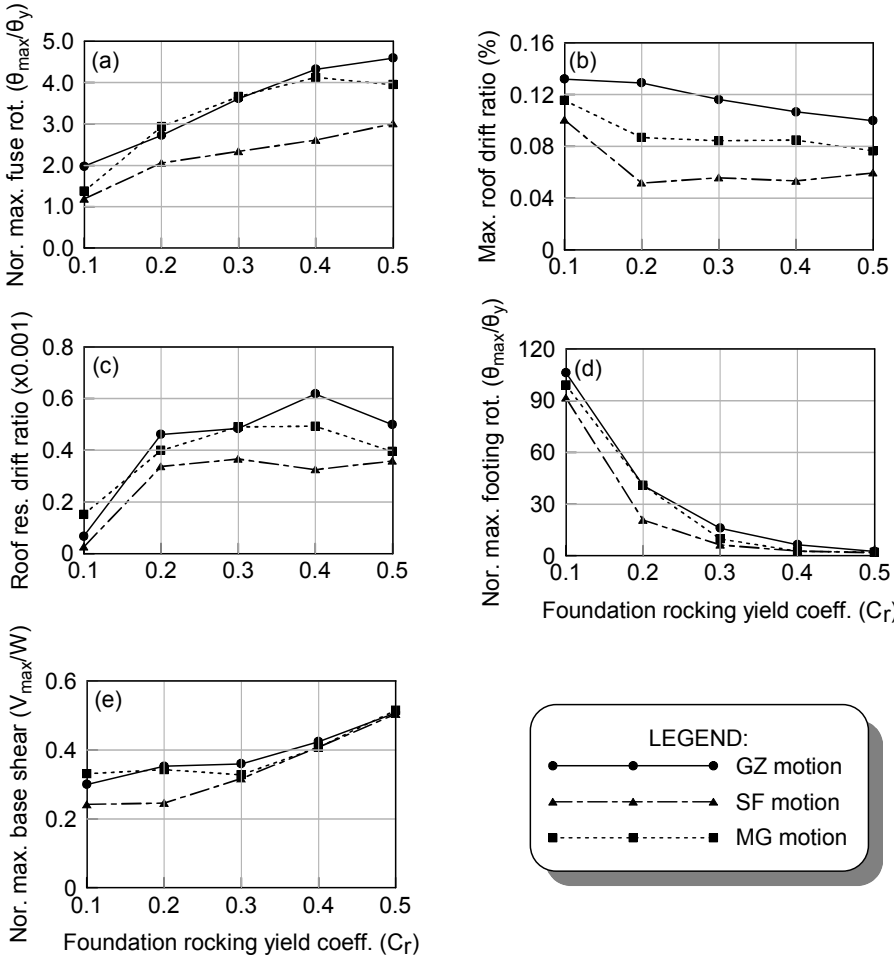

Figure 3.5 Effects of varying C_r on the system's seismic response (C_y=0.3)

3.4.4 Effect of λ_t, λ_h, and λ_m

Figure 3.6-Figure 3.8 evaluates the effects of varying three parameters which largely dictate the dynamic characteristics of the model, namely natural periods' ratio (λ_t), column height ratio (λ_h), and mass ratio (λ_m). Figure 3.6 investigates the effect of varying the second natural variation period on the seismic behavior of the building-foundation system. Given the floor mass at each level (M_1 and M_2) and the first natural period (T_1), selection of the second natural period ($T_2=\lambda_t*T_1$) requires some care to ensure a physically meaningful value; some arbitrarily selected period ratios are found to produce imaginary lateral stiffnesses of the system. In this study, the period ratios of 0.1, 0.333 and 0.4 are validated and selected herein.

The plots of Figure 3.6 generally show that the seismic response of superstructure component is less sensitive to λ_t variation. For example, the system observes nearly identical maximum drift for all λ_t scenarios, as indicated in Figure 3.6b. This can be explained by the fact that the drift response is mainly governed by the first mode of the system. In the meantime, the maximum response varies significantly amongst three motion cases. This is largely attributed to the difference of motion characteristics. As indicated in Figure 3.3 and Table 3.2, the selected motions intend to produce dramatically different spectral demand on the system. The footing ductility demand, on the other hand, is dramatically reduced as the second natural period is elongated during the SF and MG motions. A similar observation is found in the maximum base shear demand. As indicated in part (e), the normalized maximum base shear demand is decreased from 0.52 to 0.33 as λ_t is increased from 0.1 to 0.33.

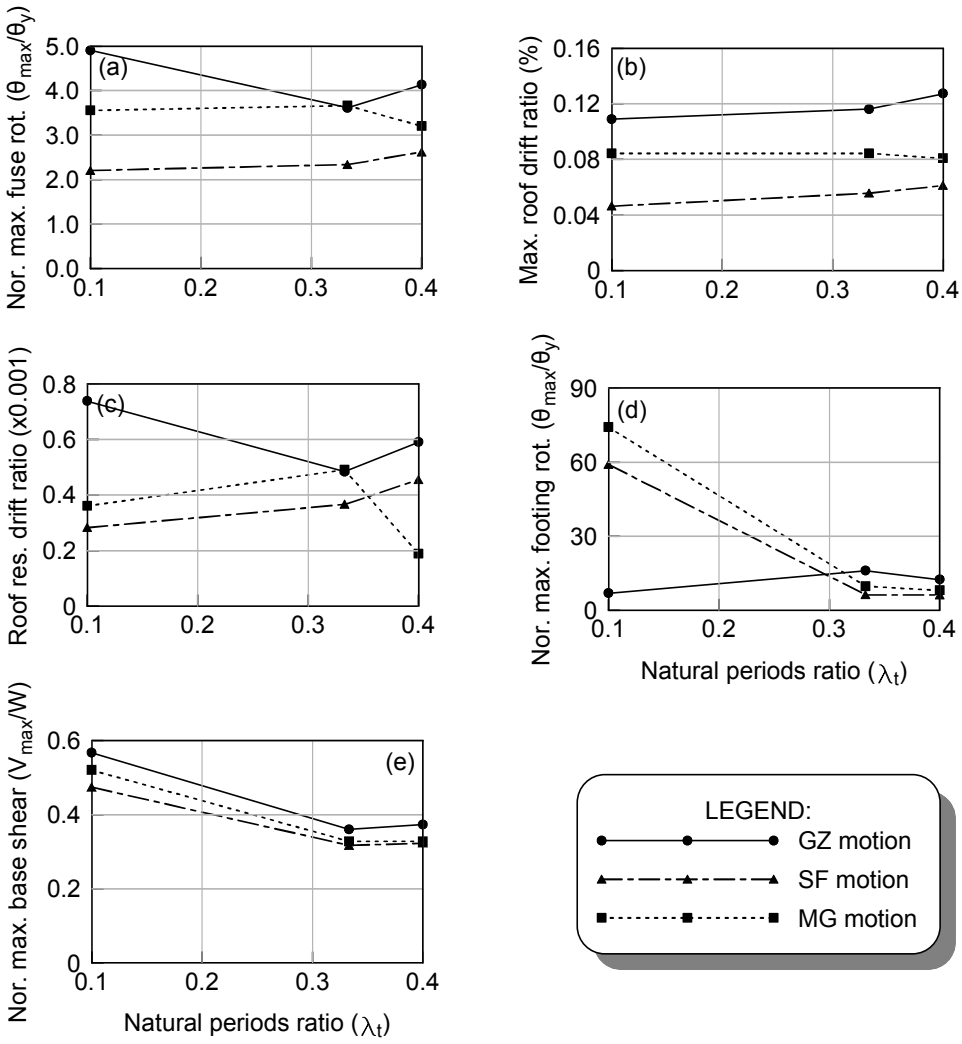

Figure 3.6 Effects of varying λ_t on the system's seismic response

The column height ratio (λ_h) is an important parameter, which will control the system's geometry. By definition, as one increases λ_h, the height of the second story column is increased. However, in order to maintain the natural period (0.3 sec) and the yield moment of the structural fuse and rocking footing (C_y=C_r=0.3), the flexural stiffness (EI) should be correspondingly increased as well prior to running the motion analyses. The results under each λ_h scenario are summarized in Figure 3.7. It shows that

the normalized rotation demand of the structural fuse is generally amplified with an increase of λ_h; however, the maximum roof drift ratio is gradually decreased. The system's residual performance is motion dependent, absent any definite or monotonic trends with λ_h variation. On the other hand, the normalized maximum footing rotation and base shear demand are less sensitive to λ_h variation particularly when it exceeds 1.

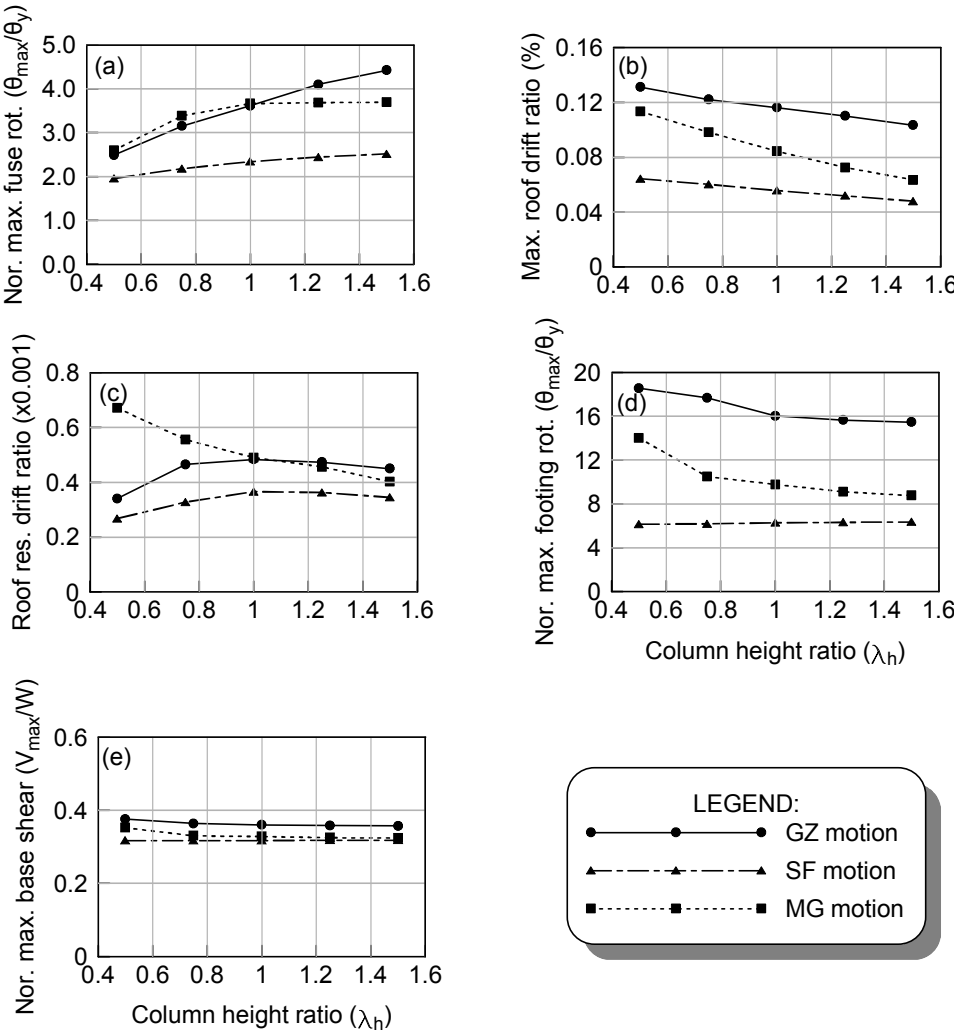

Figure 3.7 Effects of varying λ_h on the system's seismic response

In like fashion, Figure 3.8 examines the effect of varying the mass ratio (λ_m) on the system's performance. It can be understood that an increase of λ_m second floor will require a simultaneous increase of the column flexural stiffness at two levels, the structural fuse yield moment, and the rocking footing yield moment to ensure a constant T_1, C_y, and C_r. The plots in part (a) indicate that the ductility demand of the structural fuse is increased with λ_m for all motion cases. The system roof drift, however, is less sensitive to λ_m variation. In the meantime, the trend of the residual response in terms of λ_m varies significantly as the characteristic of the input motion is changed, as shown in part (c). For the footing component, its ductility demand is significantly decreased if the mass of the second story gradually increases. This may be attributed to the contribution of the second mode of the system wherein the inertia force developed at the first level will balance the demand driven by the inertia force at the second story. As such, the ductility demand imposed on the footing can be reduced even when the mass of the whole system is increased. Part (e) shows that the normalized maximum base shear is insensitive to the variation of the mass ratio for all motion scenarios.

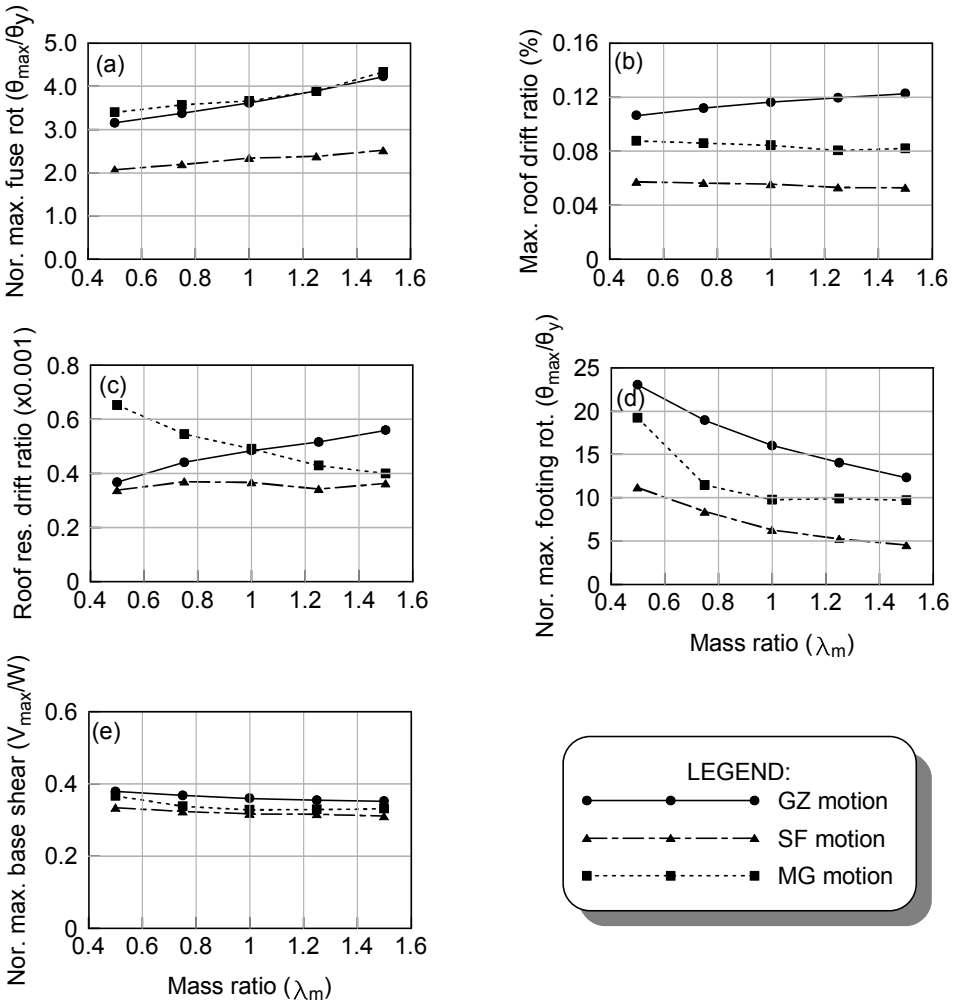

Figure 3.8 Effects of varying λ_m on system seismic performance

3.5 Conclusions

This chapter investigates the effects of varying several governing parameters on the seismic response of frame-braced foundation-building systems via inelastic time history analyses in *OpenSees*. The parameters varied are the structural fuse yield coefficient (C_y), the foundation rocking yield coefficient (C_r), the natural period ratio (λ_t), the story column height ratio (λ_h), and the story mass ratio (λ_m). The results of the numerical parametric studies indicate the following:

- As the structural fuse becomes strong, the seismic demand to the superstructure (i.e. structural fuse ductility demand and maximum roof drift) is greatly reduced, at the cost of larger ductility demand on rocking foundation. However, the foundation's ductility demand is not monotonically amplified; a reduction is observed when C_y approaches 0.3 for one motion case. Meanwhile, the maximum base shear demand is less sensitive to C_y variation.
- When the foundation rocking yield coefficient (C_r) increases, the footing rotation ductility demand and roof drift ratio are both reduced. The residual behavior, however, is motion dependent and less sensitive to C_r as it exceeds 0.2. The structural fuse ductility demand is monotonically increased with an increase of C_r. Also, the normalized maximum base shear demand is dramatically amplified when C_r exceeds the baseline value (0.3).

- The seismic response of the superstructure component is less sensitive to λ_t variation. However, the footing ductility demand and base shear is generally reduced as one elongates the second natural period.
- As one gradually increases the second story height, the ductility demand on the structural fuse is increased, but the maximum roof drift ratio is reduced instead. On the other hand, the normalized maximum footing rotation and base shear demand are less sensitive to λ_h variation particularly when it exceeds 1.
- When the second story mass is increased, the fuse normalized rotation is gradually increased; however, the maximum roof drift ratio and normalized base shear is less sensitive to its variation. Moreover, the foundation ductility demand is dramatically reduced if one increases the second story mass.

3.6 Acknowledgement

This chapter is largely a reprint of the material as it appears in the proceedings of 15th World Conference on Earthquake Engineering. Liu, W.; Hutchinson, T. C.; Hakhamaneshi, M.; Kutter, B. L., (2012). "Numerical parametric study on inelastic foundation-building models with presence of rocking foundation." *15th World Conference on Earthquake Engineering*, Lisbon, Portugal, September 24-28. The dissertation author was the primary investigator and author of this paper.

Chapter 4

Moment Frame-Foundation System Test (Test-1): Test Program and Results

4.1 Scope of this Chapter

To integrate rocking foundations into a frame-type building system, the inherent hysteretic behavior of superstructure components and that of the soil-foundation interface need to be considered simultaneously. In particular, how these two nonlinear fuse components dynamically interact with each other and share the seismic demand warrants further experimental exploration. This chapter presents the test program of the first system-level test (Test-1) of the CoSSY research project and the test results. Test-1 was intended on investigating the balance in seismic demand and resulting performance of a targeted moment frame-foundation building system with both rocking foundations and

structural fuse elements. Four moment frame-foundation building models of like geometry were built to illustrate the following conditions: (1) balanced design (BD), (2) restrained rocking (RR), (3) foundation-rocking dominated (FRD), and (4) structural-hinging dominated (SHD). The models were constructed and systematically subjected to similar suites of earthquake input motions. Results are presented in terms of time history response plots for select engineering demand parameters and hysteretic responses of both the structural fuse and rocking foundation.

4.2 Design Methodology

Structural seismic design usually requires commensurate efforts at the component detailing level and the system level to assure good structural performance globally and locally (ASCE 7-10, ASCE 2010; ASCE 2007). Although the performance of a designed structural component can be determined via large-scale reaction based or shake table tests, the sensitivity of soil behavior to its confining stress condition results in the need for centrifuge or very large soil container testing when considering the soil-foundation superstructure system as a whole. However, to induce shaking on a prototype scale soil-foundation-structure model to the point of significant nonlinear soil and nonlinear structural behavior is often cost prohibitive. Fortunately, procedures for and, importantly, scaling laws governing, centrifuge testing have been well established for many years (e.g., Kutter 1995; Table 4.1). Importantly, structural components integrated into geotechnical centrifuge models can be rationally simulated if one considers the desired local behavior of the component while targeting system dynamic behavior (Chang et al. 2007; Deng et

al. 2012; Trombetta et al. 2013). In addition, the simulated model can be designed to target key parameters important to the global seismic behavior.

Table 4.1 Basic Centrifuge Scaling Laws (N=g-level)

Quantity	Model/Prototype dimension
Time (dynamic)	1/N
Displacement, length	1/N
Velocity	1/1
Acceleration	N/1
Force	$1/N^2$
Moment	$1/N^3$
Mass	$1/N^3$
Stress, pressure	1/1
Strain	1/1

4.2.1 Proposed Balanced Design Moment Frame-Foundation Configuration

In this study, a two-story-one-bay moment frame-foundation model was constructed, and important parameters controlling its response to seismic loading were identified and used. These parameters include the natural periods of vibration of the system, the elastic and inelastic stiffnesses and strengths of the fuse component, the floor level masses, and the system geometry (Figure 4.1a; Table 4.2). It is noted that this system was studied numerically in Chapter 3 and the parameters of Table 4.2 were largely guided by the findings of the prior numerical study.

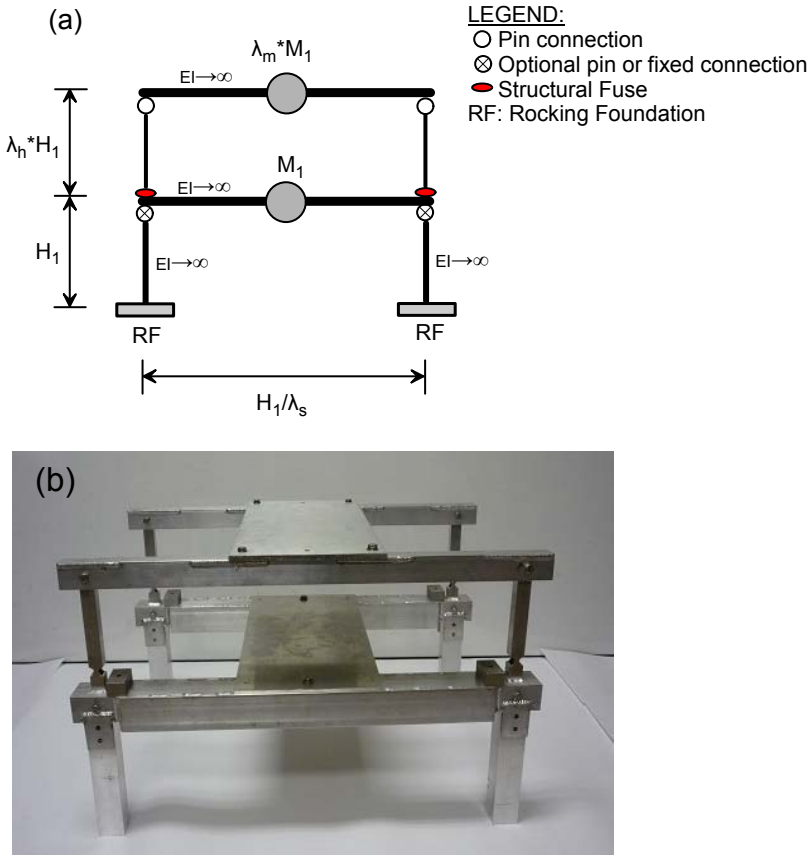

Figure 4.1 Structural model design: (a) schematic of structural configuration; (b) photograph of constructed model (footing and instrumentation omitted)

The model designs were intended to represent a typical low-rise moment-resisting frame building system. An idealized structural configuration was proposed and shown in Figure 4.1a wherein the solid ellipse represents the inelastic structural behavior (structural fuse). Pinned connections were introduced at the top of the first and second floor columns for two reasons: (1) to simplify the analysis and measurement of moments in the structural fuses and in the rocking foundations and (2) to promote an anticipated foundation rocking mechanism. It was assumed that the two plastic hinge regions, namely the footing and hinge at the bottom of the second story column, would be the sole

components that absorb seismic energy during earthquake loading, whereas the remaining structural components were designed to remain elastic or displace fairly rigidly with little to no energy dissipation.

Table 4.2 Definition of Important Global Parameters Used in Design and Target Values for the BD Case

Parameter	Parameter Description	Target value
λ_m	Ratio of mass at each level (M_2/M_1)	0.5-0.7
T_1	Flexible-base first natural period	0.3-0.5s
λ_t	Ratio of first two natural periods (T_2/T_1)	0.33
C_y	Structural fuse yield coefficient	0.3
C_r	Foundation rocking yield coefficient	0.3
λ_h	Story height ratio (H_2/H_1)	0.8-1.0
λ_s	Ratio of first story height to column spacing	0.25
k_{1p}/k_{1e}	Stiffness hardening ratio for footing	0.0001
k_{1u}/k_{1e}	Unloading stiffness ratio for footing	1
k_{2p}/k_{2e}	Stiffness hardening ratio for fuse	0.0001
FS_v	Footing vertical factor of safety	9.0

It is understood that structural fuses in conventional building design practice are more commonly placed at the ends of beam-column joints. In this idealized experiment, introduction of the pins and hinges in the upper level columns reduces structural redundancy, thereby reducing the number of nonlinear elements and enabling more reliable and accurate determination of shears and moments in each structural member of the system. With the exception of the governing ultimate collapse mechanism, this idealized hinging column system can be shown to be dynamically identical to a hinging beam system. This is confirmed by comparing the dynamic responses between a model specimen with inelastic hinges placed at the bottom of the columns and the one with hinges placed at the ends of the beam, which are determined via numerical analyses. It

should also be noted that the introduction of the pin connections at each level induces an equal amount of seismic demand at the two locations, namely the end of the beam and the end of the column. This pinned structural configuration, with a fairly large stiffness of the remaining elastic sections, creates approximately the same drift of the second story when the structural fuse section has yielded, irrespective of whether the plastic hinges are located at the bottom of the column or at the beam ends. As a result, the structural fuse location in this case does not bias the overall inelastic behavior of the proposed structural system.

The yield moments of the structural fuse and the rocking foundation are characterized by two dimensionless parameters, namely C_y and C_r, respectively, as introduced in Section 3.2. However, the footing's actual yield moment can be determined with knowledge of the footing dimension, the activated contact region, and the vertical load acting on the footing as (Gajan and Kutter 2008)

$$M_{y\_footing} = \frac{V \times L}{2}\left(1 - \frac{A_c}{A}\right) \tag{4.1}$$

where V = total downward axial load acting on the footing, L = length of the footing parallel to the shaking direction, A = footing area, and A_c = minimum contact area required for the footing to support the vertical load (when the soil's bearing capacity is fully mobilized) (Gajan and Kutter 2008). It should be noted that, by using the terminology of "yield moment" to characterize the flexural moment capacity of rocking footings in this chapter and the thesis does not imply that only the edge of the soil-footing interface reaches the incipient yielding. Instead, it indicates that the entire contact interface attains the yield stress in this dissertation throughout. The theoretical maximum

limit to $M_{y\_footing}$ is equal to V×L/2 for an infinitely strong and rigid surface footing resting on an infinitely strong and rigid soil.

To implement a compatible yielding mechanism between a structural fuse and rocking foundation, termed the balanced design (BD) condition, one may need to target equity between the aforementioned strength indexes, namely C_y and C_r, to ensure that foundation rocking and structural fuse yielding will occur at approximately the same base shear force. To promote system behavior dominated by either foundation rocking or structural hinging, one must simply control the relationship between C_y and C_r (i.e., $C_y>C_r$, or $C_y<C_r$).

4.2.2 Model Design and Construction

At the elastic stage of response, the moment frame-foundation configuration can be treated simply as a two degree-of-freedom (2-DOF) system in the lateral direction of response. With knowledge of the target natural periods and mass ratio, the stiffness of the lateral restraint of each floor level can be analytically determined from structural dynamics theory (e.g., Chopra 2007)

$$K_1 = \frac{M_1\omega_1^2+M_1\omega_2^2}{2} \pm \frac{\sqrt{A}}{2} \tag{4.2}$$

$$K_2 = \frac{M_2(M_1\omega_1^2+M_1\omega_2^2 \mp \sqrt{A})}{2(M_1+M_2)} \tag{4.3}$$

$$A = M_1^2\omega_1^4 - 2M_1^2\omega_1^2\omega_2^2 + M_1^2\omega_2^4 - 4M_1M_2\omega_1^2\omega_2^2 \tag{4.4}$$

Where ω_1 and ω_2 = natural circular frequency of the first and second mode, respectively. The lower level lateral stiffness is solely provided by the flexibility of the foundation, as

the first level column is considered to be infinitely stiff. K_1 therefore can also be expressed as

$$K_1 = \frac{2K_\theta}{H_1^2} \tag{4.5}$$

where K_θ = elastic rotational stiffness for each rocking footing.

Considering available stock material sizes and reasonable geometries to support ease of construction, the BD model was finalized with the properties identified in Table 4.3. An assembly of the model is shown in the photograph of Figure 4.1b. Although only one-dimensional shaking was imposed on the model, the tested structure was designed and constructed as a three-dimensional (3D) model to provide out-of-plane stability. The columns at each level were constructed with square hollow aluminum tubing sections of width 1.91 cm (3/4 in.) and 3.82 cm (1.5 in.) in model scale for the first and second level, respectively. The horizontal beams were assembled using an inverted U-section built up with several plates, which were welded to the U-section to increase its overall stiffness and provide additional dead load. A floor mass spanned between the two frames and was attached via a group of bolts. Moreover, several lead mass blocks were bolted to the beam elements to simulate remaining target masses. All structural and foundation elements, with the exception of the mass blocks at the ends of each beam, were constructed using Aluminum 6063. The yield strength of this material was determined through coupon tests as 206.8 MPa. The pinned connections were achieved using the shank of bolts placed in through holes between the columns and the inverted U-section beams. To restrain rocking of the system, a clamp can be used at the top of the first floor column-beam connections. This condition was facilitated via bolts installed through the

gusset plates. The fuse elements were achieved by notching the hollow aluminum column sections. This construction strategy previously demonstrated its effectiveness in providing sufficient ductility capacity and energy dissipation in prior centrifuge structural models (Chang et al. 2007; Deng et al. 2012; Trombetta et al. 2013).

The static factor of safety against vertical bearing failure (FS_v) is also considered as an important parameter controlling the design. In a prior centrifuge test program using single DOF (SDOF) foundation models, two values of FS_v were selected, 4.0 and 9.0, in an effort to represent a range encountered in conventional practice (Hakhamaneshi et al. 2011b). The foundations in this study performed well, showing good moment-rotation hysteresis. However, the footing with $FS_v = 9.0$ reported less rocking-induced settlement, and therefore this target value was selected for the BD case herein.

4.2.3 Design and Construction of other Moment Frame-Foundation Models

Adopting a similar strategy as that used for the BD moment frame-foundation model, two other models with different fuse and footing geometries were designed to render two different yielding dominant systems, which are termed as the FRD configuration and the SHD configuration. The FRD configuration was designed by targeting a rocking footing yield coefficient C_r approximately half that of the structural fuse yield coefficient C_y, thereby promoting rocking of the foundation. This was physically accomplished by enlarging the structural fuse width and reducing the footing length. All other structural components were identical with the BD model. To demonstrate an opposing mechanism of load transfer, the SHD configuration was

designed with C_r approximately two to three times that of C_y, thereby promoting yielding of the structural fuse first.

Figure 4.2 provides photographs of the corner of each model to articulate the two fuse mechanisms designed into the moment frame-foundation models, whereas Table 4.3 summarizes the achieved attributes of each model configuration. The natural periods of each system (T_1 and T_2) were determined using a numerical model constructed with in *OpenSees* (Mazzoni et al. 2009), where the foundation was modeled using a series of nonlinear Winkler springs (Raychowdhury and Hutchinson 2009).

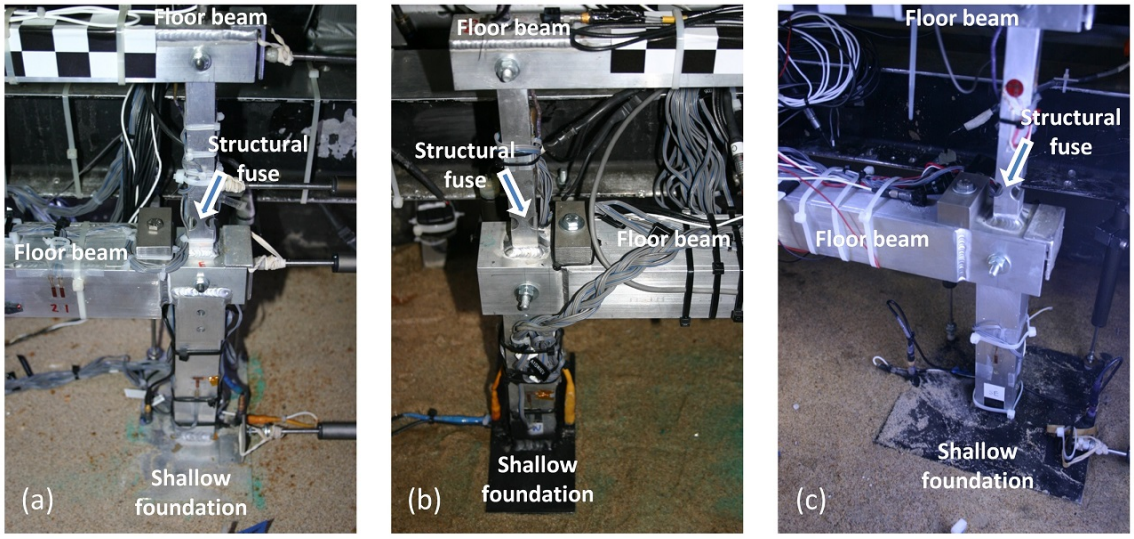

Figure 4.2 Photographs of the three models in the soil container (elevation view of one corner): (a) BD model; (b) FRD model; (c) SHD model

Table 4.3 Moment Frame-Foundation Models' Property Summary (As-Built Values)

Parameter (units)	BD model	FRD model	SHD model
M_1 (kg)	127494 (4.722)	127494 (4.722)	127494 (4.722)
M_2 (kg)	60723 (2.249)	60723 (2.249)	60723 (2.249)
Footing dimensions L×B (cm)	321×528 (10.7×17.6)	229×528 (7.6×17.6)	610×528 (20.32×17.6)
Structural fuse width (cm)	16.8 (0.56)	19.8 (0.66)	16.8 (0.56)
C_r	0.35	0.22	0.81
C_y	0.37	0.44	0.33
T_1 (s, prototype)	0.73	0.99	0.49
T_2 (s, prototype)	0.27	0.26	0.25
Footing yield moment (N-m)	958×10^3 (35.5)	619×10^3 (22.9)	2230×10^3 (83.0)
Fuse yield moment (N-m)	217×10^3 (8.05)	259×10^3 (9.59)	194×10^3 (7.18)
FS_v	9.1	6.9	14.7

Note: First value is in prototype scale, whereas the value inside the parentheses denotes the parameter value in model scale.

In Table 4.3, the structural fuse yield moment was determined from a nonlinear static displacement controlled test on a single column assembly, whereas the footing yield moment was theoretically calculated according to Equation (4.3), based on knowledge of the undrained shear strength of the clay. In addition to the FRD and SHD configurations, a restrained rocking (RR) system was investigated in this test program. In the RR system, moment transfer to the footing was prevented in an effort to represent a regular moment-resisting frame system. This configuration was accomplished by providing fixity to the top of the first story columns within the BD structural configuration.

4.3 Centrifuge Testing Program

4.3.1 Program Overview

The experimental program presented herein was performed using the NEES 9-m-radius centrifuge facility at the University of California at Davis. All the tested structural models were placed inside of a rigid container (1693×904 mm) and supported on consolidated clay (Figure 4.3a). The container was mounted on the end of the centrifuge arm and spun up to 56.0 revolutions per minute (RPM) to create a 30g level gravitational acceleration at the ground surface. Three stations were identified within this same rigid container for placement of the three moment frame-foundation models (Figure 4.3b). At the station of the BD case, the model was configured with two different beam-column connections at level one, namely pinned and fixed, resulting in a total of four different model configurations. These models were then excited with a similar series of earthquake motions input at the base of the rigid container. In addition, two vertical quasi-static push tests at two different undisturbed corner locations were conducted to assess the soil's undrained shear strength. In the following discussion, units are presented in prototype scale, unless otherwise indicated.

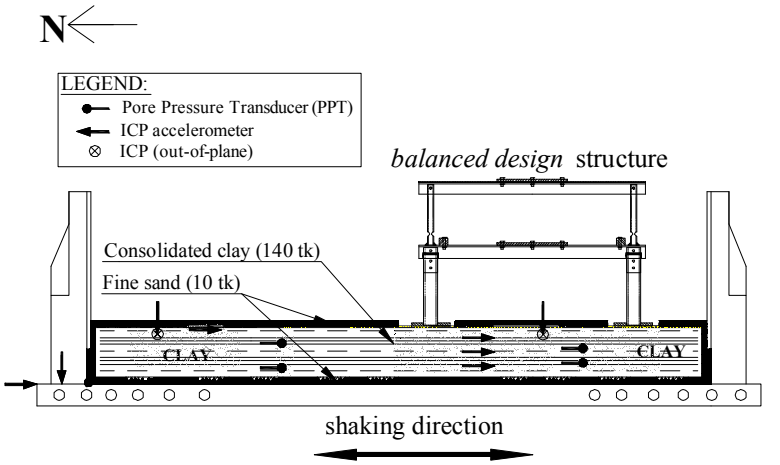

(a) Elevation View

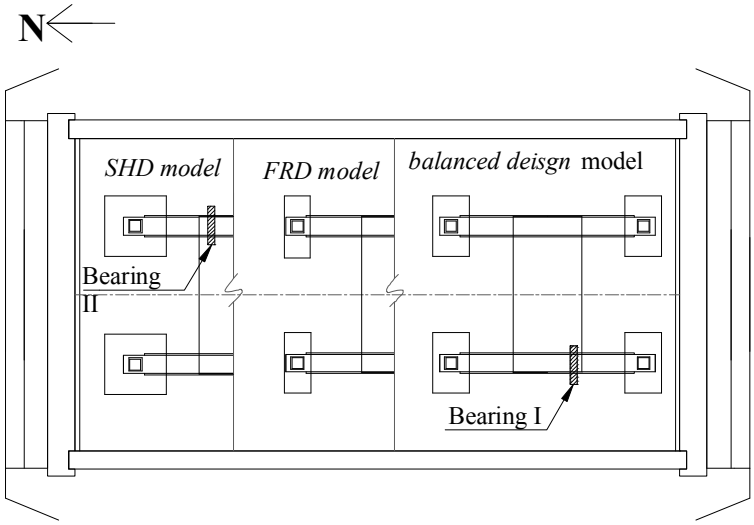

(b) Plan View

Figure 4.3 Model schematic: (a) soil profile in the rigid container, showing placement of BD model and location PPT and accelerometers in soil and (b) plan view of the model showing location of all models (instrumentation not shown for clarity) (dimensions are in model scale mm; model container length × width × height = 1759 × 1000 × 540 mm)

4.3.2 Soil Construction and Profile

The underlying geologic profile was constructed with consolidated clayey soil. As shown in Figure 4.3a, the clay layer was surrounded on its bottom and sides by fine sand (Nevada sand with relative density D_r=80%) to facilitate drainage caused by consolidation; a 0.3-m-thick (10 mm in model scale) layer of sand on top of the clay was included to retard drying caused by evaporation in the winds of the spinning centrifuge. The 4.20-m-thick consolidated clay layer was constructed from Yolo Loam, a locally available silty clay [liquid limit (LL) = 29.1%; plastic limit (PL) = 20.8%; plasticity index (PI) = 8.3%]. The Yolo Loam was mixed with water as slurry, poured into the model container, and preconsolidated in lifts using a hydraulic press. Each lift was subject to gradually increasing pressure up to a maximum vertical stress of 290.6 kPa. Later, the clay shear strength was determined by plate bearing tests conducted while the centrifuge was spinning; interpretation of the plate bearing tests indicate that the undrained shear strength of the consolidated silty clay on the centrifuge was about 70 kPa (Liu et al. 2011).

4.3.3 Instrumentation

Five different categories of instrumentation were implemented in this test series, including pore pressure transducers (PPTs), integrated circuit piezoelectric (ICP) accelerometers, microelectromechanical system (MEMS) accelerometers, linear potentiometers (LPs), and strain gauges [SGs; Figure 4.3a and Figure 4.4]. In addition, analog and digital cameras were distributed throughout the model to monitor its in-flight

responses. Six PPTs were embedded in the clay at various locations to monitor the variation of pore water pressure during consolidation when spun up. Accelerometers were oriented either horizontally or vertically, depending on the measurement objective, and placed on the structure and inside the soil. Several arrays of ICP accelerometers were buried in the clay horizontally and vertically to capture the free-field response (Figure 4.3 a). In anticipation of the footing rocking behavior, all four footings were instrumented with two vertical ICPs at two edges and one horizontal accelerometer in the shaking direction. The building superstructure was heavily instrumented with both ICP and MEMS accelerometers to obtain horizontal and vertical accelerations at each floor level (Figure 4.4). Sixteen LPs were attached to the model components and anchored to a stiff reference rack. The LPs were intended to measure the drift of each floor level and footing vertical and horizontal displacements. Forty-eight SG bridges were used to measure the moment and axial loads in each of the columns at each floor level. Half and full Wheatstone bridge configurations were implemented to obtain bending moment and axial load readings, respectively. Taking advantage of the pinned connection (zero moment boundary condition) at the top of the columns, it was also possible to estimate shear loads in each column. In total, ninety-one concurrent instruments monitored the models during each earthquake event and the spin-up and -down cycles. Additional details regarding the model construction and instrumentation plan may be found in the test series data report (Liu et al. 2011).

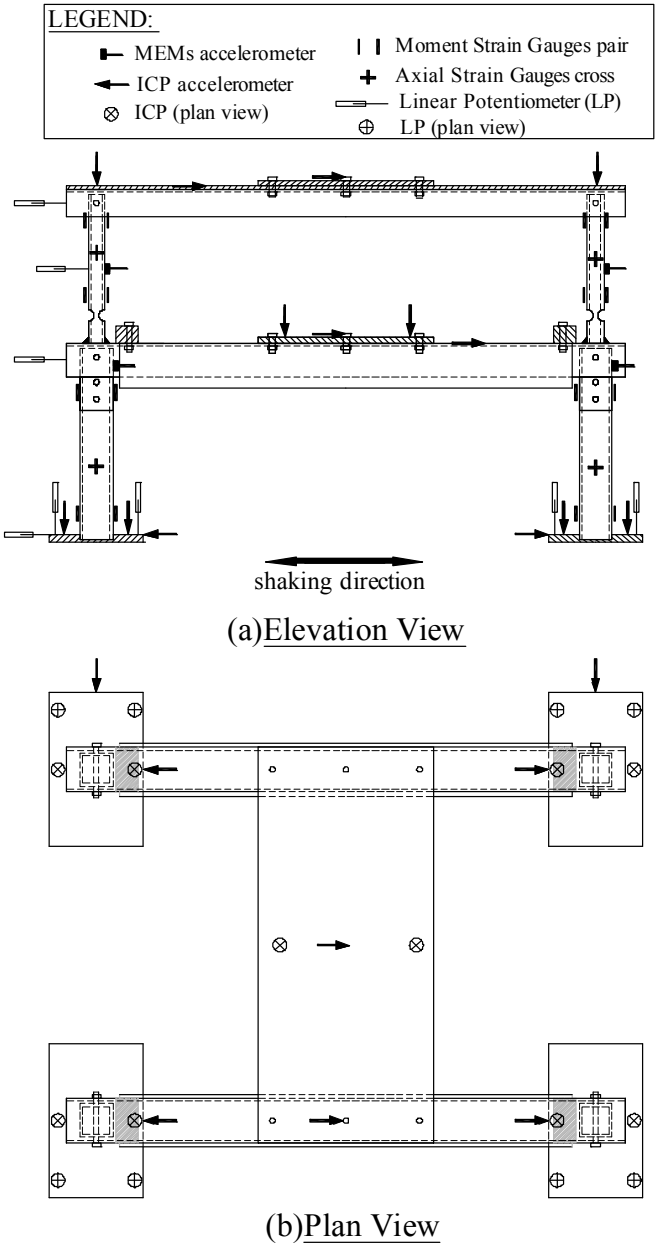

Figure 4.4 Instrumentation of the BD model: (a) elevation view; (b) plan view

4.3.4 Test Protocol

Within this experiment series, in general, a similar sequence of six unidirectional earthquake motions was imposed on all structural configurations (Table 3.2 and Table 4.5). Testing commenced with the lowest amplitude motion to induce elastic response, with the amplitude scaled in subsequent shakes with an intent to mobilize the yielding capacity of either the structural fuse or the rocking foundation (Table 4.5). These six motions originate from two different earthquake events (Table 4.4). Including the bearing tests and motion sequence, the experiment was sequenced as described in Table 4.6. Figure 4.5 provides the elastic spectral acceleration for each achieved motion at the free field ground surface, overlaid with the first natural period of each of the models. These plots are normalized by their respective zero period acceleration (ZPA).

Table 4.4 Motion source characterisitics

Motion Name	Earthquake Event	Magnitude (M_w)	Recording Station	PGA (g)	PGV (cm/s)	PGD (cm)	T_p (s)
GZ	Gazli, USSR, 1976	6.8	Karakyr	0.66	68.8	24.5	0.29
SF	San Fernando, USA, 1971	6.6	LA- Hollywood Stor FF	0.44	43.6	15.2	0.20

Notes: PGA = peak ground acceleration; PGV = peak ground velocity; PGD = peak ground displacement; T_p = predominant period as determined from the peak in the elastic 5% damped spectral acceleration plot.

Table 4.5 Test Protocol and Characteristics of the Achieved Input Base Motions

Motion Name	Input motion name	Code name	Peak input acceleration (g)	T_p (s)
1	SF	SF_0.2[1]	0.274	0.163
2	GZ	GZ_0.2	0.148	0.174
3	GZ	GZ_0.4	0.407	0.171
4	GZ	GZ_0.7	0.664	0.171
5	GZ	GZ_1.0	0.835	0.174
6	SF[2]	SF_0.4	0.576	0.237

Notes: 1. Numerical value following the code name refers to the amplitude scale factor applied to the source motion. Amplitude scaling was applied uniformly to the motion. 2. Motion #6 was not applied to the SHD model.

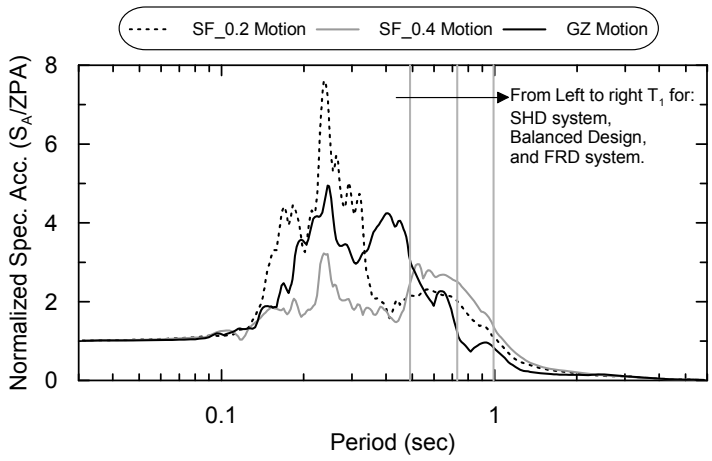

Figure 4.5 Normalized elastic 5% damped spectral acceleration of measured free field motion at ground surface for each seismic event

Table 4.6 Test Sequence

Test Objective	Description
BD system	Place *BD* model into container Spin up to 30g Six input motions applied to *BD* model Spin down to 1g - physical observations
RR system	Spin up to 30g Six input motions applied to *RR* model Spin down to 1g - physical observations
Bearing failure test (I)	Remove model, place actuator and bearing plate Spin up to 30g Quasi-static downward push test Spin down to 1g - physical observations
FRD system	Place *FRD* model into container Spin up to 30g Six input motions applied to *FRD* model Spin down to 1g - physical observations
Bearing failure test (II)	Remove model, place actuator and bearing plate Spin up to 30g Quasi-static downward push test Spin down to 1g - physical observations
SHD system	Place *SHD* model into container Spin up to 30g Five input motions applied to *SHD* model Spin down to1g - physical observations

4.4 Experimental Results

Within this section, the seismic performance of each of the moment frame-foundation models is evaluated and systematically compared. To provide insight into the responses, time history plots of select important engineering demand parameters (EDPs) and hysteretic responses for the structural fuse and rocking foundation are presented for the BD model. Subsequently, performance comparisons between the BD and RR models, and the FRD and SHD models, are presented. Response data are then synthesized and presented in scatter plot format.

4.4.1 Data Processing

All history response data presented in this Chapter and subsequent Chapters5-7 were processed to filter the noise generated during centrifuge testing. In particular, acceleration measurements during dynamic shaking were processed by using 5-order low-pass Butterworth filter. Figure 4.6a shows an example of the filtering technique, which was applied to a recorded base input motion during application of GZ_0.2 motion for the BD model. The cutoff frequency is chosen as 500 Hz in present study. Part (b) compares the raw measured history response and the filtered data. It shows that the high-frequency noises were successfully filtered.

For the dynamic transient displacement history data, it was obtained by double integrating the filtered acceleration data. However, for the residual displacement data, it was obtained from the measurements of LPs which were filtered with 5-order low-pass Butterworth filter with 100Hz cutoff frequency. Similarly, the history data obtained from

SGs were filtered via 5-order low-pass Butterworth filter but with cutoff frequency of 500 Hz.

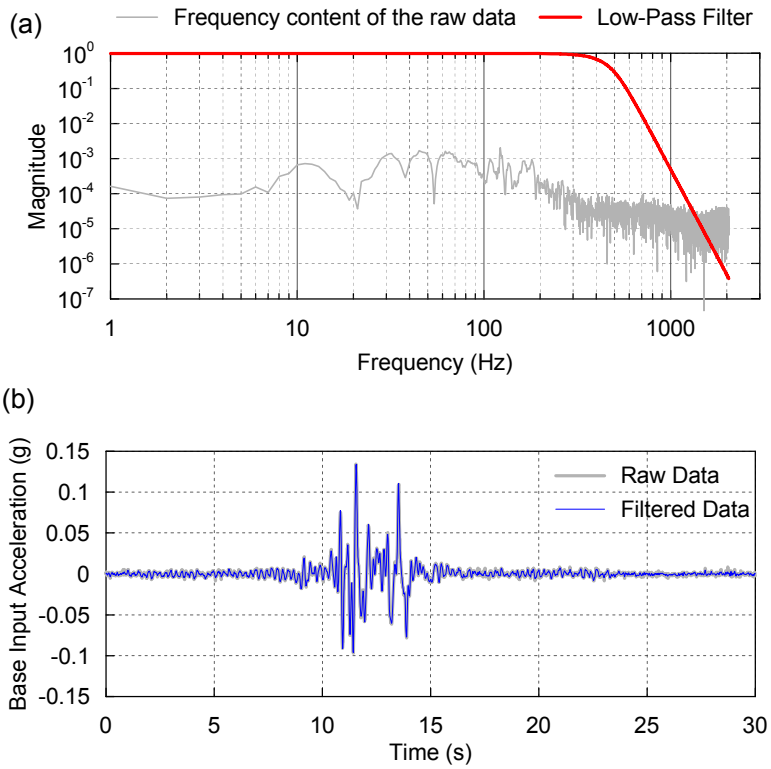

Figure 4.6 Data processing for acceleration data: (a) Butterworth filter; (b) acceleration time history comparison

4.4.2 BD Model Response

Engineering demand parameters (EDPs) measured during the GZ motion, with scale factors of 0.2 and 1.0, respectively, are presented in Figure 4.7. The EDPs selected are the horizontal absolute acceleration at the roof level, the roof drift ratio (roof horizontal relative displacement divided by the building height from the ground surface i.e., H_1+H_2), rotation demand for the fuse and footing, footing settlement, and moment

demand for fuse and footing. The moment is normalized by the respective yield strength for each component, i.e., either $M_{y\_footing}$ or M_{y_fuse}, as documented in Table 4.3.

Response histories presented in Figure 4.7 demonstrate that all EDPs consistently increase with increasing amplitude of excitation motion. The absolute maximum acceleration at the roof level, for example, increases from 0.31 to 0.56g, whereas the absolute maximum roof drift ratio increases from 0.36 to 1.80%, when the motion amplitude is increased fivefold. It is noted that a drift ratio of about 2.0% may be within typical target drift amplitudes for buildings anticipated under a design earthquake level (ASCE 2010).

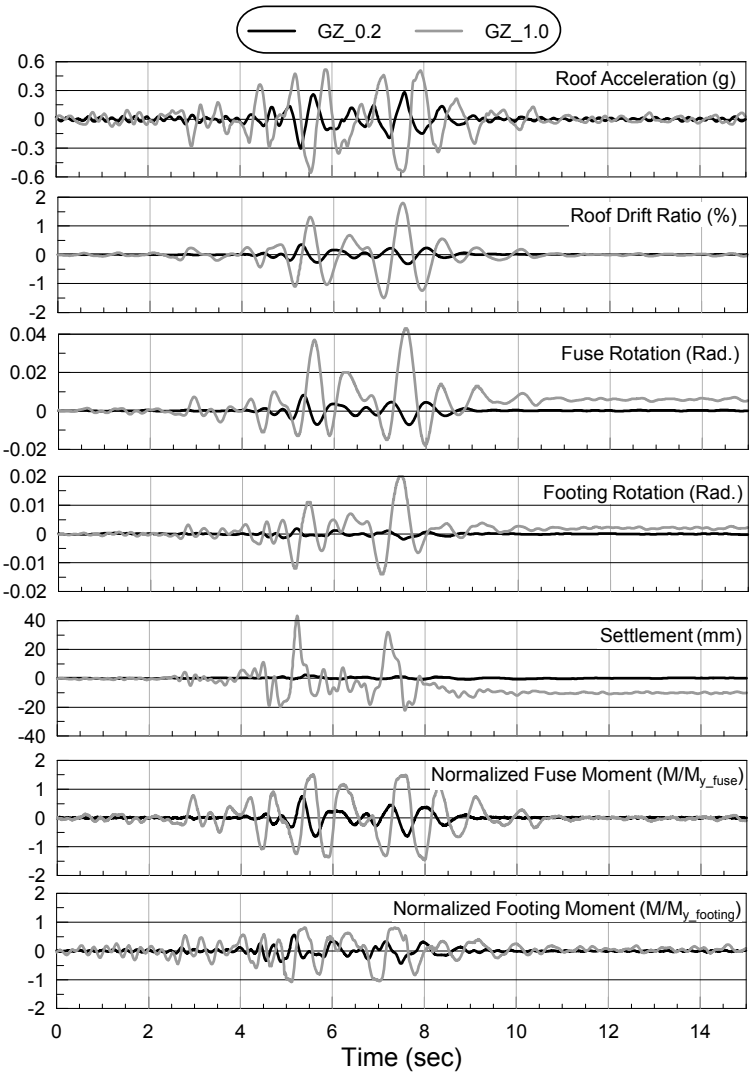

Figure 4.7 Time history response comparison for the BD model (subjected to GZ_0.2 and GZ_1.0 motion, y-axis parameter and units denoted in upper right of each plot)

The normalized fuse and foundation moment histories illustrate that under the GZ_0.2 motion, neither component yielded, whereas when subjected to the GZ_1.0 motion, several excursions to yield ($M/M_y>1.0$) are observed for each component. Despite the remarkably high transient rotation demand to the footing and structural fuse, which occurred during the GZ_1.0 event (0.02 and 0.043 rad, respectively), permanent rotations are observed to be negligibly small for both components (e.g., 0.008 rad for structural fuse). This can be largely attributed to the self-centering mechanism introduced by the rocking footings. With the promotion of a rocking foundation, dead weight acting on the structure will assist with recentering the structure even following large inelastic deformation excursions. In addition, a compatible yielding strategy enables seismic demand to be distributed in a relatively balanced fashion between the structural fuse and footing, thereby further reducing the inelastic deformation to the various components. Inspection of the footing settlement history indicates that during the larger amplitude GZ_1.0 event, maximum transient uplift and permanent settlement are observed as approximately 43 and 10 mm, respectively, which are about 1.34 and 0.31% of the footing length. These demands are relatively small considering the large roof acceleration, large roof drift, and high fuse rotation absorbed by the structural model (Figure 4.7).

Figure 4.8 depicts a family of hysteresis plots for each of the structural fuse and shallow foundation and they are organized vertically in the order of motion sequence. These plots show that the structural fuse and footing both behave approximately linear-elastically during the low-amplitude motion (i.e., GZ_0.2), with rotation demands generally less than 0.01 rad and normalized moment demand M/M_y generally less than unity. On application of the GZ_0.4 motion, it is observed that the structural fuse and

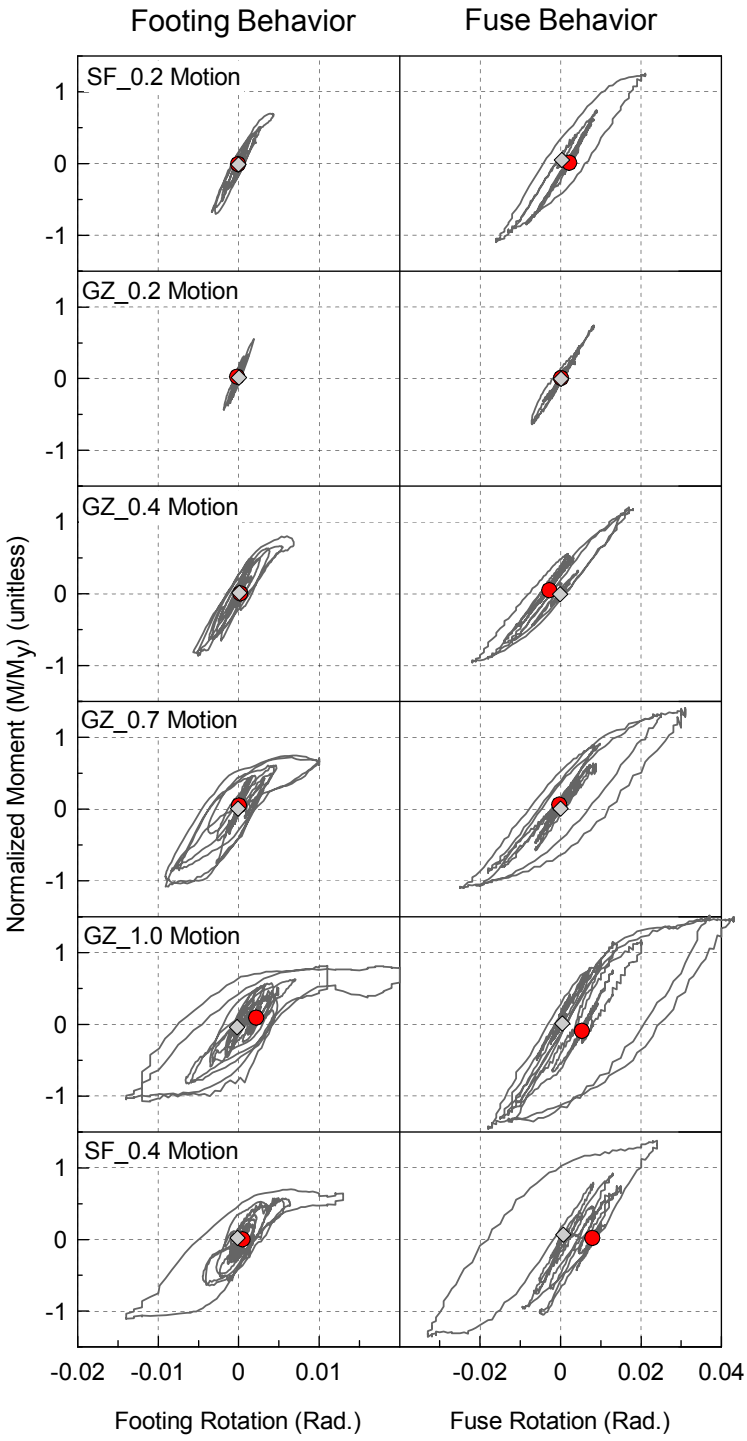

Figure 4.8 Moment-rotation response of footing and structural fuse under each motion for the BD model (solid diamond and circle denotes the starting and ending data point for each event, respectively)

footing are approaching or just at their respective yielding strengths. The footing capacity has been nearly mobilized by dynamic rotations of 0.007 rad, whereas the structural fuse also enters into the plastic region. At scale factors of 0.7 and 1.0, the moment-rotation relationships of both components present with highly nonlinear and inelastic significantly broad hysteresis. Meanwhile, the plateau of each hysteretic curve indicates a reasonably good agreement between the observed mobilized moment capacity and theoretical yield strength for each of the structural fuses and rocking foundations. However, the moment reaches a plateau just prior to $M/M_{y\_footing}=1.0$, when the footing approaches large positive rotations. This may be because of the fact that variation in the axial load acting on the footing caused by dynamic frame action (overturning axial tension) affects the critical contact area and thereby decreases the mobilized moment capacity. The variation in axial load on the footing is not directly accounted for in the calculation of $M_{y\_footing}$. These curves also demonstrate that the structural fuse and footing eventually approximately return to their initial position, with little permanent deformation. From these plots, one may conclude that compatible yielding between the structural fuse and shallow foundation has been successfully implemented and illustrated in the BD model. In addition, the BD model has demonstrated an effective means to minimize residual structural demands, despite the high transient demands under high amplitude motions (i.e., GZ_1.0 and SF_0.4).

4.4.3 Performance Comparison: BD and RR Models

To evaluate the difference in performance between the BD and RR models, the high amplitude motion case (GZ_1.0) is selected. The responses of the two models are systematically compared in Figure 4.9 and Figure 4.10, which present the response history results and hysteretic responses, respectively. Comparing results from the two models, the EDPs of the superstructure show that allowing the foundation to rock effectively reduces the seismic demands in the superstructure. For instance, the absolute maximum roof drift ratio and structural fuse rotation are reduced around 24 and 38%, respectively, compared with the fixed case. Residual values of 1.3% roof drift ratio and 0.028 rad structural fuse rotation are also attained within RR model. In addition, the roof level accelerations are about 20% larger when the foundation is restrained against rocking.

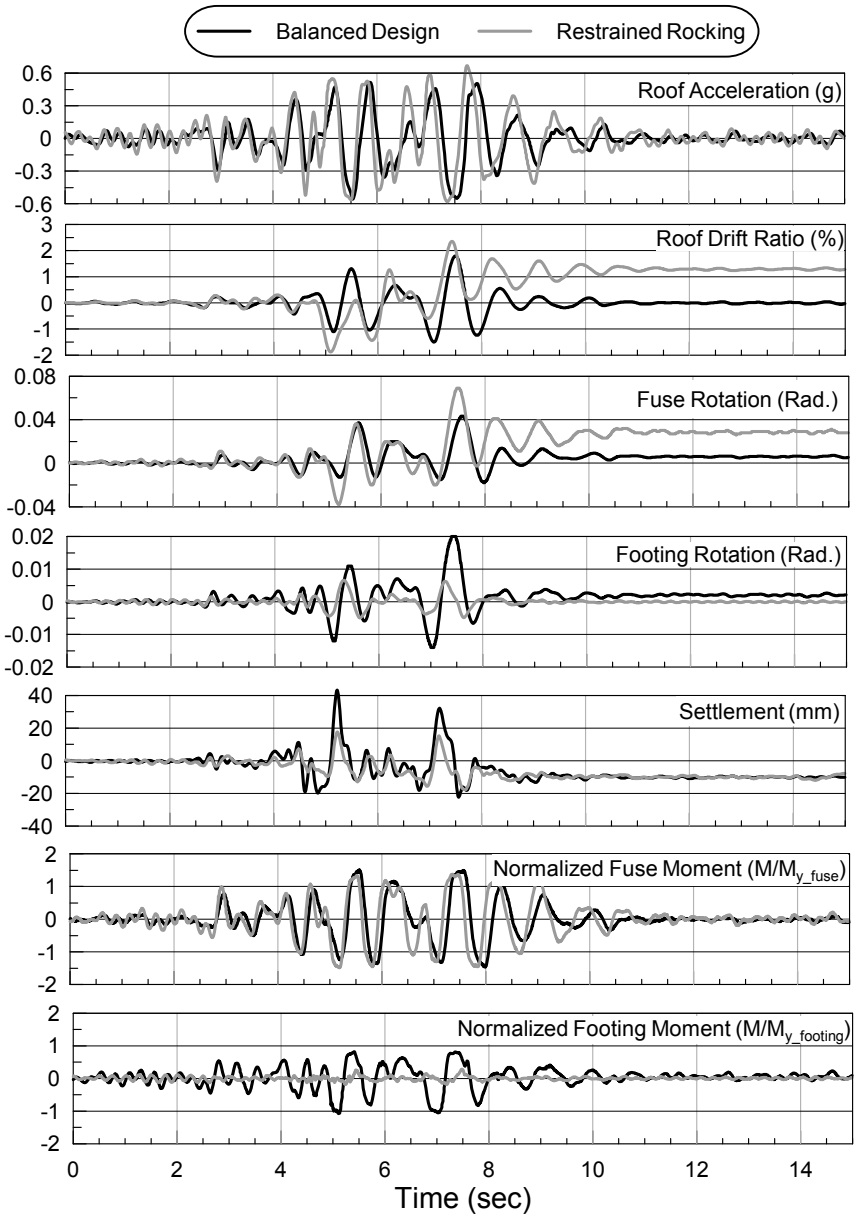

Figure 4.9 Time history response comparison between BD and RR configurations (subjected to the GZ_1.0 motion)

Footing response plots (Figure 4.9) show that the restrained footing moment demand is very small, whereas the moment demand in the structural fuse was mobilized in both cases. With respect to footing settlement, it is observed that the foundation rocking promoted system allows significant uplift and rocking of the footing. The transient uplift and rocking amplitude for the pinned system is approximately 2.5 times that of the restrained rocking system. Comparing the moment-rotation hysteresis (Figure 4.10) between the structural fuse and footing reveals that the dissipated footing hysteretic energy has been greatly reduced, whereas the structural fuse dissipates more energy and experiences severe larger inelastic demands, as characterized by both transient and permanent rotation.

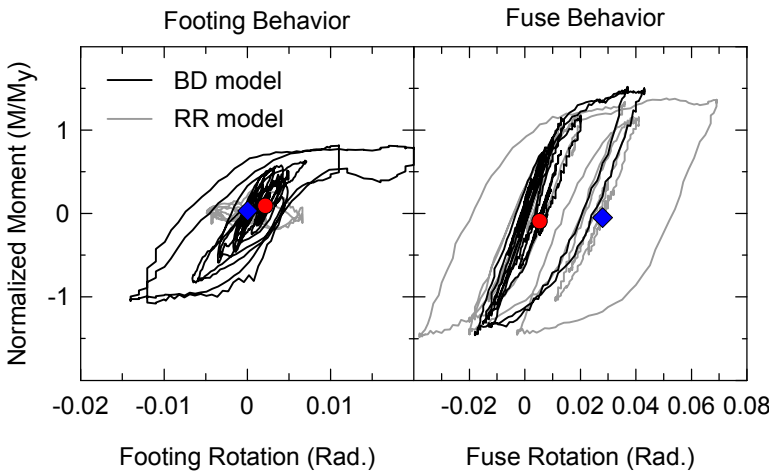

Figure 4.10 Moment-rotation response comparison (subjected to the GZ_1.0 motion, solid circle and diamond represent the end of the motion for BD and RR configurations, respectively)

4.4.4 Performance Comparison: FRD and SHD

Figure 4.11 examines the time history responses of the two other different structure-soil-foundation systems, namely the FRD and SHD models, under the strong input motion shaking GZ_1.0. Inspecting from top to bottom, one observes that the roof maximum acceleration is approximately the same for both models. The inelastic structural deformations, however, are much larger for the SHD model, with 3.25% and 0.11 rad of maximum absolute roof drift ratio and structural fuse rotation, respectively. In addition, significant permanent roof drift (2.6%) and structural fuse rotation (0.085 rad) occur in the model. The footing, on the other hand, experiences relatively low rotational demand, despite the fact that it does appear to yield. This could be easily deduced by the fact that, once the fuse component is saturated (i.e., reaches its yielding limit), the seismic demand is transmitted to the footing in a SHD configuration. Structural hinging occurs first at the SHD model (at approximately 4.5 s into the record) because the footing is designed with a much larger capacity.

For the FRD model, the superstructure seismic demands are all relatively low, with the exception of roof acceleration. Roof acceleration is a system response and will be dictated by the strength of the foundation-building system as a whole. Significant transient and permanent rotation of the footing is also observed, as anticipated for the FRD model. In this case, the footing yields a cycle prior to the structural fuse (at about 5 s compared with 5.8 s). These plots also show consistently low permanent settlement for both models despite the fact that footing uplift does occur, which are about 0.33 and 0.14% of each footing length for FRD and SHD, respectively.

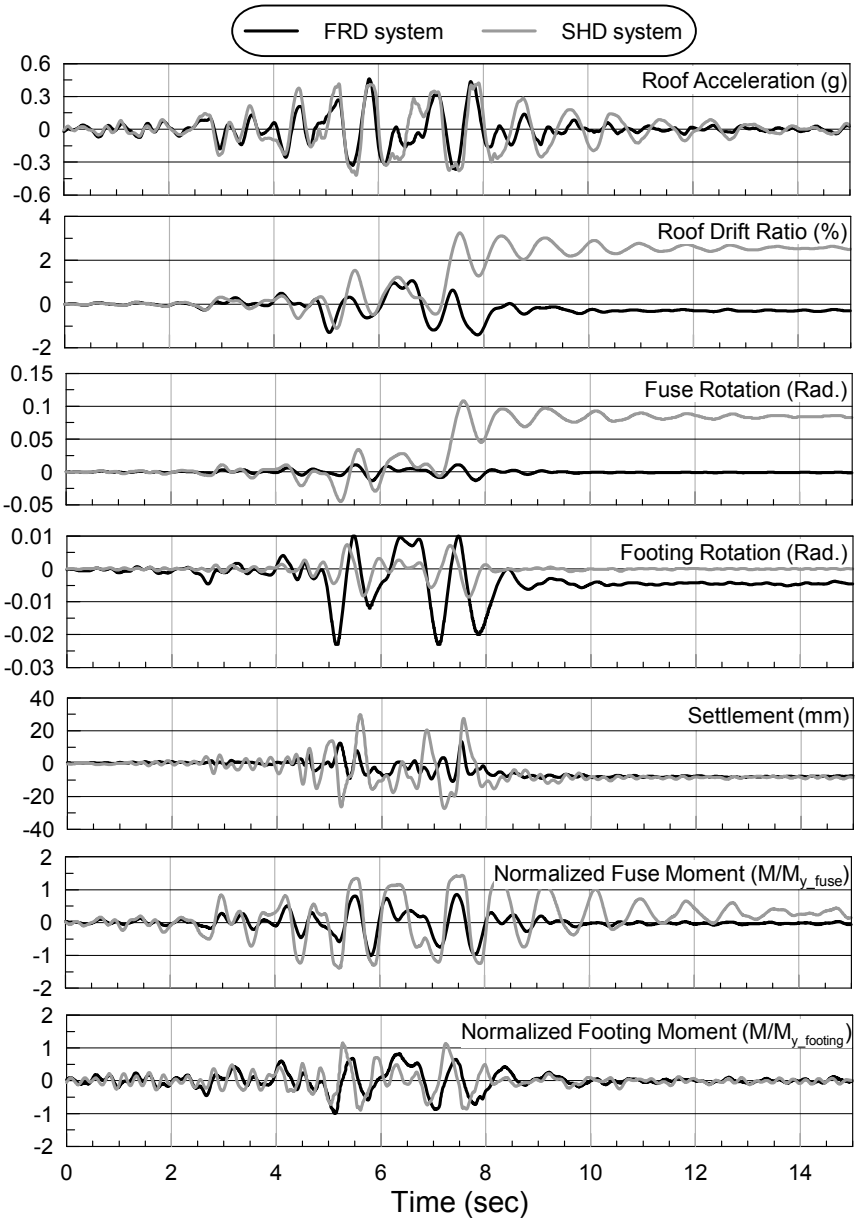

Figure 4.11 Time history response comparison between FRD and SHD systems (subjected to the GZ_1.0 motion)

Figure 4.12 presents the normalized moment-rotation hysteresis comparison. Using a smaller foundation, as illustrated in the FRD system, the foundation behaves with significant nonlinearity, receives comparatively large rotational demands, and shows significant rotational stiffness degradation, whereas the structural fuse remains linear-elastic during intense shaking. In contrast, the structural fuse in the SHD system is subjected to very large transient and permanent rotational demands and presents with a broad moment-rotation hysteresis. Although the foundation mobilizes its capacity for the SHD model, little stiffness degradation is observed, which is consistent with observations from past centrifuge tests on rocking foundations with higher FS_v (Gajan and Kutter 2008).

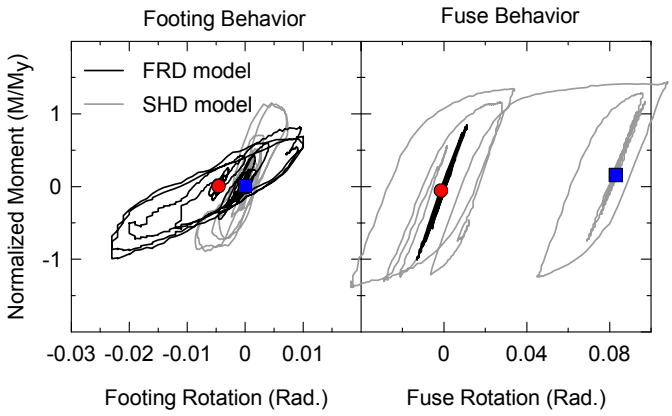

Figure 4.12 Moment-rotation response comparison between FRD and SHD systems (subjected to the GZ_1.0 motion, solid circle and square represent the residual point for FRD and SHD, respectively)

4.4.5 Synthesis of Maximum Demand

Figure 4.13 investigates the superstructure demand variation, including maximum roof drift ratio, maximum roof acceleration, maximum fuse rotation, and normalized maximum fuse moment (maximum moment divided by the yield moment). These EDPs are plotted against motion ID (Table 4.5), which in general represents increasing peak input acceleration. Data in Figure 4.13 generally demonstrate an increasing trend for all demand parameters with increasing input motion amplitude. The maximum roof drift ratio and structural fuse maximum rotation scatter plots generally show uniformly small responses at small amplitude excitation motions. However, these response parameters significantly deviate for the different models beginning with Motion ID 3 (GZ_0.4). For example, roof drift ratio in the SHD system amplifies significantly, more than two times that of the FRD system at Motion ID 5 (GZ_1.0). This clear trend is particularly significant when examining the fuse maximum rotation demand plots. Regarding the maximum roof horizontal acceleration, the restrained model generally has the largest response, followed by the BD case, whereas the SHD model had the lowest maximum roof acceleration. The structural fuse element for all structural configurations except the FRD configuration attains its yield strength for most of the motion cases. Overall, among these four models, the BD case and FRD configuration generally have a greatly reduced seismic demand on the superstructure component compared with the RR and SHD configuration.

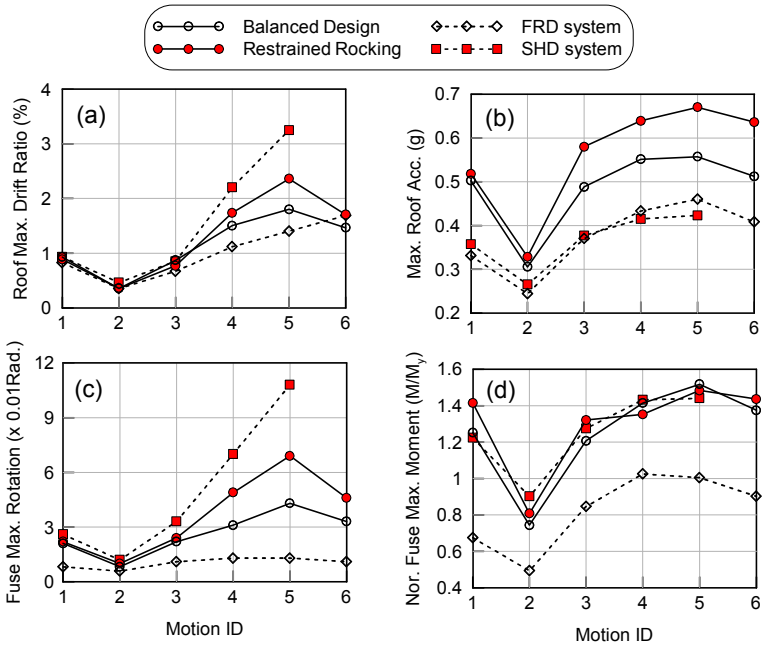

Figure 4.13 Measured superstructure EDPs: (a) roof maximum drift ratio; (b) roof maximum acceleration; (c) structural fuse maximum rotation; (d) structural fuse maximum moment

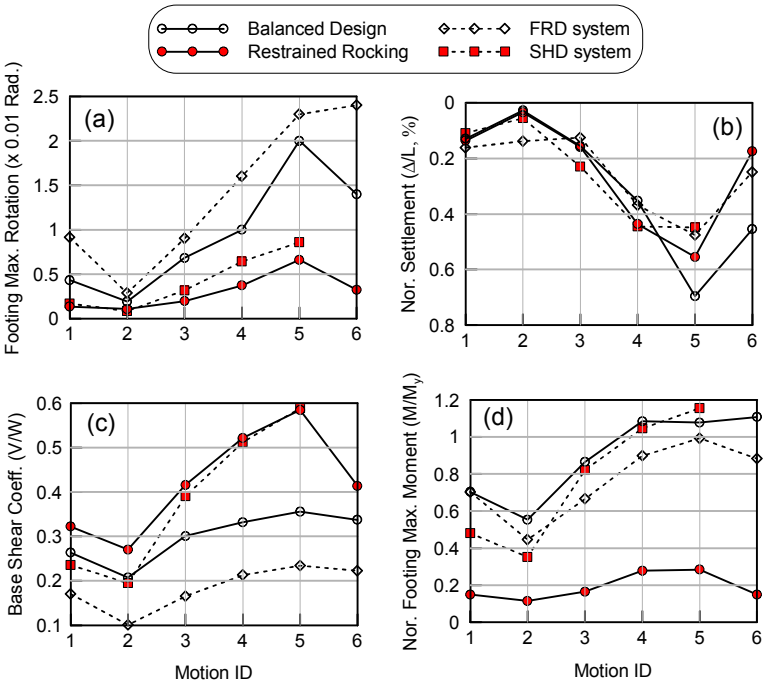

Figure 4.14 Measured footing EDPs: (a) maximum rotation; (b) normalized settlement; (c) maximum base shear coefficient; (d) maximum normalized moment

Figure 4.14 compares corresponding seismic response (engineering demand parameters) of the footing components for each configuration and each motion. This plot is organized in a similar fashion to Figure 4.13 and presents the footing maximum rotation, footing permanent settlement, base shear force, and maximum footing moment, where the last three EDPs are normalized by the footing length, the weight of the structure, and the theoretical yield moment, respectively. Results indicate that the FRD system has the largest transient rotation demand compared with other configurations tested. Moreover, maximum transient rotation increases consistently with motion amplitude in the FRD system. The BD case also observes moderate amplification of the maximum transient footing rotation. Regarding the footing permanent settlement, Figure 4.14b shows that the normalized value is always negligibly small, generally less than 0.7% of the footing length, irrespective of the configuration. The maximum base shear coefficient (Figure 4.14c) indicates that the seismic demand in terms of lateral shear force is significantly reduced when rocking is promoted as a mechanism of nonlinear deformation (BD and FRD models). The normalized footing moment data (Figure 4.14d), on the other hand, shows that the theoretical yielding capacity of each system, except for the RR model, is reached starting at Motion ID 4 (GZ_0.7). However, the theoretical footing yield moment for each case may be lower than the estimates used in the normalization of Figure 4.14d, as the axial load is changing dynamically during shaking of the model.

4.4.6 Normalized Relative Energy Dissipated by the Inelastic Components

Inelastic components of a structure may be targeted in design to dissipate seismic energy, thereby minimizing damage to the remainder of the structural system. In the models considered in this test, energy is dissipated in both the structural fuse and foundation element largely via a flexural mode (moment-rotation). Using the measured moment and rotation histories, the energy dissipated via inelastic rotation is computed by determining the total area under the moment-rotation hysteretic loop, and the normalized relative contribution of each component type is evaluated for each configuration (Figure 4.15). The energy dissipated from footing nonlinear sliding or settling is not accounted for in this calculation. This bar chart clearly shows that most of the seismic energy is dissipated within the footing-soil interface when incorporating the FRD configuration (the foundations consistently dissipate greater than 95% of the total energy). In addition, by restraining rocking of the foundation, the structural fuse becomes the main contributor to absorb seismic energy, which consistently dissipates greater than 85% of the total energy for most cases. The BD model demonstrates through this plot that it is an effective means for distributing seismic energy fairly well between the footing and the structural fuse. Although the SHD system provides a similar quantitative amount of energy dissipation, in terms of the footings relative contribution to the total, this significant amount is directly attributed to the high moment demand instead of high rotation. Severely high transient and permanent rotations in the structural fuses, observed from time history plots and scatter plots (Figure 4.11 and Figure 4.13) should discourage the use of this type of system. The optimal design is probably somewhere between the BD

and the FRD design, depending on whether the design is controlled by localized structural component ductility demand or by global drift demand.

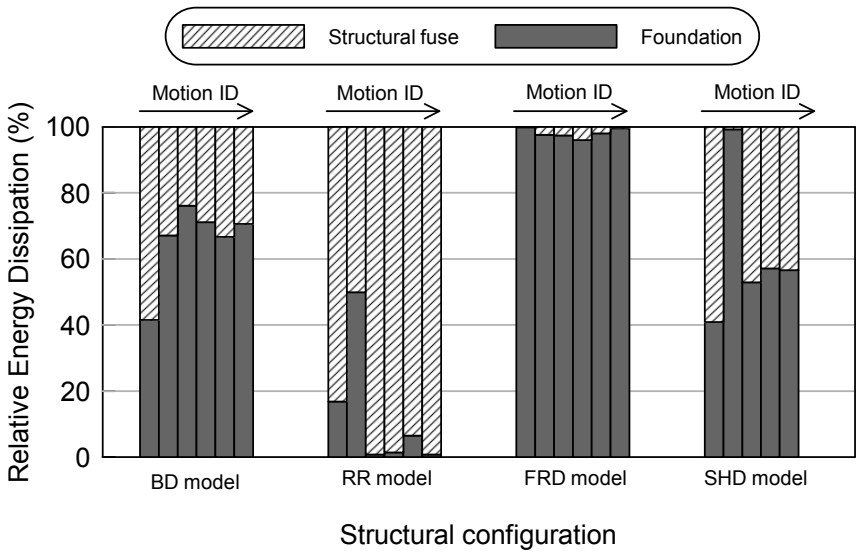

Note: (1) Motion ID for each structural configuration from left to right: 1 to 6 (Table 4.5)
(2) Motion 6 was not applied to SHD system.

Figure 4.15 Relative percentage of energy dissipated by the different components

4.5 Numerical Model Validation and Pushover Analysis

This section describes the numerical modeling of the constructed inelastic elements (structural fuse and rocking footing) and the three moment frame-foundation systems of the Test-1 program, and importantly, the results of the simulations are compared with those of quasi-static cyclic testing and dynamic shake table testing. Finally, static pushover analyses are performed for the three models to further evaluate and compare their seismic performance.

4.5.1 Modeling of Structural Fuse and Rocking Foundation

A numerical model of the structural fuse in the BD model is constructed in *OpenSees* (Mazzoni et al. 2009) to simulate its inelastic behavior. The reduced column section is discretized into 4 nonlinear displacement-based beam-column elements along its height. The cross section of each nonlinear element consisted of a dense array of fibers whose stress-strain constitutive relationship followed that of the "Steel02" material (Mazzoni et al. 2009; Menegotto et al. 1973) to capture its hardening behavior. The input *tcl* file to construct the structural fuse is provided in Appendix A.1.2.

Figure 4.16a compares the response of the constructed numerical model of the structural fuse with the experimental results. The experimental data under slow cyclic loading is available in the Test-1 data report (Liu et al. 2011). Note that the y-axis of this plot is the measured moment normalized by its yield moment (Table 4.3). The comparison indicates that in general, the numerical results agree with the experimental data fairly well. The estimated fuse yield moment, as well as the salient features of its hysteretic response such as isotropic hardening and non-degrading stiffness and strength, are nearly perfectly captured in the constructed model.

For the shallow foundation, modeling of its rocking behavior is established using the beam-on-nonlinear-Winkler foundation (BNWF) approach, wherein 57 equally distributed, independent vertical gapping nonlinear spring elements are placed to support the elastic footing element. The force-displacement relation of the vertical spring element is based on the backbone curves of "QzSimple2" uniaxial material model in *OpenSees*, which have been calibrated against shallow footing tests (Raychowdhury and Hutchinson

2009). The stiffness intensity ratio between the vertical springs in the central portion of the foundation and the edge vertical springs is chosen as 5, and the initial stiffness of each vertical spring was then derived based on a resultant rotational stiffness of the foundation according to Gazetas' formula (1991). In present study, each "QzSimple2" spring is assumed to have identical force capacity, and its amplitude is then determined with the knowledge of the critical contact length (L_c) and the total static axial load acting at the soil-footing interface (Deng and Kutter 2012). For nonlinear sliding behavior, it is modeled by using one lumped horizontal nonlinear spring, whose consecutive relationship follows "TzSimple2" uniaxial material model in *OpenSees*, to connect the middle of the footing to a fixed support. The capacity of the sliding spring is determined based on the undrained shear strength, the footing geometry, and the total axial load acting at the soil-footing interface (Raychowdhury and Hutchinson 2009). Appendix A.1.3 provides the *tcl* script for modeling the footing rocking behavior in *OpenSees*.

Figure 4.16b plots the moment-rotation response of the numerical rocking footing model, overlaid with the experimental data. The experimental data of this rocking footing is provided by Hakhamaneshi et al. (2011). The comparison shows that the BNWF model is capable of producing a reasonably accurate yield moment for a surface rectangular-type rocking footing. However, it underestimates the rotational stiffness of the footing during unloading. The mechanical properties of the "QzSimple2" nonlinear spring utilized in this model was mostly calibrated against the rocking footing tests conducted in sandy environment (Raychowdhury 2008). Its unloading behavior might not be perfectly reasonable for rocking footing resting on clayey soil as considered in this test program. As a consequence, the residual response of the rocking footing and further the entire

moment frame-foundation system might not be reliably predicted (will be mostly underestimated) by the BNWF modeling approach described in this work; however, the moment demand imposed on the foundations can be reasonably estimated.

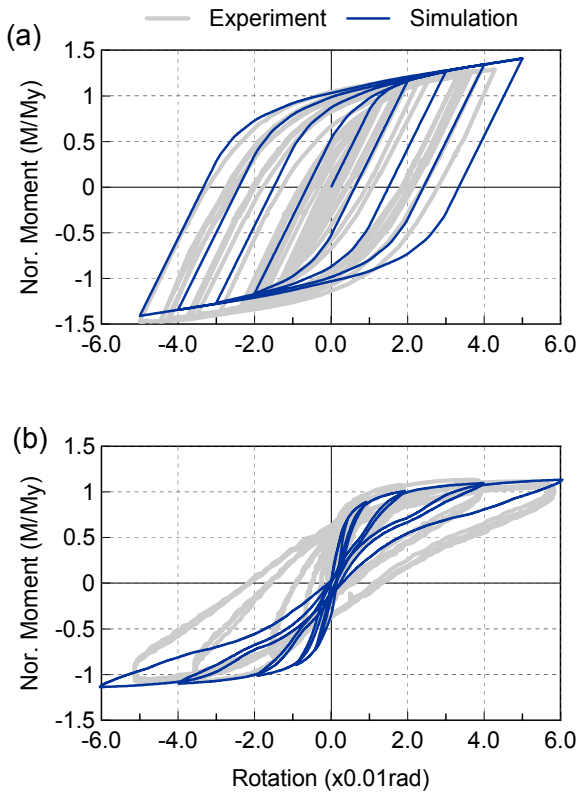

Figure 4.16 Component-level hysteretic response comparison: (a) structural fuse; (b) rocking foundation

4.5.2 Dynamic Response Comparison

Numerical simulations of each system, namely the BD, FRD, and SHD, are conducted using the validated model of the structural fuse and the rocking footing. The remaining components of the system, such as the beams at each level, the columns at each level, and the elastic footing elements, are modeled by using elastic beam-column element in *OpenSees*. The *tcl* input file for constructing the BD model in *OpenSees* is

presented in Appendix A.1.1. It is noted that during motion analysis, Rayleigh damping with 5% damping applied to the first two modes is assumed. Figure 4.17 - Figure 4.19 compare the seismic response of each model configuration when subjected to the GZ_0.4 motion excitation. The response parameters considered for comparison include the rotation and moment demand of the structural fuse rotation the rocking footing.

Figure 4.17 compares the response of the structural fuse in the BD model during the GZ_0.4 input motion. Comparing time history responses of the simulation and experiment, as plotted in part (a) and (b), indicates that the numerical model reasonably captures the response of the structural fuse. The moment history, for example, is in perfect agreement with the experimental data; however, the rotation demand in the negative direction is slightly underestimated in the numerical model. Consequently, its moment-rotation hysteretic response is slightly stiffer compared with that of the experiments.

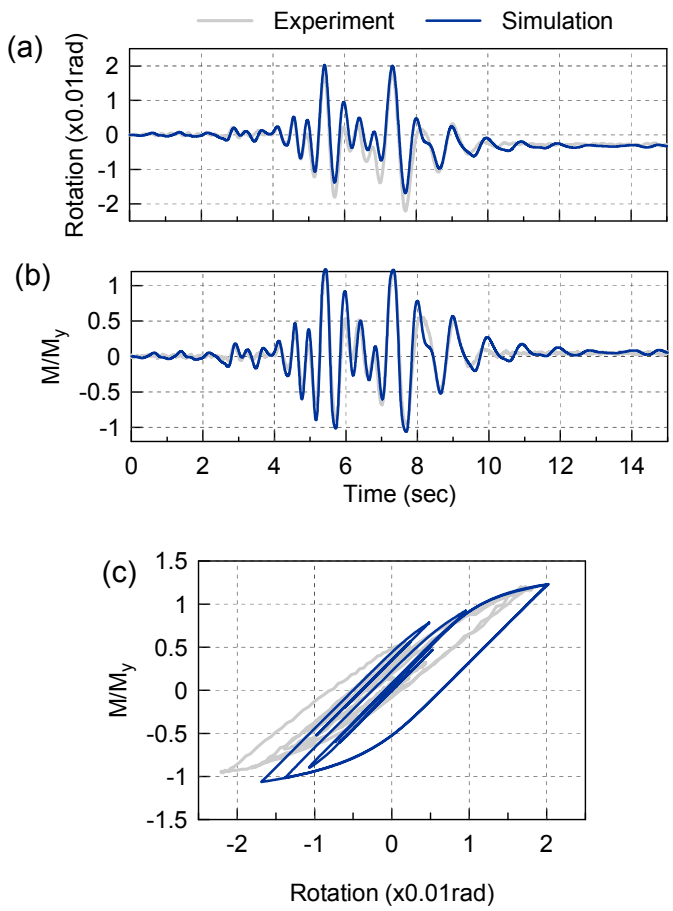

Figure 4.17 Response comparison for the structural fuse in the BD model during GZ_0.4: (a) rotation time history; (b) normalized moment time history; (c) moment-rotation response

In the meantime, the footing rocking behavior is reasonably predicted in this model. As shown in Figure 4.18, the footing's rotation history, normalized moment history, and the moment-rotation curve, are all in good agreement with the experimental data for this input motion.

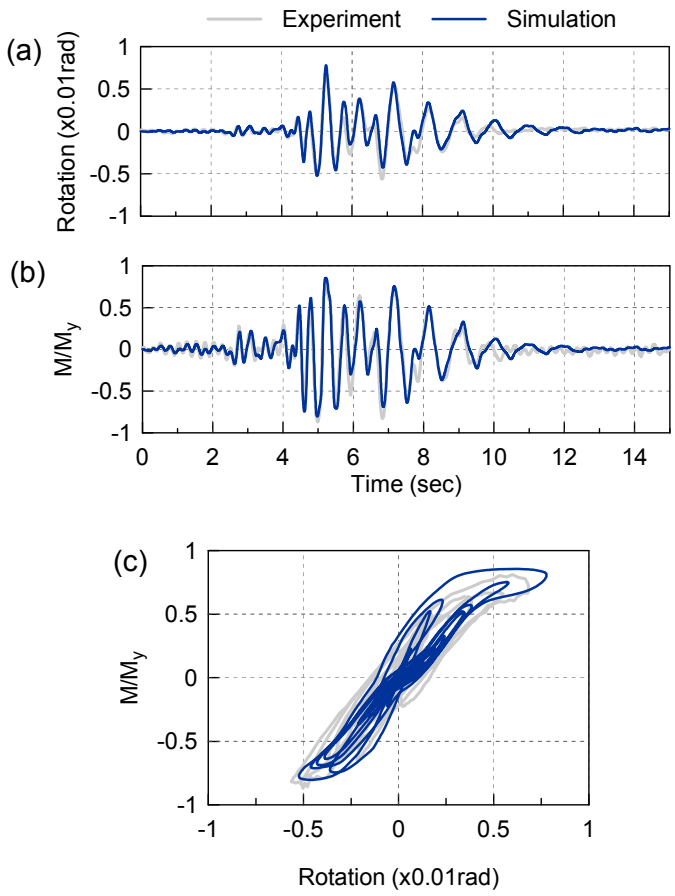

Figure 4.18 Response comparison for the structural fuse in the BD model during GZ_0.4: (a) rotation time history; (b) normalized moment time history; (c) moment-rotation response

Figure 4.19a and b compares the hysteretic response of the structural fuse and rocking footing for the FRD and SHD models during GZ_0.4 motion, respectively. Part (a) shows that the elastic response of the structural fuse in the FRD obtained from simulation is nearly identical with the response measured in the experiment. For the rocking footing's hysteretic response, although it is not perfectly captured in the numerical model, such as the unloading behavior, the peak moment demand in both directions closely matches the experimental results.

For the SHD system, the numerical model generates a similar hysteretic shape of the structural fuse with the experimental data as shown in part (b). However, it underestimates the maximum rotation demand of the fuse by about 24%. The footing's response is not perfectly predicted in terms of peak moment; the simulation under-predicts the maximum moment demand by approximately 20%, but it overestimates the minimum demand by about 20%. Nevertheless, it generally agrees with the experimental results in terms of hysteretic shape, namely almost linear elastic response for the foundation component.

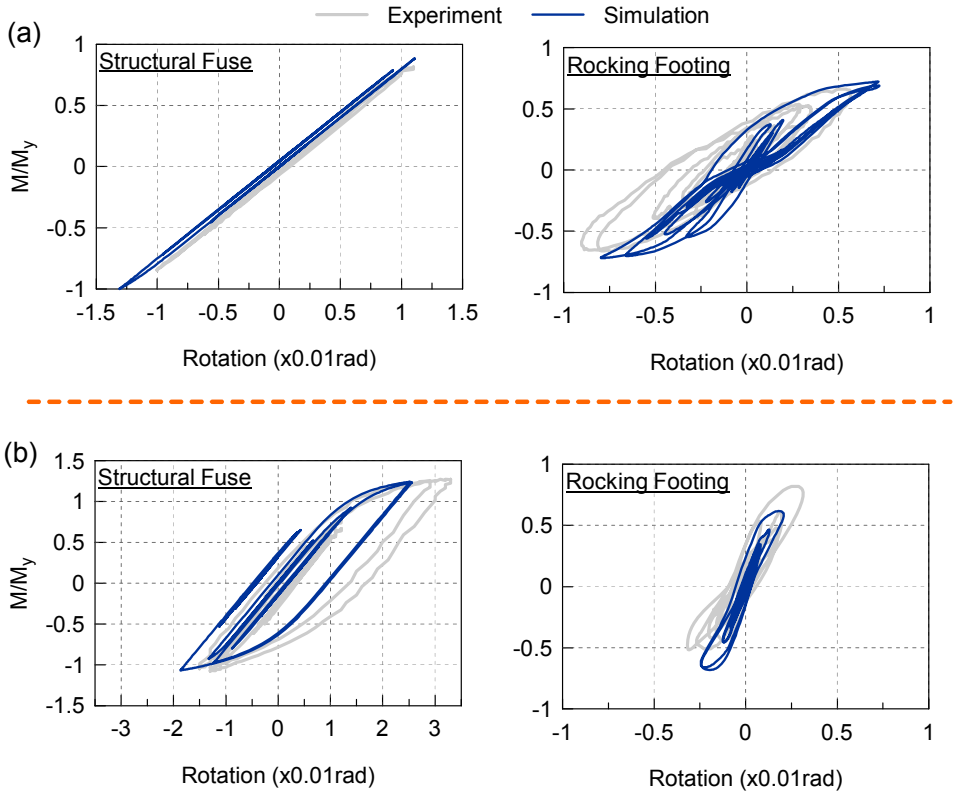

Figure 4.19 Hysteretic response comparison for the structural fuse (first column) and the rocking footing (second column) under GZ_0.4 within: (a) FRD model; (b) SHD model

Figure 4.20 summarizes the comparisons for all models under all motion cases in terms of several engineering demand parameters, including the peak rotation and moment demand of the structural fuse, the peak rotation and moment demand of the rocking footing, and the peak normalized base shear. Part (a) shows that the peak fuse rotation of the FRD and BD models is fairly well estimated in the simulation in which the discrepancies compared to the experimental results are generally within 10%. However, the demand of the SHD model is significantly underestimated, particularly during strong motions. Physical observations after the sequential shaking indicate that the fuse in the SHD experiences a significant local buckling by the end of the shaking (Liu et al. 2011), which leads to an extremely high instantaneous rotation demand. In the *OpenSees* model, however, nonlinear beam-column element is not able to consider the buckling behavior and post-buckling response. As such, the peak demand estimated in the simulation is usually less than that of the experiments. The peak moment demand obtained in the simulation, on the other hand, is in good agreement with that of the experimental values; their differences are usually within 10% with few scenarios in 20%.

For the footing's response, the peak rotation demand is generally well predicted for all models during low-intensity motions, as indicated in part (c). However, during strong motions, the peak demand gradually deviates with the experimental results but within a range of 20% with exceptions of few cases of the BD model more than 20%. Part (d) shows that the numerical models of the FRD and BD systems can produce reasonably well peak moment demand (within 10% deviation). The peak footing moment of the SHD, however, deviates with the experiments the most within a range of 20%. In the meantime, the peak base shear demand is reasonably well estimated for the FRD and

BD systems under all motion scenarios. As shown in part (e), their differences with the experimental data are fairly small (within 10%). The simulation of the SHD, on the other hand, tends to overestimate the peak base shear demand during strong motions.

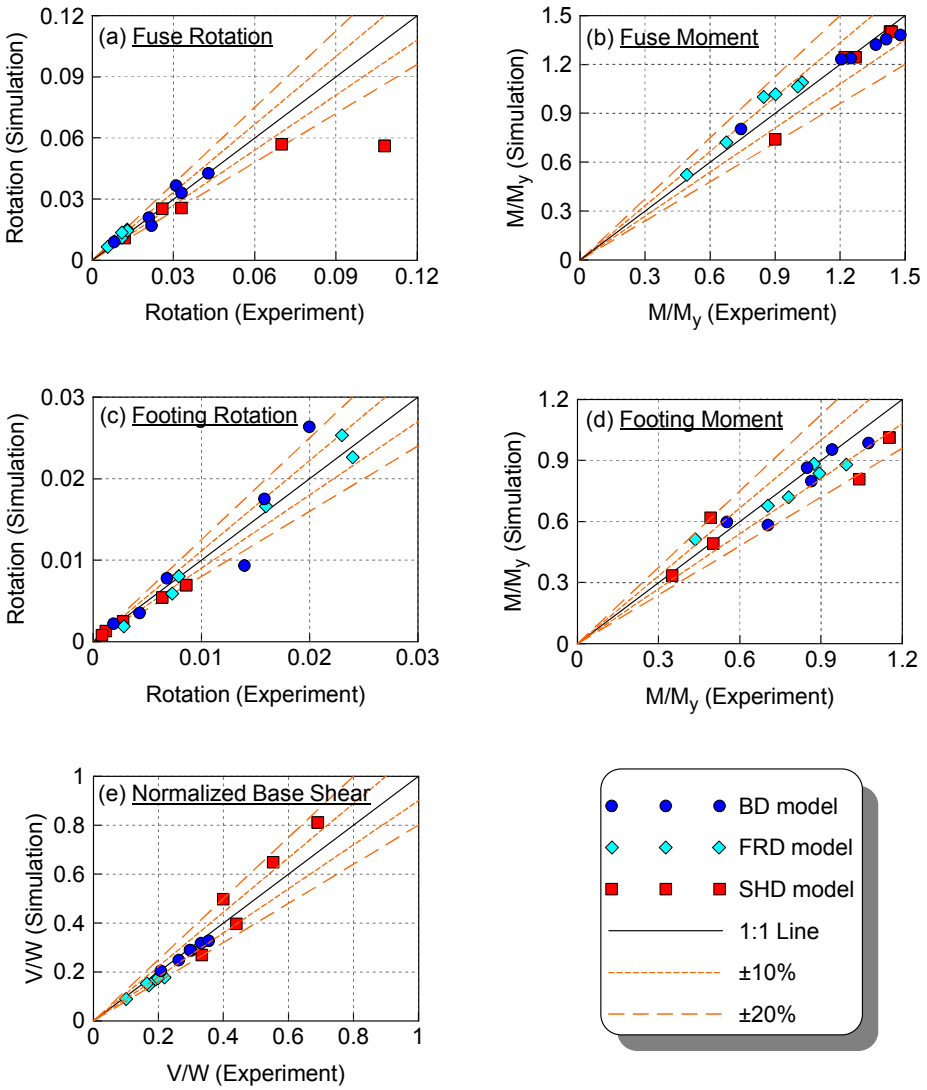

Figure 4.20 Maximum response comparison of each configuration

4.5.3 Nonlinear Pushover Analysis

In an effort to further evaluate and compare the seismic performance of each structural configuration, static pushover analyses are performed. Considering the constructed mass ratio between each floor level, namely $M_1=2M_2$ (Table 4.3), it is assumed that the lateral force is uniformly distributed at each level in this study, as schematically depicted in Figure 4.21a. The analysis is complete by using displacement-controlled method wherein the roof drift ratio is gradually and monotonically increased until it reaches 10%. It is noted that static gravity analysis is performed prior to the pushover analysis for each model to consider the P-Δ effect.

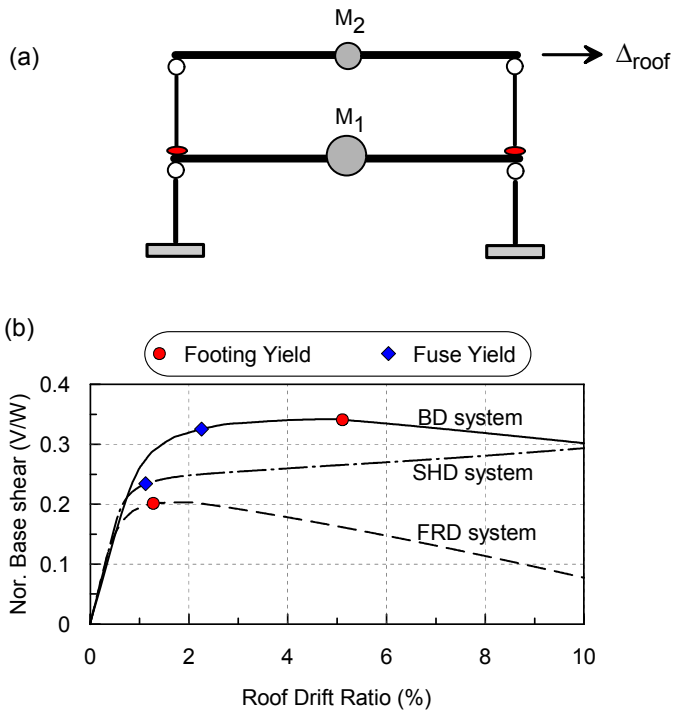

Figure 4.21 Pushover analysis: (a) schematics of the model subjected to a target roof drift; (b) system-level response comparison

Figure 4.21b compares the system-level force-displacement response of each system, where the x-axis and y-axis plot the roof drift ratio (DR) and base shear normalized by the building weight respectively. In addition, the response curves are overlaid with all identified yielding mechanisms, including the yielding of the structural fuse and the rocking footing. The results show that the rocking footing of the FRD model yields at DR of 1.3%. The system's capacity at incipient footing yielding attains 20% of the building weight, which is slightly less than its C_r (0.22, Table 4.3). This is attributed to the P-Δ effect. Upon continued loading to a high DR level, the system's load-carrying capacity is gradually deteriorated due to the P-Δ effect. When the DR reaches 10%, for example, the FRD's capacity drops to 0.08. The SHD model, on the other hand, observes the yielding of the structural fuse at DR of 1.1% with a system's capacity of 0.24. The capacity is dramatically reduced compared with its C_y (0.33) which is induced by the P-Δ effect. When the DR is gradually increased, the SHD's capacity is gradually increased because of the hardening characteristic of the structural fuse in the numerical model.

The BD model observes the largest system capacity compared with the SHD and FRD systems. It commences with yielding of the structural fuse at DR of 2.3%, and subsequently the rocking footing yields at DR of 5.1%. The peak strength of the BD model (around 0.34) occurs at yielding of the footing, which is slightly less than its dominant fuse strength (C_r=0.35, Table 4.3). Upon continued loading after footing yielding, the system's lateral-load-carrying capacity observes P-Δ induced degradation.

In summary, comparing the pushover response of all models reveals that the system's capacity of structural hinging dominated model will be highly deteriorated by the P-Δ effect prior to the yielding of the structural fuse. In contrast, the capacities of the

foundation rocking systems are less affected by the P-Δ effect prior to the yielding of the rocking footing. More importantly, a balanced design strategy is able to dramatically improve the system's lateral-load-carrying capacity compared with the FRD and SHD design strategies.

4.6 Concluding Remarks

The inelastic response of a rocking foundation has been consistently shown to beneficially dissipate seismic energy. Moreover, rocking foundations provide a natural self-centering mechanism and stable inelastic hysteretic behavior, attributes that may be incorporated in a capacity-based design. When used to dissipate energy, rocking foundations can effectively reduce the inelastic demands placed on conventional plastic hinges, thereby contributing to a well-controlled, better performing structural system with little cost. There is a necessity, however, to evaluate the load and deformation sharing within the systems, which are designed with both yielding foundations and superstructure components, both experimentally and numerically.

In this study, model structures incorporating rocking foundations and yielding plastic hinges in the superstructure were subjected to earthquake ground motions in a centrifuge test. Variations in model properties allow the balance between rocking foundation and yielding structural components to be explored. These tests are part of a research project supported through the NSF NEESR program and have been conducted at the NEES centrifuge facility at University of California at Davis. Four building models of like geometry were built with (1) balanced design, in which the same base shear

coefficient activates both structural hinging and foundation rocking mechanisms; (2) restrained rocking; (3) FRD condition; and (4) SHD condition. The models were constructed and systematically subjected to similar suites of earthquake input motions. Important observations from this test program include the following:

- The seismic behavior of the BD model indicates that compatible yielding of the structural fuse and rocking foundation components is successfully implemented in this case. The designed inelastic components are observed to remain linear-elastic at low amplitude motion input, and on further motion amplification, both the structural fuse and rocking footing component flexural capacities are mobilized. Despite the remarkably high transient rotation demand to the footing and structural fuse, permanent rotations are observed to be negligible. This can be largely attributed to the self-centering mechanism introduced by the rocking footing. Compared with a more conventional design, such as the restrained rocking and SHD model, the superstructure seismic demands are significantly reduced in the BD model, particularly with regard to maximum roof drift ratio, maximum structural fuse rotation, and maximum base shear. Finally, energy dissipated by this system is observed to be distributed fairly well between the inelastic structural and footing components.
- For the FRD model, energy dissipation is dominated by large transient and permanent rotation and moment demands at the footing-soil interface, particularly when subjected to intense input motions. The ductility demands on the structural components are significantly minimized, and

the rocking footings, in most cases, are associated with beneficial self-centering behavior. The moment-rotation hysteretic response does not show significant loss in capacity but does show significant degradation in footing rotational stiffness. For this model, more than 95% of its total energy dissipation occurs at the footing-soil interface.

- When footing rocking was prevented by a clamp at the top of the first level column (restrained rocking model), the structural fuse components experienced large transient and residual rotation demands under strong input motions. The footing response, as expected, is reduced, with lower rotation and moment demand. In general, less than 15% of the seismic energy is dissipated within the footing-soil interface, which in turn results in the structural fuse and superstructure experiencing significantly larger transient and residual rotations and roof drift ratios, respectively.
- Finally, a SHD model (which might be considered to most closely mimic typical design practice) was tested in this program, and this model experienced severe transient and residual demands in the structural fuses under high amplitude motions. The structural fuses yield first, and upon continued strong shaking, some nonlinearity, but low rotation demand is placed on the foundation component. Meanwhile, with respect to the footing settlement, all tested models are observed to have negligibly small demand despite the fact that significant footing uplift does occur for some models.

- Numerical models were constructed in *OpenSees* where nonlinear Winkler springs were implemented to capture the foundation rocking behavior. Comparisons with the experimental model response show that the numerical models can reasonably predict the local and global response of the moment frame-foundation models under cyclic and earthquake loading.
- The SHD model observes substantial P-Δ induced system-level capacity reduction when subjected to monotonic lateral load, whereas the foundation rocking models (FRD and BD) are less affected prior to the footing yielding. Moreover, the BD system observes a significantly improved lateral-load-carrying capacity compared with other models.
- The experimental raw data of the test program described in this chapter are provided at NEEShub website with a permanently assigned Digital Object Identifier (DOI) of 10.4231/D3QJ77Z1R. (http://nees.org/warehouse/experiment/2886/project/732)

4.7 Acknowledgement

This chapter, in part, is a reprint of the material as it appears in the ASCE Journal of Structural Engineering. Liu, W., Hutchinson, T. C., Kutter, B. L., Hakhamaneshi, M., Aschheim, M., and Kunnath, S. (2013). "Demonstration of Compatible Yielding between Soil-Foundation and Superstructure Components." *ASCE, Journal of Structural Engineering*, 139(8): 1408-1420. The dissertation author was the primary investigator and author of this paper.

Chapter 5

Frame-Wall-Rocking Foundation System Test (Test-2) – Part I: Test Program and Slow Cyclic Results

5.1 State of Understanding

5.1.1 Background

It is generally recognized that soil-structure-interaction (SSI) during an earthquake could elongate a system's natural period and increase system damping (e.g., Veletsos and Meek 1974), which in turn may reduce the seismic demand imposed on superstructure components. However, it is also recognized that inelastic SSI, particularly under the mode of foundation rocking, can assist with dissipating seismic energy and introduce a self-centering benefit with the assistance of the "P-Δ" effect (e.g., Wiessing 1979; Yim and Chopra 1984; Rosebrook and Kutter 2001; Gajan and Kutter 2008;

Paolucci et al. 2008; Shirato et al. 2008; Deng and Kutter 2012; Drosos et al. 2012; Figini et al. 2012; Hakhamaneshi et al. 2012; Anastasopoulos et al. 2013; Pecker et al. 2013). Several system-level experimental and numerical studies further substantiate its beneficial contributions to a structure-foundation system as a whole when subjected to seismic load (e.g., Chang et al. 2007; Raychowdhury and Hutchinson 2010; Hung et al. 2011; Carbonari et al. 2012; Gelagoti et al. 2012; Liu et al. 2013). Hence, within a performance-based seismic design framework, foundation rocking can be regarded as an alternative and effective inelastic fuse mechanism to enhance the system's seismic performance.

On the structural side, combining walls and frames as the lateral resisting components within buildings located in active seismic regions has emerged as an effective strategy. Cantilevered structural wall components can provide significant lateral stiffness to a building, resulting in greatly reduced story drifts. In addition, other undesirable failure mechanisms, such as the development of a soft-story, can be readily avoided. Furthermore, recent research has highlighted the promise of designing a hinged wall mechanism (e.g., Alavi and Krawinkler 2004). Alternative to integrating the hinge within the wall internally, the same behavior could be physically accomplished by introducing external mechanical devices, such as prestressed tendons implemented (e.g., Ajrab et al. 2004; Marriott et al. 2008). These and many other studies have shown that this strategy could render a well-controlled and uniform inter-story drift pattern along the shear wall height. Complementary to this strategy, the addition of energy dissipation capacity has been investigated via implementation of supplemental dampers (Restrepo and Rahman 2007; Toranzo et al. 2009; Pollino et al. 2013). It is unclear if cost and

constructability of these types of mechanical solutions is effective within the life-cycle of the building. The foundation rocking mechanism, on the other hand, is well poised to provide these two benefits simultaneously without introducing supplemental components. The presence of the rocking foundation in a typical wall- or frame-braced building will result in a load sharing profile different from that of a building absent rocking foundations. For this reason, experimental studies, which incorporate both inelastic foundation rocking and inelastic superstructure components, are needed.

5.1.2 Scope of this Chapter

A second centrifuge test program (Test-2) was conducted to evaluate the seismic performance of low-rise frame-wall-foundation systems. The experimental series involved three types of configurations considering strength variations between a shear wall rocking footing and a shear wall fuse, namely; structural hinging dominated (SHD), foundation rocking dominated (FRD), and balanced design (BD). Each model was first symmetrically configured and subsequently constructed with an asymmetric layout. As a result, six different low-rise frame-wall-foundation models were constructed. They were supported on dense dry Nevada sand and tested in a 30-g centrifuge environment. This chapter describes the experimental program and presents results from the quasi-static cyclic tests of two of the models, namely the symmetric FRD and BD structures. The next section (Chapter 6) presents the response of the symmetric models when subjected to a suite of increasing intensity earthquake motions, and Chapter 7 presents and compares the response of the symmetric models under cyclic and earthquake loads.

5.2 Target Frame-Wall-Foundation Models

5.2.1 Design Concept

The target frame-wall-foundation test specimens were two-dimensional models of a low-rise wall-braced building. The structural system of these models was two-story-two-bay frame-wall structural systems with equal spans. Two types of inelastic *hinging* mechanisms are considered in these target building models. The first is referred to as a *structural hinging mechanism*, wherein structural components are designed to reach their strength during moderate- or high-intensity earthquake excitation and deform plastically. The second, referred to as a *foundation rocking mechanism*, is expected to develop at the soil-foundation interface.

Figure 5.1 schematically depicts the proposed inelastic frame-wall-foundation building systems, wherein solid ellipses placed below the ground surface indicate the rocking foundations, and the remainder locates the various structural fuse mechanisms. Two different layouts were considered, namely; a symmetric system (part a) and a load resisting system with asymmetric geometry (part b), as may occur due to architectural requirements. For both layouts, structural fuses were located at the bottom of columns at each level and at the base of the shear wall (SW). It is generally understood that the SW is designed to carry the majority of the lateral load; however, it is common that gravity frame bays will be attached to a SW with the intent of carrying service loads. Inherently, however, these gravity frames will carry some lateral load. Since the SW structural hinging behavior is the dominant mechanism governing the system's inelastic response, an exact arrangement of column and beam fuses will not significantly affect the nonlinear

performance at the system level. Therefore, to simplify the design, construction, and instrumentation of the models, column hinging, rather than beam hinging, is the defined plastic mechanism within the structural portion of the frame bays. The beam elements are assumed to remain linear-elastic, and the flexural stiffness (EI) are designed to be essentially rigid. In addition, pinned-connection conditions are employed at beam-column and beam-wall connections to release some degrees of freedom to facilitate accurate measurements of shear and moment distributions in all of the members of the structures. (Liu et al. 2013b). Preliminary studies confirmed that the pushover curves for the idealized building model, namely, constructed with strong beams and weak columns and pinned beam-to-column and beam-to-wall connections, follows that of a realistic building configuration and this construction strategy greatly improves the reliability of the force demand measurement.

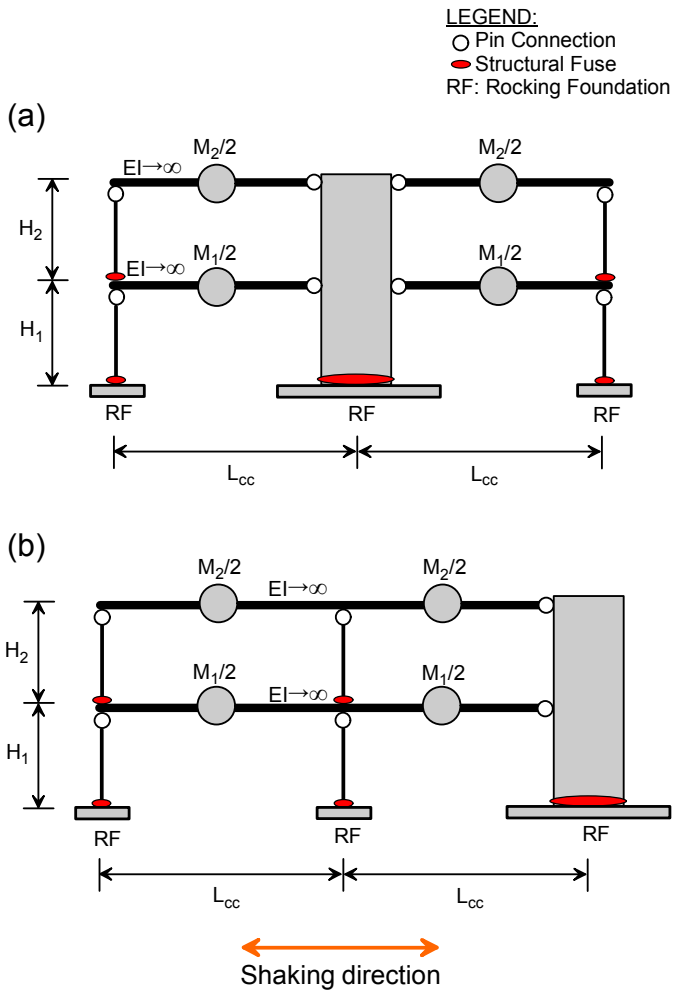

Figure 5.1 Schematics of proposed frame-wall-foundation model configurations: (a) symmetric; (b) asymmetric

5.2.2 Model Design Procedure

Minimum service load requirements adopted for regular occupancy buildings were utilized to design the model buildings (ASCE 7-10, 2010). Specifically gravity floor loads of 10.5kPa, including dead and live load, were imposed on the members. The beams were also designed to minimize floor deflection less than 1/360 of the span. Subsequently, models were designed assuring a centrifugal acceleration of N=30g applied. Kutter (1995) (or Table 4.1 in Chapter 4) provides the centrifuge scaling laws between quantities in prototype and model scale. It is noted that prototype dimensions are presented throughout, unless otherwise noted. In total, six different reduced-scale planar frame-wall-foundation models, with varying symmetry and inelastic mechanisms, were designed and constructed. Three each of these models were symmetric, while the remaining three were asymmetric. Amongst the three, the arrangement of dominant inelastic mechanisms were considered as either structural hinging dominated (SHD), foundation rocking dominated (FRD), or a balanced design (BD). In the SHD models, the SW moment strength is selected such that it occurs well before that associated with mobilization of the foundation's moment capacity. This reflects a traditional fixed-base design approach. In contrast, the FRD system incorporates a SW foundation element, which has lower strength compared with that of the SW structural fuse. The BD model concept, on the other hand, intends to mobilize the moment capacities of the SW foundation (under rocking) and the SW structural fuse (under bending) at approximately the same base shear level.

Each of the SHD, FRD, and BD models were designed with the variation of SW location, which results in the six building models in total. To differentiate model layout variation, a prefix of "s" or "a" is used in the model acronym to represent either a symmetric and asymmetric layout, respectively. For example, *sBD* represents a *symmetrical Balanced Design* system configuration. It is noted that the emphasis of this chapter is on the behavior of the symmetric models. Figure 5.2 provides an elevation view of each instrumented symmetrical models, sSHD, sFRD and sBD model.

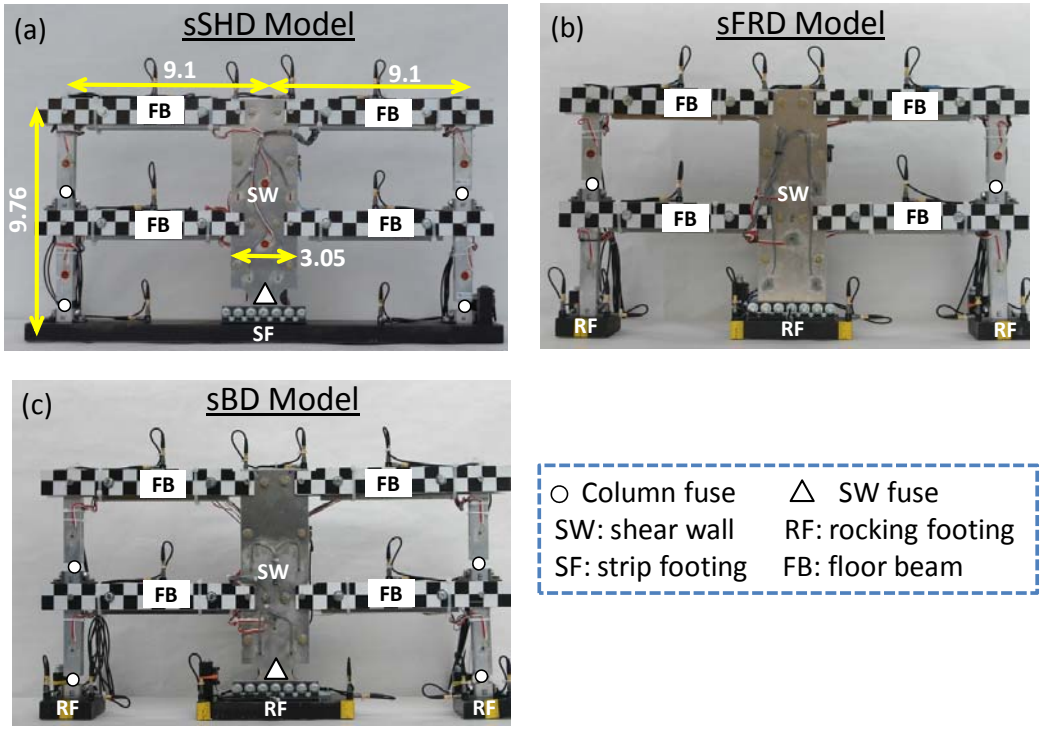

Figure 5.2 Constructed symmetric frame-wall-foundation models: (a) sSHD; (b) sFRD; (c) sBD (Dimensions in prototype scale, m)

In the design of these models, given consistent soil conditions amongst the models, the SW fuse and footing size are the critical properties controlling the system's strength and inelastic behavior. To characterize the strength of these two elements, two dimensionless parameters C_y and C_r are used (Chapter 4 or Liu et al. 2013b). The parameter C_y is defined as the structural fuse yield coefficient, and the parameter C_r is the foundation rocking yield coefficient. The various target frame-wall-foundation models were designed by controlling the relationship between these two variables. Note that C_y and C_r are solely associated with the capacity of the SW structural fuse and the SW footing, since these inelastic mechanisms will control the global performance. In other words, the total base shear to initiate yielding of the column fuses or column footings is of less significance compared with that of the SW mechanisms.

5.2.3 Model Construction

The models were constructed of a mix of Aluminum for the primary structural components, and mild steel for the floor masses. The simulated shear wall component was constructed by using two parallel annealed Aluminum plates (Alloy 1100-O, yield strength f_y=37MPa), as indicated in Figure 5.3a, with a group of high-density polyethylene (HDPE, Figure 5.3b) blocks spaced in between to provide out-of-plane stability. The thickness of each annealed Aluminum plate is 3.2mm in model scale. The columns and beams were constructed of Aluminum square tubing (25mm×25mm×3.2mm in model scale, Figure 5.3c) and inverted-U channel sections (38mm×38mm×3.2mm in model scale), respectively. Those members were made of Aluminum 6063-T52 with yield strength of 170 MPa. The floor masses were configured with several steel blocks

and placed inside of the U-channel beam elements. The pin-connection conditions were created by placing the smooth shank of bolts through holes at the beam-column and beam-wall joints. All rocking footings were constructed of rectangular Aluminum block with a thin layer of sand glued to the bottom bearing on the ground surface, initially with zero embedment. Structural fuses were located at the base of the shear wall (sSHD and sBD models) and the bottom of columns, and physically constructed by reducing the cross-section of the wall and columns to target flexural strengths (Figure 5.3). The hysteretic behavior of the constructed SW fuse was experimentally investigated via component tests conducted at both 1-g and 30-g level. Note that the three symmetric models share the same structural geometry and structural component sizes, with the exception of the length of the SW fuse and footing.

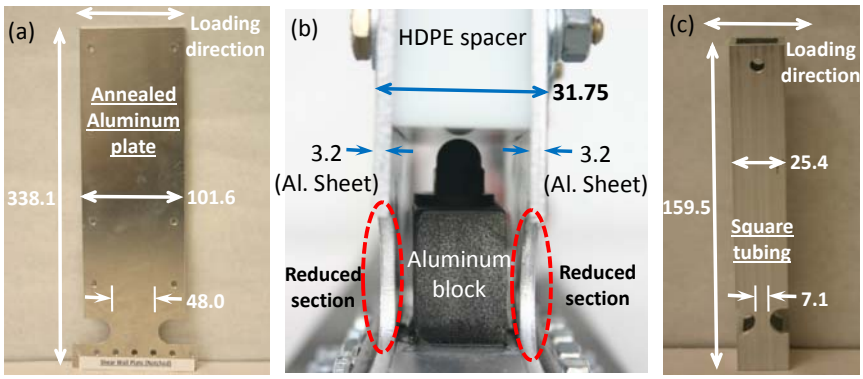

Figure 5.3 Constructed inelastic structural components: (a) shear wall elevation view; (b) shear wall fuse zoom-in side view; (c) column elevation view (dimensions in model scale, mm)

Table 5.1 summarizes the achieved properties for the as-built symmetric models. Note that the flexible-base first natural period (T_1) was a target value in the design of these models. Review of typical low-rise buildings indicates that a value of 0.2-0.4

second is anticipated. The value of T_1 was determined by examining the roof acceleration response in the frequency and time domain of the model specimens, when placed in the centrifuge and subjected to a small amplitude motion excitation (step wave motion). Inspection of the controlling parameters C_y and C_r summarized in Table 5.1 indicates that for the structural hinging model (sSHD), C_r is about 7.5 times C_y, assuring the yielding of the SW structural fuse without foundation rocking. Likewise, the foundation rocking model (sFRD) has a large C_y, around 5.6 times of the C_r, assuring mobilization of the rocking foundation without yielding of the SW. The balanced design model (sBD) adopts the same SW structural fuse from the sSHD model, yet a relatively larger SW footing size compared with that of the sFRD model to ensure an approximately equal value between C_y and C_r.

Table 5.1 Summary of symmetric frame-wall-foundation models as-built values

Parameter	Description	sSHD	sFRD	sBD
T_1	Flexible-base first natural period (sec)	0.37	0.36	0.38
C_y	SW structural fuse yield coefficient	0.29	1.29	0.29
C_r	SW rocking footing yield coefficient	2.17	0.23	0.29
FS_v	SW footing static vertical factor of safety	27	10	16
$M_1=M_2$	Floor mass at each level (kg)	110,970		
$H_1=H_2$	Story height at each level (m)	4.50		
L_{cc}	Center-to-center spacing (m)	9.10		
H_{SW}/W_{SW}	SW aspect ratio (height/width)	3.33		
L_{SWftg}	SW footing length (m)	21.34	5.33	6.86
$M/(V\times L_{SWftg})$	SW footing moment-to-shear ratio	0.35	1.41	1.09
L_{CLftg}	Column footing length (m)	n/a	2.29	
B_{ftg}	All footings' width (m)	3.05		
t_{ftg}	All footings' thickness (m)	0.76		
D_{ftg}	All footings' depth of embedment (m)	0		

In the meantime, Table 5.1 provides the static vertical factor of safety (FS_v) for each SW footing, which is defined as the ratio between the ultimate vertical load against bearing failure the footing can support and the initial static vertical load. In addition, the moment-to-shear ratio for each SW footing is also presented. It is determined by the rocking footing yield moment divided by the resultant lateral load to mobilize the capacity and its lever arm to the bottom of the footing.

Table 5.2 summarizes the theoretical yield moment of each inelastic fuse element. The flexural capacities of the column and SW fuses were determined assuming elastic-perfectly-plastic behavior at each fiber; namely, for a rectangular cross section, the section's yield moment can be computed as:

$$M_{y\_fuse} = \frac{1}{4} \times f_y \times L_{fuse}^2 \times t_{fuse} \tag{5.1}$$

where f_y is the yield strength of the material, L_{fuse} is the length of the fuse about the bending axis (Figure 5.3), and t_{fuse} is the fuse thickness. Again, as mentioned in Section 4.2.1, by using the terminology of "yield moment" to define the capacity of the structural fuse in this chapter and the thesis does not imply that only the extreme fiber section of the structural fuse attains the incipient yielding. Instead, it indicates that the entire cross section reaches the yield stress.

The rocking footing yield moment is dependent on the total axial load acting on the footing-soil interface as well as its geometry:

$$M_{y\_footing} = \frac{P \times L_{ftg}}{2} \times \left(1 - \frac{A_c}{A_{ftg}}\right) \tag{5.2}$$

where P is the total downward force acting on the footing-soil interface under gravity load, including the footing weight, L_{ftg} is the length of footing perpendicular to the

rocking axis, A_{ftg} is the footing's area of contact with the soil when rotation is zero, and A_c is the minimum contact area required for the footing to support the total axial load when the soil's bearing capacity is fully mobilized (Gajan and Kutter 2008). Data in Table 5.2 supports the intent that the SW will be the dominant lateral load carrying component in the models, with its yield moment consistently approximately ten times that of the column fuses.

Table 5.2 Theoretical yield moment of each inelastic fuse component

Fuse short name	Location	Yield Moment M_y (kN-m)		
		sSHD	sFRD	sBD
CL_fuse1	Column fuse at lower level	404	n/a	404
CL_fuse2	Column fuse at upper level	404	404	404
SW_fuse	Shear wall structural fuse at bottom of wall	4,220	18,900	4,220
CL_ftg	Column rocking footing	n/a	794	745
SW_ftg	Shear wall rocking footing	41,500	4,790	5,780

5.3 Experimental Program

5.3.1 Attributes of Centrifuge Modeling

The experimental program was conducted at the Network for Earthquake Engineering Simulation (NEES) 9-meter-radius centrifuge facility at the University of California, Davis (UCD). Centrifuge modeling has been consistently acknowledged as an effective experimental tool to study geotechnical problems, particularly considering its capability to simulate large-scale field response. For geotechnical materials whose mechanical characteristics are greatly influenced by confining stress, imposition of an amplified gravitational field results in a replication of prototype stress within the model

specimen. Centrifuge scaling laws equally apply to other materials as well. For example, reduced-scale metal structural models have been incorporated into centrifuge specimens, with detailing targeted towards achieving inelastic structural member behavior (e.g., Chang et al. 2007; Deng et al. 2012; Liu et al. 2013; Trombetta et al. 2013).

5.3.2 Model Soil

In these tests, the underlying geologic environment was constructed by air pluviating a uniform layer of dense dry Nevada sand in a rigid wall container (1693mm×904mm in model scale). The Nevada sand is poorly-graded, with a mean grain diameter ranging between 0.14mm to 0.17mm. Additional properties of Nevada sand batch, which were determined by Cooper Testing Labs in January of 2008, are provided in Table 5.3. To attain a well-defined hysteretic response for rocking footings and minimize the potential for excessive settlement, the relative density (D_r) was targeted to at least 80%. The achieved D_r was observed to be relatively uniform within the soil container with a value of 90%. Figure 5.4 shows a plan and elevation view of the soil profile combined with two of the instrumented models.

Table 5.3 Properties of Nevada sand batch used in these tests

Parameter	Description	Value
C_c	Coefficient of curvature	0.87
C_u	Coefficient of uniformity	2.07
G_s	Specific gravity	2.66
D_r	Relative density (%)	90
ρ_d	Mass dry density (kg/m^3)	1760
ϕ	Friction angle (deg.)	39
G_{max}	Maximum shear modulus (MPa)	27.23

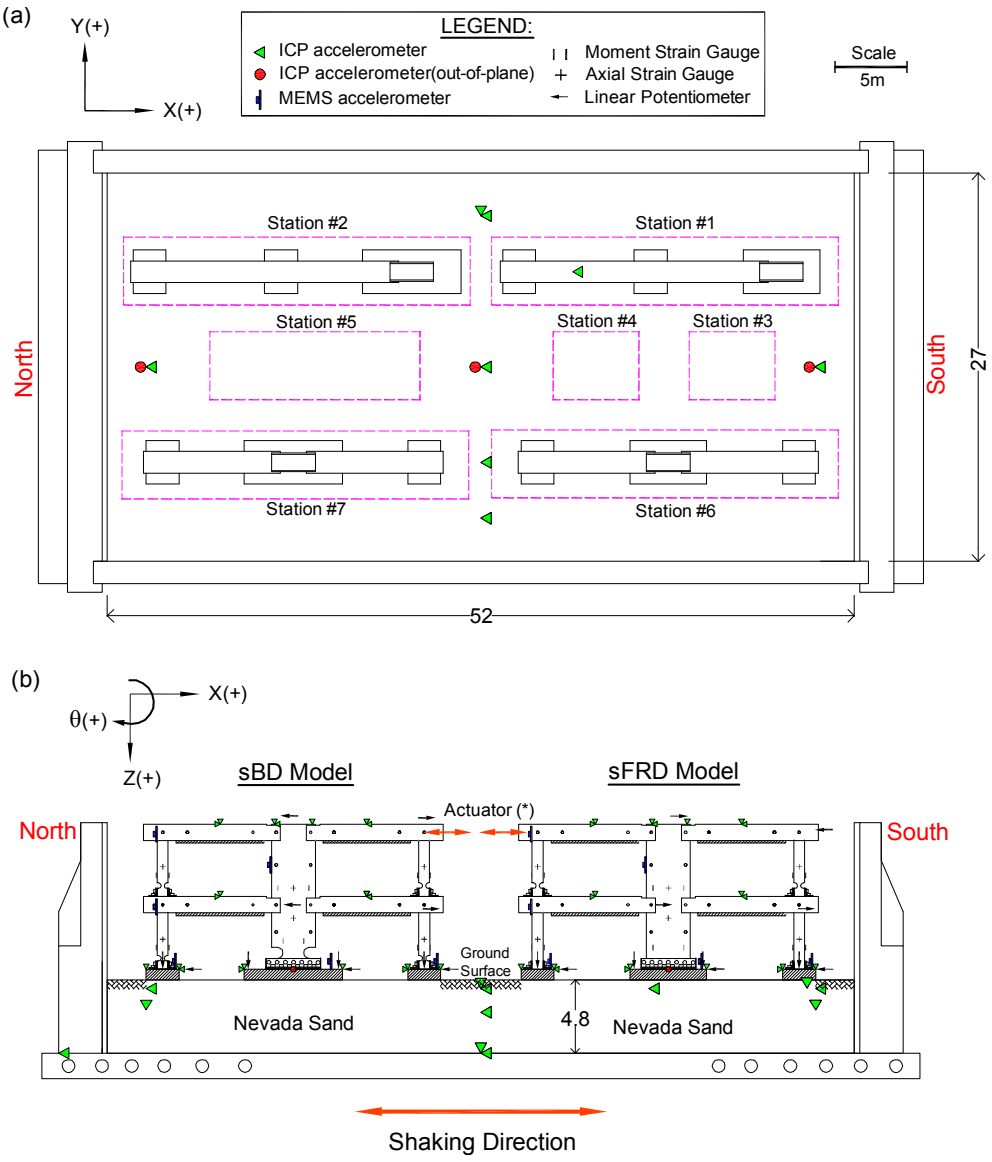

Figure 5.4 Schematics of model placement and instrumentation: (a) plan view; (b) elevation view. (*) Note: single actuator was used only during slow cyclic testing. (All dimensions are in prototype scale, m)

5.3.3 Instrumentation

The building models and soil were heavily instrumented with four types of sensors, namely integrated circuit piezoelectric (ICP) accelerometers, micro-electro-mechanical system (MEMS) accelerometers, linear potentiometers (LPs), and strain gauges (SGs) (Figure 5.4). Embedded in the sand, several arrays of ICP accelerometers were distributed at various depths to capture the free field acceleration response. The superstructure was heavily instrumented with accelerometers to obtain horizontal accelerations at each floor level and rocking at the footings. A number of LPs were connected horizontally and vertically to the frame-wall-foundation models and anchored to a stiff reference rack. During data processing, acceleration measurements were integrated to determine the transient displacement responses. Recordings from LP measurements, on the other hand, were used to provide the residual displacement response. Thirty pairs of strain gauges were installed to the surface of the columns and the SW plates at each floor level for each model. To minimize temperature-induced drifts, half- and full-bridges were utilized to capture bending moments and axial loads. In total, about one hundred concurrent instruments were recording during testing. In addition, eight analog and two high-speed digital cameras were distributed inside of the container to monitor the specimens' in-flight response. Additional details regarding the instrumentation plan may be found in the centrifuge test report (Liu et al. 2013c).

5.3.4 Experimental Sequence

Table 5.4 shows the experimental test sequence in chronological order. The experimental program primarily consisted of two types of tests: dynamic base shake table test and quasi-static slow cyclic tests. In total, ten spin up-spin down cycles were performed in which eleven tests were conducted. As indicated in Figure 5.4a, stations with larger plan areas (i.e., #1-2 and #6-7) were allocated for testing (dynamic and cyclic) of the frame-wall-foundation models, whereas the smaller stations (i.e., #3-5) were used for slow cyclic testing of the isolated shear wall and footing component. Quasi-static slow cyclic tests were conducted on the inelastic components and on three of the six systems, namely the sFRD, sBD, and aFRD model, and each of these were performed after the completion of a series of earthquake tests. Physical observations after the sequential earthquake shaking tests indicate that structural components and the surrounding soil were not significantly damaged or deformed (Section 5.5). As a result, the present quasi-static slow cyclic evaluation is considered a reasonable means to characterize the models' seismic behavior. It is also noted in this table that only a pair of models were placed in the container during each spin of shaking.

Table 5.4 Experimental Series

Test ID	Objective	Station	G-level
1	Cyclic test of SW fuse component	n/a	1g
2	Cyclic test of SW footing component	#3	30g
3	Dynamic shake table test of aFRD and aBD models	#1 and #2	30g
4	Cyclic test of aFRD model	#1	30g
5	Cyclic test of SW fuse component – second trial	#5	30g
6	Dynamic shake table test of aSHD and sSHD models	#1 and #2	30g
7	Cyclic test of SW fuse component – third trial	#5	30g
8	Cyclic test of SW footing component – second trial	#4	30g
9	Dynamic shake table test of sFRD and sBD models	#6 and #7	30g
10	Cyclic test of sFRD model	#6	30g
11	Cyclic test of sBD model	#7	30g

5.3.5 Quasi-Static Cyclic Test Protocol

A displacement-controlled hydraulic actuator was connected to the top of the building model prior to the spin. The load transfer between the model and actuator was facilitated via a pin-connection to the model on one side while a vertical roller-type connection was applied on the other side to connect the actuator. This connection mechanism was intended to ensure unidirectional horizontal loading while minimizing the development of additional axial or moment loading to the building model. The target roof drift ratio (DR) imposed on each model is shown in Figure 5.5. In general, the building models were subjected to seven different packets of cyclic loading, with each packet containing three cycles of a sinusoidal displacement history of constant amplitude. The DR amplitude was initially small (0.1%), and then gradually doubled (0.25%, 0.5%, 1.0%, 2.0%, 4.0%, and 4.5%). Following the final cycle to DR = 4.5%, a monotonic push was imposed. Note that due to the flexibility of the loading mechanism, the achieved DR was typically less than the target value.

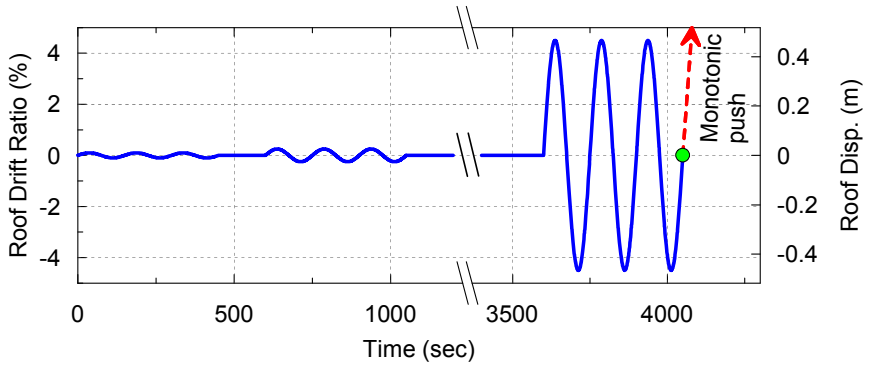

Figure 5.5 Target roof drift ratio history

5.4 Characterization of the Inelastic Fuses

5.4.1 Shear Wall Structural Fuse at 1-g

Figure 5.6 describes the SW fuse component test setup conducted at 1-g level (part a) and its moment-rotation response (part b). Note that the moment demand on the y-axis is normalized by the theoretical yield moment (Table 5.2). The hysteretic curve shows that the yield moment of the SW fuse reaches at a rotation of around 0.005 rad. Upon continued loading, isotropic hardening is observed. At conclusion of the test, at a rotation of 0.03 rad., its strength is observed to amplify by 67% compared with the theoretical value. However, the rotational stiffness of the fuse does not degrade. In general, the load-deformation curve for this constructed shear wall is favorable, with a broad hysteresis absent pinching and demonstrating substantial ductility.

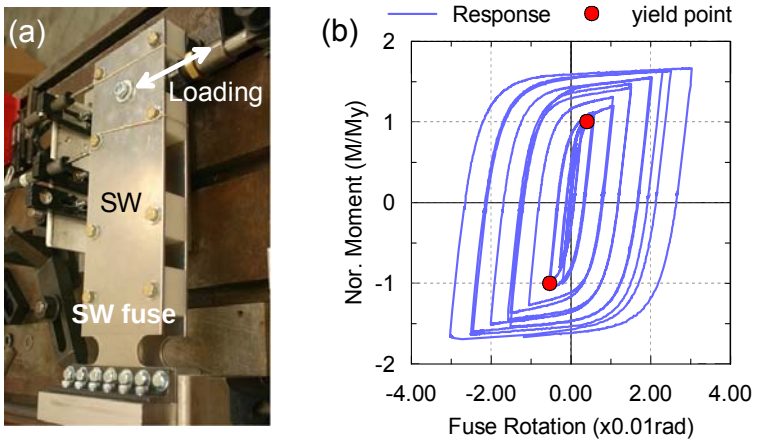

Figure 5.6 Characterization of the shear wall fuse at 1-g: (a) test setup; (b) test result

5.4.2 Shear Wall Structural Fuse at 30-g

Within a 30-g centrifuge environment, the SW component must support a significant portion of the building weight, and it could affect the hysteretic behavior of the SW structural fuse. To this end, a similar slow cyclic component test was performed in the 30-g centrifuge environment. In this case, mass blocks were attached between the SW plates in this case to mimic the expected axial load.

Figure 5.7a-b shows the setup and the response results. The moment was calculated by multiplying the load cell measurement by the lever arm plus the P-Δ induced moments, and the rotation was determined directly from LP measurement. The result shows that the SW fuse still exhibits a hardening behavior; however, the strength is increased by 51% at a rotation of 0.021 rad. in this case. When loading continues to large rotation excursions (i.e., 2.5% or above), the fuse capacity and the rotational stiffness gradually and significantly degrade due to an added out-of-plane P-Δ effect. The moment strength degrades to approximately 50% at a rotation of 0.38 rad. Moreover, the strength loss is slightly asymmetric. This may be partially due to the asymmetric performance of the loading mechanism during pulling and pushing. Part c and d provides photographs of the deformed specimen, clearly showing a permanent offset of the SW in the out-of-plane direction. The primary elastic part of SW completely settles down and touches the base. This is an undesirable mechanism from a system kinematics standpoint; therefore, a designed Aluminum block was placed inside of the SW fuse section to minimize the potential for this to occur in system-level dynamic tests, as indicated in Figure 5.3b.

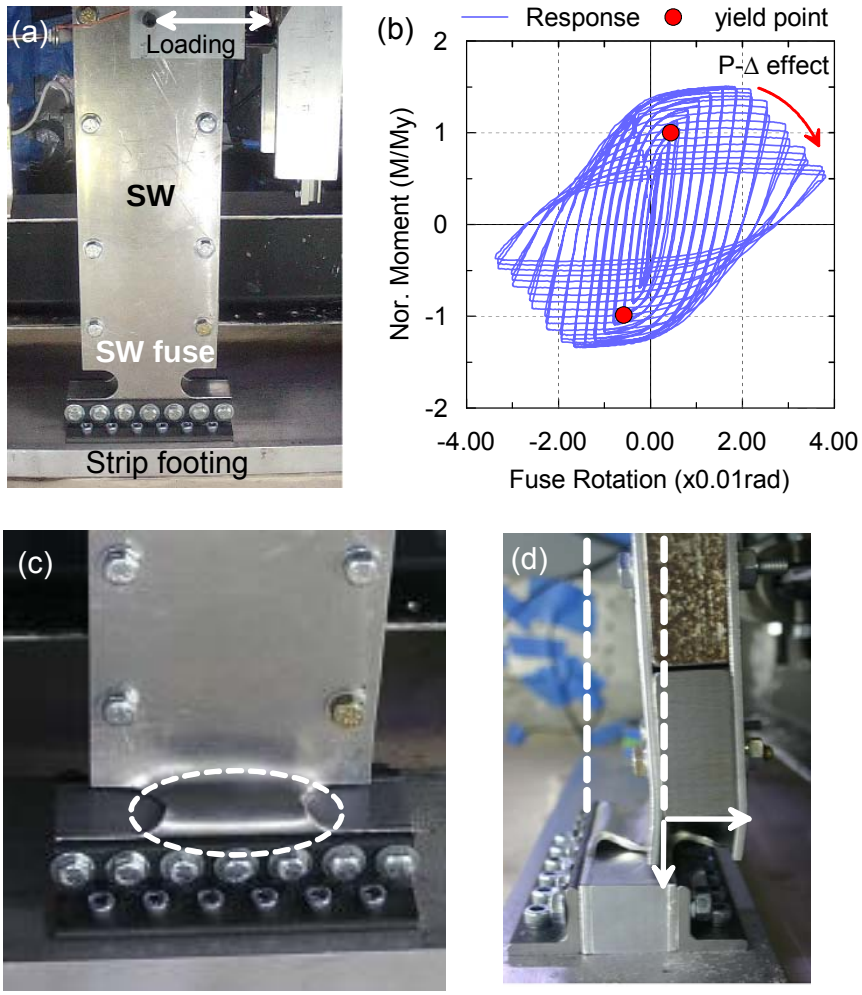

Figure 5.7 Characterization of the shear wall fuse at 30-g: (a) test setup; (b) test result; (c) photograph at failure (elevation view); (d) photograph at failure (side view)

5.4.3 Rocking Footing

A rocking footing component test was carried out while in a 30-g centrifuge environment as well to characterize the footing fuse inelastic behavior. The wall-footing assembly utilized the SW footing of the sFRD model and an equivalent mass. Figure 5.8 presents the test setup (part a) and hysteretic responses (part b).

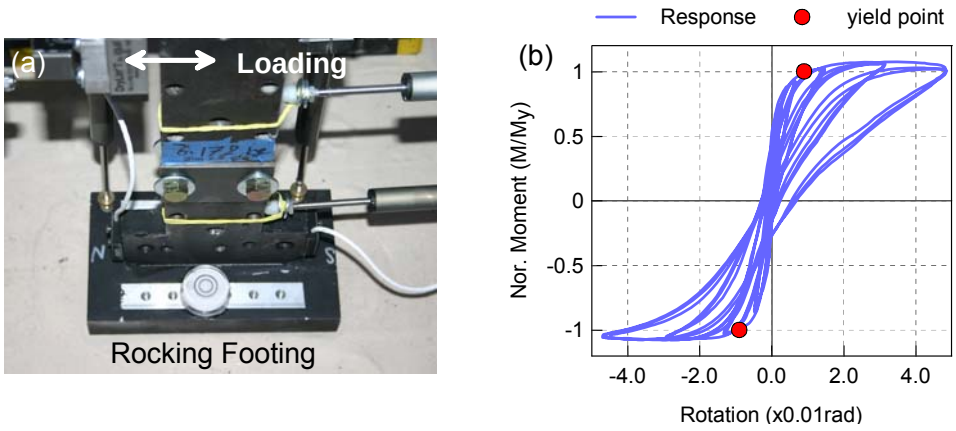

Figure 5.8 Characterization of the rocking footing at 30-g: (a) test setup; (b) test result

The experimental results indicate that the rocking footing presents a robust hysteresis with similar characteristic features observed in rocking footing tests of similar FS_v (e.g., Gajan and Kutter 2008; Deng and Kutter 2012; and Hakhamaneshi et al. 2012). Namely, the footing strength does not degrade after its capacity is mobilized (around 0.009 rad), and importantly, very little residual rotation cumulates despite the large imposed rotations. The unloading rotational stiffness, on the other hand, does tend to gradually deteriorate at larger rotations. These characteristics are inherently related to the self-centering tendency of the foundation rocking mechanism, where dead load from the

superstructure assists the foundation to return and close the gap between the footing and soil during unloading.

5.5 Slow Cyclic Response of the sFRD and sBD Models

Within this section, the behaviors of the sFRD and sBD models under quasi-static reversed cyclic loading are thoroughly presented and compared. As mentioned previously, the slow cyclic testing was performed after a series of dynamic shaking for both models. Figure 5.9 schematically shows the residual states of rocking footings in the sFRD model after the completion of shaking table test. It clearly shows that the permanent deformations (settlement and sliding) of each footing are negligibly small. The sBD model, however, was removed out of the container after shaking, and the ground surface was manually and carefully compacted and leveled prior to placing the model back.

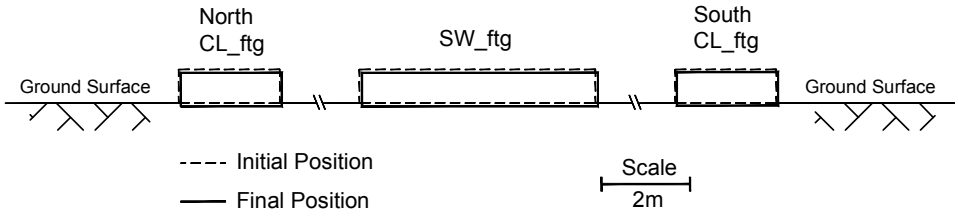

Figure 5.9 Schematic of the residual state of the sFRD's footings

5.5.1 Symmetric Foundation Rocking Dominated (sFRD) Model

Figure 5.10 shows a photograph of the symmetric foundation rocking dominated model (sFRD) subjected to a final monotonic push after the cyclic program. In this model, three types of plastic hinges are anticipated to develop, namely; rocking of the shear wall footing (SW_ftg), rocking of the column footing (CL_ftg), and column fuse hinging at the second level (CL_fuse2). The remainder of the structural components is intended to remain elastic during cyclic loading.

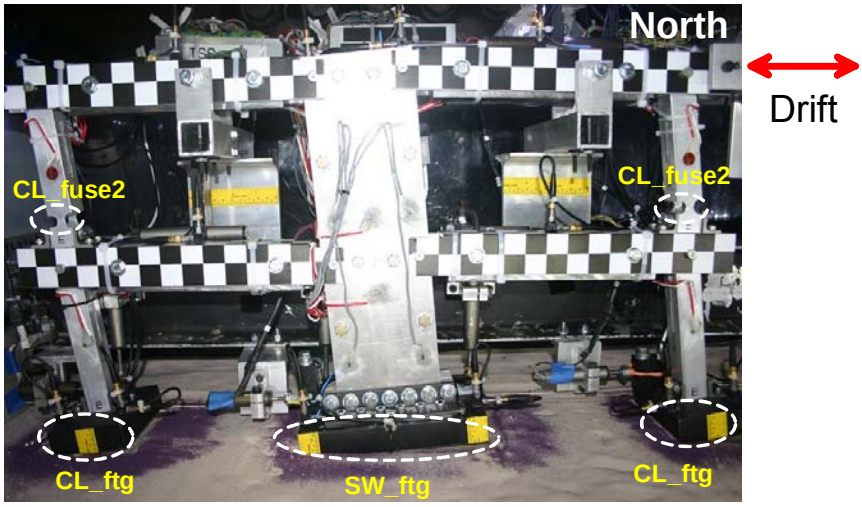

Figure 5.10 The sFRD model in the container at completion of slow cyclic testing

Figure 5.11 shows hysteretic responses of each inelastic element under three different achieved DRs, namely 0.24%, 1.4%, and 3.6%. In these plots, the y-axis represents the moment demand, which is measured from the SGs and normalized by its respective yield moment (Table 5.2). The x-axis is the rotation of each component

determined from LP measurements. Part (a) shows the moment-rotation response of the column fuse at the upper level (CL_fuse2). Note that the actual rotation of the CL_fuse2 is typically larger than the DR because the fuse section was constructed 25mm (model scale) above the beam-column joint. It is evident that the column fuse exhibits many of the same characteristics as the SW fuse, namely, development of isotropic hardening and no strength nor stiffness degradation. As a result, its hysteresis is broad and sustains high levels of rotation. The hysteretic responses of the SW_ftg continue to display self-centering, some energy dissipation, and no strength degradation. The north column rocking footing (CL_ftg; Figure 5.11c) produces similar hysteretic characteristics as the SW_ftg; however, it has a relatively wider hysteresis since its vertical factor of safety (FS_v=7.3) is lower than that of the SW_ftg (FS_v=10.1). It is also noted that its theoretical yield moment is not obtained in the positive direction. This is maybe due to frame action of the frame bay columns, which imposes additional axial load on the column footings and in turn increase the footings' capacities.

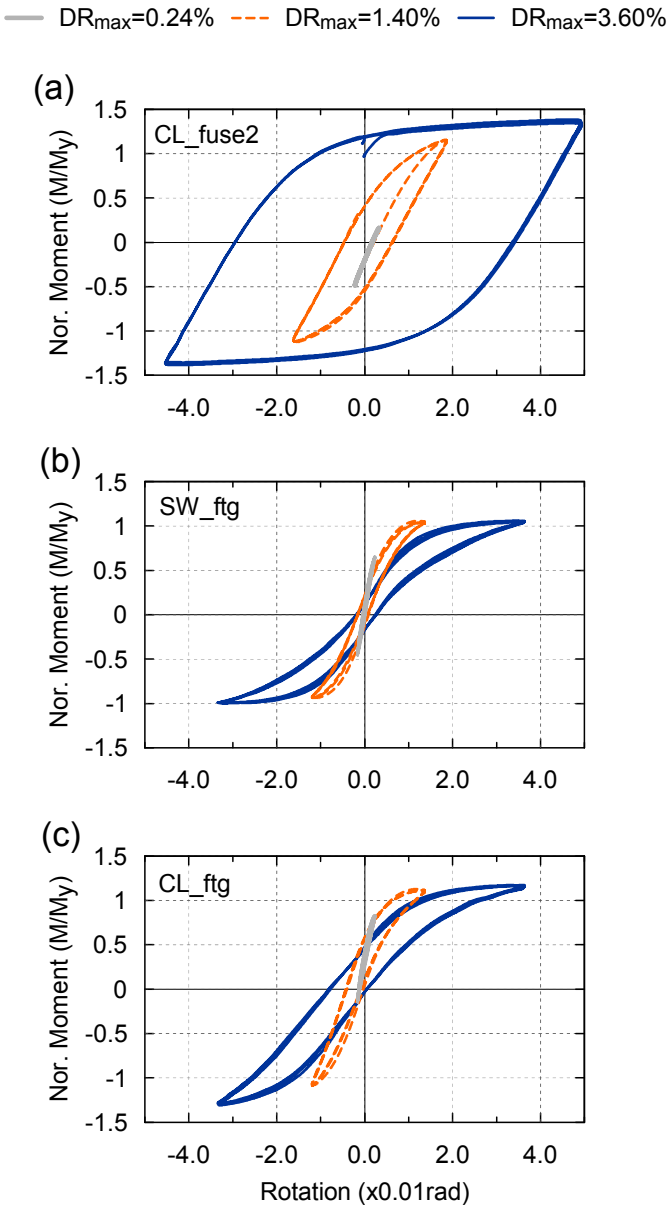

Figure 5.11 Hysteretic responses of the inelastic elements in the sFRD model: (a) column fuse at upper level (CL_fuse2); (b) shear wall rocking footing (SW_ftg); (c) column rocking footing (CL_ftg)

Figure 5.12a shows the resultant system-level force-displacement curves from the test. The horizontal axis is the achieved DR, which is obtained from the measurement of the LP mounted at the roof level divided by the model elevation from ground surface. The y-axis represents total base shear normalized by the dead weight of the superstructure. The system-level hysteresis generally indicates a fairly ductile and stable global behavior of the sFRD system. There is no significant loss of system capacity even when the system is pushed to a DR of 3.6% in the final cycle. Moreover, very little residual is observed during unloading, i.e., the hysteresis curve has little drift when the base shear passes through zero. These beneficial characteristics are largely attributed to the foundation rocking, which has the largest capacity and therefore dominates among other inelastic components within the system.

Figure 5.12b shows an average of the system capacity curves for both directions extracted as the envelope of the cyclic results, overlaid with all identified yielding mechanisms. The plot shows that the sFRD system commences with mobilization of the CL_ftg at DR of 0.39%, and subsequently the SW_ftg yields (DR=0.49%). This sequencing may be explained by the fact that a rocking footing with lower FS_v is prone to yield at a lower rotation amplitude. Upon continued loading, the inelastic behavior of the upper column fuses gradually develops (DR>0.87%). After all inelastic components yield, the system's capacity continues to gradually ascend and reaches its climax at DR=2.61%. The ultimate lateral-load-carrying capacity is around 29% of the superstructure weight. Continued deformation of the system results in a subtle descending behavior, which may be attributed to P-Δ effects. As the rocking footings attain large rotations, axial load acting at the displacement induced by this rotation will contribute a significant moment to

the soil-foundation interface, which in turn reduces the lateral capacity accordingly at the global level.

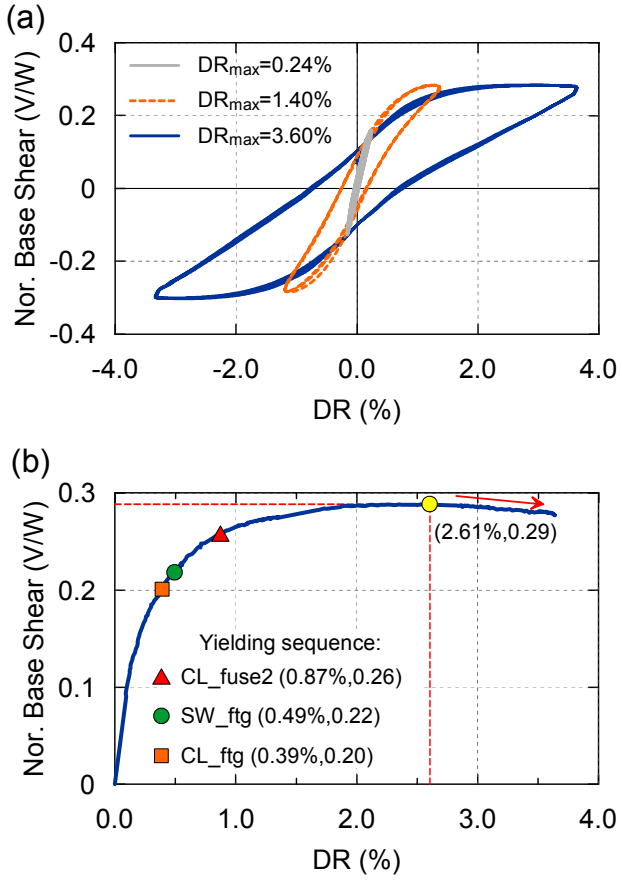

Figure 5.12 Global response of the sFRD model: (a) cyclic force-displacement response; (b) envelope of the cyclic force-displacement response

Figure 5.13a compares the energy dissipation contribution amongst the three yielding mechanisms as a function of the maximum achieved DR during each event. The energy dissipation is computed by integrating the area of the moment-rotation hysteresis for each inelastic component. The relative dissipated energy is then determined by normalizing each by the summation. A dash line is added in this figure to delineate the structural and footing contributions. Prior to yielding of the CL_fuse2 (i.e., DR<0.87%),

the rocking footings consistently dissipate more than 95% of the total energy. However, under a large amplitude roof drift excursion, column fuses dominate the relative energy dissipated due to their broad hysteresis (Figure 5.11a). During the last two cyclic DR amplitudes (DR=3.2% and 3.6%), for example, the column fuses steadily diffuse 53% of the total energy of each amplitude while the SW_ftg and the CL_ftgs contribute 32% and 15% respectively.

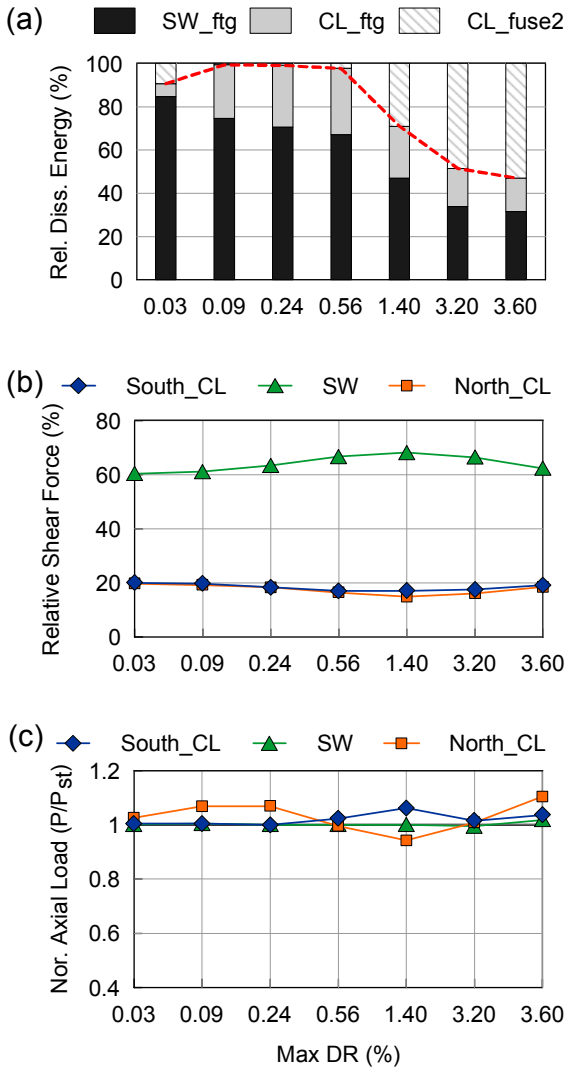

Figure 5.13 Response of the sFRD model: (a) relative energy dissipation; (b) relative shear force; (c) normalized axial load

Figure 5.13b presents the shear force distribution amongst the three supporting components, namely the north and south column (CL) and the SW. This scatter plot shows that the SW component consistently carries 60-70% of the total base shear. After all footings attain their incipient yielding, the SW gradually attracts more relative lateral load as the drift increases because the CL_ftg experiences significant rotational stiffness degradation. Towards the largest drift amplitude, the SW_ftg suffers a significant stiffness loss as well that decreases its lateral load contribution to 60% of the total. It is also noted that the load sharing between the north and south columns is highly balanced due to the symmetry of the structural layout. Figure 5.13c examines the uncorrelated maximum axial load variation developed at each supporting component. The y-axis denotes the axial load demand normalized by its static value. This figure shows that the columns are subjected to axial load fluctuation of 10%, which could be induced by the frame action developed in the frame bay. The SW, however, observes nearly no axial load variation.

5.5.2 Symmetric Balanced Design (sBD) Model

In like fashion, the sBD model was subjected to an identical quasi-static cyclic test after the completion of the dynamic shaking. In contrast to the sFRD, two additional inelastic fuse mechanisms were considered in this model, namely the SW structural fuse (SW_fuse) and the column fuses at first level (CL_fuse1), as shown in Figure 5.14.

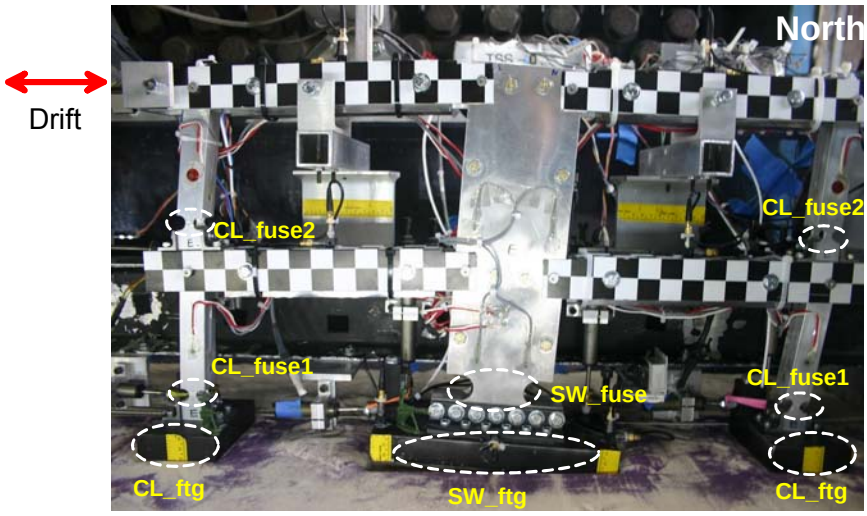

Figure 5.14 The sBD model in the container at completion of slow cyclic testing

Figure 5.15 presents the hysteretic responses of each inelastic element in the sBD model under three different achieved DRs, namely 0.30%, 1.5%, and 3.7%. The CL_fuse2 response is nearly identical to the CL_fuse2 in the sFRD model when under a same rotation amplitude since they share the same size of the fuse. The CL_fuse1, on the other hand, observes a relatively smaller rotation demand. This is because the system displacement demand at upper level in frame bay portion is only attributed to the CL_fuse2's rotation. At bottom level, however, it is attributed to rocking of the CL_ftg and rotation of the CL_fuse1 as they are placed in series. The CL_ftg behaves almost linear-elastically under low DR amplitudes, and it ultimately yields during the final excursion. Comparison between the yield moment of the CL_fuse1 and CL_ftg (Table 5.2) indicates the CL_fuse1 would yield first, serving as a weak link compared with the CL_ftg in frame bay. As a result, the rocking of the CL_ftg is greatly limited by the inelastic behavior of the CL_fuse1.

Inspection of the SW_fuse behavior indicates that, under a 1.5% DR, its flexural capacity is fully mobilized. However, upon continued loading, its hysteretic shape remains nearly unchanged even when the DR attains 3.7%. This could be understood by the two facts: (1) the SW_fuse and SW_ftg are connected in a series fashion; (2) the SW-fuse develops significant hardening at large rotations. After each of two elements attain the respective incipient yielding, any imposed additional displacement demand in wall-footing assembly will be largely attributed to the SW_ftg rocking since its yield moment limits the hardening development of the SW_fuse, despite the fact that they are designed to yield at same base shear level. The hysteretic response of the SW_ftg, on the other hand, exhibits a similar characteristic compared with that in the sFRD model. However, its shape is relatively thinner since its FS_v is 60% larger than the SW_ftg in the sFRD model (Table 5.1).

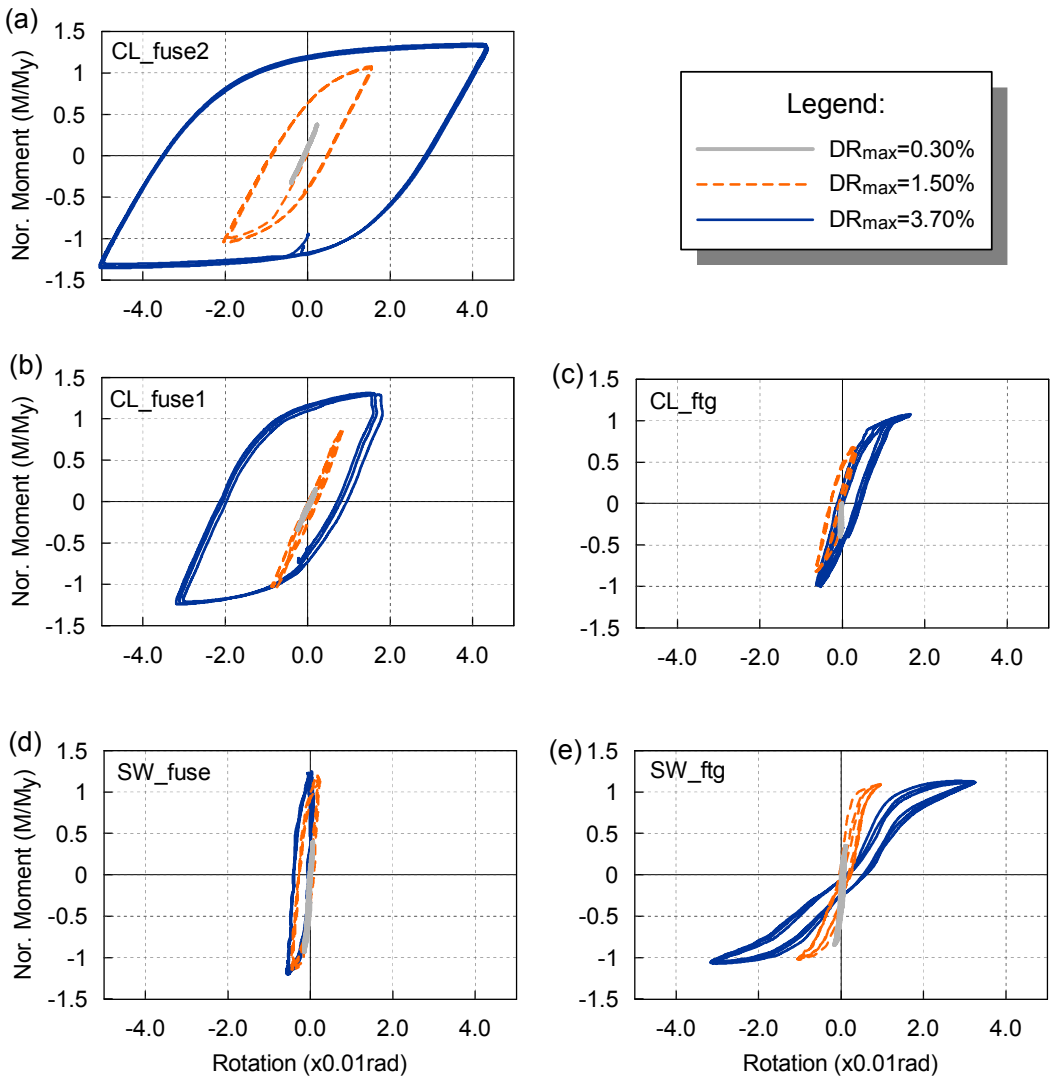

Figure 5.15 Hysteretic responses of the inelastic elements in the sBD model: (a) column fuse at upper level (CL_fuse2); (b) column fuse at lower level (CL_fuse1); (c) column rocking footing (CL_ftg); (d) shear wall fuse (SW_fuse); (e) shear wall rocking footing (SW_ftg)

Figure 5.16a shows the system-level force-displacement curves of the sBD model. The system strength does not degrade with increasing roof drift, despite the inelastic structural fuse mechanisms at the bottom level (i.e. CL_fuse1 and SW_fuse). In addition, the stiffness does not significantly degrade, leading to a relatively broad hysteresis. However, the DR at zero base shear indicates that the sBD's system self-centering tendency is reduced compared with the sFRD model. In part b, an averaged response envelop is provided by adopting a similar approach in the sFRD model. In this system, the capacity of the SW_fuse is firstly mobilized amongst all inelastic components at DR=0.65%. As the DR increases to 0.86%, the ensuing plastic hinge is formulated at the CL_fuse2. Upon continued loading, the SW_ftg, the CL_fuse1, and the CL_ftg successively attains its yield moment within a small range of DR from 1.1 to 1.4 %. This sequence is well understood by examining the difference in yield moment of each inelastic component. When the sBD model is subjected to a DR of 3.11%, the global strength gradually reaches its ultimate capacity at 35% of the superstructure weight. Subsequently, the system experiences a P-Δ induced load-carrying capacity reduction, but in an extremely subtle and negligible manner.

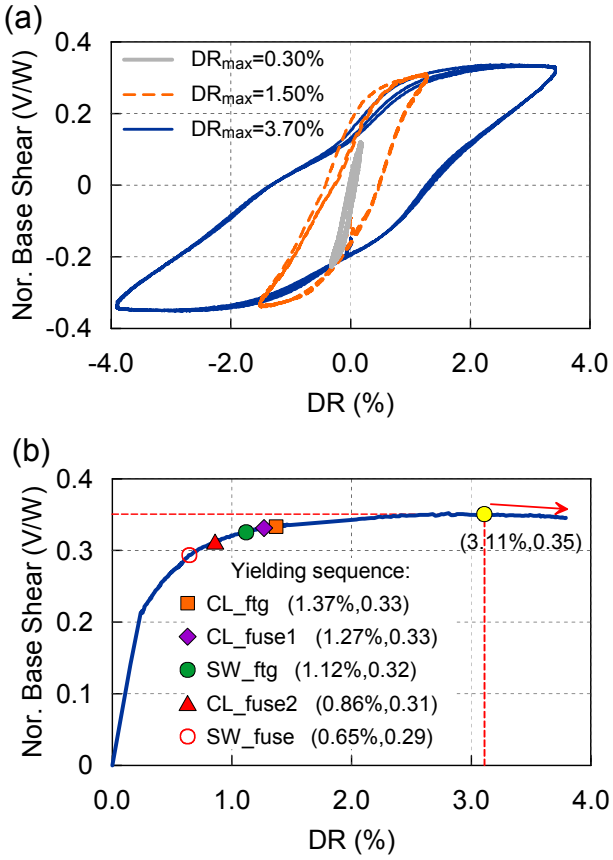

Figure 5.16 Global response of the sBD model: (a) cyclic force-displacement response; (b) envelope of the cyclic force-displacement response

Four plots in Figure 5.17 scrutinize the sharing of displacement demand, hysteretic energy distribution, the sharing of lateral force amongst the inelastic components, and maximum axial load variation respectively. Part a compares the rotation contribution between the SW_fuse and the SW_ftg as a function of the achieved maximum DR. At elastic stage (DR<0.30%), the SW_ftg rotation generally contributes around 30% and the SW_fuse rotation contributed about 70% of the total rotation of SW. However, rotation demand shifts to the footing as the model is loaded to larger DRs. For example, the SW_fuse rotation only provides 30% of the total rotation when the DR

approaches 0.62%, and it gradually drops to 18% for the largest DR. This trend is explained by the strain hardening behavior of the Aluminum Alloy SW_fuse.

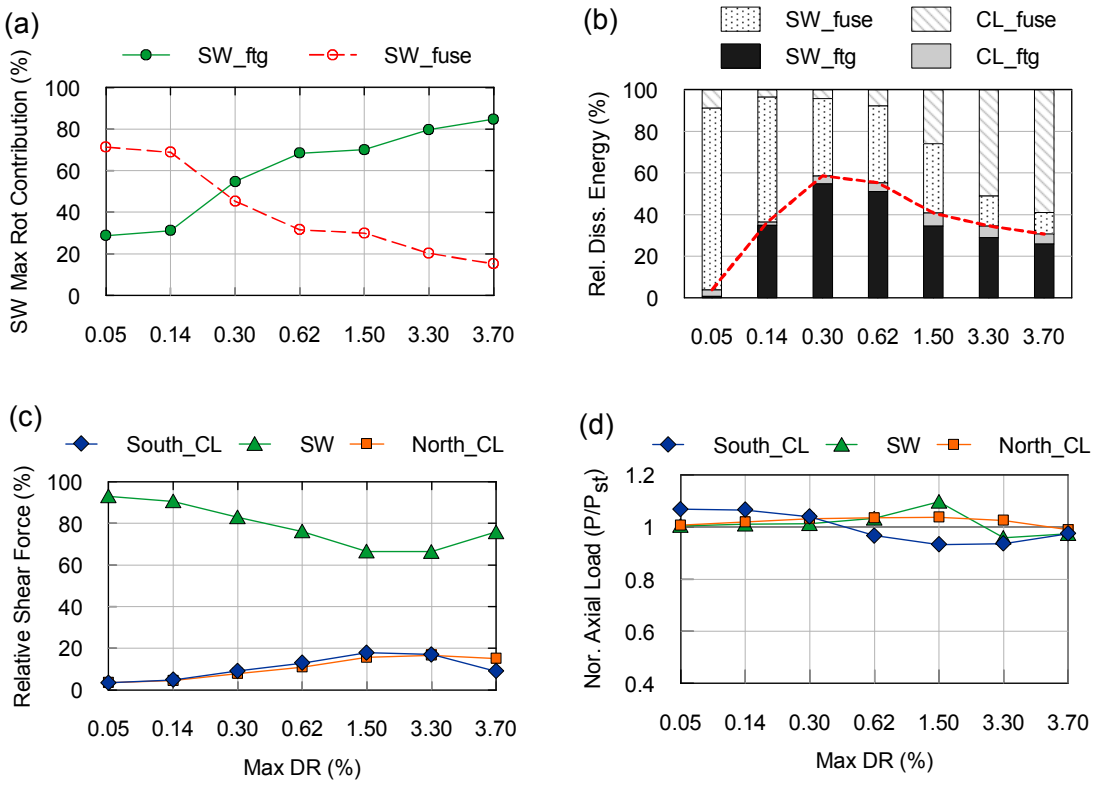

Figure 5.17 Response of the sBD model: (a) SW maximum rotation contribution; (b) relative energy dissipation; (c) relative shear force; (d) normalized axial load variation

Part (b) shows the energy dissipation distribution amongst each inelastic component. For nearly all DR amplitudes, this plot shows that the inelastic superstructure components absorb the majority of the hysteretic energy. These components are particularly dominating in the first two, low amplitude DRs, contributing 96 and 64% of the total, respectively. As the DR increases, a larger portion of the dissipated energy is associated with the rocking footings. However, for the extremely large DR amplitudes (i.e. 3.3% or 3.7%), the inelastic behaviors of the structural fuses dominate the diffused

energy (>60%) as a result of their broad hysteresis. Note that the contributions from the CL_ftgs are consistently less than 6% since its rocking capacity is larger than the capacity of the CL_fuse1. In general, with the exception of the first, very low amplitude cycle, the dissipated energy is distributed in a balanced fashion between the inelastic superstructure and substructure elements in the sBD model.

The relative shear force demand for each vertical component in the first level is plotted and compared in Figure 5.17c. In contrast to the sFRD, the SW component generally carries a greater portion of the system shear force, ranging from about 65-95% of the total. This may be attributed in part to the larger footing below the SW. At larger DRs, the rotational stiffness deterioration of the SW_ftg decreases the SW's ability to resist additional lateral load and therefore a greater portion of the system shear force demand is transferred to the frame bay columns. Part d examines the uncorrelated maximum axial load variation developed at each supporting component. It shows that each component is subjected to an axial load variation within 10% of its static value for all DR amplitudes.

5.5.3 Performance Comparison

Figure 5.18 compares the system-level hysteretic response of the sFRD and sBD models under three different DR amplitudes. Under an extremely small DR amplitude (part a), both systems have a similar elastic response, namely a similar initial stiffness (K_o). It is estimated of approximately 24 MN/m based on the secant stiffness of the

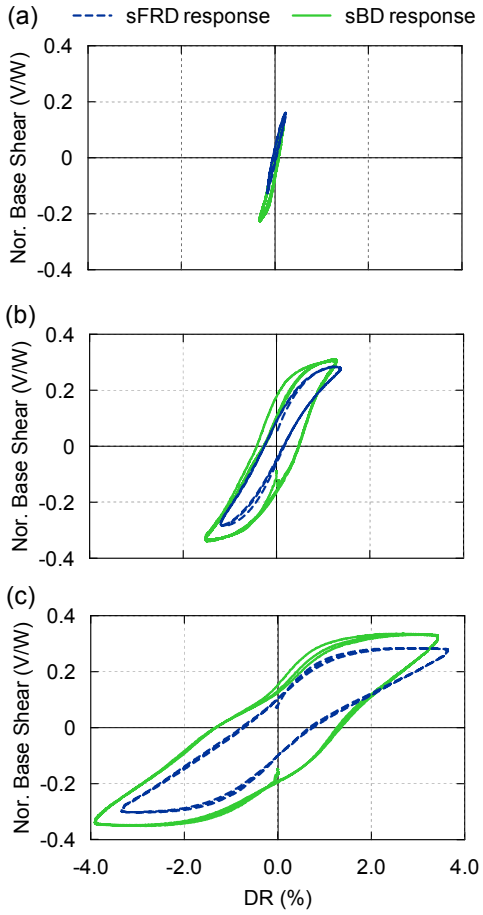

Figure 5.18 Hysteretic response comparison between the sFRD and sBD models under different DR amplitudes: (a) DR_{max}=0.30%; (b) DR_{max}=1.50%;(c) DR_{max}=3.70%

elastic response curve. Upon a large DR amplitude loading (part b and c), the unloading stiffness of the sBD model does not significantly degrade compared with that of the sFRD model, leading to a relatively broad hysteresis. However, the sBD's DR at zero base shear is larger than that of the sFRD, indicating a reduced self-centering tendency. In addition, the sBD model observes a larger lateral load-carrying capacity than the sFRD.

Figure 5.19 compares the response envelop and stiffness degradation of the sFRD and sBD models. Part a continues to show the similar initial stiffness and capacity difference between these two models. Beyond the systems' elastic response, the sFRD

generally articulates a lower base shear capacity, with a maximum difference of 17% at ultimate load. The sequence of yielding of the inelastic components varies as well. In the sFRD model, first yielding occurs in the CL_ftg at 0.39% DR, whereas it is postponed to 0.65% DR and attributed to the SW_fuse in the sBD model. In addition, the collaboration amongst the multiple fuses in the sBD model postpones the P-Δ induced system strength reduction to a large DR. It is also observed that the CL_fuse2 consistently yields at a DR of 0.86% for both models. This can be explained by the fact that its rotation demand is linearly proportional to the system DR as indicated by the structural layout (Figure 5.1).

If compared with a traditionally fixed-base modern lateral load resisting system, both systems generally behave in a very ductile, well-controlled, non-degrading, and robust manner. The system-level load-carrying capacity negligibly deteriorates even at large DR of >3.5%. These characteristics are largely attributed to the addition of the foundation rocking mechanism and strain hardening of the SW_fuse.

Figure 5.19b presents the system-level lateral stiffness degradation. The system stiffness (K) at each roof DR is estimated by analyzing the central linear-wise portion of the hysteretic curve, similar to that presented by Gajan et al. (2005). Subsequently, the K value for each cyclic DR amplitude normalized by the initial stiffness (K_o), and plotted as a function the achieved maximum DR. Based on the scatter data, two trend lines are added assuming second-order polynomial fit to log-linear space. This plot shows that at moderate- and high- DR amplitudes, the lateral stiffness of the sBD model degrades less than that of the sFRD. However, upon a continued loading to the largest drift demand (i.e. DR=3.6%), they converge to a similar reduced stiffness. These observations illustrate that the strategy of considering compatible yielding between the SW structural fuse and the

SW rocking footing helps to postpone the system stiffness reduction during moderate and large DR.

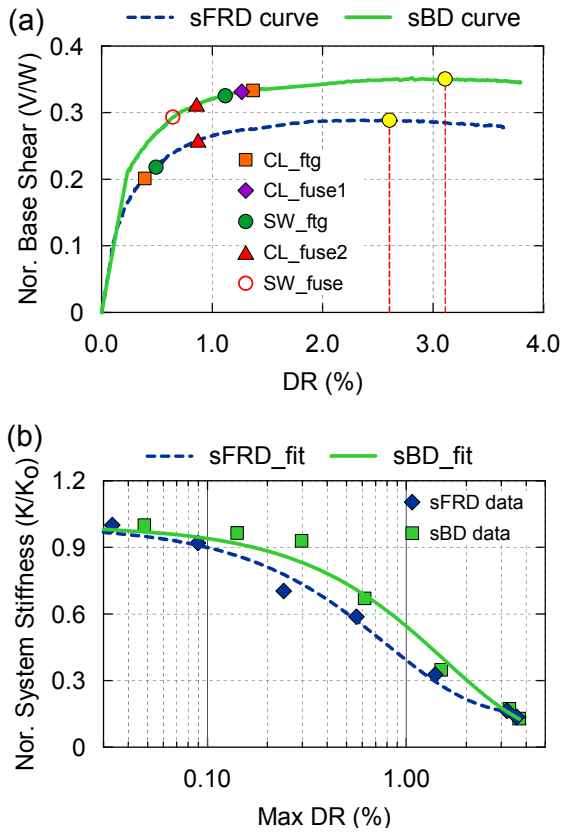

Figure 5.19 Experimental behavior comparison between the sFRD and sBD models: (a) system capacity; (b) system stiffness degradation

5.6 Conclusions

A centrifuge test program was conducted to evaluate the seismic performances of low-rise frame-wall-foundation systems with and without rocking foundations. Considering the strength difference between a shear wall (SW) rocking footing and a SW fuse, as well as SW location variation, six two-story-two-bay small-scale structures were

constructed and tested in a 30-g centrifuge environment. This chapter summarizes the experimental program and results from the quasi-static cyclic tests of two of the models. Key conclusions from this study are as follows:

- The SW fuse in the model test was composed of annealed aluminum and thus it exhibited a fairly broad hysteresis without stiffness and strength degradation. The rocking foundation component had non-degrading capacity too, but it followed a more narrow hysteretic response, consistent with a re-centering mechanism.
- When the rocking foundation is designed to be the predominant hinging mechanism in this system, the system performs in a ductile, robust, and stable manner. The load-carrying capacity does not descend appreciably even at large drift ratio (DR) of 3.5%. Importantly, very little residual DR accumulated throughout the cyclic history, indicating a strong self-centering tendency. Moreover, the rocking footings dissipate more hysteretic energy than the structural fuses at low and moderate amplitudes of DR.
- Models constructed with a larger rocking footing and weaker SW fuse can be designed such that these two components initially yield at approximately the same base shear level. The advantages of the prior foundation rocking dominated model are well maintained in this system. However, its self-centering tendency is reduced normally. In contrast, its lateral load resisting capacity is greater than that of the foundation rocking dominated model, and the system-level lateral stiffness does not

significantly degrade at a large DR. Finally, the absorbed hysteretic energy is well distributed between the superstructure and substructure inelastic elements after the yielding of the SW fuse in this system.

- The experimental raw data of the test program described in this chapter are provided at NEEShub website with a permanently assigned Digital Object Identifier (DOI) of 10.4231/D3NG4GR9C. (http://nees.org/warehouse/experiment/4940/project/732)

5.7 Acknowledgements

This chapter, in part, is currently being prepared for submission to technical journals. The article is tentatively titled "Seismic Behavior of Frame-Wall-Rocking Foundation Systems-Part I: Test Program and Slow Cyclic Test Results" with a preliminary author list of Weian Liu, Tara C. Hutchinson, Andreas G. Gavras, Bruce L. Kutter, and Manouchehr Hakhamaneshi (201X). At completion of this dissertation, its final form was in preparation. However, the dissertation author is the primary investigator and first author of these papers.

Chapter 6

Frame-Wall-Rocking Foundation System Test (Test-2) – Part II: Dynamic Shake Table Test Results

6.1 Benefits and Limitations of Cyclic Test

Quasi-static cyclic testing is recognized as one of the most economical and straightforward experimental techniques to characterize the inelastic behavior of structural components or subassemblies. By using a predefined loading history from a computer, an attached actuator, usually in displacement-control, is commanded to impose this history to a specimen at a slow rate. The consequence of this approach is that the force contribution which would occur due to inertia and damping is excluded from the specimen's restoring force during testing; therefore, the effects of material nonlinearity and inelasticity, which may be seen in the hysteretic load-deformation response, can be

directly captured. Measured data is usually fairly smooth and clean, which enables researchers to correlate the hysteretic characteristics with its physical changes. In addition, by gradually increasing the displacement amplitude for each loading cycle, quasi-static cyclic tests further permit physical observation of inelastic modes and failure mechanisms. Considering those benefits, several cyclic tests were conducted in this test program at component-level (the shear wall structural fuse and rocking footing), as well as system-level (two constructed frame-wall-foundation models), as summarized in Chapter 5.

Despite the above benefits of quasi-static cyclic testing, earthquakes are at dynamic rates and do induce inertial and damping forces in a system. As a result, system-level cyclic testing may be unable to consider realistic load distribution patterns along a structure's height, particularly if higher dynamic modes are expected to contribute to the system's response. The system capacity obtained from cyclic testing, in this regard, may not be strictly accurate. However, the general shape of each system's hysteresis, as well as the yielding sequence should not be significantly affected due to two facts: (1) the inelastic behavior of each inelastic component is controlled by the displacement; and (2) the imposed displacement profile along its elevation is maintained as a triangular distribution even it is loaded only at roof level. In this respect, the results obtained from quasi-static cyclic tests of like specimens are quite reasonable for comparison purposes. At the same time, there is still a necessity, to impose dynamic shaking (earthquake relevant rates and histories) onto test specimens in an effort to capture their more realistic response.

In this chapter, the test program described in Chapter 5 is extended to investigate the dynamic response of three frame-wall-foundation building models subjected to a similar suite of earthquake motions. The three models were designed such that their inelastic mechanisms are (1) dominated by the SW structural fuse (sSHD), (2) dominated by the SW rocking foundation (sFRD), or (3) equally contributed via the SW structural fuse inelastic behavior and the foundation rocking mechanism (sBD).

6.2 Dynamic Testing Protocol

6.2.1 Earthquake Motions

A suite of twelve earthquake-like motions were imposed on each of the centrifuge models generally in order of increasing intensity. Table 6.1 summarizes the source motion details and main characteristics of these motions as achieved in the free field ground surface. Note that the trailing number within the motion short name indicates the amplification factor. The achieved characteristics in Table 6.1 demonstrate the varied predominant frequency content of these motions (T_p ranges from 0.16 to 0.36 sec) as well as the range of increasing peak free field acceleration (PFFA) (0.12-1.19g). These motions are generally of a short duration with t_d less than 11 second with an exception of TCU_0.6 (t_d=25.7 sec). Small amplitude motions were applied to the models initially to produce elastic response, within moderate- and high-intensity motions subsequently imposed to elicit highly inelastic response. In an effort to characterize the period of each system, a very small amplitude artificial motion, composed of two pulses with a PFFA of

Table 6.1 Source motion details and achieved characteristics in the free field ground surface motion

Motion ID	Name	Earthquake Event	M_w	Recording Station	PFFA (g)	$S_a(\overline{T}_1,5\%)$ (g)	T_p (s)	t_d (s)
1	GZ_0.2	Gazli, USSR, 1976	6.8	Karakyr	0.13	0.32	0.17	6.3
2	SF_0.2	San Fernando, USA, 1971	6.6	Pacoima Dam	0.28	0.30	0.16	7.1
3	SF_0.25	San Fernando, USA, 1971	6.6	Pacoima Dam	0.37	0.61	0.32	8.7
4	MG_0.4	Morgan Hill, USA, 1984	6.2	Coyote Lake Dam	0.49	0.64	0.30	4.5
5	KB_3.0	Kobe, Japan, 1995	6.9	Takarazuka	0.42	1.27	0.36	10.1
6	GZ_0.8	Gazli, USSR, 1976	6.8	Karakyr	0.80	2.10	0.18	6.4
7	TCU_0.6	Chi-Chi, Taiwan, 1999	7.6	TCU078	0.61	1.49	0.16	25.7
8	KB_4.0	Kobe, Japan, 1995	6.9	Takarazuka	0.63	1.76	0.36	10.6
9	CMS_1.0	Artificial (Combined Morgan with steps)	n/a	n/a	0.90	1.67	0.21	6.5
10	CMS_ -1.5	Artificial (reverse polarity of #11)	n/a	n/a	1.15	2.49	0.21	7.0
11	CMS_1.5	Artificial (150% of #9)	n/a	n/a	1.14	2.59	0.20	7.4
12	CMS_1.8	Artificial (180% of #9)	n/a	n/a	1.19	3.08	0.21	7.0

Notes: PFFA = peak free field acceleration at ground surface; $\overline{T}_1$= average period of all three models (0.37sec); T_p = predominant period, taken as the period at the peak of the elastic acceleration spectrum; t_d = Strong duration is estimated by computing the time difference between the 5% and 95% Cumulative Arias Intensity.

around 0.02g, was applied prior to the implementation of select earthquake motions (Motion#1, #9, #11, and #12).

Figure 6.1 shows the 5% damped elastic spectral acceleration spectrum of the free field ground surface recording for each earthquake event, normalized by the PFFA and overlaid with each system's first period. This plot shows that two of the source motions, namely GZ and CMS, present with ascending spectral acceleration demands during period elongation of the system, while the other two present with descending demands.

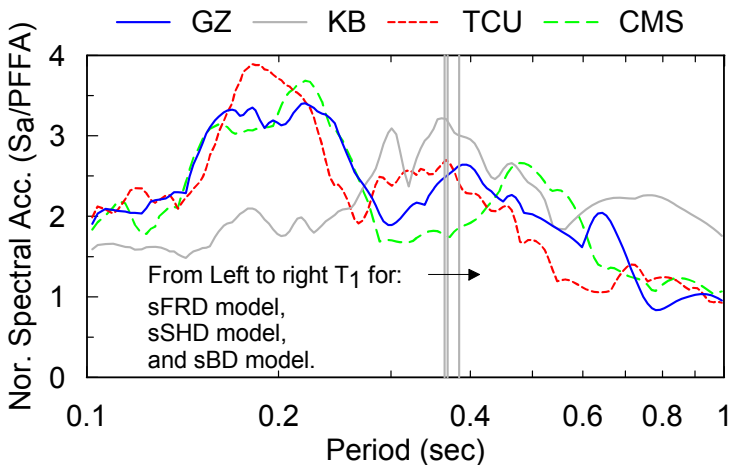

Figure 6.1 Normalized elastic spectral acceleration spectrum of the achieved free field motions with 5% damping

6.2.2 Shaking Consistency

The dynamic shaking of the sFRD and sBD models was performed during the same spin; however, the sSHD model dynamic tests were conducted during different spins (Table 5.4). Although the same displacement history file was commanded to control the movement of the actuation for both spins, it is necessary to evaluate the shaking consistency for the purpose of performance comparison among the three models. Figure

6.2 compares the achieved free field spectral acceleration evaluated at the average fundamental period ($\overline{T}_1$) of the models (0.37 sec) for the two different spins. This plot illustrates that, the shaking at two different spins in general generated similar 5% damped elastic spectral accelerations at 0.37 sec (within 5% difference) for all but one event, which deviates by 10%. Therefore, the shaking of two different spins is considered acceptably consistent.

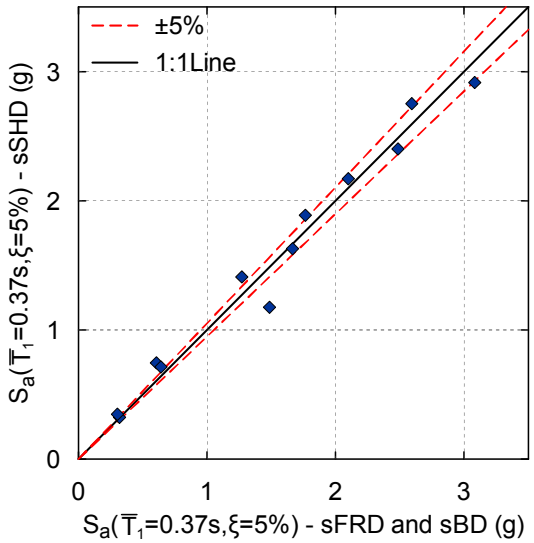

Figure 6.2 Elastic spectral acceleration (at $\overline{T}_1$=0.37 sec and 5% damping) comparison for two different spins

6.3 Foundation versus Free-Field Response

6.3.1 Frequency Domain Response Comparison

The motion of the foundation is generally regarded as the building input motion when assessing the superstructure's seismic performance under a fixed-base condition. However, at the same time, the footing motion usually deviates from the recorded free

field motion due to kinematic- and inertia-induced soil foundation structure interaction (SFSI) (e.g., Stewart et al. 1999). Kinematic interaction, manifested via base slab averaging, usually does not significantly alter the motion characteristic for a surface-type flat foundation, as considered in this test program. On the other hand, large inertia-induced forces acting on the foundation could cause the foundation to displace, i.e. rotating, sliding and settling, resulting in a significant change in motion characteristics. Particularly under this circumstance where significant footing uplifting is allowed, this inertia-driven SFSI effect may be significant.

To evaluate the variation between the foundation level motion and the free-field motion, the power spectral density (PSD) of each is calculated. The PSD is a non-negative frequency-dependent parameter, which serves as an important indicator of the motion characteristics in the frequency domain. The PSD for a given motion x(t), usually denoted as $S_{xx}(f)$, is the Fourier transform of its auto-correlation function $R_{xx}(\tau)$ (e.g, Clough and Penzien 1993), which are determined by the following equations:

$$S_{xx}(f) = \int_{-\infty}^{\infty} R_{xx}(\tau) \cdot e^{-2\pi i f \tau} d\tau \tag{6.1}$$

$$R_{xx}(\tau) = \sum_{t=0}^{N-|\tau|} x(t) \cdot x^{*}(t+\tau) \tag{6.2}$$

where N is the number of data points in the motion x(t) and * denotes the complex conjugation.

Figure 6.3 examines the PSDs of the achieved motion at the shear wall footing level (SW_ftg) and the free field motion for the three systems during the strongest motion (CMS_1.8). For the sSHD model, part (a) shows that the footing motion is almost identical with the free field motion across the important frequencies of the models

response (<5 Hz). An extremely oversized footing element, as implemented in the sSHD model, has the largest capability to ensure synchronous movement between the footing and surrounding soil. In contrast, the models with foundations designed to rock both observe a significant attenuation of the PSD amplitude at the foundation level (Figure 6.3b and c) for frequencies less than 2 Hz. However, the footing motion is amplified at higher frequencies. For example, the PSD evaluated at 1Hz is reduced by almost 50%, but it is amplified by about 100% at around 2.5 Hz. When the footing size is reduced to promote rocking, the inertial forces developed from the superstructure under strong motion excitation may give rise to a horizontal movement between the footing and the soil that is unsynchronized. As a result, a significant amount of instantaneous footing sliding and uplifting may occur, and this movement may filter out the lower frequency input and amplify the higher frequency input to the superstructure.

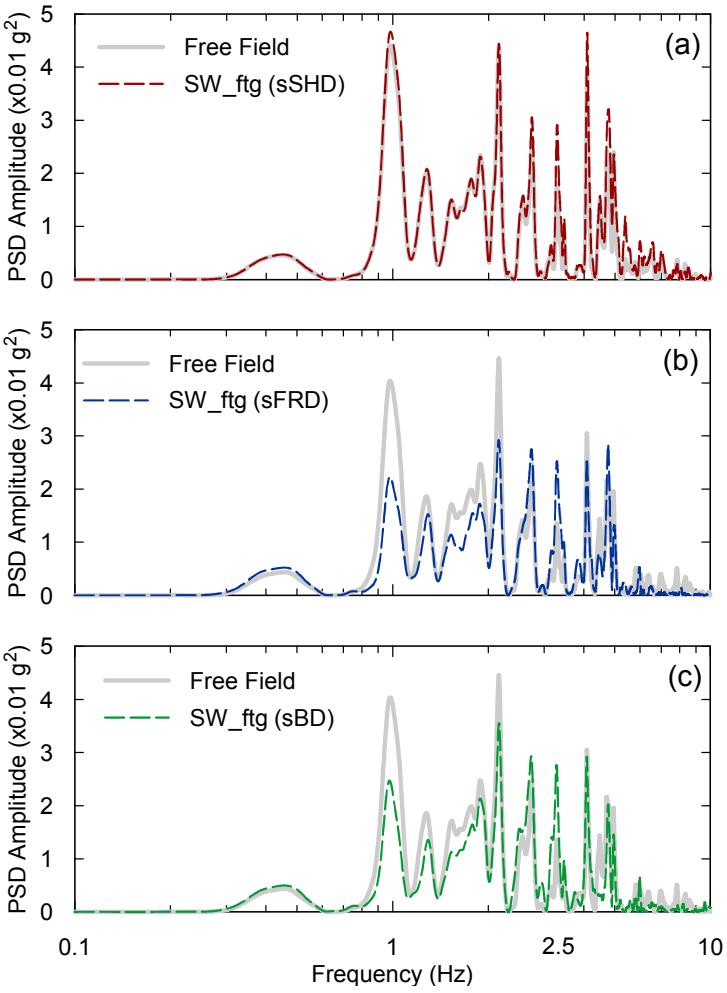

Figure 6.3 Power spectral density comparison between the foundation and free field ground surface motion under the highest intensity motion CMS_1.8: (a) sSHD model; (b) sFRD model; (c) sBD model

6.3.2 Peak Response Comparison

Figure 6.4 examines the relationship between the SW footing and free field motion with respect to the peak acceleration response for the three systems. Three nonlinear trend lines are regressed through the test data using a second-order polynomial assumption. This plot indicates that the sSHD footing peak acceleration response is amplified compared with the free field motion when the motion intensity is high (PFFA>0.8g). This is perhaps due to site amplification. The sensor measuring the free field response was located 0.6 meter below the ground surface, whereas the sensor monitoring the footing response was placed at the top of the footing.

Data from the sFRD and sBD models illustrate an opposite tendency at high intensity motions, namely the footing peak accelerations are attenuated relative to the PFFAs. This observation is similar with the findings of others regarding inertia-induced SFSI (e.g. Stewart et al., 1999). One may conclude that, under the circumstance of foundation rocking, the footing peak acceleration response as well as its PSD (at low frequencies) will tend to decrease compared with those of the free field motion.

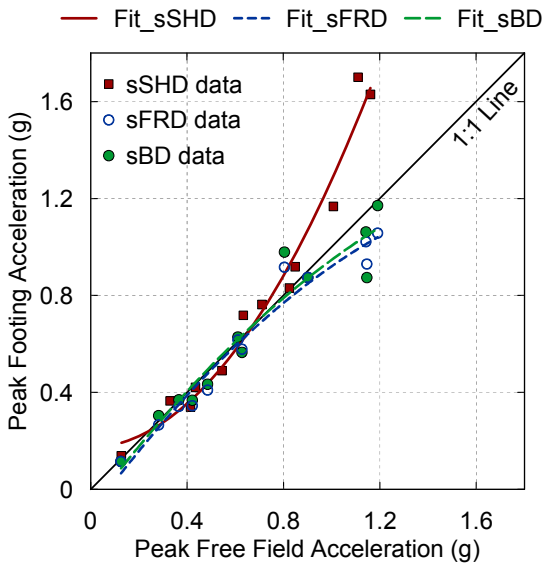

Figure 6.4 Peak footing acceleration versus peak free field acceleration

6.4 Superstructure Peak Response Comparison

This section compares the superstructure peak response among the three models, considering a variety of engineering demand parameters (EDPs). The EDPs of particular interest include roof acceleration, roof drift, total base shear, and free-field acceleration amplification distribution.

6.4.1 Peak Roof Acceleration

Figure 6.5 compares the peak roof acceleration (PRA) response of each model. Part (a) provides the sequence-based performance comparison from each earthquake event. This plot shows in general, the sSHD model tends to develop the largest roof acceleration demand while the sFRD model generally reports lower peak accelerations than the other models. Note that the as-built models have slightly different first natural period and different strengths of the dominant fuse elements (Table 5.1). Therefore, comparing the event-based peak response alone would not be adequate to compare the performance generated by the different fuse mechanisms of structural hinging and foundation rocking.

For this purpose, Figure 6.5b compares the performance in a different format. The x axis is the elastic spectral acceleration at T_1 of each model, evaluated using the measured free field motion. Second-order polynomial trend lines and one-to-one line are added in this plot. The plots show that, during low-intensity motions, all models receive PRAs similar with its elastic spectral acceleration demand (around 1:1 line), with exceptions of few scenarios which are located above 1:1 line. This is probably due to

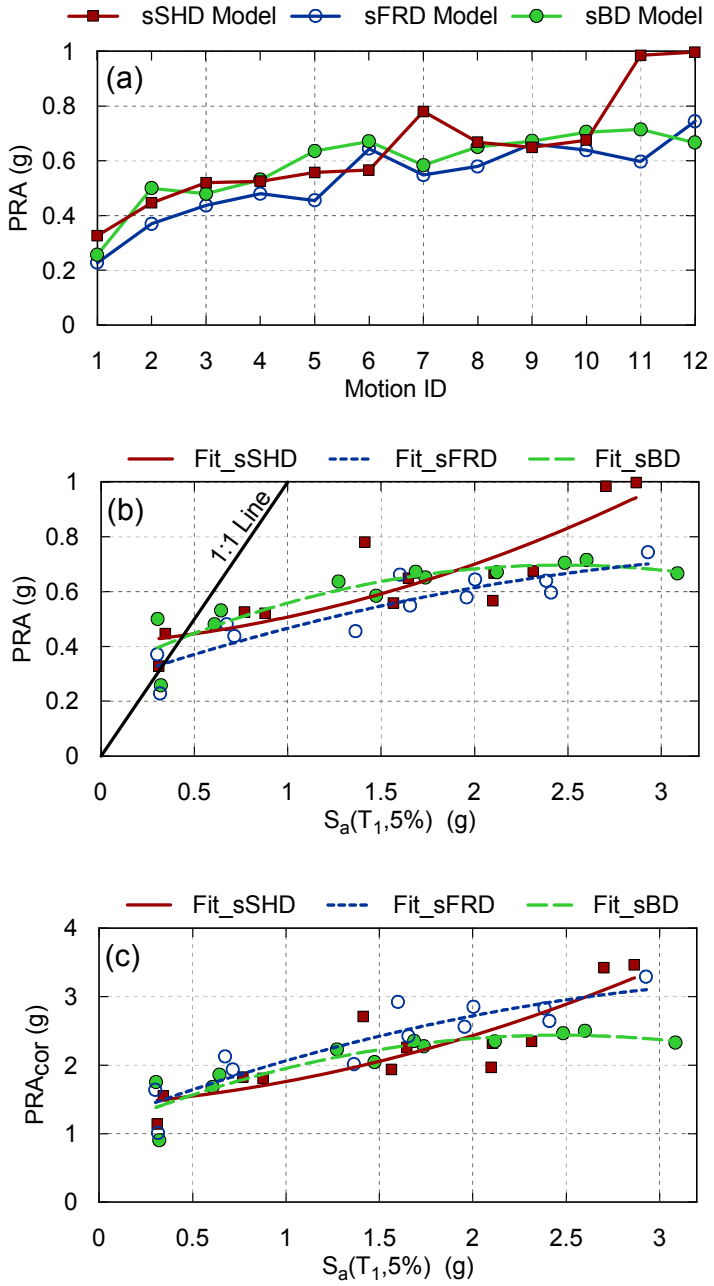

Figure 6.5 Peak roof acceleration (PRA) comparison: (a) PRA vs motion ID; (b) PRA vs the free field S_a (T_1, 5%); (c) corrected PRA (PRA_{cor}) vs S_a (T_1, 5%)

inaccurate estimation of the system damping when computing S_a. As the intensity increases, the PRA of each model is greatly attenuated compared with its elastic spectral acceleration demand (under 1:1 line). When subjected to extremely high intensity motion excitation (e.g. S_a>2.5g), the foundation rocking models (sFRD and sBD) are likely to attenuate the elastic acceleration demand much greater and develop a smaller PRA compared with structural hinging dominated system (sSHD).

In addition, the as-built models were constructed with slightly different strengths of the dominant fuse elements. To eliminate the strength difference between the models, the PRA of part (c) is corrected by normalizing by the minimum of the structural fuse yield coefficient C_y and the foundation rocking yield coefficient C_r, i.e.:

$$\mathrm{PRA_{cor}} = \frac{\mathrm{PRA}}{\min\left(C_y, C_r\right)} \tag{6.3}$$

The correction is based on a premise that the attained PRA generally increases with the fuse's capacity. Therefore, by dividing the PRA by the dominant fuse strength coefficient, one can adjust for the strength difference.

In this figure, similar observation is found that the sSHD model is likely to receive the largest PRA compared with other models when adjusted to same dominant fuse strength. In addition, during the extremely high intensity motion, the balanced design (sBD) is likely to attenuate the elastic acceleration demand the greatest and develop the smallest peak roof acceleration amongst all models when adjusted to same dominant fuse strength and motion intensity.

6.4.2 Peak Drift Ratio

Figure 6.6 presents the peak transient drift ratio (PDR) interpreted in three different ways. Part (a) plots the PDR, obtained via double integration of the measured roof acceleration data normalized by the total building height and as a function of the sequential motion imposed. It shows that the PDRs of the foundation rocking models (sFRD and sBD), are consistently larger than that of a like structure absent foundation rocking (sSHD). The difference is pronounced under moderate- and high-intensity motion inputs, i.e. after motion#5, where PDRs began to exceed 1%. The PDRs of the foundation rocking structures will be dictated by the rotational stiffness provided by the SW footing, rather than the wall lateral resistance. As the PDR increases, the SW rocking footing experiences significant stiffness degradation, which in turn increases the system's flexibility and thereby the peak roof drift. Comparison between the sFRD and sBD models indicates a relatively larger displacement developed in the sFRD model. This is attributed to the lower SW footing strength (C_r=0.23) compared to that of the sBD (C_r=0.29).

In part (b), the x-axis plots the elastic spectral displacement S_d at T_1 of the models normalized by the building height. Second-order polynomial trend lines and one-to-one line are added in this plot as well. The results indicate that the peak drift demand of the sSHD model is slightly larger than the elastic spectral drift demand. When the SW foundation is allowed to rock, the peak drift demand of the system is significantly amplified than the elastic demand, as indicated by the fit lines of the sBD and sFRD model. For example, given an elastic drift demand of 1.0% of the building height, the

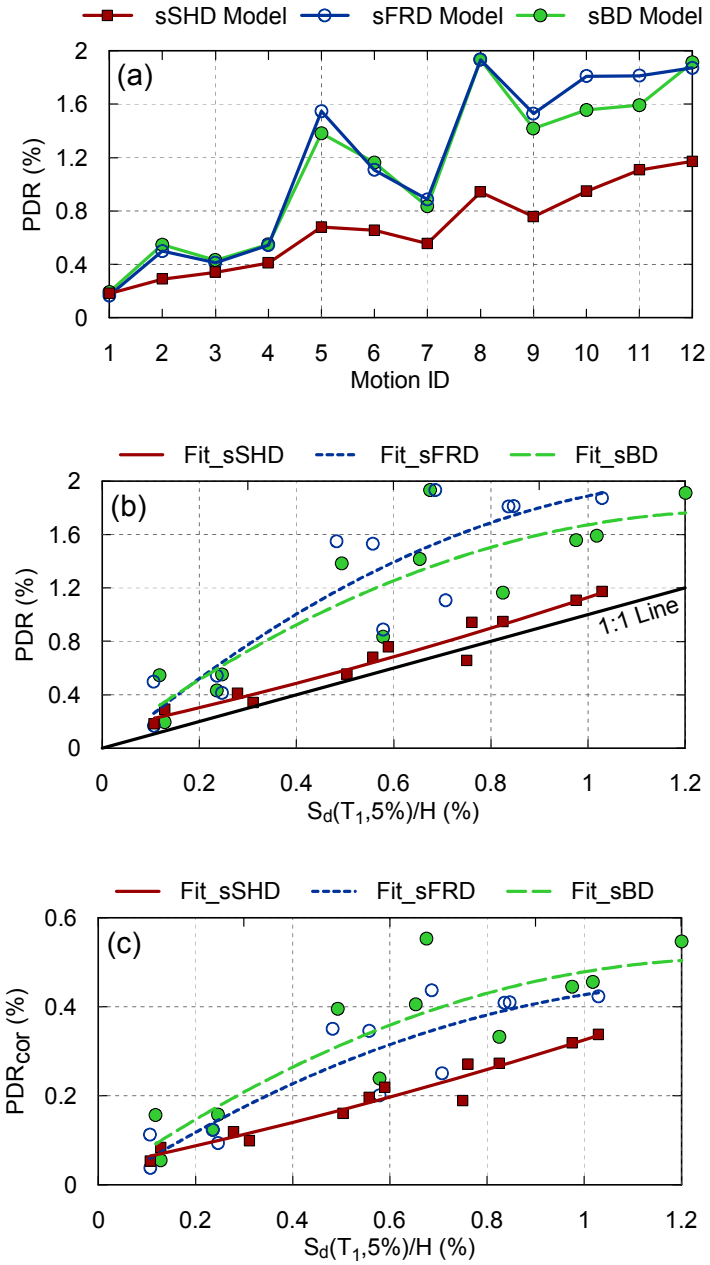

Figure 6.6 Peak drift ratio (PDR) comparison: (a) PDR vs motion ID; (b) PDR vs the free field normalized S_d (T_1,5%); (c) Corrected PDR (PDR_{cor}) vs the normalized S_d (T_1,5%)

sBD and sFRD model are likely to receive a PDR of 1.7% and 1.9% respectively, whereas the sSHD model is likely to observe 1.1% PDR.

Figure 6.6c attempts to correct the PDR on the y-axis to eliminate the strength variation in the models by using the equation:

$$\mathrm{PDR_{cor}} = \mathrm{PDR} \times \min\left(\mathrm{C_y}, \mathrm{C_r}\right) \tag{6.4}$$

In contrast to Equation (6.3), the PDR is modified by multiplying by the dominant strength coefficient, recognizing that the system drift demand is inversely proportional to the fuse capacity. The corrected data reveals similar observations as those of Figure 6.6a and b. Namely, the foundation rocking models are inherently more flexible and prone to receive large roof displacement demands. However, it also shows that the sBD-type system has a tendency to deform slightly more than the sFRD model. This may be explained by the fact that the double hinging configuration of the balanced design system, where hinges are placed in a series fashion, could result in an increase to its overall flexibility above that of a foundation rocking only system.

6.4.3 Peak Base Shear

Peak base shear demand is an important design parameter needed to estimate demand to the system and components. Figure 6.7 examines the measured peak base shear for each model, first shown normalized by the model's weight W, (i.e. $C_s=V_{total}/W$; where V_{total} = total base shear), and subsequently corrected to account for the strength difference in the models. In these tests, the base shear is linearly proportional to the moment demand in the first floor columns because of the pinned connection conditions. Therefore, it is computed by dividing the moment demand (measured via strain gauges

directly) by the corresponding lever arm. The total base shear (V_{total}) is then obtained by summing the contribution from each component at the first level.

Comparing the direct results of each model indicates that the sSHD model consistently receives the largest peak base shear demand, whereas the sFRD model observes the lowest demand, which is typically about 35% less than that of the sSHD model. These observations are further confirmed by examining the trend lines provided in part (b). By using the elastic S_a at T_1 of each model on the x axis, the plots indicate that, under similar moderate- and high-intensity motions, the foundation rocking mechanism (sFRD and sBD) has a strong tendency to enable the systems to reduce the base shear significantly compared with the model that solely relies on structural hinging.

To correct for the strength variation, C_s is normalized by the minimum strength coefficient in the system in Figure 6.7c, i.e.

$$C_{S,cor} = \frac{C_S}{\min(C_y, C_r)} \tag{6.5}$$

This plot continues to substantiate that the sSHD model tends to receive larger peak base shear than that of the foundation rocking models. Moreover, when considering simultaneous yielding between the SW fuse and footing, as indicated in the sBD system, the corresponding base shear is likely to decrease further than that of the foundation rocking dominated model (sFRD).

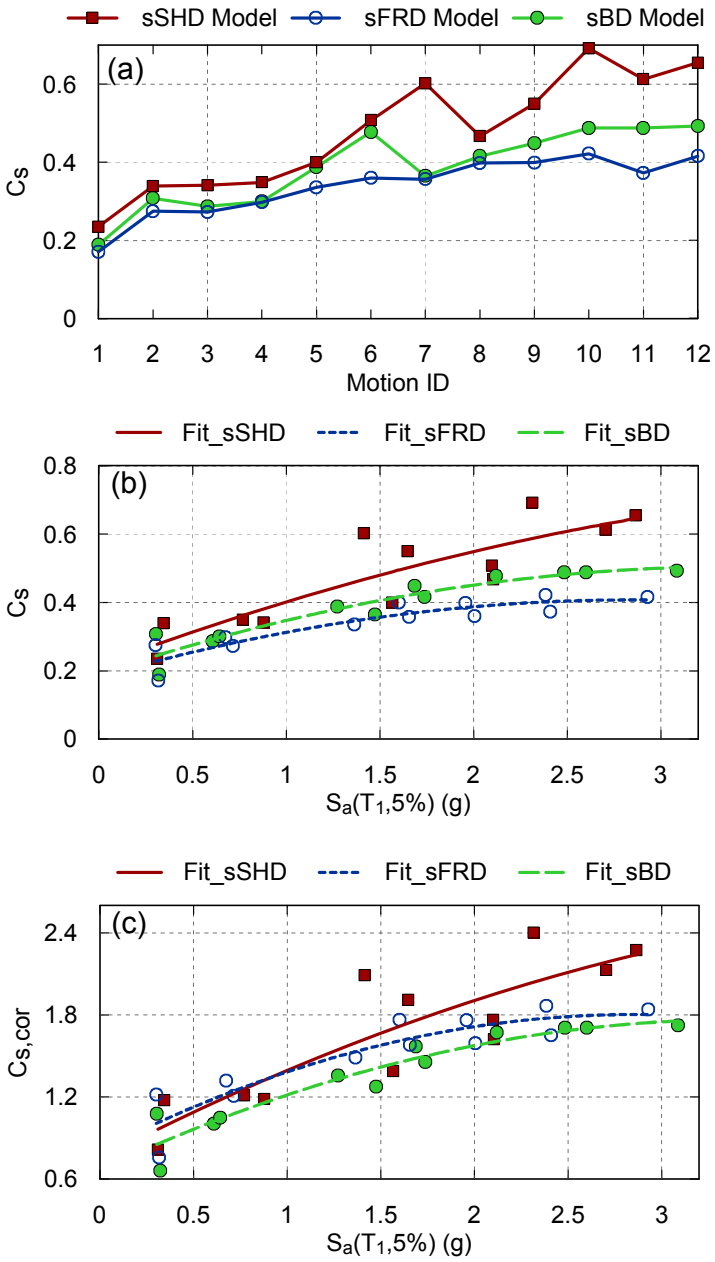

Figure 6.7 Peak base shear coefficient (C_s) comparison: (a) C_s vs Motion ID; (b) C_s vs the free field S_a (T_1,5%); (c) Corrected C_s ($C_{s,cor}$) vs S_a (T_1,5%)

6.4.4 Acceleration Amplification Profile

The distribution of peak floor accelerations in a building is important in the design of floor level components (both structural sections and nonstructural components). Typically, these are compared with the PFFA by computing an acceleration amplification ratio Ω at each floor level. The parameter Ω is defined as the absolute value of peak acceleration at each floor level divided by the PFFA. It should be noted that the peak floor level acceleration may not necessarily occur at the same time as the PFFA. Figure 6.8 plots the uncorrelated Ω as a function of the building height. In addition, a mean amplification profile is added for each model based on all of the dynamic testing data.

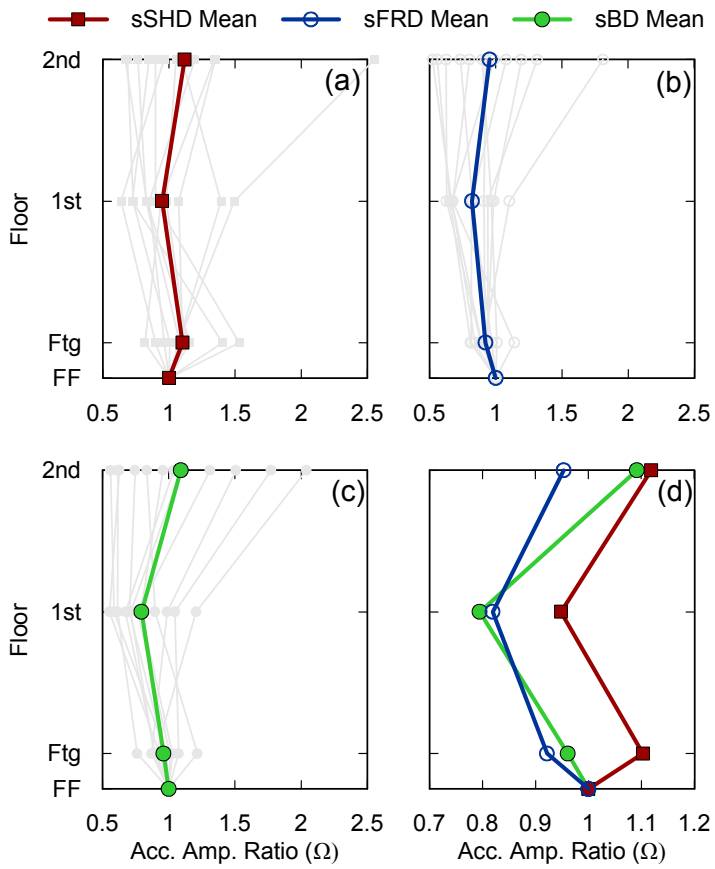

Figure 6.8 Acceleration amplification ratio along the structure height: (a) sSHD model; (b) sFRD model; (c) sBD model; (d) comparison (Note: FF = free field, Ftg = Footing)

In general, the acceleration amplification ratio increases from the first story to the roof level, reflecting the fact that all models are predominantly controlled by their first modes. Comparison of the mean amplification profile for the three models (Figure 6.8d) shows that the acceleration amplification ratio of the foundation rocking models (sFRD and sBD) is generally less than that of the traditional fixed-base building model (sSHD) at each level. Foundation rocking in these models provides an isolation-like mechanism in the rotational direction, elongating the system's natural period and helping to decrease the motion amplitudes developed in the superstructure.

6.5 Residual Response Comparison

6.5.1 System-Level Residual Behavior

During strong shaking, the inelastic behavior of components within a building-foundation system will inevitably result in residual deformations. If significant, it may directly affect the functionality and/or occupancy of the building. Therefore, the residual demand of each frame-wall-foundation models is examined. Figure 6.9a plots the cumulative residual drift ratio (RDR) for each model as a function of the sequential motion imposed, whereas part (b) plots event-based RDR for each type of model relative to the footing against its respective peak roof drift (PRD). Note that measurements of residual deformations are taken directly from displacement sensors, in contrast to the peak deformations, which are obtained via double integration of accelerations.

Figure 6.9a shows that the sSHD model suffers a significant residual response towards the end of the sequential shaking, cumulating about 2% RDR. It should be noted that this behavior may be dramatically worse for reinforced concrete wall structures, due to the presence of strength deterioration, characteristic not articulated in the shear wall model (Section 5.4). Inspecting the development of the cumulative residual demands in the sSHD model, one notes that the largest residual contributions occur in the last two earthquake motions, which causes a catastrophic-type failure in the sSHD model. The sFRD and sBD systems, on the other hand, experience a nearly negligible permanent deformation under the same motions. These results support the contention that the structural hinging mechanism has the lowest potential for recovering the system state once its inelastic behavior ensues. Foundation rocking models, on the other hand

illustrate their beneficial re-centering capability, and even when designed with a strength equal to the structural fuses demonstrate this positive attribute. In this case, the cumulative residual displacement is reduced by about two thirds compared with the structural hinging only system. Figure 6.9b further substantiates the advantageous re-centering benefit of the foundation rocking mechanism by examining the trend lines based on the event-based data. Given a PRD of 1.2%, for example, the sSHD system is likely to experience a RDR of 0.85% which is about 13 times of those of the sFRD and sBD systems.

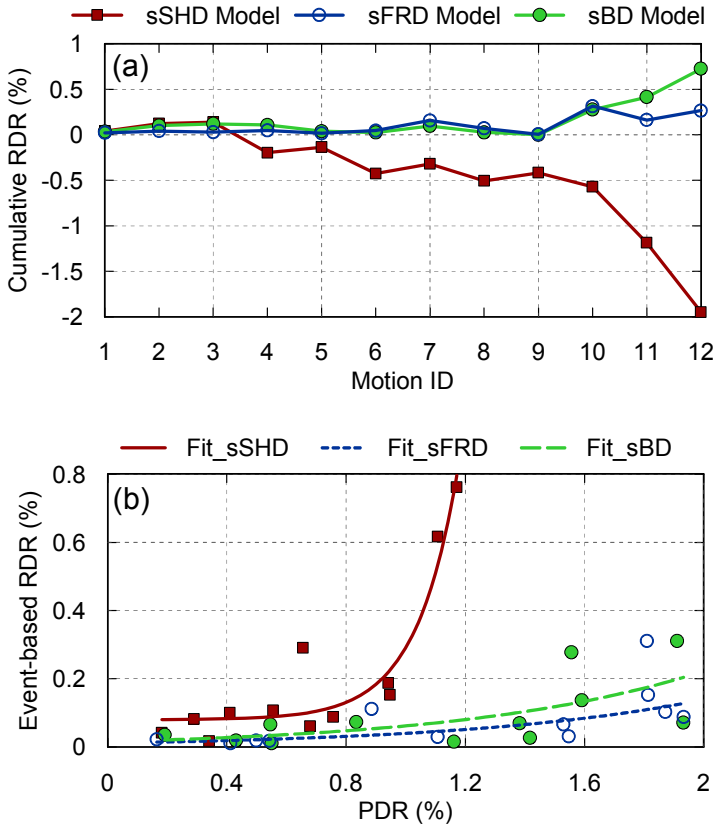

Figure 6.9 Residual drift ratio (RDR) comparison: (a) Cumulative RDR vs Motion ID; (b) Event-based RDR vs Peak drift ratio (PRD)

6.5.2 Footing Residual Deformation

Under earthquake loading, a foundation component may settle, slide, or tilt permanently, and this deformation could affect the building's functionality. Figure 6.10 and Figure 6.11 summarize the cumulative residual sliding and settlement for the SW and column footings relative to the free field, respectively. Since the north and south column footing observe a similar residual response for both models, the data represented herein is the average of these two. Note that the values are normalized by their respective footing lengths (Table 5.2).

Figure 6.10a illustrates that the sFRD's footings generally experience a relatively larger normalized permanent settlement, compared with those of the sBD model since they have lower FS_v against bearing failure. This difference is more pronounced in the column footings, as indicated in part (b). For example, the sFRD's column footings settle 2.9% of its length towards the end of sequential shaking compared with 2.4% observed in the sBD.

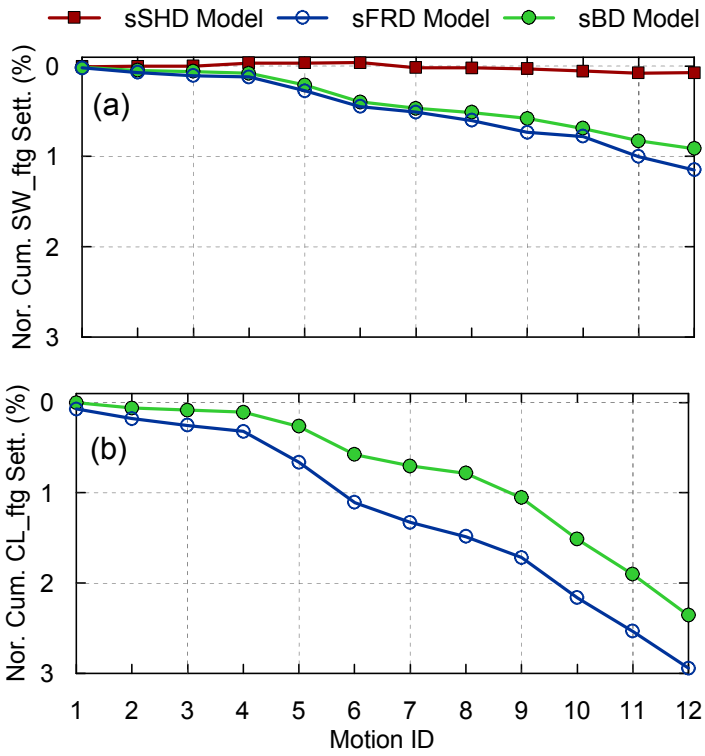

Figure 6.10 Footing settlement comparison: (a) cumulative shear wall footing (SW_ftg) settlement; (b) cumulative column footing (CL_ftg) settlement;

With regard to the sliding response, the SW footing of the sBD model undergoes a larger residual response than the sFRD, particularly during the last two events, as indicated in Figure 6.11a. This can be attributed to the lower moment-to-shear ratio (M/(V×L)) of the SW footing in the sBD model (1.09 for sBD; 1.41 for sFRD). A footing with low of a moment-to-shear ratio indicates that sliding could play an unavoidable and important role in the footing's movement beyond rocking (Gajan and Kutter 2009). In contrast, the column footings of the sBD model observe a lower residual sliding, as illustrated in part b. This is due to the lower strength of the column fuse limiting the imposed seismic demand. In the sFRD configuration, the column footings suffer a

significant residual sliding, which may be elicited by the permanent sliding of the SW footing.

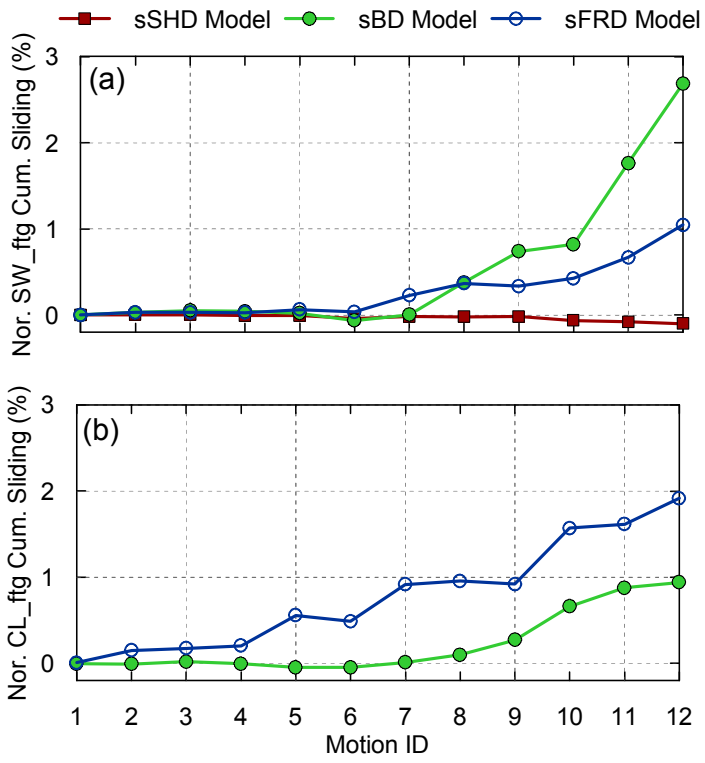

Figure 6.11 Footing sliding comparison: (a) cumulative SW_ftg sliding; (b) cumulative CL_ftg sliding

6.6 Inelastic Elements Hysteretic Response and Energy Dissipation

Energy dissipation is a vital attribute of inelastic components within any type of seismic resisting system. In current provisions, ductile elements are strategically designed and encouraged to perform inelastically such that seismic input energy can be absorbed. Using the dynamic data from these tests, the hysteretic response of the two dominant

inelastic elements, namely the SW rocking footing and the SW structural fuse, are investigated and compared.

6.6.1 Hysteretic Response Comparison

Figure 6.12 presents a suite of hysteretic curves, where each row represents the performance under input motions of increasing intensity (top to bottom) and the columns represent different fuse components. Four motions are selected to represent different levels of intensity, ranging from low-level (elastic response) to high-level (significant inelastic response). It should be noted that the y-axis of these plots is the moment demand normalized by its respective yield moment (Table 5.2).

It is evident that each of the components performs almost linear-elastically under the first motion excitation (GZ_0.2). During the fifth motion (KB_3.0), the SW footing of the sFRD and sBD models observes a moderate level of nonlinearity, yet nearly elastic hysteretic response. These curves display an "S-shape" characteristic indicating a substantial self-centering capability. The SW fuse of the sBD model attains incipient yielding and develops a slight amount of inelasticity. The SW fuse of the sSHD model, on the other hand, during motion KB_3.0, responds with relatively broad hysteresis.

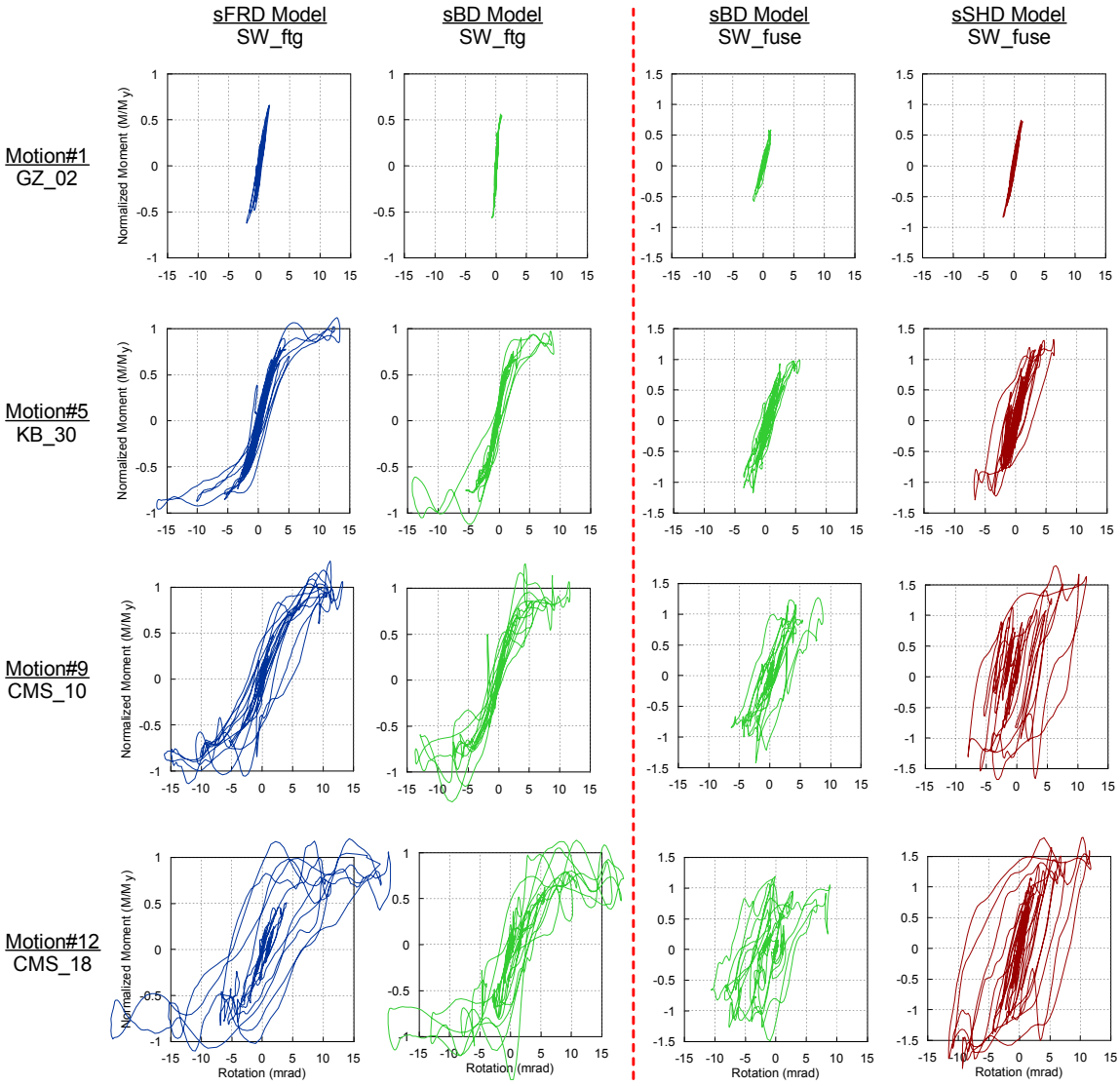

Figure 6.12 Hysteretic response of the SW rocking footing (two left columns) and the SW fuse (two right columns) under four different motion intensity levels. Note that the y-axis of the fuse components response (columns3+4) have an expanded range

When all models were subjected to the CMS_1.0 motion, the imposed ductility demand to all fuse elements observes substantial increases. The footing hysteretic curve becomes wider for both models, which indicates that a fair amount of energy is dissipated at the soil-footing interface. Simultaneously, its self-centering behavior is still maintained, and particularly in the sBD model. Importantly, after the SW fuse in the sBD model yields, its rotation demand is less than that of the SW footing. This is notable since the SW footing can recover rotation demand, whereas the SW fuse does not have a natural tendency to do so. The SW fuse of the sSHD model, on the other hand, experiences significant inelasticity as well.

When the same motion was amplified by 80% (CMS_1.8), similar observations are noted, with the exception of the re-centering behavior of the rocking footings. While re-centering still occurs, it is not as significant. The SW footing of the sFRD model, for example, cumulates a maximum residual rotation of 0.007 rad. In contrast, the SW footing of the sBD model cumulates about 0.003 rad. Moreover, the demands imposed on the SW fuses are both increased in the sBD and sSHD model. Nonetheless, the peak rotation demand developed in the SW fuse is less (50%) than that attained in the foundation of the sBD model.

6.6.2 Peak Ductility Demand Comparison

This section summarizes and compares the peak ductility demands of selected inelastic elements under each motion, including SW_ftg, SW_fuse, and column fuse at second level (CL_fuse2). Herein, CL_fuse2 is selected for comparison since it is the only

shared inelastic element by all three models beyond the dominant fuse elements (SW_ftg and SW_fuse). The peak ductility demand is determined by dividing the peak rotation demand by its yield rotation. The yield rotation of each fuse element is obtained during cyclic test program (Section 5.5) and summarized in Table 6.2.

Table 6.2 Yield rotation of selected inelastic elements

Fuse short name	Location	Yield Rotation (mrad)
CL_fuse2	Column fuse at second level	11.9
SW_fuse	Shear wall structural fuse	5.0
SW_ftg (sBD)	SW footing of the sBD model	7.6
SW_ftg (sFRD)	SW footing of the sFRD model	4.9

Comparing the first two columns of Table 6.3 indicates that the ductility demand imposed on the SW footing of the sBD model is significantly reduced compared with that of the SW footing in the sFRD. Under motion#10, for example, the SW_ftg's peak ductility demand in the sBD is 2.33, which is 42% of the peak ductility demand in the sFRD model. The peak ductility demand of the SW_fuse in the sBD is reduced as well compared with that of the sSHD model. In the meantime, the peak ductility demand imposed on the SW_fuse is similar with that of the SW_ftg in the sBD model. This finding is important in that the balanced design strategy reduces and equally distributes the ductility demand imposed on each inelastic element compared with single-fuse-dominated systems.

Inspection of the peak ductility demand of the CL_fuse2 reveals that the sFRD model has the largest demand compared with other models. It can be understood by the fact that the rotation of the CL_fuse2 is linearly proportional to the model drift due to

pinned-connections at beam-column and beam-wall joints. Since the sFRD model develops the largest peak roof drift (Figure 6.6), its CL_fuse2 accordingly observes the largest ductility demand. It is also clear that the CL_fuse2 demand in sSHD model is the lowest due to its lowest PDR.

Table 6.3 Peak ductility demand of select inelastic elements

Motion ID	SW_ftg	SW_fuse		CL_fuse2		
	sFRD	sBD	sBD	sSHD	sFRD	sBD	sSHD
1	0.42	0.13	0.34	0.36	0.24	0.25	0.21
2	1.21	0.53	0.68	0.64	0.60	0.78	0.36
3	0.88	0.40	0.45	0.53	0.50	0.57	0.30
4	1.20	0.55	0.67	0.80	0.68	0.73	0.46
5	3.37	1.89	1.13	1.10	1.90	1.95	0.63
6	2.34	1.45	1.26	1.60	1.41	1.65	0.92
7	1.92	0.91	0.78	1.10	1.08	1.14	0.63
8	4.23	2.62	1.47	1.65	2.39	2.76	0.94
9	3.24	1.81	1.74	1.89	1.83	1.98	1.08
10	5.53	2.33	2.05	2.30	3.13	2.23	1.32
11	5.06	2.10	2.13	2.46	2.86	2.27	1.41
12	5.03	2.66	2.11	2.70	2.84	2.74	1.55

6.6.3 Energy Dissipation Distribution

The energy dissipated by each inelastic component is computed by integrating the area of the moment-rotation hysteresis. The relative dissipated energy is then calculated by normalizing each by the total. Note that the energy dissipated from other non-flexural modes, such as footing nonlinear sliding or settlement, is not accounted for in this calculation.

Figure 6.13 depicts the dissipated energy distribution for each model under all motion inputs. For the sFRD and sBD models, a dashed line is added to separate the contribution from the substructure components (rocking footings) and superstructure

components (SW and column structural fuses). To relate these results to typical design, the engineering demand parameter PDR for each motion is added on the secondary x-axis. For the sSHD model (Figure 6.13a), the majority of the seismic energy (around >80% for most motions) is dissipated by the SW fuse section, with the remaining dissipated via the column fuses since foundation rocking is discouraged. In contrast, more than about 70% of the total energy is dissipated within the soil-footing interface in the sFRD (part b) with

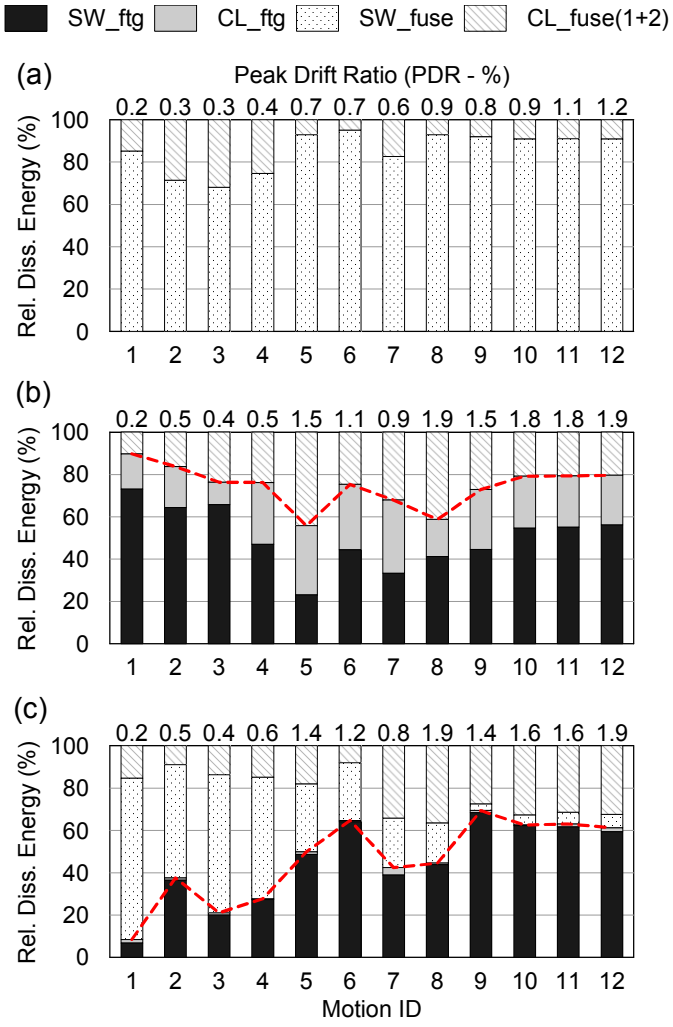

Figure 6.13 Relative energy dissipation distribution: (a) sSHD model; (b) sFRD model; (c) sBD model

the exception of the two moderate-intensity motions (#5 and #8), where the column fuses diffuse a considerable amount of energy (about 40%) resulting in a balanced distribution. Comparing the contributions from the column footings to that of the SW footing in the sFRD model reveals that column footings undergo significant inelasticity during dynamic loading, which contribute considerably to the hysteretic energy dissipated.

For the balanced design model (part c), the superstructure inelastic components are subjected to yielding first (Figure 5.16); therefore, they tend to dominate the energy dissipation during low-intensity motions (i.e., >80% when the PDR<0.4%). Once the capacities of all fuse components are mobilized (after motion#4), the energy dissipation distribution is quite appealing with the relative quantities well-distributed between the superstructure and substructure components irrespective of motion intensity. It is also observed that, during strong input motions, the relative energy dissipated by the SW fuse gradually decreases since it is protected from large plastic deformations by the footing rocking. Figure 6.13c also continues to reveal the limited impact of the column footings in the sBD model since they consistently contribute less than 3% of the total hysteretic energy.

6.7 Conclusions

In this chapter, the dynamic response of three frame-wall-foundation models under a series of earthquake motions of increasing amplitude at centrifuge scale. The three models are strategically designed considering the strength variation between the shear wall (SW) structural fuse and rocking foundation as follows: (1) symmetric

foundation rocking dominated (sFRD) model, (2) symmetric structural hinging dominated (sSHD) model, and (3) a balance of both structural hinging and foundation rocking (sBD) model. This work complements the presentation of the slow cyclic response of two of these models presented in Chapter 5. Relative to the dynamic response results, several main conclusions emerge:

- When the foundation is encouraged to mobilize its capacity in a rocking mode, as intended for the sBD and sFRD models, the power spectral density (PSD) amplitude at low frequencies, as well as the peak response of the recorded motion at the footing level, are significantly attenuated compared with that of the free field ground surface motion.
- As a consequence of the amplified footing accelerations, demands to the superstructure of the sSHD model observe the largest peak roof accelerations, while those to the sFRD model are the smallest. However, when corrected to similar strengths, foundation rocking systems (sBD and sFRD) still demonstrate their greatest potential to develop a lower peak roof acceleration compared with the sSHD-type system.
- The peak roof drift tends to be amplified in foundation rocking models (sFRD and sBD models). However, these systems have a substantial capacity to recover from large amplitude transient displacement. In these tests, the sSHD model observes the lowest ability to recover the system under high-intensity motion excitations, which leads to significant permanent deformations.

- The reduced acceleration demands of the sFRD model translate to low base shear force demands. Importantly however, when the system strength and input motion intensity are adjusted to be equatable for each frame-wall-foundation system, the sBD and sFRD model tend to develop the smaller peak base shear compared with the sSHD.
- Normalized settlements are larger in both the SW and column footings of the sFRD model, when compared with the sBD design. Under strong earthquake input, however, the SW footing of the sBD model observes relatively larger permanent sliding than the sFRD SW footing.
- Inspection of the dynamic hysteretic moment-rotation responses of the inelastic components within these models reveals a strong re-centering capacity of the SW rocking footings compared with the SW structural hinging. In terms of energy dissipation via the moment-rotation mode of these components, the majority of the energy is dissipated in the SW fuse section of the sSHD model. In contrast, the rocking foundations in the sFRD-type system absorb most of the energy for low-level and high-level motions. When a balance in inelastic contributions is targeted (sBD model), the dissipated energy is well distributed between the superstructure inelastic components and rocking footing elements under moderate- and high-intensity motion excitation.
- The experimental raw data of the test program described in this chapter are provided at NEEShub website with a permanently assigned Digital Object Identifier (DOI) of 10.4231/D3NG4GR9C.

(http://nees.org/warehouse/experiment/4940/project/732)

6.8 Acknowledgements

This chapter, in part, is currently being prepared for submission to technical journals. The article is tentatively titled "Seismic Behavior of Frame-Wall-Rocking Foundation Systems-Part II: Dynamic Shake Table Test Results" with a preliminary author list of Weian Liu, Tara C. Hutchinson, Andreas G. Gavras, Bruce L. Kutter, and Manouchehr Hakhamaneshi (201X). At completion of this dissertation, its final form was in preparation. However, the dissertation author is the primary investigator and first author of these papers.

Chapter 7

Frame-Wall-Rocking Foundation System Test (Test-2) – Part III: Effect of Seismic-Induced Axial Load Fluctuation

7.1 Background and Research Scope

7.1.1 Background

Architectural aesthetics or building functionality often leads to requirements for large open bays in buildings. Structural shearwalls however are highly successful in minimizing inter-story drift demands induced by earthquake. Many buildings emulate a compromise between these two competing needs and are constructed of mixed systems, i.e. walls and frames, with multiple load resisting systems. It is highly likely that the

building load path becomes asymmetric. When subjected to lateral wind or seismic load, building asymmetry could produce a coupled response between its lateral and torsional modes, which greatly complicates the analysis of the system. Many researchers have realized this issue and proposed approximate analytic solutions (e.g., Rutenberg et al. 1977; Balendra et al. 1984), or developed simplified numerical methods for estimating the seismic demand to these structures (e.g., Kilar and Fajfar 1997; Chopra and Goel 2004; Reyes and Chopra 2011). These and other studies also highlight another key aspect of the asymmetry, namely that axial load on the components fluctuates significantly during lateral loading. Asymmetry has a pronounced potential to generate an uneven distribution of vertical load in the vertical components when the system is subjected to lateral load. For some structural components, such as walls or shallow foundations, a significant change in axial load affects its capacity and therefore its seismic performance. Ultimately, this impacts the entire structure-foundation system.

7.1.2 Significance of Axial Load Variation

The yield moment of a shallow footing is a function of the imposed axial load (e.g, Gajan and Kutter 2008; Deng and Kutter 2012). As a result, a rugby-shaped failure envelope has been suggested to characterize the footing axial-moment (P-M) interaction (e.g., Chatzigogos et al. 2009; Gajan and Kutter 2009b; Figini et al. 2012). However, previous research characterizing the rocking footing's seismic behavior is mostly founded on the hypothesis that the axial load on the footing remains constant during loading. From a system perspective, this assumption is not valid. When the system is subjected to lateral load, kinematic interactions amongst load-bearing structural components, such as

columns, structural walls, and beams, will redistribute axial load in vertical elements. This has the potential to influence the yield moment of footings that will rotate and ultimately the seismic behavior of the entire structure-footing system.

This significance of axial loads on the response of reinforced concrete (RC) and steel frame members is well known and typically characterized in design via the well known P-M interaction diagram (e.g., Abrams 1987; Saadeghvaziri 1997; Como et al. 2003; Esmaeily and Xiao 2005). In contrast, few studies have examined its effect on the response of rocking footings and in particular how this impacts the systems response, although it is well known that a footing's yield moment is dependent on its axial load. Gelagoti et al. (2012) numerically conducted a pushover analysis of a two-story-one-bay concrete frame structure founded on rocking footings. It reports a significant variability of moment-rotation response between the two identical rocking footings, which is greatly attributed to the axial load fluctuation on each footing. In a centrifuge experiment by Trombetta et al. (2014), axial load variation induced by frame action on a one-story moment frame-shallow foundation model demonstrates that instantaneous yield moment reduction can occur at the footing.

7.1.3 Scope of this Chapter

Considering the importance of axial load on a footing's response under cyclic moment-dominated loads induced during an earthquake, it warrants investigation via model experiments. In particular, systems whose layout may cause asymmetric frame-action are particularly susceptible to intensified axial load fluctuations. These effects could be either detrimental or beneficial, depending on the initial axial loading condition,

the geometrical and material property of the foundation and soil environment, and the seismic demand.

As described in Section 5.3, Test-2 program was also geared towards assessing the seismic performance of three different asymmetric frame-wall-foundation models beyond their symmetric counterparts. Herein, the goal of this chapter is to compare the seismic response of the asymmetric frame-wall-foundation models with their symmetric counterparts in an effort to shed light on the impacts of axial load variation and structural asymmetry.

7.2 Properties and Instrumentation of Asymmetric Models

7.2.1 Asymmetric Model Configuration

The frame-wall-rocking foundation systems considered in Test-2 are schematically shown in Figure 5.1. The systems were two-dimensional idealizations of a single wall and two framing bays arranged with equal spans and supporting two stories of a building. Two types of hinging mechanisms, namely structural hinging and foundation rocking, are incorporated into the design of these models. The models are divided into two major groups considering the shear wall (SW) location, namely the symmetric (center-Figure 5.1a) and asymmetric (end-Figure 5.1b) system. The design of the models and the experimental program details are summarized in Sections 5.2 and 5.3.

Figure 7.1 provides an elevation view of three asymmetric models and one symmetric model, namely the models aSHD, aBD, aFRD, and sFRD. It is important to

note the positive sign convention defined in this figure, where a movement towards the SW (right) or down and a clockwise rotation is positive. Each asymmetric model shares the same structural components' sizes and materials to that of its symmetric counterpart, the only difference therefore being the wall location. For complete design and construction of each of the models, one may refer to Section 5.2.2.

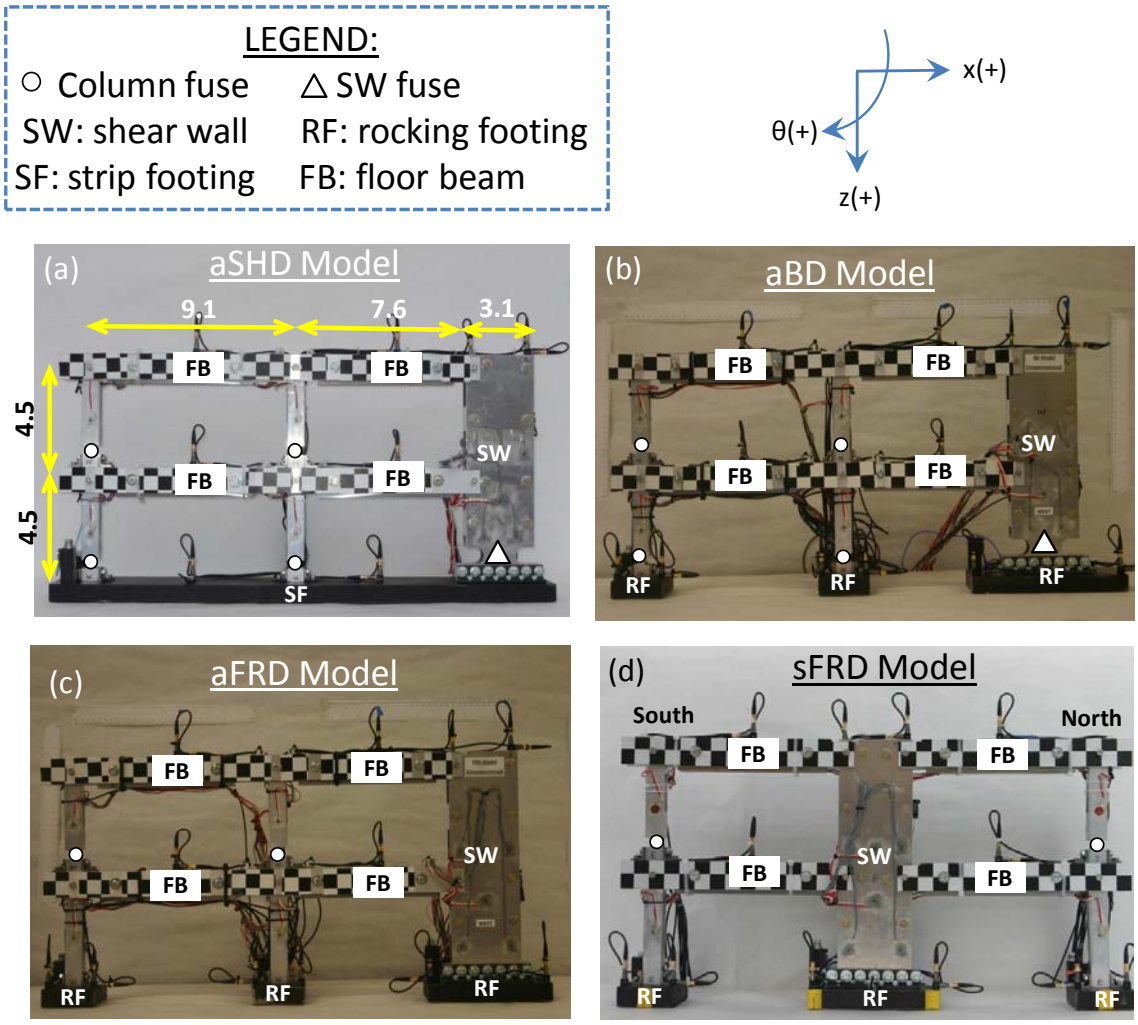

Figure 7.1 Constructed frame-wall-foundation models: (a) aSHD model; (b) aBD model; (c) aFRD model; (d) sFRD model (in prototype unit: m)

7.2.2 Engineering Properties of Asymmetric Models

Table 7.1 summarizes the achieved properties of the constructed asymmetric models. Note that the parameter C_r of the asymmetric models is obtained assuming that static (gravity-induced) axial loads are imposed on the SW. Inspecting the relationship between C_y and C_r for the aSHD and aFRD model indicates that desired yielding hierarchies are achieved between the SW fuse and rocking footing for both models. However, in the aBD model, the SW rocking footing's yield coefficient (C_r=0.24) is slightly less than that of the SW fuse (C_y=0.29). This is due to the fact that placing the SW outboard reduces the tributary axial load distributed to the SW and therefore the SW rocking footing's yield moment. It is noted that Table 1 also provides the first elastic flexible-base natural period (T_1) of each model. Values of T_1 have been determined examining the acceleration response in the frequency and time domain of each model when they were subjected to a small amplitude excitation (step wave motion) at centrifuge scale. It is noted that a nominal variability in T_1 exists, although most models are within 0.36-0.39 sec. For example, the aSHD and aBD models are slightly more flexible with T_1 of about 0.47-0.48 seconds.

Table 7.2 provides the theoretical yield moment of each implemented inelastic element. The yield moment of the structural fuses can be obtained with knowledge of the size of the fuse and the yield strength of the material (Equation 5.1), whereas the rocking footing's yield moment can be determined with knowledge of the footing size, axial load, and the soil's property (Equation 5.2). Note that the footing yield moment (M_{y_st}) is

calculated under static gravity loads. Table 7.2 also provides the total static axial load acting at each soil-footing interface, which includes the footing's dead weight.

Table 7.1 Summary of asymmetric frame-wall-foundation models as-built values

Parameter	Description	aSHD	aFRD	aBD
T_1	Flexible-base first natural period (sec)	0.47 (0.37)*	0.39 (0.36)	0.48 (0.38)
C_y	SW structural fuse yield coefficient	0.29 (0.29)	1.29 (1.29)	0.29 (0.29)
C_r	SW rocking footing yield coefficient	2.28 (2.17)	0.18 (0.23)	0.24 (0.29)
FS_v	SW footing static vertical factor of safety	28 (27)	15 (10)	21 (16)
M_1=M_2	Floor mass at each level (kg)	110,970		
H_1=H_2	Story height at each level (m)	4.50		
L_{cc}	Center-to-center spacing (m)	9.10		
H_{SW}/W_{SW}	SW aspect ratio (height/width)	3.33		
L_{SWftg}	SW footing length (m)	22.10	5.33	6.86
$M/(V\times L_{SWftg})$	SW footing moment-to-shear ratio	0.35	1.41	1.09
L_{CLftg}	Column footing length (m)	n/a	2.29	
B_{ftg}	All footings' width (m)	3.05		
t_{ftg}	All footings' thickness (m)	0.76		
D_{ftg}	All footings' depth of embedment (m)	0		

*Note: values in parenthesis are associated with the symmetric model counterpart (Table 5.2).

Table 7.2 Summary of yield moments of all inelastic components and static axial loads of rocking footings

Quantity	Fuse	Location	aSHD	aFRD	aBD
Yield Moment (M_y, kN-m)	CL_fuse1	Column fuse at lower level	400	11020	400
	CL_fuse2	Column fuse at upper level	400	400	400
	SW_fuse	Shear wall structural fuse	4220	18900	4220
Yield Moment (M_{y_st}, kN-m)	ExCL_ftg	Exterior column rocking footing	N/A*	670	740
	InCL_ftg	Interior column rocking footing	N/A	1000	890
	SW_ftg	Shear wall rocking footing	N/A	3220	4840
Static Axial Load (P_{st}, kN)	ExCL_ftg	Exterior column rocking footing	N/A	850	960
	InCL_ftg	Interior column rocking footing	N/A	1520	1270
	SW_ftg	Shear wall rocking footing	N/A	1470	1660

*Note: A single, large strip footing supports the exterior and interior columns and the SW in the aSHD.

7.2.3 Soil Environment and Instrumentation

The underlying geologic environment used for supporting the asymmetric models is identical with the symmetric models, namely uniform dense Nevada sand. The detailed properties of the sand are summarized in Section 5.3.2 and Table 5.3. In the meantime, the asymmetric models were heavily instrumented with accelerometers, strain-gauges (SGs), and linear potentiometers (LPs) to monitor the system's response during cyclic or dynamic loading. Figure 7.2 schematically shows the placement and instrumentation of two asymmetric models, namely the aBD and aFRD models.

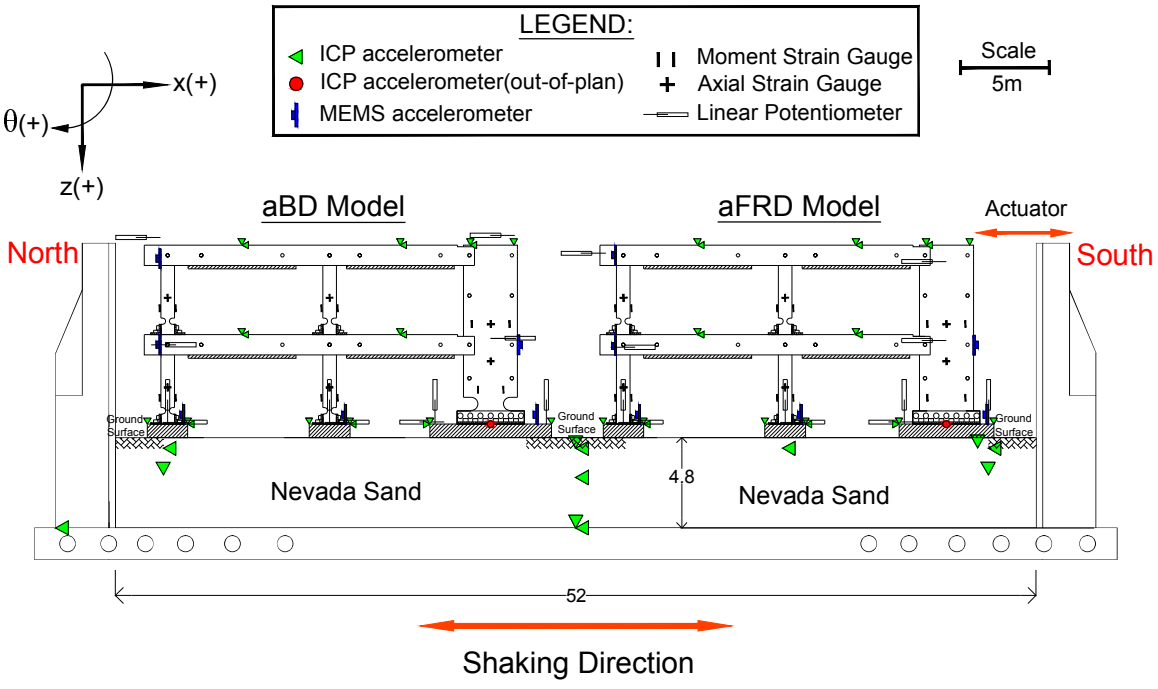

Figure 7.2 Schematics of asymmetric models placement and instrumentation (All dimensions are in prototype scale, m)

7.2.4 Motion Protocol of Asymmetric Models

In contrast to the motion protocol of symmetric models, a suite of eleven earthquake motions were applied to the asymmetric models, generally in order of increasing intensity. The source motion details and main characteristics of these motions as achieved in the free field ground surface are summarized in Table 6.1. Note that motion#12 has not been applied to asymmetric models.

Figure 7.3 shows the 5% damped elastic spectral acceleration spectrum of the free field ground surface recording for each earthquake event, normalized by the PFFA and overlaid with each asymmetric and symmetric systems' first period (Table 7.1). This plot shows that CMS source motion presents with ascending spectral acceleration demands during period elongation of the systems, while the other three present with descending demands.

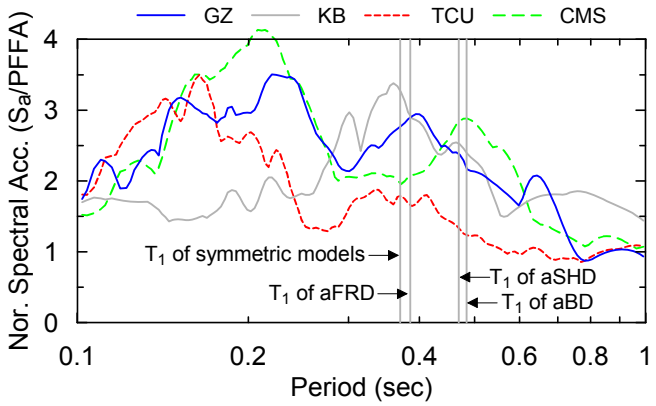

Figure 7.3 Elastic spectral acceleration spectrum of the achieved free field motions with 5% damping

After completion of the earthquake sequence, the aFRD model was subjected to a sequence of displacement-controlled cyclic loading imposed using a hydraulic actuator

attached to the top of the wall component. The model was subjected to six different packets of cyclic loading, with each packet containing three cycles of a sinusoidal displacement history of constant amplitude. Amplitudes were initially small (roof drift ratio = 0.1%), and then gradually doubled for each subsequent cyclic amplitude (i.e., 0.25%, 0.5%, 1.0%, 2.0%, and 4.0%). Note that due to the flexibility of the loading mechanism, the achieved drift ratio was typically less than the command (target) value.

7.3 Cyclic Response of the aFRD and sFRD Models

This section examines and compares the response of the aFRD and sFRD models under the quasi-static cyclic loading. Although these tests were carried out after the sequential dynamic shaking, physical observations after the sequential dynamic shaking indicate that the structural components and surrounding soil of both models were not severely damaged or deformed (Section 5.5). Therefore, the post-dynamic quasi-static cyclic testing is a reasonable means to characterize the model's seismic performance. Amongst the six drift amplitudes in the cyclic testing program, the last amplitude with the target peak roof drift ratio (PDR) of 4.0% is examined as it represents the large deformation demands on the system.

Figure 7.4 shows a photograph of the asymmetric foundation rocking dominated model (aFRD) subjected to a final monotonic push after the cyclic program. In this model, four types of plastic hinges are anticipated to develop, namely; rocking of the exterior column footing (ExCL_ftg), rocking of the interior column footing (InCL_ftg), rocking

of the shear wall footing (SW_ftg), and column fuse at the second level (CL_fuse2).The remainder of the structural components is intended to remain elastic during cyclic loading. A photograph of the sFRD model in the container is shown in Figure 5.10.

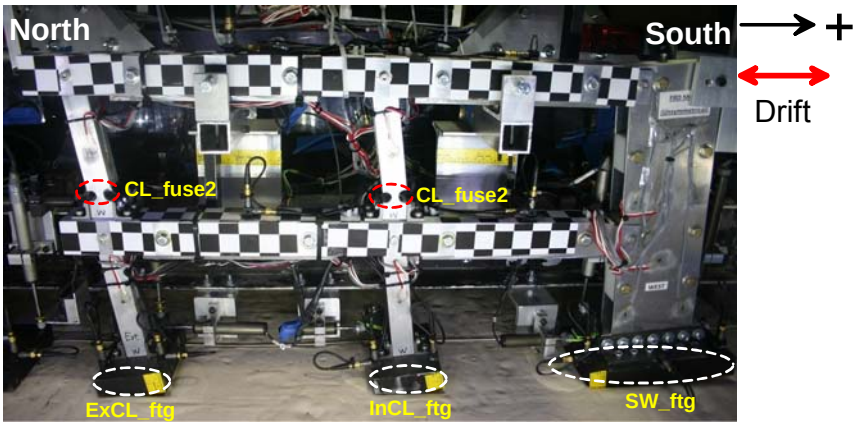

Figure 7.4 The aFRD model in the container at completion of slow cyclic testing

7.3.1 Axial Load Response

Figure 7.5a-c presents model schematics and the achieved drift ratio (DR) history under this cyclic DR amplitude. The DR is obtained by subtracting the footing sliding from the roof drift, which were both measured by linear potentiometers, normalized by the model elevation from ground surface. Two DR extrema are identified in this plot, where the solid circle-line and diamond-dashed line combinations represents the minimum and maximum DR, respectively.

Figure 7.5d shows the axial load response history resulting at each foundation of the sFRD model, including the north column footing (NCL_ftg), south column footing (SCL_ftg), and the shear wall footing (SW_ftg). The axial load is obtained by adding the footing weight to the axial SG measurement, which was recorded at the bottom of the

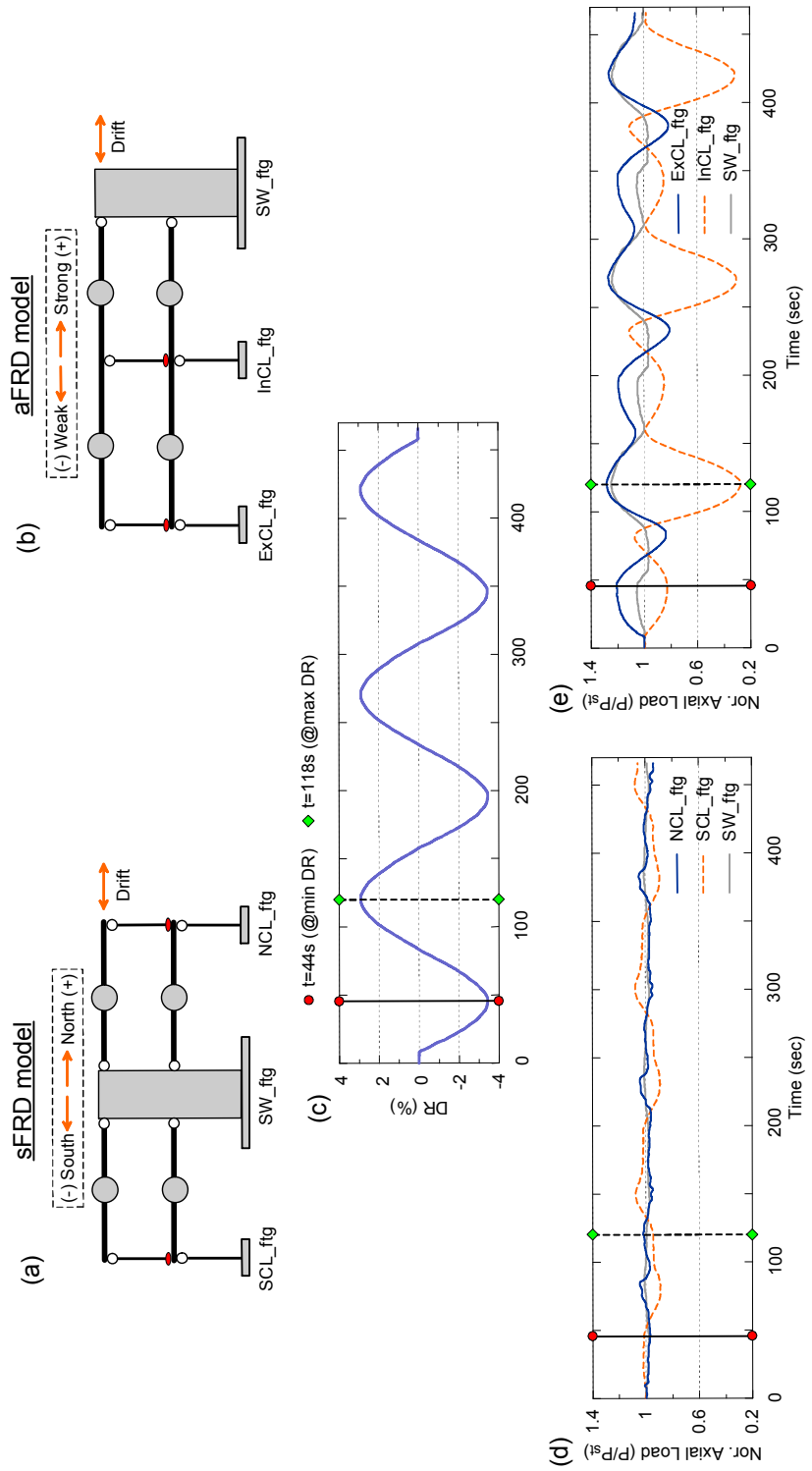

Figure 7.5 Observed axial load variation: (a) sFRD model schematic; (b) aFRD model schematic; (c) drift ratio (DR) time history; (d) normalized axial load history of the sFRD footings; (e) normalized axial load history of the aFRD model (Note: P_{st} of each footing is provided in Table 7.2)

columns or the wall. To facilitate comparison, each axial load response is normalized by its respective static value (i.e., 1070N, 800N, and 2330N for NCL_ftg, SCL_ftg, and SW_ftg respectively). The results indicate that the column footings are subjected to only a very slight axial load fluctuation, of no more than ±10% of their static values. The slight fluctuation can be attributed to frame action developed in the frame bay. The SW_ftg, however, observes nearly no axial variation.

Similarly, part (e) examines the normalized axial load response of the aFRD's rocking footings, namely the exterior column footing (ExCL_ftg), the interior column footing (InCL_ftg), and the SW_ftg. This plot shows that, in contrast to the sFRD footings' responses, all axial loads in the aFRD model develop significant variation, and their history of response generally exhibits a nonharmonic and irregular periodic manner, although the DR imposed is sinusoidal. Moreover, the performance of the interior footing (InCL_ftg) and the exterior footings (ExCL_ftg and SW_ftg) are fundamentally different. The InCL_ftg (dash line) consistently observes axial load reduction, with the largest reduction of over 72% at the maximum DR (t=118s). In contrast, the ExCL_ftg and the SW_ftg are subjected to amplification relative to their static axial loads nearly throughout the history.

The axial load variability of the aFRD model may be understood by examining the kinematics of the model (Figure 7.6). When the model is pushed towards the negative direction, the wall-footing subassembly tends to rotate around its left corner. As the roof drift increases, yielding of the column fuses at the upper level will generate pin-connections between the upper columns and first-story beam. At the same time, the beam element is fairly stiff against in-plane deformations. Therefore, rocking of the wall-

footing subassembly could tilt the beam, elevating the bottom interior column, and eventually reducing the total axial load imposed on the interior footing. The total axial load, however, remain unchanged since no external vertical load is applied. As such, tilting of the beams tend to compress the exterior column and SW as they seats in the soil, and thereby reinforcing the vertical load carried by the SW and exterior column accordingly. Likewise, if the system is loaded in the positive direction (towards the right), as shown in Figure 7.6b, a similar vertical load variation is observed. However, in this case, the beam-wall joint has a larger rocking radius (R_2) than the previous case (R_1) given a same roof drift, which implies that the interior column tends to be uplifted more when the model is pushed towards its positive direction. As a result, the InCL_ftg experiences a more notable axial load reduction during a positive DR excursion.

Part (c) schematically illustrates the load transfer mechanism under gravity load. The dead weight from the superstructure imposes eccentric axial loads on the wall component due to the asymmetry, resulting in an unbalanced counterclockwise static moment bias in the footing-soil interface, as denoted by M_o in this figure. This static moment bias could affect the lateral-force-resisting performance of the SW rocking footing and further the entire frame-wall-foundation system. When the model is loaded to the negative direction, the added initial moment will facilitate the mobilization of the SW rocking footing's capacity at a lower amplitude than anticipated in the symmetric model, which in turn attenuates its lateral force resisting capability. Therefore, the system tends to be weaker when pushed away from the SW, namely negative direction. Reversing the loading towards the SW (+) direction, an additional amount of lateral force is needed to

balance the static bias prior to mobilizing the SW footing's capacity; consequently, the system will behave relatively stronger when resisting a positive lateral load.

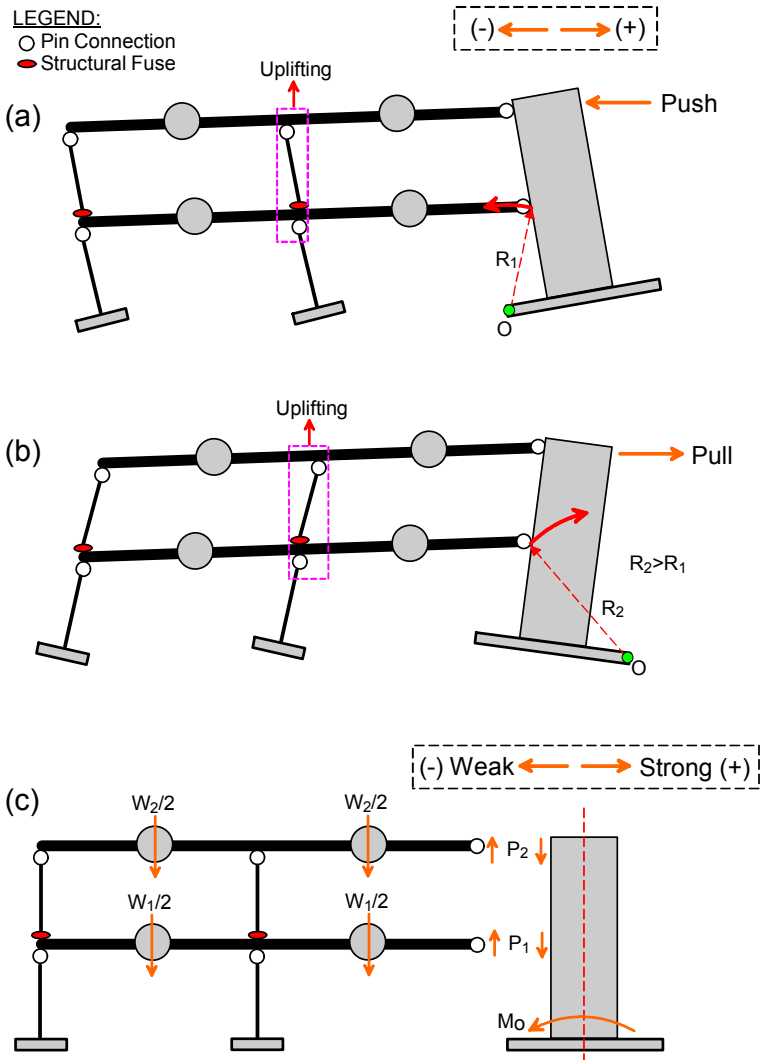

Figure 7.6 Kinematics of the aFRD model when subjected to: (a) negative horizontal roof displacement; (b) positive horizontal roof displacement; (c) static vertical load.

7.3.2 Hysteretic Response of Rocking Footings

Figure 7.7 examines the hysteretic response of rocking footings in the sFRD and aFRD model in terms of moment-rotation and moment-axial behavior. For all plots, the axial load is normalized by the static load (P_{st}), and the moment demand is normalized by the yield moment under a static axial load condition (i.e. M_{y_st} in Table 2). Note that the yield moment of the sFRD column footing and SW footing is 790 kN-m and 4790 kN-m respectively (Table 5.2). In addition, overlaid in axial-moment plot (P-M diagram), theoretical limits are provided assuming the footing and soil are infinitely strong (i.e M = P×L/2).

A cluster of response curves in Figure 7.7a indicate that the sFRD rocking footings perform symmetrically during reversed cyclic loading, and the axial loads of those components do not significantly vary, leading to an almost vertical line in the P-M interaction diagram. In contrast, all rocking footings of the aFRD model observe highly asymmetric hysteretic responses (Figure 7.7b). The axial load variation at each footing results in the inconsistent performance in the two directions. For example, the ExCL_ftg mobilizes its capacity during negative rotation, however it does not yield and it behaves relatively stiffer during a similar rotation in the positive direction. The variability in M-θ behavior is directly attributed to the instantaneous axial load on the footing. The P-M diagram shows that the static axial load is amplified by 28% during peak positive rotation, while it has a slightly less, 20% amplification at peak negative rotation. A larger axial load usually generates a larger yield moment and rotational stiffness. The InCL_ftg, on the other hand, yields in both directions; however, it observes an unusual and significant

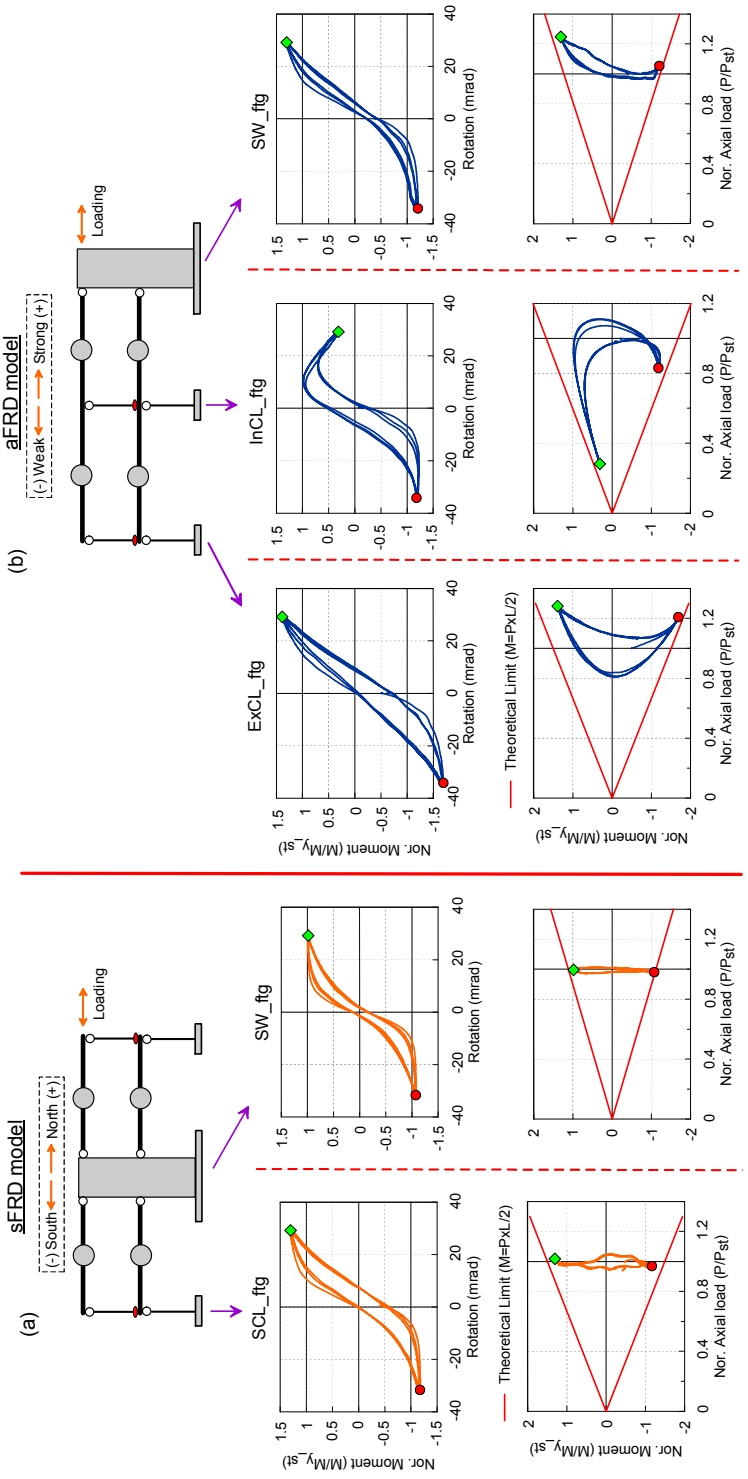

Figure 7.7 Moment-rotation (top row) and moment-axial (bottom row) response of: (a) the sFRD rocking footings; (b) the aFRD rocking footings (Note: circle and diamond denotes the time at the minimum and maximum DRs respectively as defined in Figure 7.5)

post-peak softening during positive rotation. The capacity at the maximum rotation (0.029 rad.) is reduced by about 70% compared with that achieved at a rotation of 0.01 rad. This "bend-over" hysteretic characteristic is directly attributed to the axial load reduction in the positive direction, with the corresponding axial load at about 0.2 P_{st}. The moment-rotation hysteresis of the SW_ftg has similar characteristics with that of the ExCL_ftg in terms of the normalized capacity and stiffness since both footings experience amplified axial loads in both directions. However, its hysteresis is narrower because its vertical factor of safety against bearing failure (FS_v=15) is larger than that of the ExCL_ftg (FS_v=9). One may also note that all P-M response curves are bounded by the theoretical limits, although all footings are subjected to significant axial load fluctuation.

7.3.3 System-Level Hysteretic Response

Figure 7.8 compares the system-level hysteretic response and response envelop of the aFRD and sFRD models. Part (a) compares the resultant system-level force-displacement curve of the aFRD and sFRD models under this cyclic amplitude of 4.0% target DR. The horizontal axis is the achieved DR, and the y-axis represents the total base shear normalized by the dead weight of the superstructure and footings. The sFRD model observes a symmetric system-level response, where the capacity attains about 30% of the building weight consistently towards the positive and negative directions. In contrast, the aFRD exhibits a highly asymmetric response in terms of the capacity and the stiffness. It is able to resist a lateral load of 35% of the building weight during the positive drift, whereas the strength drops to 22% in the negative direction. Moreover, the aFRD's

capacity is fully mobilized at early stage of the negative push while it has a strong tendency to stiffen when loaded in the opposite direction, as the roof drift reaches the maximum (DR = 2.9%). These characteristics further substantiate the significant impact of axial load variation and static moment bias on the system response.

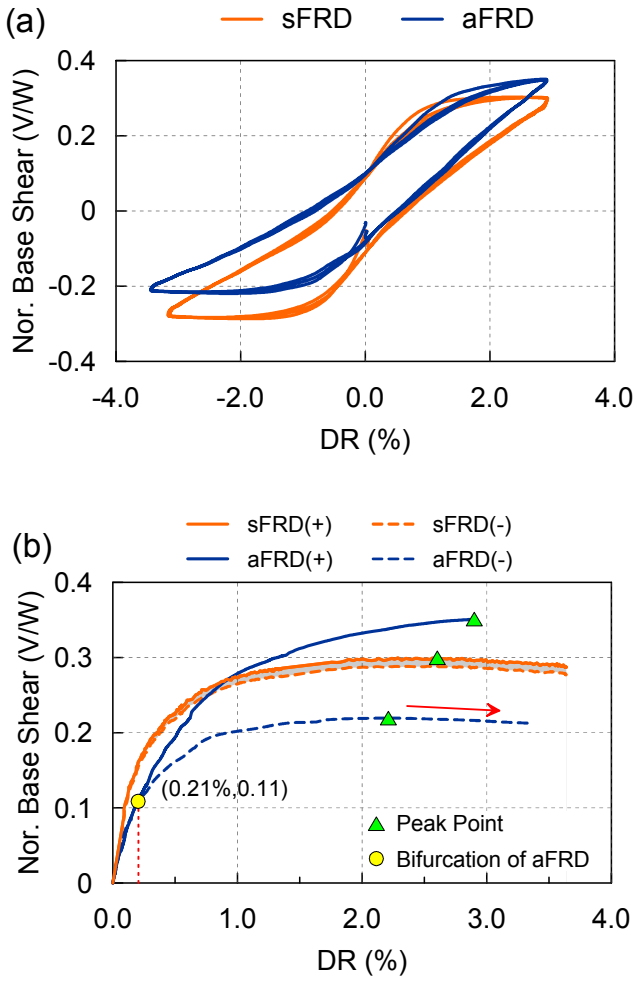

Figure 7.8 Hysteretic response of the aFRD model (cycle to target DR = 4%) compared with that of the sFRD model: (a) force-displacement; (b) response envelopes

Figure 7.8b provides the response envelops of the two models in each direction. These plots have been generated using all quasi-static cyclic DR amplitudes, by selecting the force at achieved maximum displacements during the first cycle. Inspection of the

aFRD response envelops reveals that the system behaves identical in both directions during near elastic response. When the DR exceeds than 0.21%, the force-displacement envelopes gradually diverge, and the difference between them becomes fairly significant beyond about 0.8% DR. At the peak achieved DR=2.9%, lateral-force-resisting capacity observed in the positive direction is about 60% larger than that in the negative direction. The system capacity in the negative direction is slightly deteriorated and demonstrates a negative slope due to P-Δ effects beyond about 2.2% DR. In contrast, the sFRD envelopes show that symmetric systems with little axial load fluctuations observe symmetric force-displacement envelopes. It is also apparent that its capacities in positive (+) and negative (-) directions are located in between the aFRD's capacities in either direction. Importantly, the sFRD model observes relatively larger system stiffness than the aFRD. This is because a relatively larger tributary axial load is allocated to the SW_ftg of the sFRD model, which increases the footing capacity, footing's rotational stiffness, and eventually the system stiffness.

7.3.4 Peak Footing and System Response

Figure 7.9 compares the engineering demand at maximum and minimum DRs under all cyclic events, including the axial load and shear force demand of the bottom of each component. Part (a) presents the axial load variation as a function of achieved DR. This plot continues to reveal the fundamental difference between the sFRD and aFRD models. Shaded regions demonstrate that the axial loads of the sFRD column footings vary within a small range (-5%, 11%); however, the fluctuations of the aFRD model are monotonic and dramatic. For example, the InCL_ftg is consistently subjected to

reductions in both directions (-17% at -3.45% DR, -72% at 2.92% DR), whereas the ExCL_ftg and SW_ftg experience pronounced amplifications at high drift levels.

Figure 7.9b compares the shear force demand carried by each component. These are shown as the relative contribution of the individual component. This plot illustrates that components of the sFRD model show little variability in their lateral load carrying shear, with about 17-20% going to each column and about 60-66% to the SW, for all cyclic events. In contrast, for the aFRD model, as a consequence of the significant axial load variation and the layout asymmetry, large fluctuations in relative normalized shear force is carried by the various components. The interior column, for example, initially carries 34% of the total lateral load, and its contribution dramatically decreases as the DR increases in positive direction (e.g., 11% at 2.92%). Conversely, the shear demand transferred to the shear wall and exterior column monotonically increase with the roof drift. The induced axial load reduction significantly degrades the interior footing's capacity, and thereby progressively reduces its ability to resist lateral load. In contrast, the SW and exterior column footing are stiffened due to axial load amplification, and correspondingly, their contributions tend to gradually ascend. When the model is subjected to a negative lateral load, the trends are completely different. The SW's relative shear force demand decreases from 41% to 26% as the DR increases from 0.08% to 0.34%, and the demand imposed on the columns are gradually amplified at initial stage. Static moment bias accelerates the yielding of the SW footing at low drift levels, which significantly decreases the SW footing's ability to resist lateral load and accordingly transmits the load to the column footings. As the DR increase in the negative direction,

the column footings will yield. Consequently, their lateral force resisting capability is reduced, and the SW footing gradually attracts more lateral load in the end.

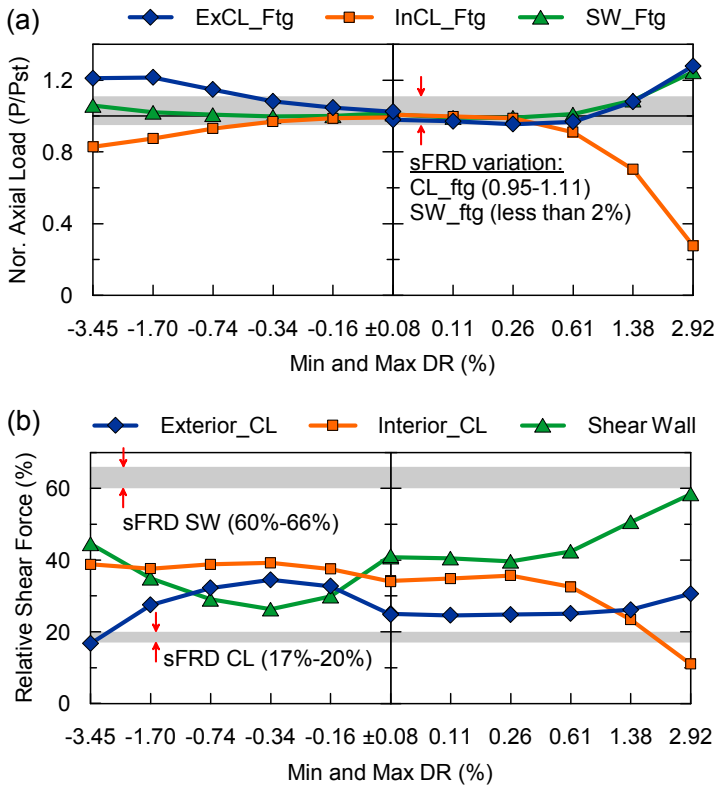

Figure 7.9 Peak engineering demand comparison under different cyclic events: (a) normalized footing axial load; (b) relative shear force at bottom level. (Note that scatter plot and shaded regions represent the data of aFRD and sFRD models respectively)

7.4 Seismic Performance Comparison: Peak Response

This section compares the peak seismic response of the symmetric and asymmetric models in terms of a variety of engineering demand parameters (EDPs). The EDPs of particular interest include the roof acceleration, the roof drift, and the total base shear.

7.4.1 Peak Roof Acceleration

Figure 7.10a-c compares the peak roof acceleration (PRA) response between the aFRD and sFRD models, the aBD and sBD models, and the aSHD and sSHD models, respectively. Considering the capacity difference of each asymmetric model in different directions, the peak response is decomposed into peak positive and peak negative directions for all models. These results indicate that for foundation rocking models (BD and FRD), the PRA of symmetric models is consistently larger than that of the asymmetric models in both directions. This difference is particularly pronounced for the BD models. The smaller PRA response is dictated by its lower footing strength (C_r in Table 7.1). For the SHD models, however, the symmetric case observes a lower PRA. There is a slight SW fuse strength reduction for both SHD models due to an initial stress induced by the static axial load; however, the strength of the sSHD model will be reduced further since it has twice the tributary axial load, compared with that of the aSHD model. As a result, the PRA is smaller for the sSHD model.

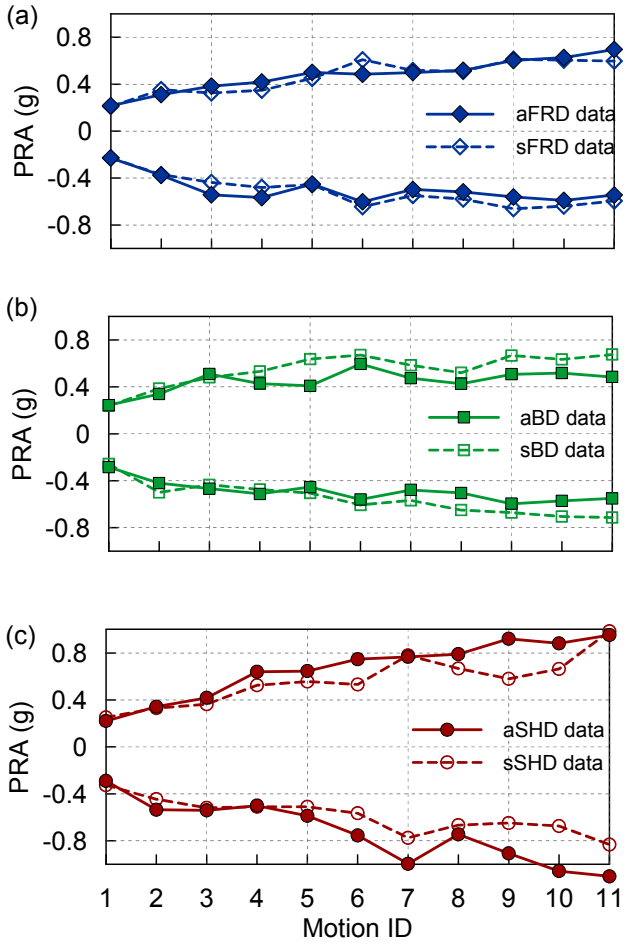

Figure 7.10 Peak roof acceleration (PRA) comparison: (a) FRD models; (b) BD models; (c) SHD models

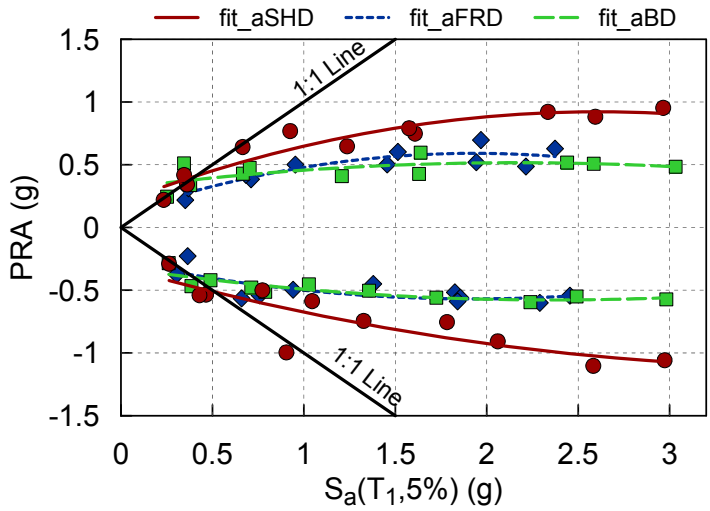

Figure 7.11 PRA comparison amongst the asymmetric models: PRA vs the free field S_a (T_1, 5%) (Note: the lengend of scatter points is provided in Figure 7.10)

Figure 7.11 compares the PRA response of each asymmetric model in a similar format with that of Figure 6.5b. Namely, the x axis is the elastic spectral acceleration at T_1 of each model, evaluated using the measured free field motion. Second-order polynomial trend lines and one-to-one line are added in this plot as well. This plot shows that, as the shaking intensity increases, significant inelasticity is developed in all models since their PRAs are all located below 1:1 lines in both directions. Importantly, the asymmetric foundation rocking systems (the aBD and aFRD models) are likely to attenuate the PRA in both directions compared with the asymmetric structural hinging dominated model (aSHD).

7.4.2 Peak Roof Drift Ratio

In like fashion, Figure 7.12 compares the peak transient roof drift ratio (PDR) of each asymmetric and symmetric models. The roof drift ratio (DR) is obtained via double integration of the relative roof acceleration and presented relative to the footing level, and normalized by the total building height from the ground surface. Part (a) shows that the aFRD model receives nearly identical peak drift response with the sFRD for most of the motion scenarios. This implies that the axial load variation and building asymmetry have a minimal impact on the FRD systems in terms of the PDR demand. When the inelastic structural fuse mechanism is engaged (BD models), however, the asymmetric model is consistently subjected to a larger PRD demand, as indicated in part (b). This observation is further substantiated by examining the response difference between the SHD models. As illustrated in part (c), the axial load variation associated with the asymmetry dramatically increases the PRD demand to the aSHD model.

Figure 7.13 plots the PDR as a function of the elastic spectral displacement S_d at T_1 of the models normalized by the building height for all asymmetric models. Second-order polynomial trend lines and one-to-one line are added in this plot as well. The results continue to show that the peak drift demand of the sSHD model is slightly larger than the elastic spectral drift demand even during a high-intensity motion. The foundation rocking models, particularly the aFRD model, on the other hand, tend to significantly amplify their PDRs in both directions. This observation is consistent with that observed in the symmetric models (Section 6.4.2).

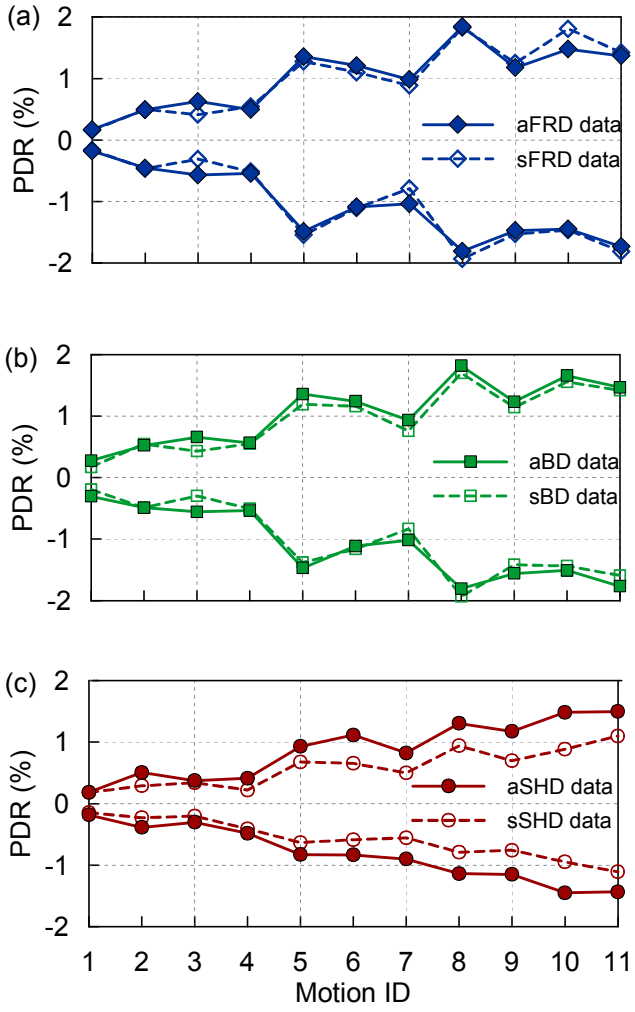

Figure 7.12 Peak drift ratio (PDR) comparison: (a) FRD models; (b) BD models; (c) SHD models

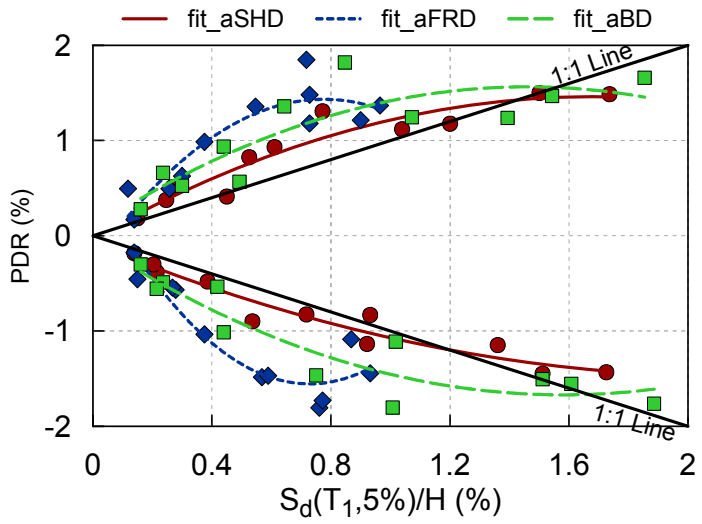

Figure 7.13 PDR comparison amongst the asymmetric models: PRA vs the normalized free field S_d (T_1, 5%) (Note: the lengend of scatter points is provided in Figure 7.12)

7.4.3 Peak Base Shear

Lastly, the peak base shear demand is compared between the asymmetric and symmetric models in Figure 7.14. For all plots, the base shear (V_{base}) is normalized by the model's weight (W) as expressed in a base shear coefficient (C_s=V_{base}/W) shown on the y-axis.

Similar with the PRA response, the observed base shear demand is consistently smaller for the asymmetric foundation rocking models (the aFRD and aBD models) compared with the symmetric cases, as shown in part (a) and part (b). This can be explained by the fact that the base shear demand is dictated by the system's strength. Furthermore, the difference is relatively larger in the negative direction. This observation continues to substantiate the incommensurate system-level capacity in two directions which is induced by the axial load fluctuation and building asymmetry. For the SHD

models, its symmetric setup is likely to receive a smaller base shear compared with the asymmetric counterpart. As noted previously, a double axial load acting on the SW fuse in the sSHD model reduces its flexural strength more than the aSHD model and thereby the lateral-load-carrying capacity.

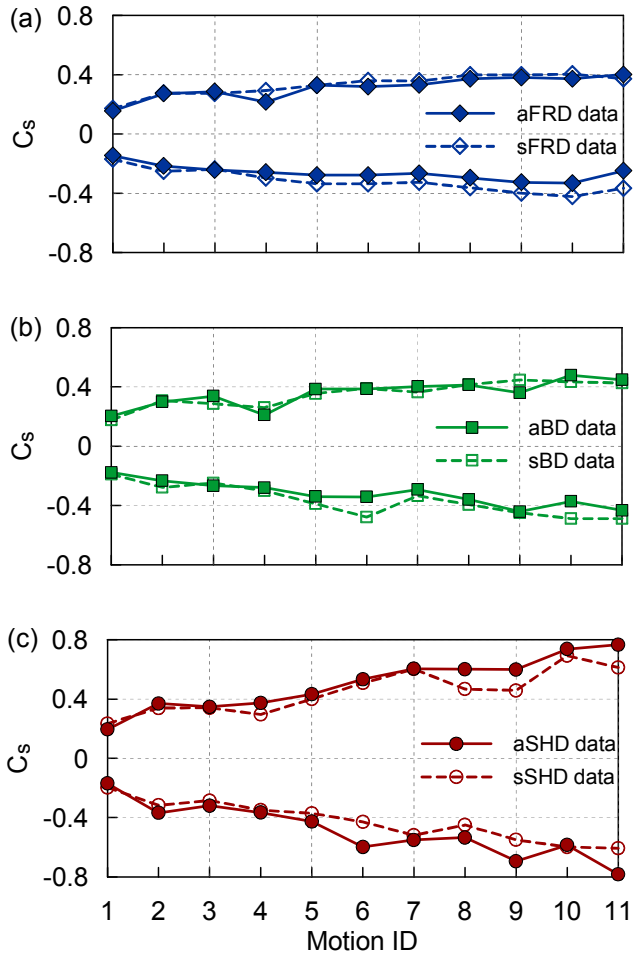

Figure 7.14 Normalized peak base shear (C_s) comparison: (a) FRD models; (b) BD models; (c) SHD models

Figure 7.15 compares the peak base shear demand amongst the asymmetric models by using the elastic S_a at T_1 of each model on the x axis. The plot indicate that,

under similar moderate- and high-intensity motions, the aSHD model consistently observes the largest peak base shear demand. The foundation rocking dominated model (aFRD), on the other hand, tends to receive the smallest peak base shear compared with other models in both directions. These observations are consistent with the results when comparing amongst symmetric models (Section 6.4.3; Figure 6.7).

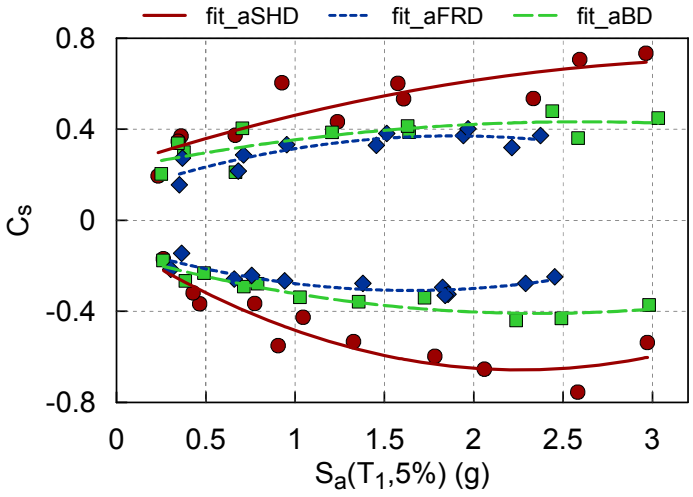

Figure 7.15 Normalized peak base shear (C_s) comparison amongst the asymmetric models: Cs vs the free field S_a (T_1, 5%) (Note: the lengend of scatter points is provided in Figure 7.14)

7.5 Seismic Performance Comparison: Axial Load Fluctuation and Hysteretic Response

7.5.1 Dynamic Axial Load Fluctuation

Axial load fluctuation induced by building asymmetry during seismic loading is summarized in Figure 7.16. This figure plots the uncorrelated maximum and minimum

axial load response of each rocking footing for each asymmetric model as a function of motion ID. Note that all axial load response plotted on the y-axis are normalized by their static axial load values acting on footing (Table 7.2). The corresponding values of the aSHD vertical components, however, are used by the axial load recorded at the bottom of the vertical components since they are supported by a big strip footing. The static axial load recorded at the exterior column, interior column, and the shear wall for the aSHD model are 540, 1180, and 630 kN respectively.

Part (a) compares the axial load variation at the exterior column footing (ExCL_ftg). The plot shows that the exterior column of the aSHD observes the largest axial load fluctuation. Starting from motion #7, its response can be amplified or reduced by up to 60%. For the aFRD and aBD models, the axial load of their exterior column foting varies a considerable amount as well; however, it tends to receive more amplification than reduction. This tendency is more pronounced for the aBD model during strong motions. In contrast, the interior column footing (InCL_ftg) experiences more reduction than amplification, particularly for foundation rocking models, as illustrated in Figure 7.16b. The amplification is generally less than 10% even under the strongest motions; however, the reduction can attain more than 40%. In particular, the aBD model observes more than 60% reduction in its InCL_ftg during high-intensity motions (e.g., after motion#8). This significant reduction can be explained by recalling the structural kinematics (Figure 7.6). When the model is subjected to a lateral load, rocking of the SW foundation tends to uplift the interior beam-column assembly which in turn will mitigate the vertical load transmitted to the interior column. The interior column

of the aSHD model, however, has a steady axial load response which fluctuates within 20% of its static load.

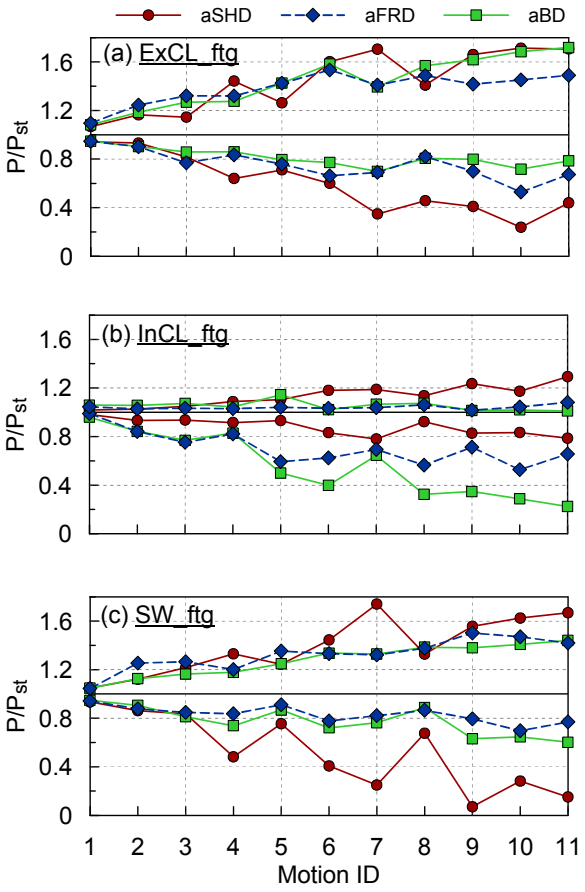

Figure 7.16 Normalized axial load (P/P_{st}) fluctuation during earthquake loading: (a) exterior column footing (ExCL_ftg); (b) interior column footing (InCL_ftg); (c) shear wall footing (SW_ftg)

Part (c) compares the axial load variation observed in the wall component of all models. Similar with the exterior column's response, the aSHD's SW observes the biggest axial load fluctuation. For example, its axial load can be either amplified by up to 74% (motion #7) or reduced up to 93% (motion#9). For the aBD and aFRD models, the SW footing experiences a slightly more amplification than reduction. During moderate-

intensity motions (e.g., from #5 to #8), their axial loads vary from -20% to 35%. Upon high-intensity shaking, its fluctuation range is expanded to (-40%, 50%).

7.5.2 System-Level Hysteretic Response

Figure 7.17 presents a suite of system-level hysteretic curves of all asymmetric models, where each row represents the performance under input motions of increasing intensity (top to bottom) and the columns represent different model configuration. The y-axis for all plots is the base shear normalized by the building weight, and the x-axis represents the transient drift ratio. In addition, the response of each symmetric counterpart under the same motion is added.

When subjected to a low-intensity motion (GZ_0.2), all models perform almost linear elastically. Comparing to the elastic response of the symmetric models reveals that the initial stiffness of each asymmetric model is slightly less than that of its symmetric counterpart. During the fifth motion (KB_3.0), all models observe nonlinear inelastic response. The foundation rocking dominated models (aFRD and aBD) behave slightly asymmetric in terms of the capacity and stiffness in both directions. These systems' capacities in the negative direction for are mobilized at a DR of approximately -0.5%, while they yield at around 1.0% DR and perform relatively stiffer in the positive direction. These asymmetric performances are largely attributed to the axial load variation and static moment bias induced by the asymmetry. The aSHD model, however, observes the least impact to the hysteretic response since it is nearly symmetric in both directions. When applied the strongest shaking (CMS_1.5), the asymmetric response becomes more pronounced, particularly for the aFRD model. The normalized peak base shear in the

negative and positive directions attains -0.25 and 0.40 respectively. Nonetheless, the aSHD model under this motion case still observes a nearly symmetric inelastic response in both directions.

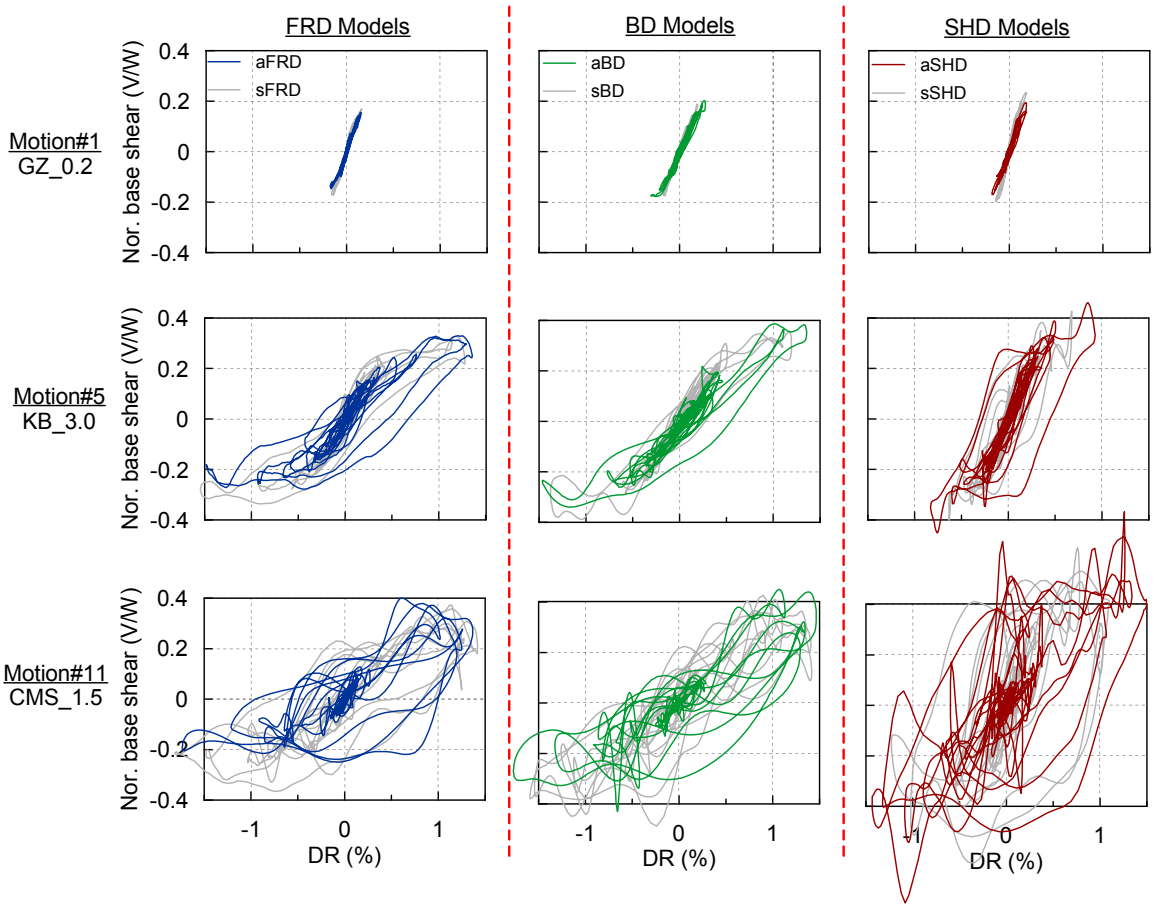

Figure 7.17 System-level hysteretic response comparison between symmetric and aymmetric models under three motions with differen intensity

7.5.3 Relative Energy Dissipation

Relative dissipated energy of all inelastic components for the asymmetric models are investigated and shown in Figure 7.18. The dissipated energy is computed by integrating the area of the moment-rotation hysteresis, and the relative dissipated energy

is calculated by normalizing each by the total. Note that the energy diffused by other non-flexural modes, such as footing nonlinear sliding or settlement, is not considered in this calculation. For the results of the aFRD and aBD models, a dashed line is added to separate the contributions from the inelastic substructure components (rocking footings) and superstructure components (SW and column structural fuses). In the aSHD model, the dashed line divides the contribution between the SW fuse and column fuses. In addition, straight lines are provided to display the corresponding energy distribution observed in its symmetric counterpart (Figure 6.13).

Part (a) shows that, under low-intensity motions (#1-#4), the majority of the dissipated energy in the aFRD model are contributed by the rocking of the footings (>70%). As the intensity increases, the inelastic flexural behavior of the column fuses dissipates a considerable amount of energy due to its broad hysteresis (Figure 5.11a). In the aBD model (part b), more energy is dissipated within the superstructure inelastic elements under low-intensity shaking (e.g., nearly >60% for motions #1-#4). Upon moderate- and high-intensity shaking, the relative energy dissipated by the rocking footings gradually ascends resulting in a well-distributed mode between the superstructure and substructure. In the aSHD model, as indicated in part (c), the inelastic flexural behavior of the SW fuse dominates the energy dissipation (>90%) during moderate- and high-level motions. Lastly, it is important to note that the energy distribution mode observed in all asymmetric models (dashed lines) is almost consistent with that of the symmetric models (solid lines). As such, it can be concluded that the building asymmetry or the axial load fluctuation will not significantly alter the inherent

energy dissipation mode of the low-rise frame-wall-foundation systems regardless of the motion intensity and the yielding hierarchy between the dominant inelastic elements.

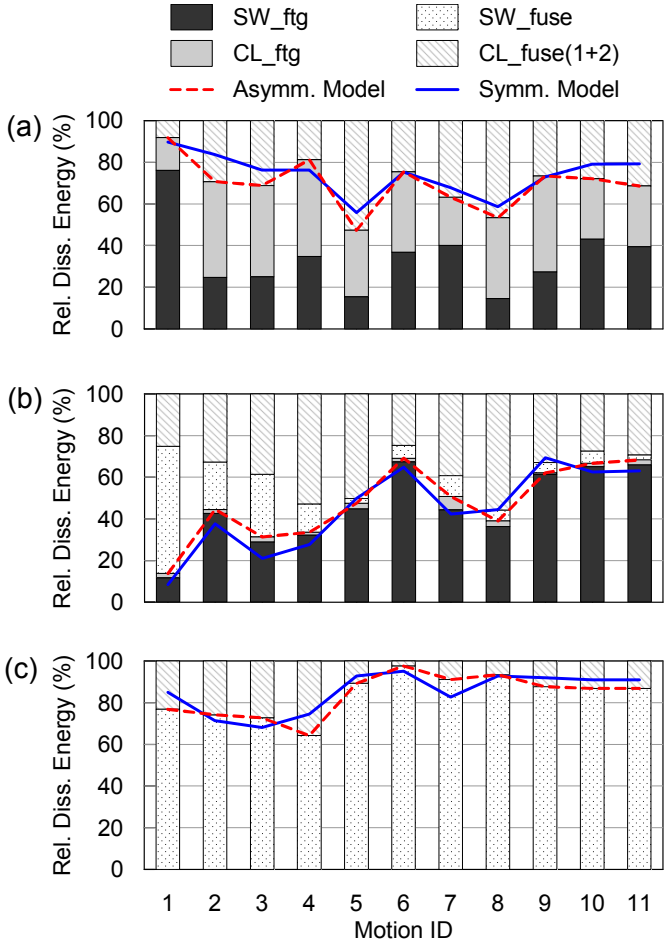

Figure 7.18 Relative energy dissipation distribution: (a) aFRD model; (b) aBD model; (c) aSHD model

7.6 Seismic Performance Comparison: Residual Response

7.6.1 Residual Drift

During strong shaking, components' inelastic behaviors could induce residual deformations, which will directly affect the functionality and/or occupancy of the building if significant. Therefore, the residual demand is an important damage state index for evaluating the seismic performance of each frame-wall-foundation model.

Figure 7.19a-c compares the cumulative residual drift ratio (RDR) relative to the foundation of each asymmetric and symmetric model. The measurements of residual deformations are taken directly from displacement sensors in contrast to the peak response obtained via double integration method. These plots show that all symmetric models cumulate less permanent deformation than their asymmetric counterparts, particularly for the sFRD and sBD models. Therefore, it is concluded that considering a symmetric layout could help to minimize the system-level residual deformation of the frame-wall-foundation system. In addition, all asymmetric models cumulate a negative residual deformation, as indicated by the straight lines, which continue to confirm their weak load-carrying capability in the negative (weak) direction.

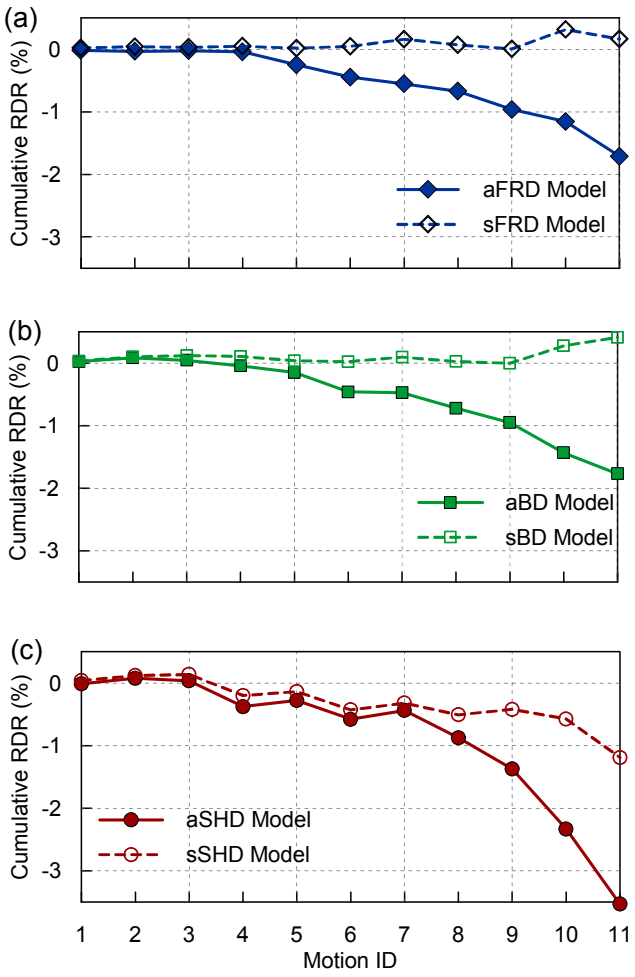

Figure 7.19 Cumulative residual drift ratio (RDR) comparison between: (a) FRD models; (b) BD models; (c) SHD models.

Figure 7.20 compares the residual performance of the asymmetric models in two different ways. Part (a) plots the cumulative residual drift ratio (RDR) of each model as a function of the sequential motion imposed, whereas part (b) plots event-based RDR for each type of model relative to the footing against its respective peak roof drift (PRD). Note that measurements of residual deformations are taken directly from displacement sensors, in contrast to the peak deformations, which are obtained via double integration of accelerations.

Part (a) shows that all three models experience a similar and small cumulative RDR after the first 7 motions (around -0.5%). Upon the last four high-intensity shaking, the aSHD cumulates the RDR up to -3.5%, whereas the aFRD and aBD models observe -1.71% and -1.77% respectively. This observation continues to support the contention that the structural hinging mechanism has the lowest potential for recovering the system once its inelastic behavior is developed. Foundation rocking models, especially the FRD-type system, on the other hand can still maintain its beneficial re-centering capability despite that the SW is placed to the extreme end of the building.

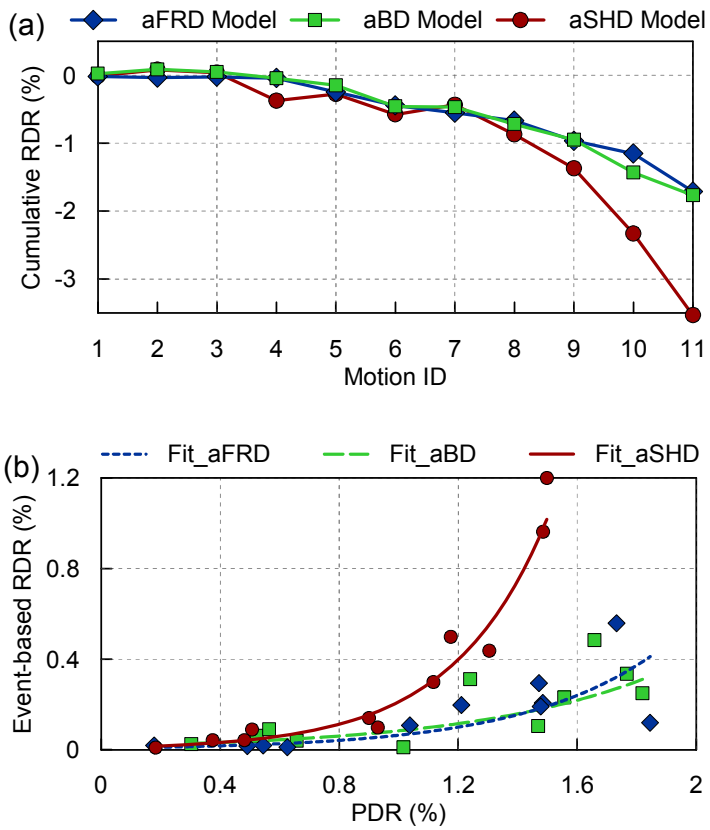

Figure 7.20 Residual drift ratio (RDR) comparison amongst asymmetric models: (a) Cumulative RDR vs Motion ID; (b) Event-based RDR vs Peak drift ratio (PRD)

Part (b) plots event-based RDR against the peak roof drift (PRD) for all asymmetric models. Three second-order fit lines are added in this plot. Consistent with the response of the symmetric SHD model, as shown in Figure 6.9b, the asymmetric SHD model has also shown its greatest tendency to develop the largest residual drift compared with the foundation rocking models. Given a PRD of 1.5%, for example, the aSHD system is likely to experience a 1.0% RDR which is about 4 times of those of the aFRD and aBD systems. Therefore, the advantageous re-centering benefit of the foundation rocking mechanism is further substantiated.

7.6.2 Foundation Residual Settlement

Foundation residual behaviors, such as permanent settlement, sliding, or rotation, could affect the building's functionality as well. Figure 7.21a-b presents the cumulative settlement of the SW and column footings relative to the free field ground surface for the aFRD and aBD models, respectively. Note that all footings' settlement data are normalized by its respective footing length (Table 7.1). The plots in part (a) show that, the aFRD's interior column footing (InCL_ftg) experiences the largest normalized cumulative settlement (2.88%) by the end of the sequential shaking. This is because it carries a significant amount of axial load (Table 7.2), and the footing size is small. On the other hand, its shear footing (SW_ftg) observes the least normalized permanent settlement since its size is much larger. Similar observations are found in the aBD model (part b). In addition, all footings in the aBD model in general settle less than that the aFRD model, which implies that a moderate enlargement of the SW footing's size could help to minimize the permanent settlement for the entire frame-wall-rocking foundation system.

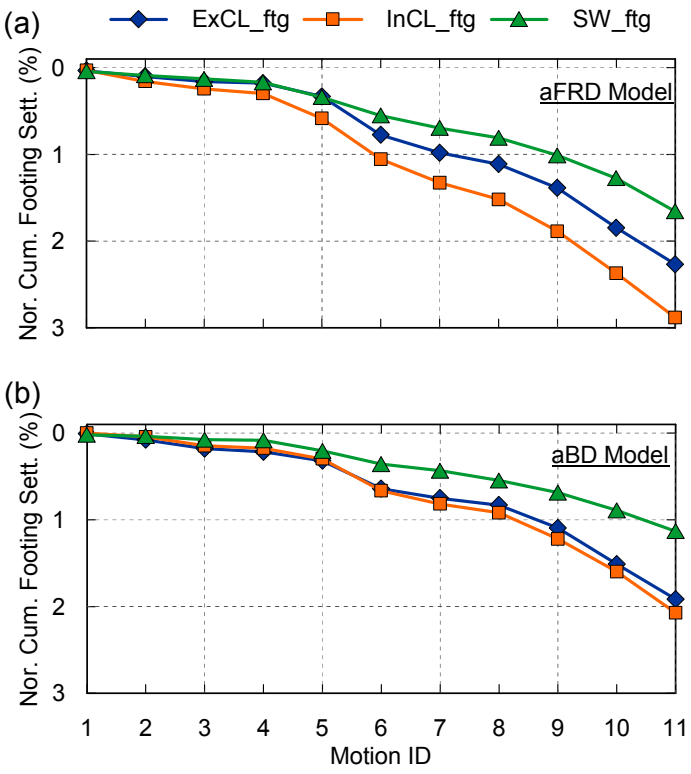

Figure 7.21 Normalized cumulative footing settlement comparison: (a) aFRD model; (b) aBD model

7.6.3 Foundation Residual Sliding

Figure 7.22 investigates the normalized cumulative permanent sliding response for the aFRD and aBD models. Part (a) continues to reveal the seismic deficiency of the column footings in the aFRD model. The InCL_ftg and ExCL_ftg cumulate a permanent sliding of -2.5% and -1.9% of the footing length by the end of sequential shaking, respectively. The SW_ftg however undergoes a normalized residual sliding of -0.4%. The aBD model observes a different residual sliding response, as indicated in Figure 7.22b. The column footings of the aBD model experience less severe normalized permanent sliding (0.4% for the ExCL_ftg and -1.1% for the InCL_ftg). Those small responses can be understood by the fact that the yield moment of column fuses is less than that of the column footing (Table 7.2). Thus, the column footings' movement is greatly discouraged. The SW_ftg, on the other hand, observes a significantly large normalized permanent sliding (-1.8%) compared with that observed in the aFRD. This is related to its low moment-to-shear ratio (Table 7.1). A rocking foundation with this ratio low indicates that sliding mode can contribute to the footing's movement beyond rocking (Gajan and Kutter 2008).

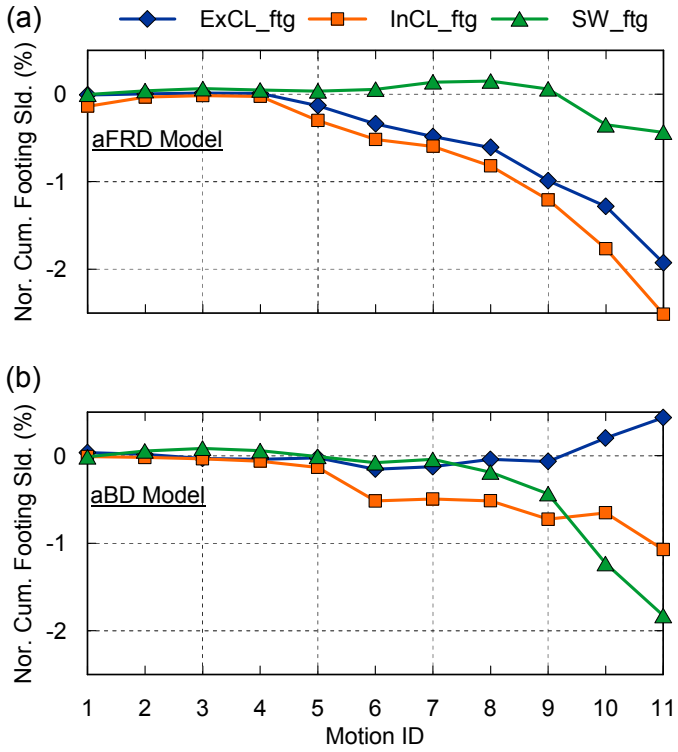

Figure 7.22 Normalized cumulative footing sliding comparison: (a) aFRD model; (b) aBD model

7.7 Conclusions

The yield moment of a rocking foundation is highly dependent on the imposed axial load; therefore, axial load fluctuation can affect the shape of its moment-rotation hysteresis, and potentially the seismic performance of the entire structure-footing system. Particularly for a frame-wall-foundation system constructed with an asymmetric layout, the likelihood of axial load fluctuation can be increased, and its effects to the seismic performance can become more severe. This chapter studies the impacts of the axial load variation and building asymmetry on the seismic performance of two-story-two-bay frame-wall-rocking foundation systems. Test-2 constructed and tested three types of reduced-scale models with like geometry considering the capacity variation between the shear wall (SW) structural fuse and rocking foundation, namely; structural hinging dominated (SHD), foundation rocking dominated (FRD), and balanced design (BD). Importantly, these models were tested within both symmetric and asymmetric layouts considering the variation of SW location. Comparing the seismic performance of asymmetric models and their symmetric counterparts when subjected to quasi-static cyclic and earthquake loading may draw the conclusions as follows.

- All footings of the aFRD model are susceptible to the variation of the axial load compared to those of the sFRD model when subjected to high amplitude cyclic loading. In particular, the interior column footing observes a significant axial load reduction when the model is loaded towards the positive (strong) direction. This reduction leads to a highly asymmetric moment-rotation hysteresis with a “bend-over” characteristic.

In addition, the system-level lateral load-carrying capacity of the aFRD is highly incommensurate in both directions.

- When subjected to a suite of earthquake loading, all asymmetric rocking foundation systems observe smaller peak roof accelerations and peak base shear demands compared with the symmetric cases particularly in the negative (weak) direction. The peak roof drifts, however, are slightly larger in the asymmetric models.
- During strong motions, axial load acting on each footing of the aFRD and aBD models fluctuate significantly; in addition, their system-level hysteretic curves are highly asymmetric in terms of the capacity and stiffness in both directions. Despite that the aSHD model observes the largest axial load fluctuation in the shear wall (SW) and exterior column, the system still performs nearly symmetrically in both directions.
- The hysteretic energy is mostly concentrated within the soil-footing interface for the aFRD model, whereas it is well distributed between the inelastic superstructure and substructure components in the aBD model during moderate and strong shaking. Moreover, the fluctuation of the axial load and building asymmetry do not significantly influence the relative energy dissipated by inelastic superstructure and substructure components irrespective of motion intensity and the yielding hierarchy between the dominant inelastic elements.
- Placing the SW in the middle of the frame-wall-foundation system can greatly minimize the residual deformation developed at each asymmetric

model. In the aFRD model, the interior column footing experiences the largest normalized residual settlement and sliding compared with the other footings. However, the SW footing of the aBD model observes the largest cumulative permanent sliding.

- The experimental raw data of the test program described in this chapter are provided at NEEShub website with a permanently assigned Digital Object Identifier (DOI) of 10.4231/D3NG4GR9C. (http://nees.org/warehouse/experiment/4940/project/732)

7.8 Acknowledgements

This chapter, in part, is currently being prepared for submission to technical journals. The article is tentatively titled "Effect of Seismic-Induced Axial Load Fluctuation on Asymmetric Frame-Wall-Rocking Foundation Systems" with a preliminary author list of Weian Liu, Tara C. Hutchinson, Bruce L. Kutter, Andreas G. Gavras, and Manouchehr Hakhamaneshi (201X). At completion of this dissertation, its final form was in preparation. However, the dissertation author is the primary investigator and first author of these papers.

Chapter 8

Correlation between Energy Dissipation and Self-Centering Characteristics for Idealized Inelastic Systems

8.1 Introduction

8.1.1 Background

Performance based design (PBD) requires select structural components be strategically designed to respond beyond their elastic limit during moderate and high seismic events (e.g. Paulay and Priestley 1992). The inelastic response of these components are intended to dissipate hysteretic energy and thereby mitigate the demand or damage imposed on other components. This strategy reduces overall construction costs

since an excessively conservative design is not necessary to withstand an earthquake. Clearly, a key to successfully implementing PBD then is the design of structural components with ample capability to dissipate energy under seismic loading. Unfortunately, however, an inherent shortcoming associated with these energy dissipating components is their potential to suffer residual deformation. For many of the existing structural connections or other elements designed to dissipate hysteretic energy, they are unable to recover from the large deformations, which are well beyond yield, imposed during a design seismic event. As a result, it will cause permanent deformation. If the permanent deformation is excessive, it may directly affect the functionality and/or occupancy of the structural system, and could render the structure sufficiently weakened and unable to carry service loads or aftershocks following the main event.

To minimize seismic-induced residual deformations, structural engineers have proposed a variety of external self-centering devices, which are intended to assist the structure in returning to its original position. For example, unbonded prestressed tendons have been introduced into concrete frame structures at beam-to-column connections to render a self-centering response (i.e. Priestley and Tao 1993; Stanton et al. 1993). Subsequently, this idea is extended to cantilever Reinforced Concrete (RC) rocking wall units (Holden et al. 2003; Kurama and Shen 2004; Ajrab et al. 2004) and steel moment-resisting frame structures (Ricles et al. 2001; Christopoulos et al. 2002; Christopoulos et al. 2008). In an effort to improve the energy dissipation capability of these hybrid systems, ductile and dissipative elements, such as mild steel reinforcement (Holden et al. 2003; Palermo et al. 2005; Restrepo and Rahman 2007), customized energy dissipating bars or steel plate dampers (Christopoulos et al. 2002; Ikenaga et al. 2006; Takamatsu et

al. 2006), or ductile steel brace elements (Tremblay et al. 2008), have been proposed and implemented into hybrid self-centering systems.

The idea of a rocking block however accomplishes (naturally) similar restoring tendencies of all of the aforementioned self-centering devices. The elegance of this idea, however, is that through the bodies own dynamic actions it will naturally tend to restore itself to its original position, provided the line of action of the resultant vertical force with the body does not exceed the outer bounds of the base of the rocking block (at which time it would overturn). Indeed, this rocking mechanism has been highlighted as another important seismic design alternative since the rocking component can sustain large displacements without incurring significant and with minimal damage or residual deformations (e.g. Housner 1963). In recognition of these beneficial attributes, a number of large-scale experiments have been conducted to evaluate the seismic benefits of rocking behavior when introduced into frame systems (Clough and Huckelbridge 1977; Kelley and Tsztoo 1977; Eatherton et al. 2010; Ma et al. 2010), a bridge pier system (Pollino and Bruneau 2008), and concrete and masonry wall systems (Restrepo and Rahman 2007; Toranzo et al. 2009). Allowing a shallow foundation to rock can also provide some of these desirable response characteristics, such as energy dissipation and a self-centering tendency (see literatures presented in Section 2.3). When this mechanism is integrated into structural systems with other inelastic (superstructure) elements, e.g. bridge structures (Deng et al. 2012), frame-type buildings (Chapter 4; Liu et al. 2013), or frame-wall-foundation systems (Chang et al. 2007; Chapter 5-7), the entire structure-footing system's seismic performance is greatly improved.

8.1.2 Scope of this Chapter

Considering the aforementioned benefits of energy dissipation and re-centering, it is desirable to collectively evaluate them in a system in order to fully characterize its seismic performance. Using an idealized hysteretic curve, this chapter proposes two dimensionless parameters, namely the energy dissipation ratio (R_{ED}) and the re-centering ratio (R_{RC}), to quantify the abilities of an inelastic structural system to dissipate hysteretic energy and recover from induced inelastic deformations, respectively, during cyclic loading. It is noted that these parameters are designed to represent the potential capacity of a system to elicit both types of benefits. For any inelastic structural component or system, these two parameters are not independent, but rather they are inherently related. As such, analyzing these two parameters by correlating them provides additional insight into the system's seismic characteristics. The primary goal of this chapter is to establish a diagram relating these two parameters, and importantly, to utilize this diagram to characterize hysteretic performances of several simplified (idealized) inelastic structural systems. The simplified systems are constructed by one single fuse or multiple fuse elements placed in parallel and/or series and numerically studied in the simulation platform *OpenSees*. Parametric studies are performed to examine the effects of varying the governing parameters of single fuse elements or varying strength among multiple fuses on the R_{ED}-R_{RC} relation. Finally, the observed cyclic test data of frame-wall-foundation models constructed in Test-2 are analyzed via the R_{ED}-R_{RC} diagram in order to evaluate the seismic performance of each model.

8.2 Definition of Energy Dissipation Ratio and Re-centering Ratio

8.2.1 Definition of R_{ED} and R_{RC}

To schematically introduce the energy dissipation and re-centering ratios, Figure 8.1 provides a simplified force-displacement hysteresis of an inelastic element under one full cycle of loading. In this response, the attained maximum deformation and its associated force is termed δ_{max} and F_{max}, respectively. Correspondingly, the peak response in the negative direction is termed δ_{min} and F_{min}. It is assumed that the system cumulates a total differential deformation of $\Delta\delta$ at zero force, and the enclosed area of the hysteresis (shaded area), which represents the actual dissipated hysteretic energy, is denoted as A_{HT}. With knowledge of all these parameters, the energy dissipation ratio (R_{ED}) is defined as the ratio of the hysteretic area (H_A) to the maximum potential hysteretic area enclosed by the dashed lines, as expressed in the equation (8.1). It is noted that the region enclosed by the dashed line represents an idealized rigid, perfectly plastic response, which would result in optimally large hysteresis (absent negative post-yield response - which is undesirable due to P-Δ effects and the potential for system instability during an earthquake.

$$R_{ED} = \frac{H_A}{(F_{max} - F_{min}) \times (\delta_{max} - \delta_{min})} \tag{8.1}$$

Note that the values of F_{min} and δ_{min} are assumed as negative.

With regard to the re-centering ratio, it is introduced by examining the relation between the cumulative residual deformation at zero force demand ($\Delta\delta$) and the

experienced peak deformation demand (δ_{max} and δ_{min}), which is determined by equation (8.2).

$$R_{RC} = 1 - \frac{\Delta\delta}{(\delta_{max} - \delta_{min})} \tag{8.2}$$

Note that the $\Delta\delta$ is always taken as positive.

By definitions, both R_{ED} and R_{RC} range from 0 to 1, where a larger value indicates a larger capacity for dissipating energy or re-centering the system. Note that the term of "re-centering" in the R_{RC} terminology does not necessarily imply that the system has an inherent self-centering behavior as many structural engineers expect. But rather, it quantifies how well the system can recover from peak displacements.

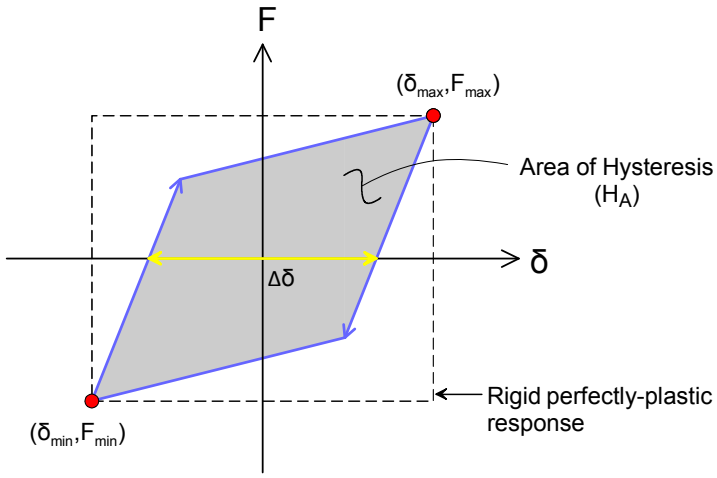

Figure 8.1 Schematic force-displacement to illustrate parameters R_{ED} and R_{RC}

8.2.2 Illustrative Force-Displacement Responses

To illustrate the utility of R_{ED} and R_{RC}, four extreme force-displacement responses are provided in Figure 8.2. Ordered from (a) to (d), these represent linear elastic, rigid perfectly-plastic, perfect re-centering, and elastic-perfectly plastic behavior.

Note that in part (d), the term μ is used to define the displacement ductility, which may be determined as δ_{max}/δ_y, where δ_y = yield displacement.

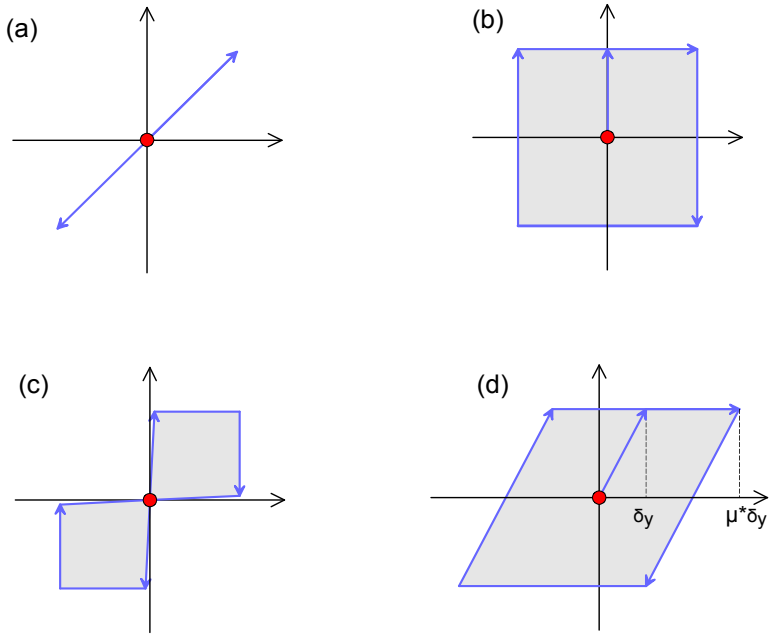

Figure 8.2 Four illustrative force-displacement responses: (a) linear-elastic; (b) rigid perfectly-plastic; (c) perfect re-centering; (d) elastic-perfectly plastic response.

For a linear-elastic response, no hysteretic energy is dissipated, therefore R_{ED}=0; however, it can perfectly re-center the system from the peak displacement demand, therefore R_{RC}=1. In contrast, for a rigid perfectly-plastic response, theoretically the broadest hysteretic loop can be realized, indicating an optimal energy dissipation capability (R_{ED}=1), whereas it is unable to recover its initial position (R_{RC}=0). There are very few systems which are able to achieve these characteristics. One such system is magnetorheological dampers (e.g. Spencer et al. 1997). In contrast, with employment of prestressed tendons and customized energy dissipaters, a flag-shaped hysteretic response can be achieved, indicating a perfect re-centering behavior. Based on this concept, part (c)

depicts a hypothetic hysteretic response wherein the system is assumed to perform nearly plastically in positive and negative directions, however eventually it is able to return to its initial position during unloading. This type of response provides a perfect re-centering potential. By definition, R_{ED} of this type system is calculated as 0.5, whereas the R_{RC} is 1.0. Part (d) presents an idealized elastic-perfectly plastic (EPP) response, which can be anticipated in steel constructed systems. For this type of behavior, the two ratios are greatly dependent on the peak deformation, which is characterized by the displacement ductility demand (μ). Assuming perfect symmetry (in positive and negative directions), the ratios R_{ED} and R_{RC} may be related to μ as:

$$R_{ED} = 1 - \frac{1}{\mu} \tag{8.3}$$

$$R_{RC} = \frac{1}{\mu} \tag{8.4}$$

8.2.3 R_{ED}-R_{RC} Relation

The parameters R_{ED} and R_{RC} are each fundamentally related to the shape of the hysteresis; therefore, they are not independent of each other. Therefore, correlating these two parameters graphically provides an alternative perspective to assess a system's seismic performance. In this regard, the parameters R_{ED} and R_{RC} are plotted in Figure 8.3, with x-axis and y-axis presenting the re-centering ratio (R_{RC}) and the energy dissipation ratio (R_{ED}) respectively. The responses of the previous four idealized systems are identified in this diagram. Since the two parameters of the first three systems, namely linear-elastic, perfectly plastic, and perfect re-centering system, are independent of the imposed peak displacement, they are distributed as a scatter pattern in this diagram.

However, for the EPP system, it is interesting to note that its R_{ED} and R_{RC} are linearly related. This could be understood by summing the two parameters, i.e.

$$R_{ED}+R_{RC}=1 \tag{8.5}$$

As indicated by the straight line in Figure 8.3, the EPP's response is located between the linear elastic and perfectly plastic response. In this diagram, the response at different ductility demands (from 1 to 10) is provided. It is noted that, as the ductility demand increases, the EPP system approaches that of a rigid perfectly plastic system.

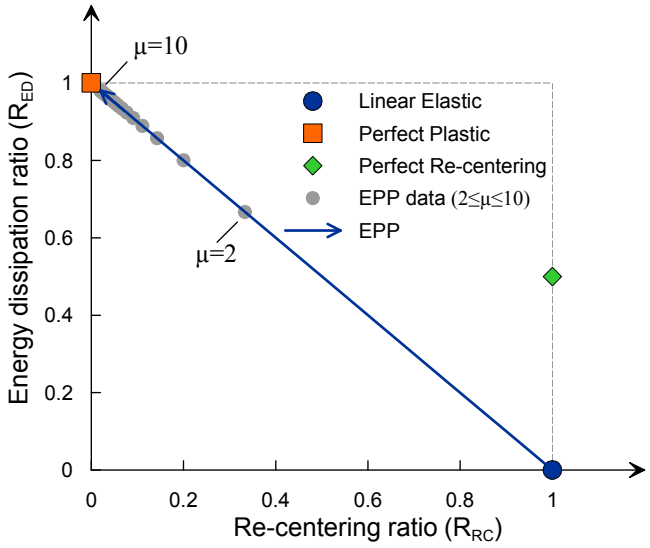

Figure 8.3 R_{ED}-R_{RC} relation for the four idealized responses

To better understand the relation between R_{ED} and R_{RC} four different zones are considered as shown in Figure 8.4. Each division represents an inherently different type of seismic response. For example, zone 1 describes a yielding system with lower potential to dissipate energy and self-center. Zone 1 is considered an unfavorable area. Zone 2 is characterized as an *energy dissipation prone zone* since the energy dissipation capacity is large and the re-centering capability is low. In contrast, a completely different

response is delineated in zone 3, where R_{RC} is larger than R_{ED}. Zone 3 is defined as a *re-centering prone zone*. The last area, zone 4, can be described as the most advantageous seismic-resistant zone where both R_{ED} and R_{RC} are large. Theoretically zone 4 is ideal, however, in reality, this zone is difficult to achieve with common systems.

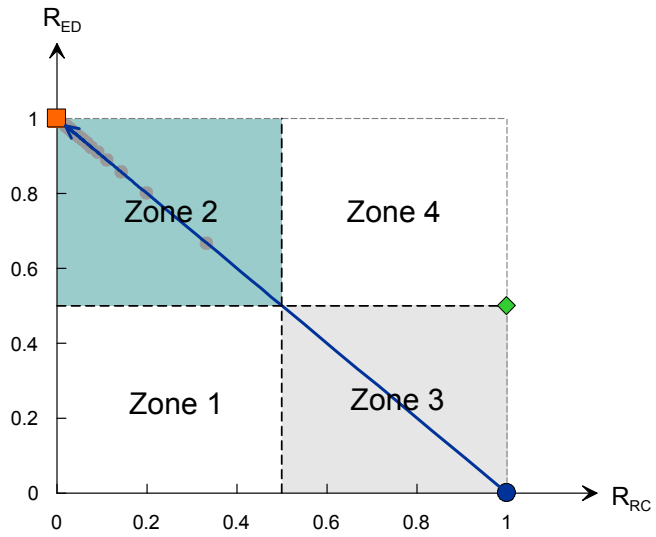

Figure 8.4 Divisions of the R_{ED}-R_{RC} relation

8.3 Characterization of Simplified Inelastic Systems with a Single-Fuse (SF) Mechanism

This section studies the R_{ED}-R_{RC} relation for simplified single-degree-of-freedom (SDOF) single-fuse inelastic structural systems. It is assumed that the hysteresis of a SDOF system is controlled by one of the following: elastic-plastic with overstrength (EPO), stiffness degrading and pinching (SDP), or foundation rocking (FR) mechanisms. The investigation begins by identifying the key parameters governing the hysteretic response, and subsequently, parametric studies are carried out to investigate the effects of

their variations on the R_{ED}-R_{RC} relation. Investigations conducted in this section and the following sections are completed by constructing numerical models with the pertinent fuse elements in *OpenSees* (Mazzoni et al. 2009) and then applying cyclic load at different ductility levels. The numerical model is constructed by a single 2-D zero length inelastic element with two nodes wherein one end is fully fixed at three degrees-of-freedom and the other end is only allowed to move laterally. Therefore, the system is considered a simplified SDOF system. Depending on the objective, the force-displacement relationship of the inelastic element follows by EPO, SDP, or FR mechanism.

8.3.1 Elastic-Plastic with Overstrength (EPO) System

The first examined inelastic mechanism is the system with elastic-plastic with overstrength behavior (EPO). As shown in Figure 8.5, this hysteretic response has two characteristics: (1) the post-yield stiffness is linearly proportional to its initial stiffness by a factor, which is defined as post-yield stiffness ratio α; (2) the unloading stiffness is identical to the initial stiffness. This type of hysteretic response is very common for steel structural members. For example, hysteretic response of Buckling-Restrained Brace (BRB) (Black et al. 2004), as provided in Figure 8.6, and the simulated shear wall fuse hysteresis in Test-2 (Figure 5.6), belong to this category.

The key parameter controlling the hysteretic shape is the post-yield stiffness ratio α. Based on the geometry of the hysteresis, for a given ductility ratio μ, the parameters R_{ED} and R_{RC} can be mathematically derived as follows:

$$R_{ED} = \frac{1}{\mu \times \alpha - \alpha + 1} - \frac{1}{\mu} \tag{8.6}$$

$$R_{RC} = \frac{1-\alpha}{\mu} + \alpha \tag{8.7}$$

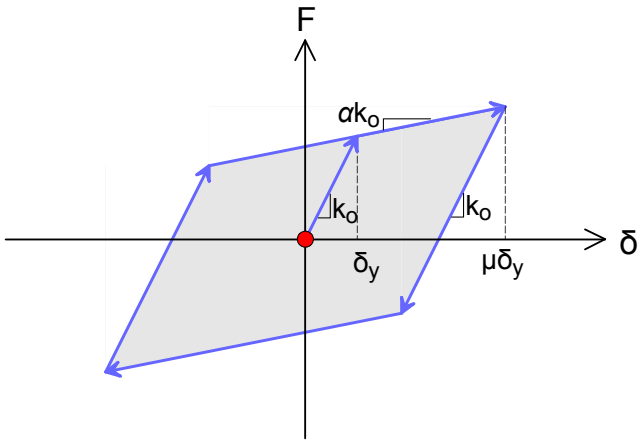

Figure 8.5 Generlized hysteretic curve of an EPO system - one full cycle of loading

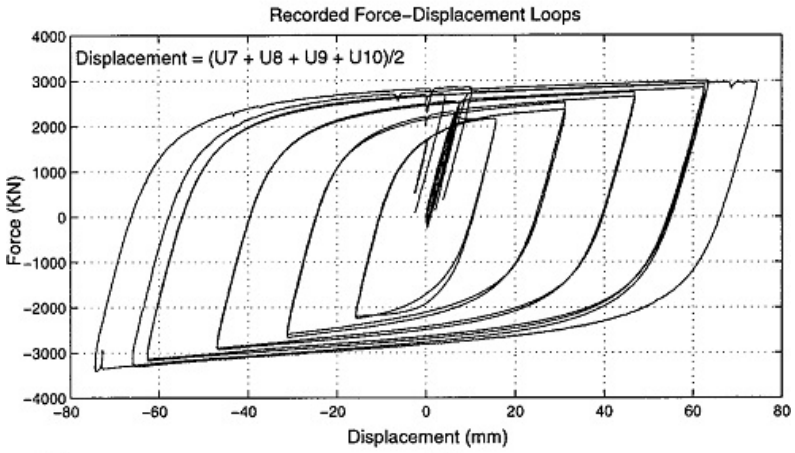

Figure 8.6 Axial load-displacement response of Buckling-Restrained Brace (Black et al. 2004)

Figure 8.7 plots R_{ED} and R_{RC} to μ considering different α scenarios. Three cases with different post-yield stiffness ratios are examined and compared, namely 0.01, 0.05, and 0.20. The R_{ED} plots (part a) indicate that the EPO's energy dissipation ratio typically increases as the ductility demand increases except for the case of α=0.20, where the R_{ED} gradually decreases when μ exceeds 3.0. Figure 8.7a also shows that, for a given ductility

demand, a larger α yields a lower R_{ED} for this system. With regard to the R_{RC} response, it is observed that the R_{RC} is dramatically reduced as one increases μ for all three α scenarios. In addition, an increase in α results in an increase in R_{RC}.

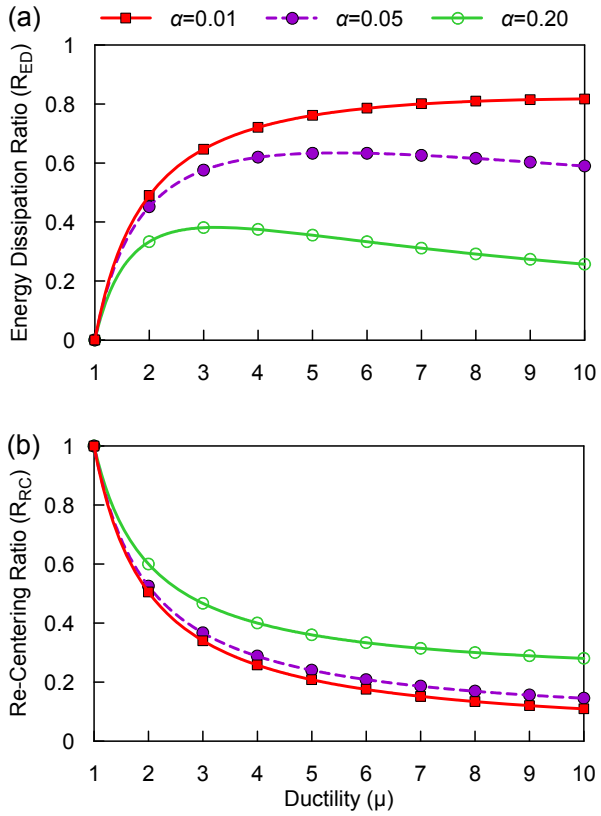

Figure 8.7 Effect of the post-yield stiffness ratio α on the hysteretic performance of the EPO system: (a) R_{ED} vs μ; (b) R_{RC} vs μ

These observations may be understood by examining the hysteretic curve for the various α values, as shown in Figure 8.8 (μ is selected 5 herein). This plot illustrates that as the post-yield stiffness ratio increases, the dissipated hysteretic energy relative to the boundary become smaller, which implies a smaller energy dissipation capacity. However, the cumulative deformation at zero force decreases, indicating an improved re-centering behavior.

Subsequently, these results are incorporated into R_{ED}-R_{RC} plots, as shown in Figure 8.9. It is observed that an EPO system with a smaller α (0.05 or below) possesses an effective energy dissipation mechanism as it falls into the zone 1. As α increases, the potential for hysteretic energy dissipation gradually reaches the unfavorable zone area at high ductility levels. It is also noted that the impact of increased μ is least sensitive to changes in R_{ED} for the system with an $\alpha = 0.05$ particularly for $\mu \geq 3.0$.

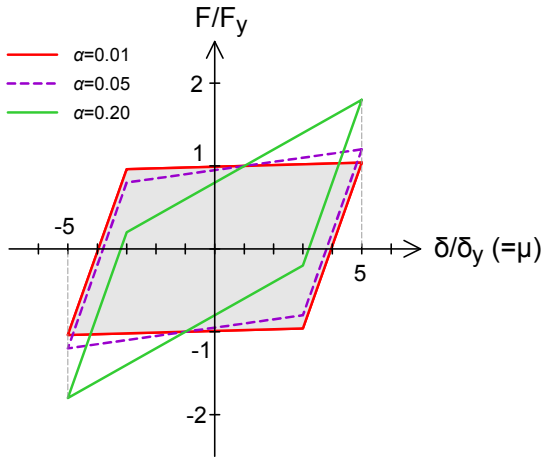

Figure 8.8 Normalized hysteretic curves of the EPO system with different α when μ=5

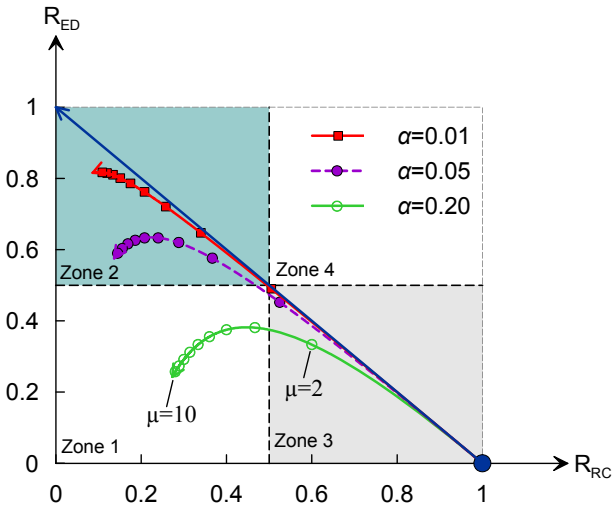

Figure 8.9 Effect of the post-yield stiffness ratio α on the EPO's R_{ED}-R_{RC} relation

8.3.2 Stiffness Degrading and Pinching (SDP) System

The second inelastic fuse mechanism of particular interest is called stiffness degrading and pinching (SDP). Figure 8.10 displays a generalized hysteretic response of this system under a full cycle of loading, overlaid with its backbone curve. The basic rule of this hysteresis is that the reloading path always targets the previously achieved maximum displacement (Clough and Johnston 1966). However, considering the pinching effect, the reloading path is usually divided into two parts by the "break point" (Ibarra et al. 2005). The "break point" is identified by two parameters, κ_d and κ_f, which define the pinched displacement and strength respectively. For unloading, the stiffness is related to the initial stiffness by a ratio, which is expressed as a function of ductility demand and unloading stiffness parameter (β), as indicated in Figure 8.10. The behavior shown in Figure 8.10 is common to many types of structural components. For example RC shear walls (Sittipunt and Wood, 1995), steel plate shear wall (Driver et al., 1998), and wood frame shear wall (Figure 8.11; Shenton et al., 1998).

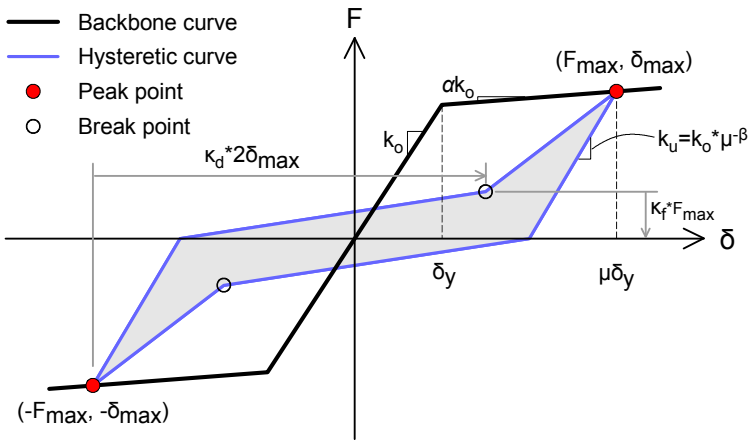

Figure 8.10 Generalized hysteretic curve of the SDP system

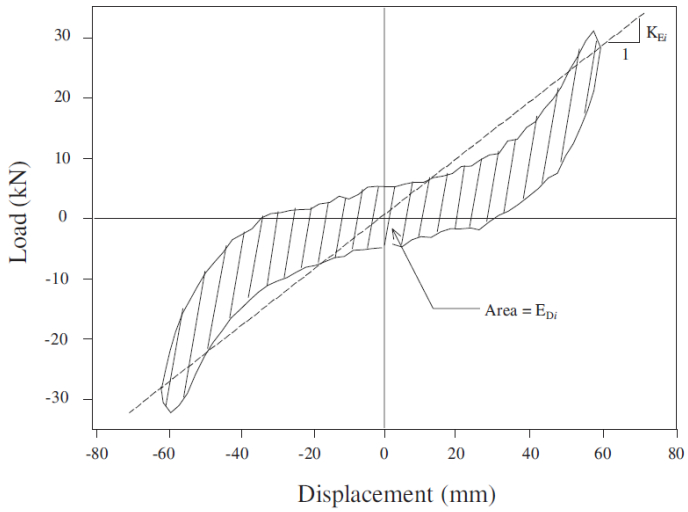

Figure 8.11 Examples of wall hysteretic response: wood frame shear wall (Shenton et al. 1998)

In this response, the displacement and strength pinching factors (κ_d and κ_f) and the unloading stiffness parameter (β) are the key parameters controlling the hysteretic shape. In this subsection, a set of numerical parametric studies are conducted in the *OpenSees* environment to investigate the effect of each parameter on the hysteretic response. In *OpenSees*, a uniaxial material object "*Hysteretic*" (Mazzoni et al. 2009) is used to model the hysteretic response of the SDP system. Herein, seven different cases are considered, as listed in Table 8.1. It is noted that the values of the baseline case are selected based on the test results on wood frame shear wall by Shenton et al. (1998).

Table 8.1 Cases considered for the SDP system

Case No.	κ_d	κ_f	β
Baseline (#1)	0.7	0.3	0.0
#2	0.9	0.3	0.0
#3	0.5	0.3	0.0
#4	0.7	0.1	0.0
#5	0.7	0.5	0.0
#6	0.7	0.3	0.2
#7	0.7	0.3	0.4

8.3.2.1 Effect of displacement pinching factor (κ_d)

Figure 8.12 plots R_{ED} and R_{RC} for the SDP system under the different κ_d scenarios. In general, it is observed that the SDP's R_{ED} slightly increases as μ increases, whereas the R_{RC} is dramatically reduced with an increase of μ. In addition, a larger κ_d produces a smaller R_{ED}, while R_{RC} is completely independent of κ_d.

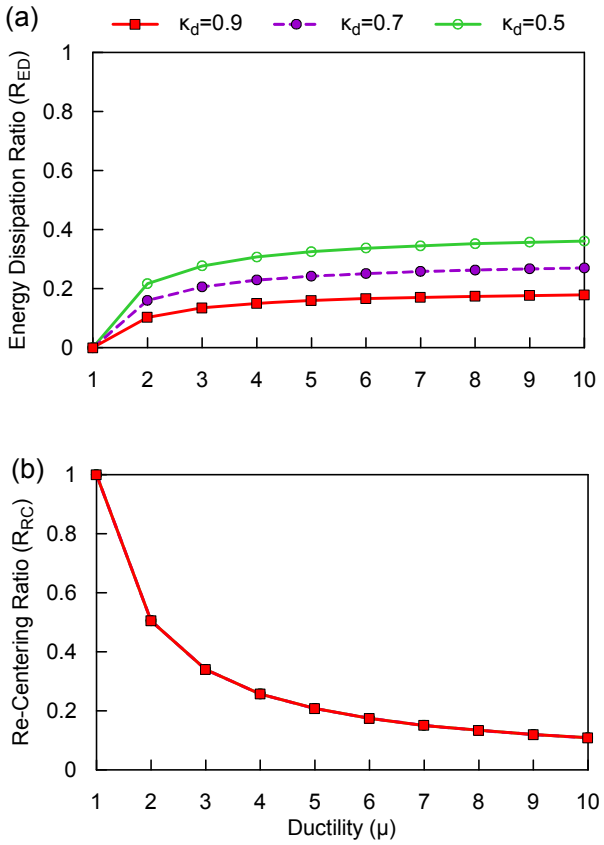

Figure 8.12 Effect of displacement pinching factor (κ_d) on the hysteretic performance of the SDP system: (a) R_{ED} vs μ; (b) R_{RC} vs μ (κ_f=0.3, β=0)

Figure 8.13 compares the normalized hysteretic curve of the SDP system with the baseline case (Table 8.1) under three different ductility demand, namely μ=2.0, 5.0, and 8.0. The plots show that, given constant values of the κ_d, κ_f, and β, the cumulative displacement at zero force relative to the peak displacement is dramatically increased as

one increases the μ. It means that an increase in μ will decrease the R_{RC}, which confirms the results shown in Figure 8.12a.

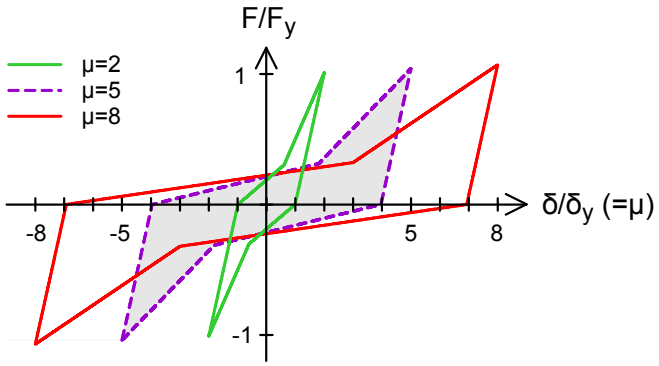

Figure 8.13 Normalized hysteretic curves of the SDP system (baseline) under different μ (κ_d=0.7, κ_f=0.3, β=0)

The effects of the κ_d variation on R_{ED} and R_{RC} can be explained by examining the hysteretic curve for each scenario, as displayed in Figure 8.14. The comparison reveals that, as κ_d decreases, the break point shifts towards the left during positive reloading. The hysteretic loop becomes broader, and therefore, the dissipated hysteretic energy is increased. However, the re-centering performance is not influenced by the location of the break point since the unloading stiffness is unchanged.

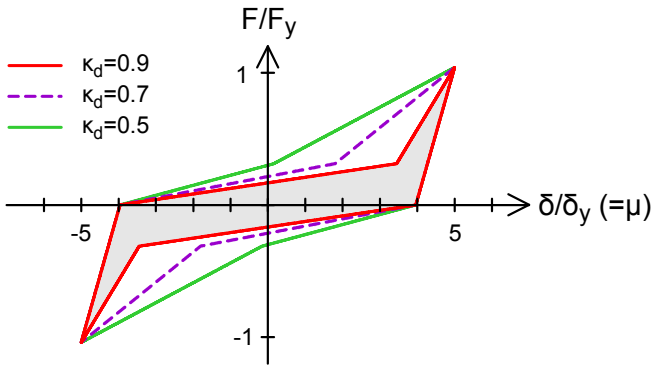

Figure 8.14 Normalized hysteretic curves of the SDP system with different κ_d when μ=5 (κ_f=0.3, β=0)

Figure 8.15 presents the R_{ED}-R_{RC} relation for the SDP system under the three different κ_d cases. In general, the SDP inelastic mechanism observes an unfavorable hysteretic performance as the ductility increases to a relatively high level since all three cases are located in the unfavorable zone (zone 1). However, if one can control and decrease κ_d, the performance can be improved.

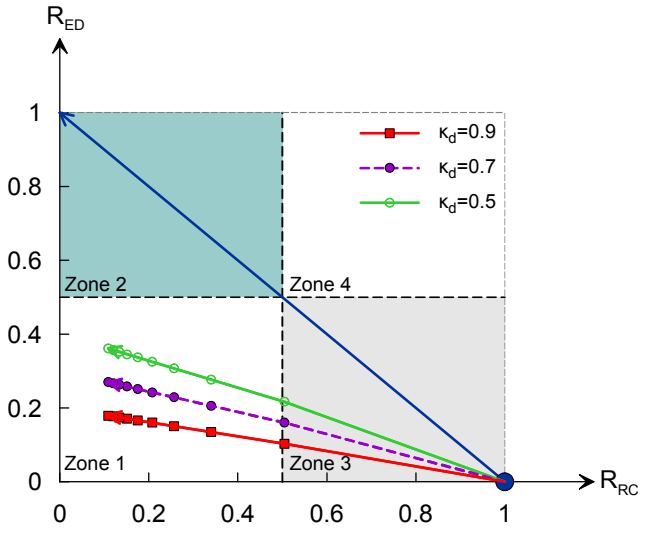

Figure 8.15 Effect of κ_d on the SDP's R_{ED}-R_{RC} relation (κ_f=0.3, β=0)

8.3.2.2 Effect of strength pinching factor (κ_f)

Figure 8.16 shows the effects of κ_f variations on the R_{ED} and R_{RC} parameters. These plots indicate that an increase in κ_f could help to improve the energy dissipation ratio; and similar to κ_d, the re-centering ratio is also not affected by κ_f.

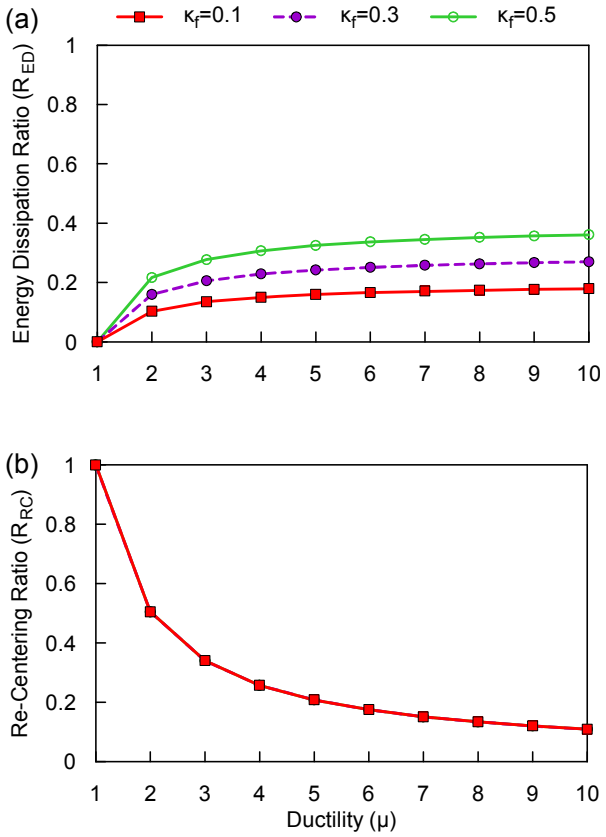

Figure 8.16 Effect of strength pinching factor (κ_f) on the hysteretic performance of the SDP system: (a) R_{ED} vs μ; (b) R_{RC} vs μ (κ_d=0.7, β=0)

Again, this phenomenon can be explained by examining the hysteresis for the different κ_f cases. As illustrated in Figure 8.17, an increase in κ_f elevates the break point during negative reloading, which in turn increases the area of hysteresis and the energy dissipation capability. However, it does not affect the unloading path; therefore, the re-centering ratio is not sensitive to κ_f. Figure 8.18 reveals the influence of varying κ_f on the

R_{ED}-R_{RC} relation. In contrast with the observation in Figure 8.15, an increase in κ_f could render a relatively favorable hysteretic performance. For example, a large κ_f(0.9) at high ductility level ($\mu \geq 6.0$) can result in hysteresis too pinched to support Zone 2 type behavior.

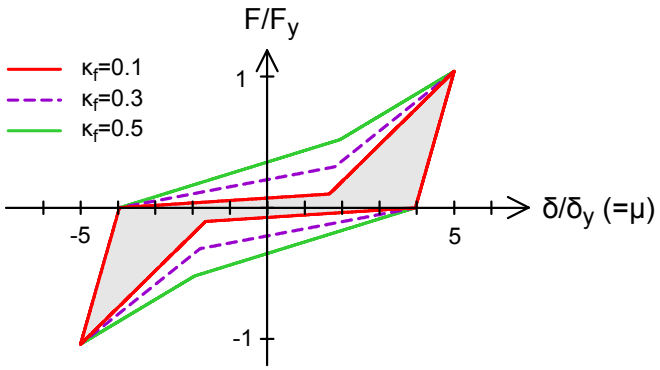

Figure 8.17 Hysteretic curves of the SDP system with different κ_f when μ=5 (κ_d=0.7, β=0)

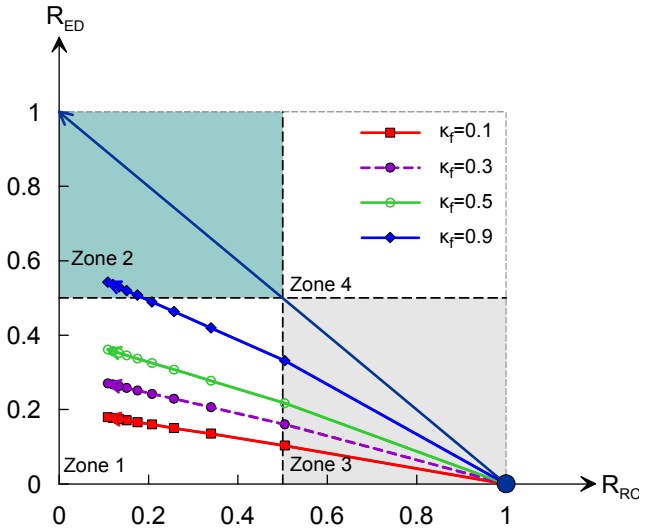

Figure 8.18 Effect of κ_f on the SDP's R_{ED}-R_{RC} relation (κ_d=0.7, β=0)

8.3.2.3 Effect of unloading stiffness parameter (β)

Finally, the influence of varying the unloading stiffness parameter (β) on the R_{ED} and R_{RC} responses are examined in Figure 8.19. As β increases from 0 to 0.4, the value of R_{ED} is slightly reduced; however, the re-centering performance is moderately enhanced. It is noted that across this range of β, the R_{ED} is not significantly influenced. This could be understood by inspecting the hysteretic responses. As indicated in Figure 8.20, a larger β implies a lower unloading stiffness, and thereby a smaller hysteretic area and smaller residual deformation. Finally, it is interesting to note that varying β has no impact on the SDP's R_{ED}-R_{RC} relation. As illustrated in Figure 8.21, the R_{ED}-R_{RC} relations of all three β scenarios fall into one straight line.

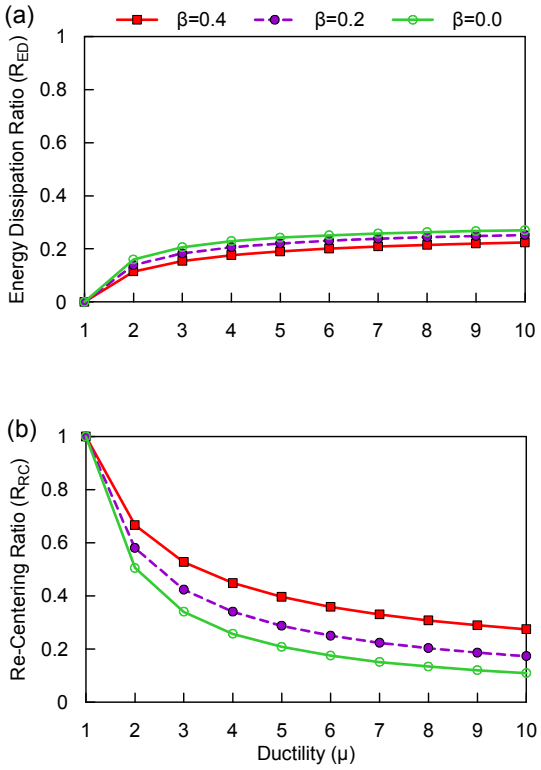

Figure 8.19 Effect of unloading stiffness parameter (β) on the hysteretic performance of the SDP system: (a) R_{ED} vs μ; (b) R_{RC} vs μ (κ_d=0.7, κ_f=0.3)

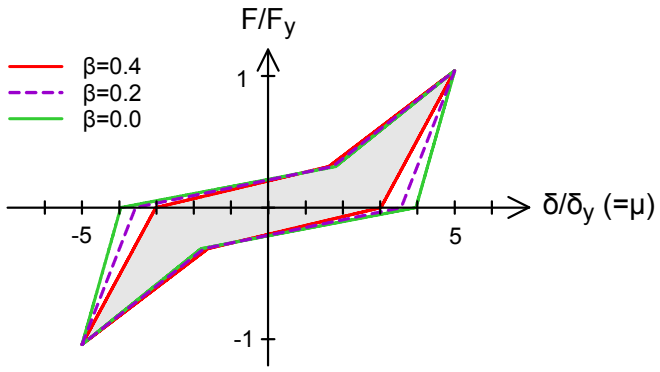

Figure 8.20 Hysteretic curves of the SDP system with different β when μ=5 (κ_d=0.7, κ_f=0.3)

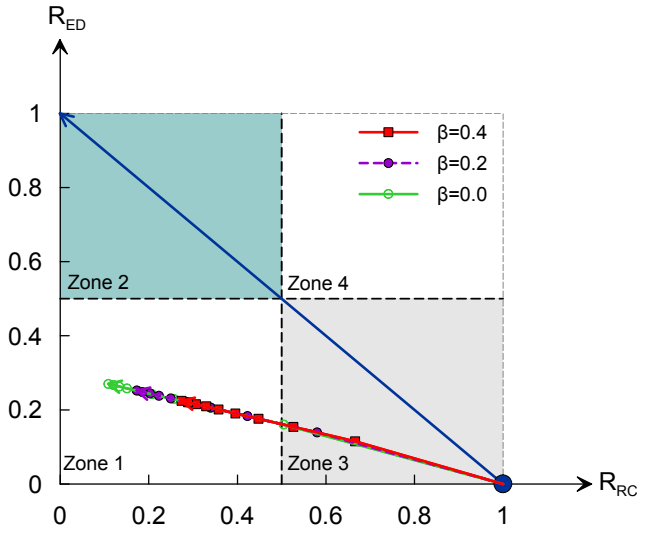

Figure 8.21 Effect of β on the SDP's R_{ED}-R_{RC} relation (κ_d=0.7, κ_f=0.3)

8.3.3 Foundation Rocking (FR) System

The final examined individual inelastic mechanism is that of which is realized when a foundation rocks. When a shallow footing is allowed to rock, its hysteretic response is greatly dependent on the soil properties, footing geometry, and the total axial load acting on the soil-footing interface. However, when the footing is founded on competent soil (e.g., dense sand) with a high vertical factor of safety (i.e., FS_v>10) against bearing failure, it can usually return back to its initial position without suffering significant residual deformations during seismic loading. This type of hysteresis is selected as the target.

In an effort to simplify the rocking footing's hysteresis, a multi-linear hysteretic model has been proposed to capture the rocking footing's inelastic characteristics (e.g., Deng 2012; Johnson 2012). Following this idea, the rocking footing's hysteretic response is represented by a bilinear relationship herein, as shown in Figure 8.22 part (a). In this simplified hysteretic model, the post-yield stiffness is assumed to be zero, and the unloading path is defined such that the system always returns to its initial position. Part (b) compares this simplified hysteretic model with observed rocking footing data during Test-2. The rocking footing shallowly rested on dry dense Nevada sand with FS_v=10, and it was subjected to slow cyclic loading at different rotation levels (Section 5.4.3; Figure 5.8). The comparison reveals that the proposed simplified hysteretic model can reasonably capture the hysteretic response of rocking foundation under competent soil condition. Clearly, its R_{RC} is always 1, and the R_{ED} can be obtained based on the geometry of the hysteresis as described in Equation (8.8).

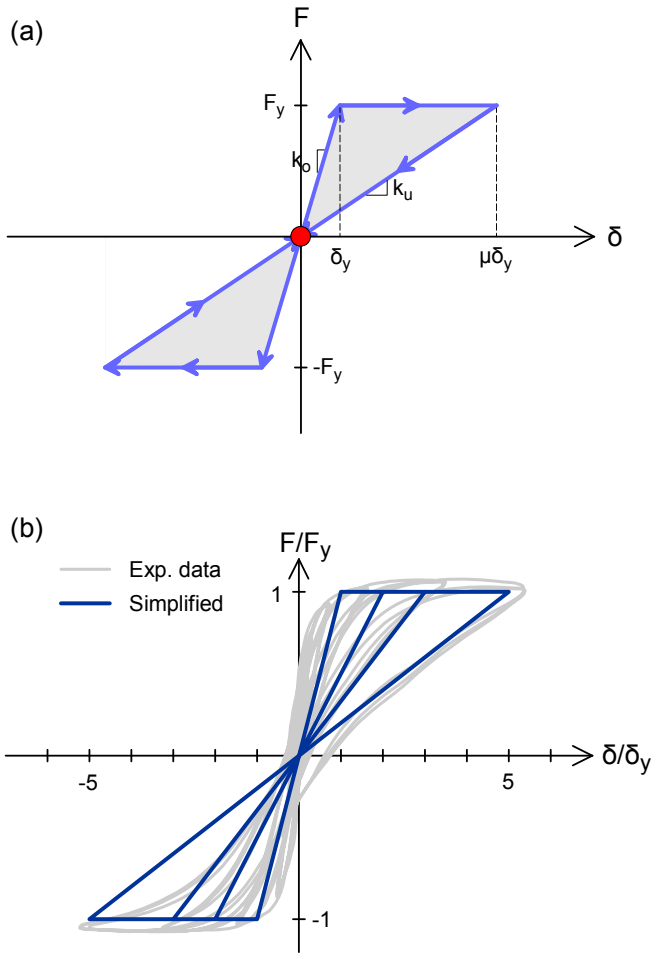

Figure 8.22 Simplified FR system: (a) idealized hysteretic curve schematic; (b) comparison with experimental data (Note the data is obtained from footing component test during Test-2; details are prvided in Section 5.4.3)

$$R_{ED} = \frac{1}{4}\left(1 - \frac{1}{\mu}\right) \tag{8.8}$$

Figure 8.23 plots the R_{ED} as a function of μ. This plot shows that as μ increases, R_{ED} gradually and slightly increases, with the most significant increase at low μ (≈4); simultaneously, R_{RC} remains unchanged. As a result, a plot of R_{ED} vs. R_{RC} is a vertical line located in the re-centering prone zone area (zone 3), as indicated in Figure 8.24.

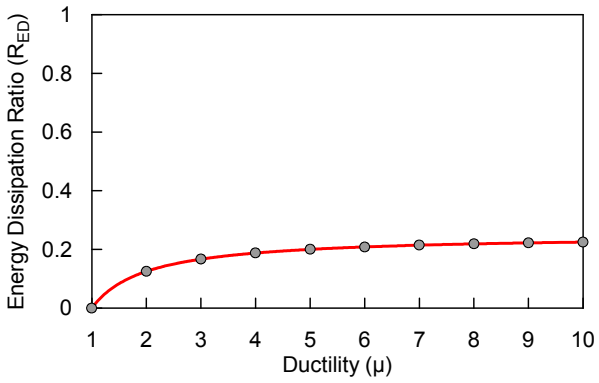

Figure 8.23 Hysteretic performance of the FR system: R_{ED} vs μ

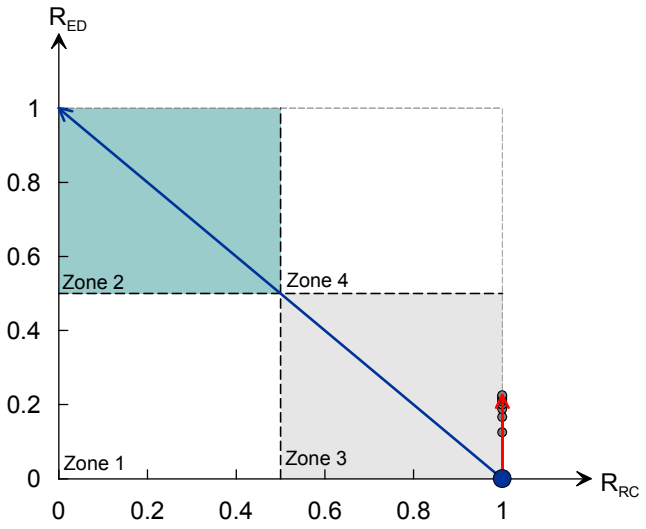

Figure 8.24 The FR system's R_{ED}-R_{RC} relation

8.4 Characterization of Simplified Systems with Multiple-Fuse-in-Parallel (MFP) Configurations

In practice, the structural system usually consists of multiple inelastic elements at various locations. Therefore, interactions amongst those inelastic elements would lead to a more sophisticated system-level hysteretic response. The goals of the following two sections are to study the hysteretic responses of the multiple-fuse structural systems and specifically to investigate their R_{ED} and R_{RC} performances via numerical analyses. Considering the arrangement mode amongst the fuse elements, two types of systems can be formulated, namely Multiple-Fuse-in-Parallel (MFP) system and Multiple-Fuse-in-Series (MFS) system. This section examines the MFP simplified structural system.

In a MFP system, the multiple fuse elements are arranged such that they share the same displacement demand or the displacement demand is coupled when subjected to seismic loading. Figure 8.25 provides a schematic of the simplified MFP system. This type of system is a very common arrangement in design. For example, in a low-rise frame-wall structural system, the wall component and its adjacent base columns would be subjected to the same displacement demand if the diaphragm remains rigid. The sFRD and sSHD model constructed in Test-2 belong to this category as well since the rotation of the SW rocking footing or SW structural fuse is coupled with the rotation imposed on the column rocking footing or column fuse, respectively.

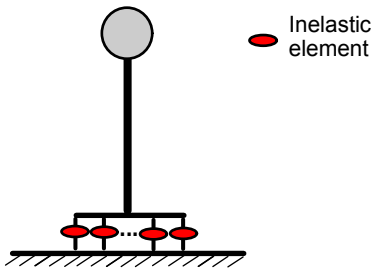

Figure 8.25 Schematic of a simplified MFP system

In this study, the examined simplified MFP system consists of two of the previously investigated inelastic mechanisms. Therefore, selecting two fuse mechanisms out of three would yield three different systems in total. Table 8.2 lists the three considered MFP systems. For each considered MFP system, the yield capacity of each inelastic member can be significantly different; however, its yield rotation might not be dramatically varied. As such, the strength is considered as the primary variable throughout this study.

Table 8.2 Considered MFP systems

System short name[1]	Fuse Mechanisms[2]	
	Fuse1	Fuse2
MFP_ES	EPO	SDP
MFP_EF	EPO	FR
MFP_SF	SDP	FR

[1]MFP = Multiple-Fuse-in-Parallel

[2]EPO = Elastic-Plastic with Overstrength ;SDP = Stiffness Degrading and Pinching; FR = Foundation Rocking

8.4.1 MFP_ES system

The first examined MFP system consists of an EPO fuse and a SDP fuse, termed MFP_ES system. Considering the strength variation between the two fuse elements, three

scenarios are examined as listed in Table 8.3. It is assumed that each fuse element has a same yield displacement δ_y for each scenario.

Table 8.3 Three MFP_ES cases considered

Case ID	Strength of EPO	Strength of SDP
1	F_y	F_y
2	F_y	$0.1*F_y$
3	$0.1*F_y$	F_y

Analyses of these three systems are completed by constructing numerical models in *OpenSees* (Mazzoni et al. 2009) and then applying cyclic load at ten different ductility levels (μ starts from 1 to10). The numerical model of each case is constructed by a single 2-D zero length lumped inelastic element with two nodes wherein one end is fully fixed at three degrees-of-freedom and the other end is only allowed to move laterally. The inelastic element is constructed by using "Parallel" uniaxial material (Mazzoni et al. 2009) which is composed of the EPO and SDP fuses placed in parallel. The hysteretic behaviors of these two fuses can be realized by using "Steel01" and "Hysteretic" uniaxial materials (Mazzoni et al. 2009) in *OpenSees*, respectively. For both materials, the post-yield stiffness ratio, namely α, is chosen as 0.01; κ_d, κ_f, and β of the SDP are adapted from the baseline case listed in Table 8.1. In addition, the yield displacement δ_y is chosen as 0.01, and the baseline yield strength F_y is selected as 100. Note that arbitrary selections of δ_y and F_y will not affect the system's normalized hysteretic curve. Appendix A.2.1 provides the *OpenSees* input file for the MFP_ES system.

Figure 8.26 describes the normalized local-level (each individual fuse) and system-level hysteretic curves of each scenario when μ=5. It shows that when the strength of each fuse is equated (case#1), the superimposed hysteresis has the largest area

as shown in the first row. However, its R_{ED} is less than that of case#2 by definition since its boundary area becomes correspondingly large. For case#2, its hysteretic behavior is dominated by the EPO's inelastic behavior despite that significant inelasticity is developed within the SDP fuse as well. Since the SDP fuse has a significantly lower strength, its contribution to the system-level hysteresis is negligible compared with that of the EPO. In like fashion, the system-level hysteretic response of case#3 is dominated by the SDP's inelastic behavior.

Figure 8.27 compares the obtained R_{ED} and R_{RC} performance for the three MFP_ES cases. As indicated in part (a), the second case wherein the EPO fuse has a yield strength 10 times that of the SDP observes the largest R_{ED}, whereas the reversed scenario (case#3) observes the smallest response. When the two fuses designed with compatible strength (case#1), the R_{ED} response to μ is between that of Case#2 and Case#3. With regard to R_{RC}, each case observes an identical response as shown in part (b). This is because the unloading stiffness of each fuse element is prescribed as the same with its initial stiffness in this study. Part (c) compares the R_{ED}-R_{RC} relation for each scenario. This plot shows that as μ increases, case#2 falls into the energy dissipation prone zone (zone 2), and case#3 is located at the unfavorable zone (zone 1). The first case, however, is located between these two cases.

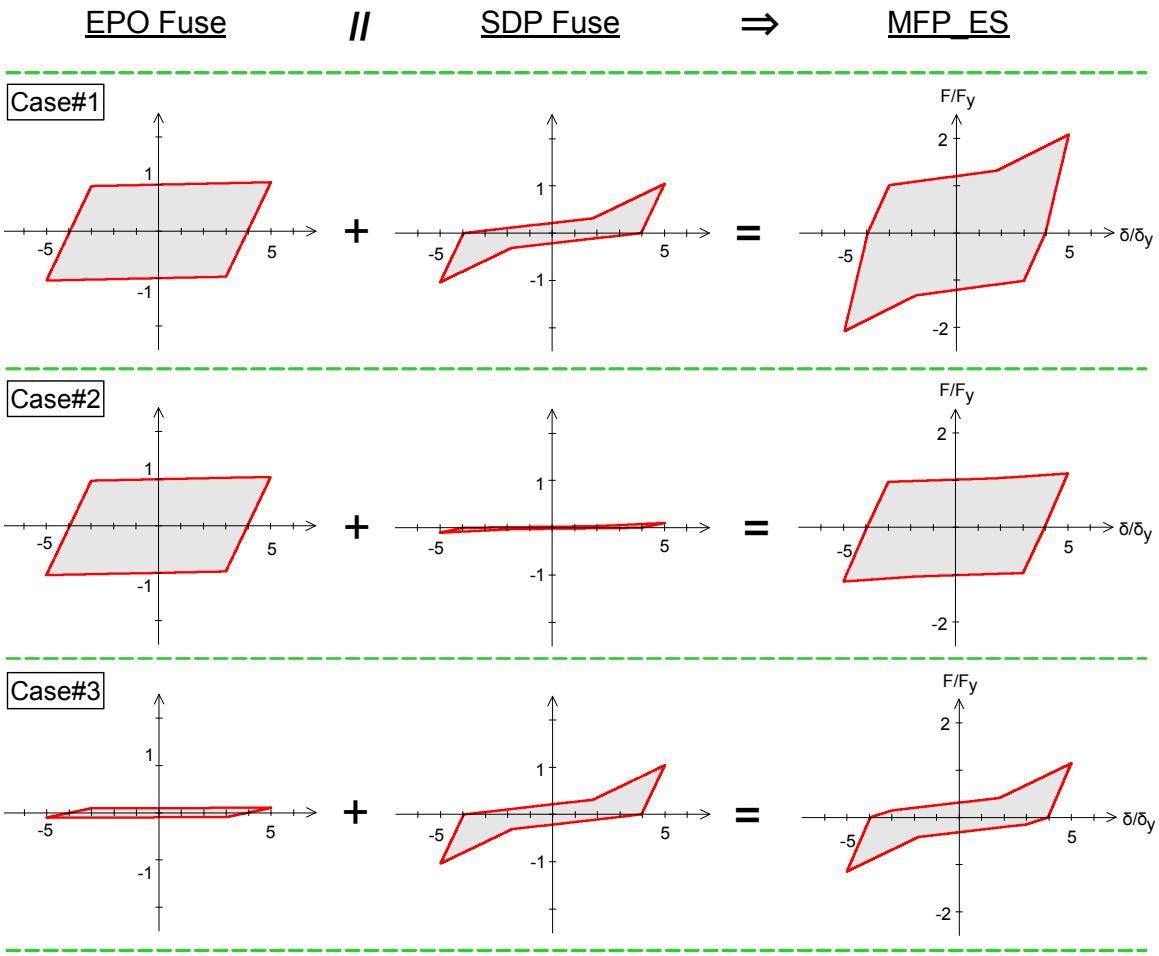

Figure 8.26 Hysteretic responses of three MFP_EP cases when μ=5

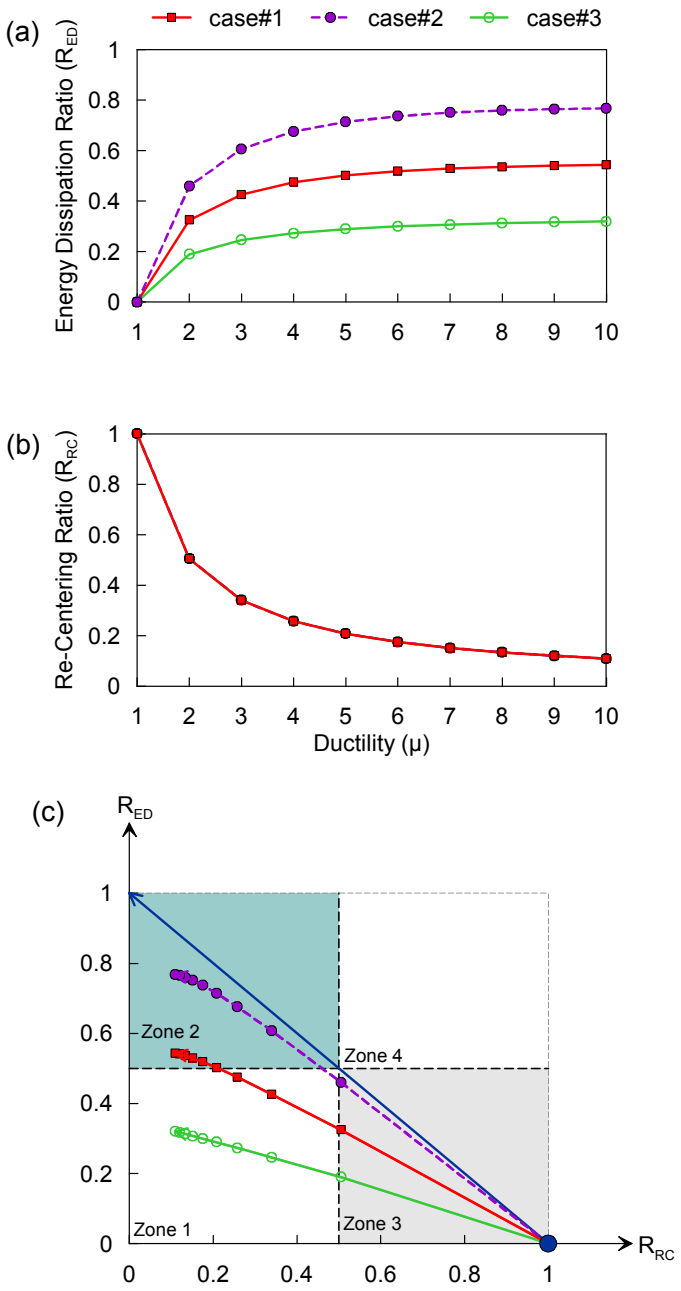

Figure 8.27 Performance comparison for the three MFP_EP cases: (a) R_{ED} vs μ; (b) R_{RC} vs μ; (c) R_{ED}-R_{RC} relation

8.4.2 MFP_EF system

The second examined MFP simplified system (MFP_EF) is composed of an EPO fuse and an FR fuse. Similarly, three different MFP_EF scenarios are investigated in this section considering the strength difference between the EPO and FR fuses, as listed in Table 8.4. The modeling procedure of this system is similar with that of the MFP_ES as described in Section 8.4.1. Note that the FR fuse can be modeled by using "Hysteretic" uniaxial materials (Mazzoni et al. 2009) in OpenSees. However, the unloading stiffness parameter of this material, namely β, needs to be updated at different ductility level to ensure a perfect re-centering behavior during unloading.

Table 8.4 Different MFP_EF cases considered

Case ID	Strength of EPO	Strength of FR
1	F_y	F_y
2	F_y	$0.1*F_y$
3	$0.1*F_y$	F_y

Figure 8.28 and Figure 8.29 show and the hysteretic curve of each case and the results of the R_{ED} and R_{RC}. When the strength of the EPO fuse is significantly larger than that of the FR, as considered in case#2, the system-level hysteretic response is dominated by the EPO. As such, the MFP_EF system observes the largest R_{ED} but the smallest R_{RC} and falls into zone 2 (energy dissipation prone zone).

In contrast, when the capacity of the FR fuse is significantly large (case#3), the MFP_EF system observes the largest R_{RC} but the lowest R_{ED}. In this case, the resultant hysteretic response is dominated by the FR response instead. Consequently, it maintains a

substantial re-centering performance and responds entirely within the re-centering prone zone (Zone 3).

When the capacities of both fuse elements are equated (case#1), the superimposed hysteretic response observes a larger R_{ED} but a smaller R_{RC} compared with case#3. However, compared with case#1, its re-centering behavior is improved and energy dissipation behavior is slightly reduced. Therefore, case#1 observes a balanced performance between the two extreme cases. However, this case is still characterized as energy dissipation prone system as it still falls into zone 2.

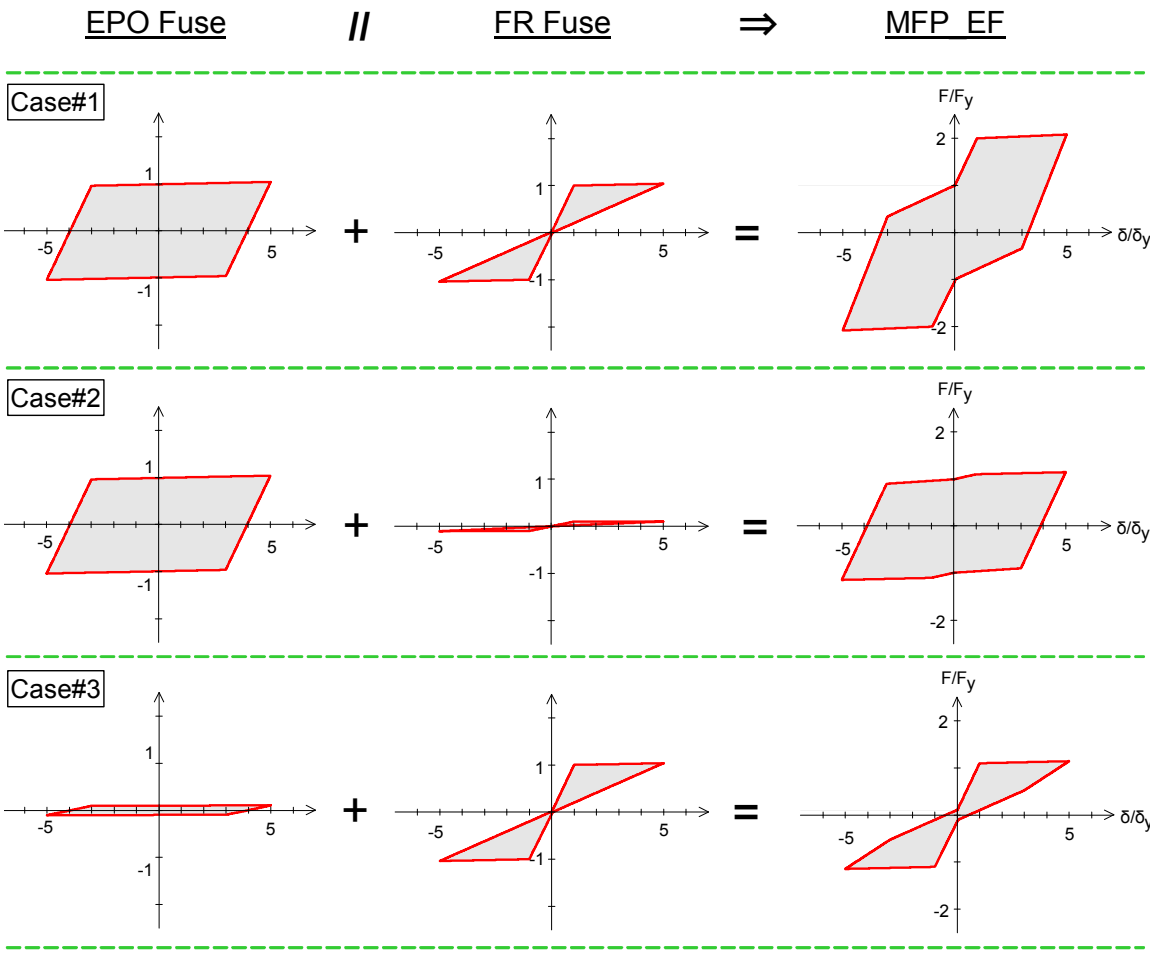

Figure 8.28 Hysteretic curve of three MFP_EF scenarios when μ=5

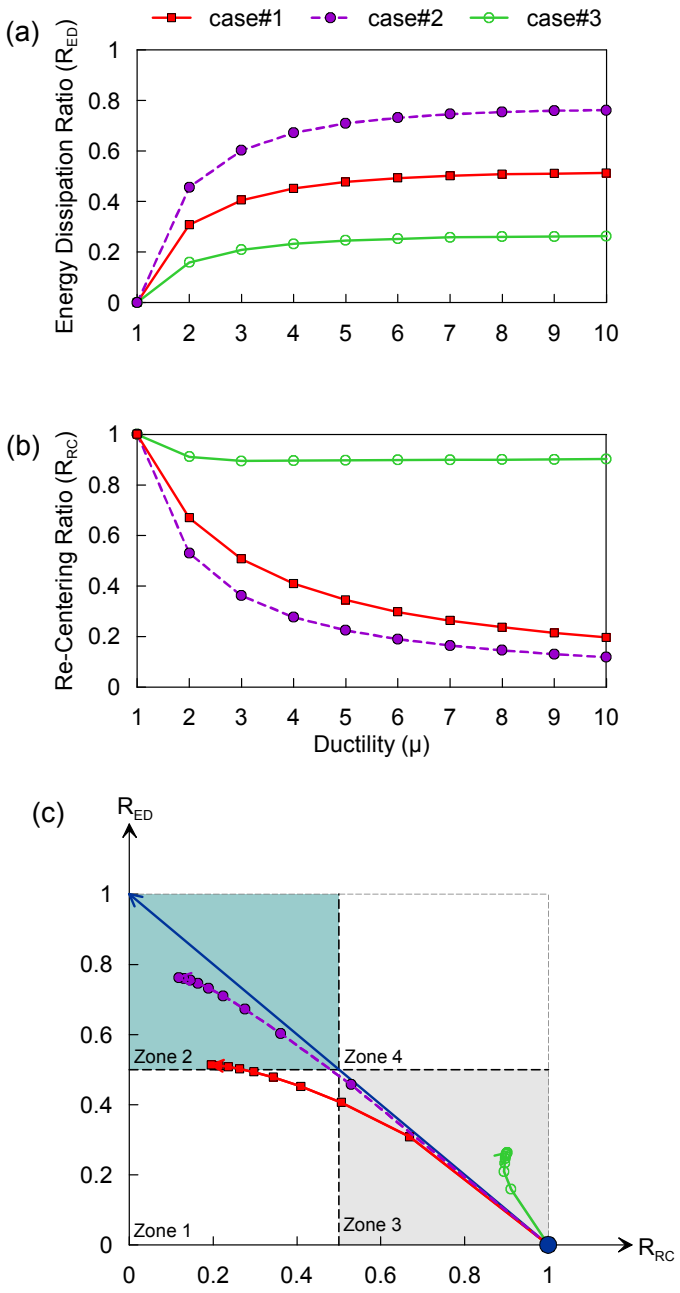

Figure 8.29 Performance comparison for the three MFP_EF systems: (a) R_{ED} vs μ; (b) R_{RC} vs μ; (c) R_{ED} vs R_{RC}

8.4.3 MFP_SF system

The final MFP system incorporates the SDP and FR fuses, termed MFP_SF. In like fashion, Table 8.5 lists three different MFP_SF scenarios considering the strength difference. Numerical model construction is similar with the previous systems (MFP_ES and MFP_EF). Note that both fuses in the MFP_SF system are constructed by using "Hysteretic" uniaxial material in OpenSees.

Table 8.5 Different MFP_SF cases considered

Case ID	Strength of SDP	Strength of FR
1	F_y	F_y
2	F_y	$0.1*F_y$
3	$0.1*F_y$	F_y

Similarly, Figure 8.30 and Figure 8.31 provide the analysis results in terms of the hysteretic response and the R_{ED} and R_{RC} performance. As expected, case#2 and case#3 observes the main hysteretic characteristics of the SDP and FR fuse mechanisms since they are dominated by each of them respectively. Namely, case#2 observes the lowest re-centering performance and falls the unfavorable zone (zone 1), whereas case#3 approaches re-centering zone area (zone 3).

When the strengths are balanced (case#1), this strategy produces a nearly desirable flag-shape system-level hysteretic response, as indicated in the first row of Figure 8.30. As a consequence, its re-centering capability is significantly improved compared with the SDP-dominated case (case#3), as shown in Figure 8.31b. In the meantime, its R_{ED}-R_{RC} response remains in the re-centering zone. This observation is encouraging since the FR fuse implemented via a balanced design strategy demonstrates

significant improvement in the re-centering behavior over conventionally considered SDP systems.

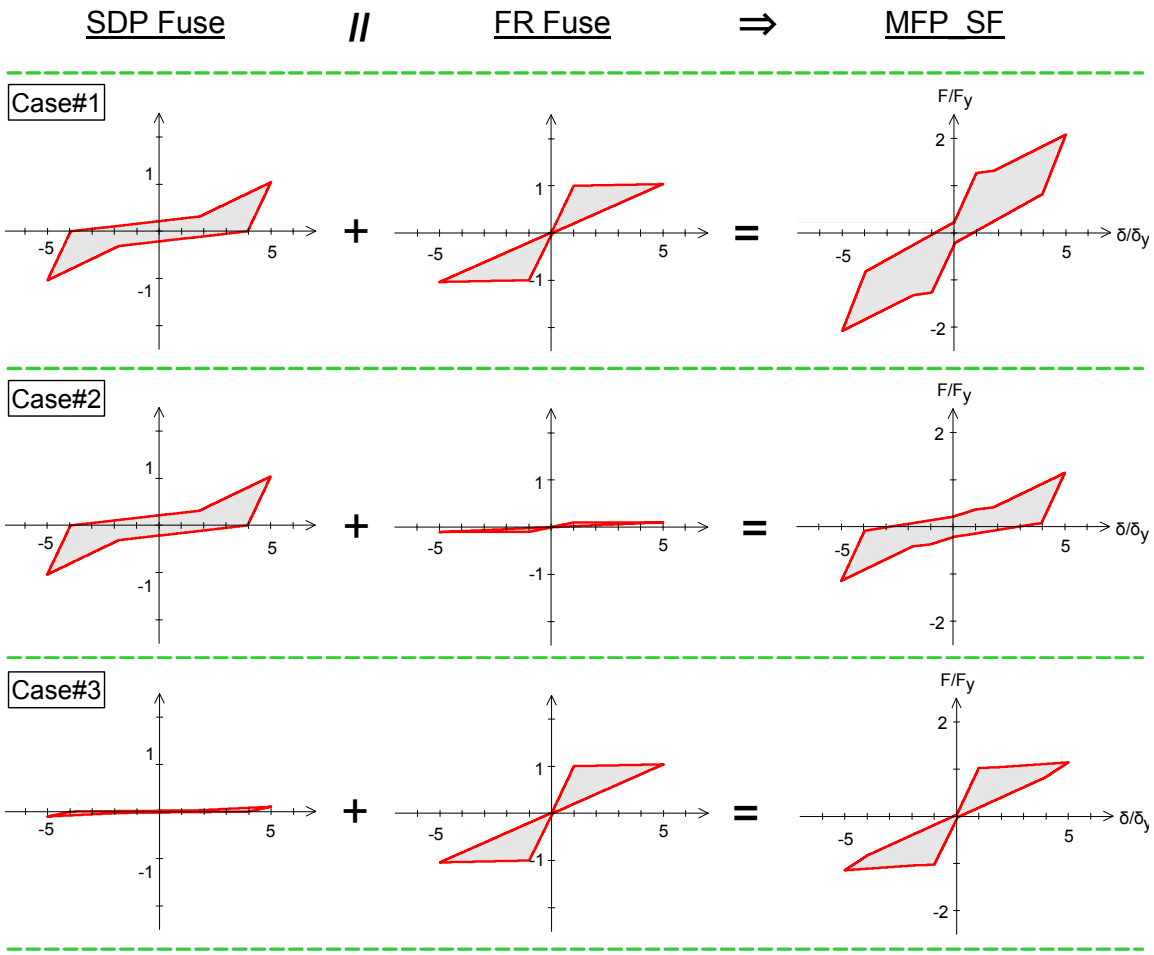

Figure 8.30 Hysteretic curve of three MFP_SF cases when μ=5

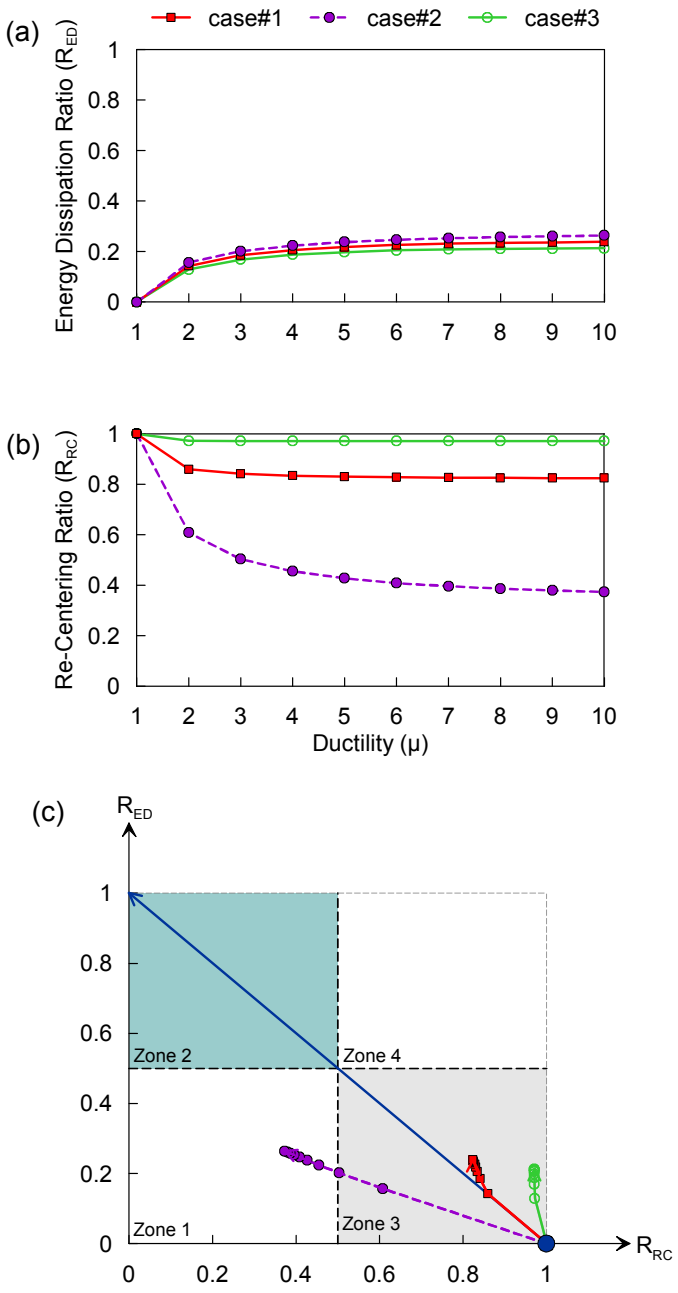

Figure 8.31 Performance comparison for the three MFP_SF systems: (a) R_{ED} vs μ; (b) R_{RC} vs μ; (c) R_{ED} vs R_{RC}

8.5 Characterization of Simplified Systems with Multiple-Fuse-in-Series (MFS) Configuration

The examined hybrid system in this section is the Multiple-Fuse-in-Series (MFS) structural configuration. In this system, multiple inelastic elements are arranged in a way such that each element shares the same force demand or the force demand is coupled when subjected to seismic loading. However, the displacement of each element is independent. Figure 8.32 shows a schematic of a simplified MFS system. This configuration is not rare in practice. For example, an RC concrete wall structure designed with a dual-plastic hinge concept (Panagiotou and Restrepo 2009) falls into this category since it encourages the development of two plastic hinge mechanisms within the same cantilevered wall at different locations. The sBD model constructed in Test-2 is another example, since the moment demand imposed on the SW structural fuse and the SW rocking footing is coupled. Three types of MFS system are considered in this study when combining two different fuse elements out of three. Table 8.6 lists the considered MFS systems.

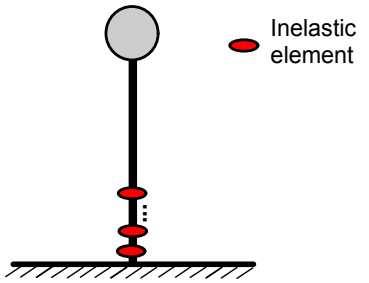

Figure 8.32 Schematic of a simplified MFS system

Table 8.6 Considered MFS systems

System short name[1]	Fuse Mechanisms[2]	
	Fuse1	Fuse2
MFS_ES	EPO	SDP
MFS_EF	EPO	FR
MFS_SF	SDP	FR

[1]MFS = Multiple-Fuse-in-Series

[2]EPO = Elastic-Plastic with Overstrength ;SDP = Stiffness Degrading and Pinching; FR = Foundation Rocking

8.5.1 MFS_ES System

This first examined series system considers a combination of the EPO and SDP fuse elements and is termed a MFS_ES system. Similar to the study of parallel systems, three different scenarios are investigated in MFS_ES system considering the strength differences between the two fuse elements, as shown in Table 8.7.

Table 8.7 Different MFS_ES cases considered

Case ID	Strength of EPO	Strength of SDP
1	F_y	F_y
2	$10*F_y$	F_y
3	F_y	$10*F_y$

The numerical model of the series system is also constructed by a single 2-D zero length lumped inelastic element in *OpenSees*. The inelastic element is modeled by using "Series" uniaxial material (Mazzoni et al. 2009) which is composed of the EPO and SDP fuses placed in series. The modeling of each individual inelastic element and values of the parameters governing the hysteretic curve of each follow the study on the parallel systems (Section 8.4.1). Appendix A.2.2 provides the *tcl* script for the MFS_ES system.

Figure 8.33 shows the normalized local-level (each individual fuse) and system-level hysteretic curves of each scenario when μ=5. When the strengths of both fuses are equated (case#1), the system observes a large hysteretic area since both elements equally contribute to the hysteresis. In case#2, the resultant hysteresis is nearly identical with the response of the SDP fuse. This is because the EPO fuse has a larger strength and is thereby protected by the SDP. Similarly, the SDP fuse performs linear elastically in case#3, which leads to an EPO-type system-level hysteretic response.

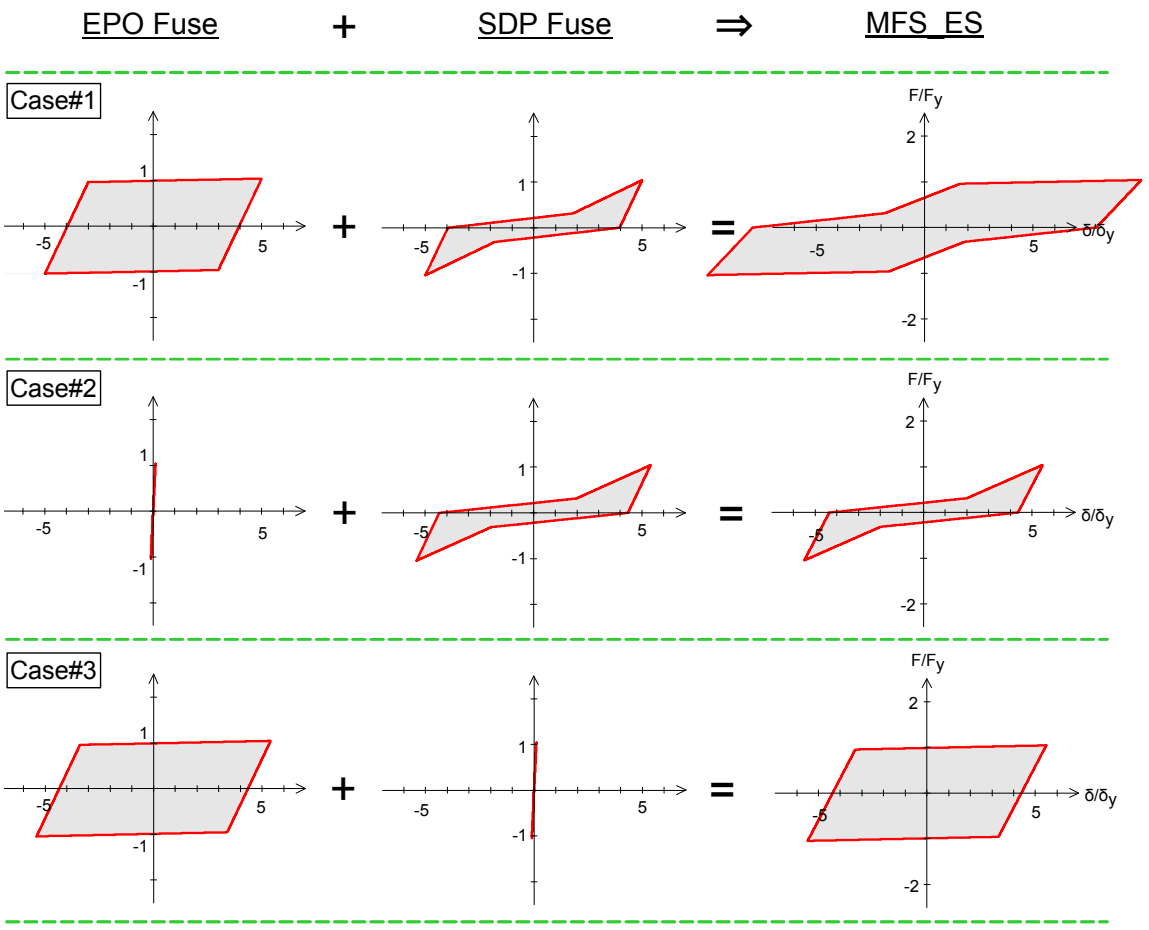

Figure 8.33 Hysteretic curves of three MFS_ES cases when μ=5

Figure 8.34 compares the hysteretic performance among the three MFP_ES cases in terms of their R_{ED} and R_{RC} responses. When the strength of the EPO fuse is 10 times larger than that of the SDP (case#2), this MFS_ES system observes the smallest R_{ED}. This is because the system-level energy dissipation response of this case is dominated by the SDP fuse mechanism and the EDP fuse behaves elastically, as illustrated in Figure 8.33. As a consequence, it falls into zone 1 (unfavorable zone) in terms of its R_{ED}-R_{RC} response.

Likewise, when the strength of the SDP fuse is significantly large, as in case#3, the SDP will perform elastically and the EPO will be subjected to a significant inelasticity. Hence, this case is described as EPO-dominated system, which possesses the largest R_{ED} and enters into zone 2 (energy dissipation prone zone).

Note that the re-centering behaviors of all cases are the same. This is because the unloading stiffness of each fuse is assumed to be the same as the initial stiffness in this study. Since all fuse mechanisms of the MFS_ES system lack re-centering capability, the EPO-dominated case (case#3) or the balanced case (case#1) is optimal real design due to its stronger energy dissipation capacity.

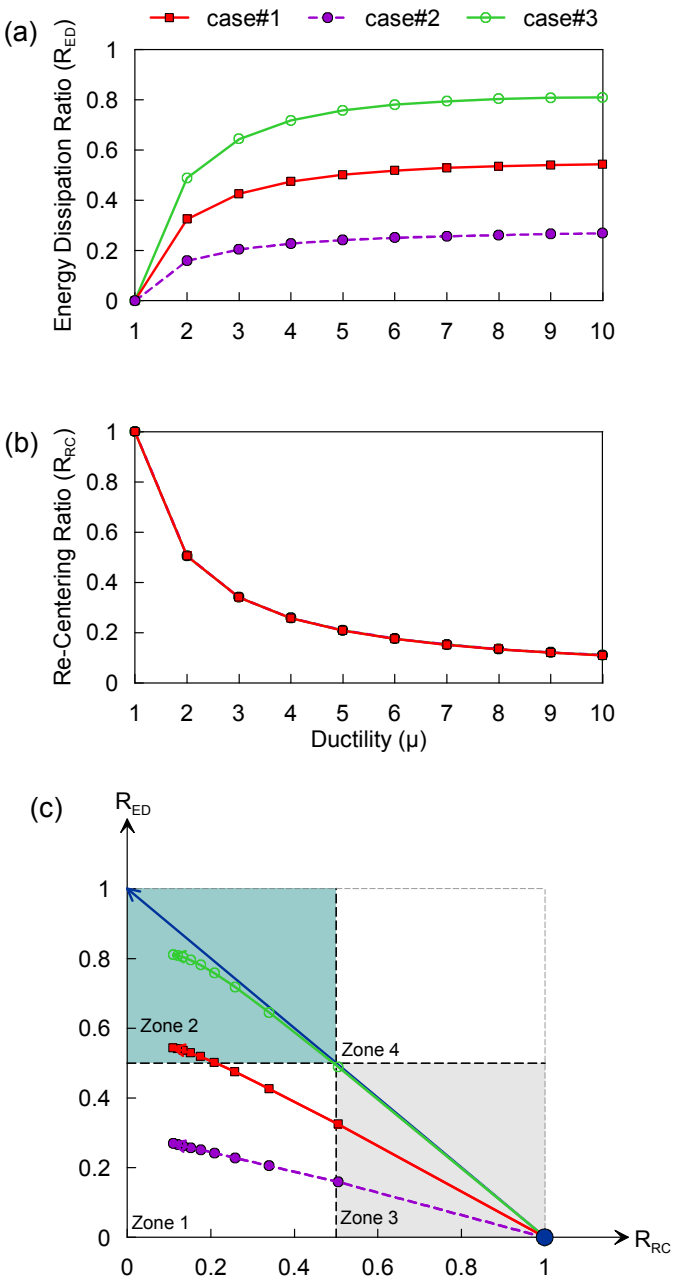

Figure 8.34 Performance comparison for the three MFS_ES systems: (a) R_{ED} vs μ; (b) R_{RC} vs μ; (c) R_{ED} vs R_{RC}

8.5.2 MFS_EF system

The second MFS system is constructed by EPO and FR fuses, termed MFS_EF. In like fashion, three different MFS_EF scenarios are investigated considering the strength difference between the EPO fuse and the FR fuse, as listed in Table 8.8. Numerical modeling follows the procedure described in Section 8.5.1and 8.4.2.

Table 8.8 Different MFS_EF cases considered

Case ID	Strength of EPO	Strength of FR
1	F_y	F_y
2	$10*F_y$	F_y
3	F_y	$10*F_y$

Figure 8.35 and Figure 8.36 provide the analysis results in terms of hysteretic responses and R_{ED} and R_{RC} performance. As expected, case#2 behaves nearly identical to the single FR system (Section 8.3.3) since the EPO fuse responds linear elastically (second row in Figure 8.35). Similarly, case#3 is an EPO-dominated scenario wherein the FR fuse behaves linear elastically.

When the strengths of both fuses are equated (case#1), the MFS_EF's R_{ED} and R_{RC} response are also balanced between case#2 and case#3. For example, its energy dissipation capacity is significantly improved compared with that of the FR-dominated (case#2); in addition, its re-centering behavior is significantly improved than case#3 (EPO-dominated). As a result, this strategy keeps the system within the re-centering zone, as indicated in Figure 8.36c. This observation is encouraging and important since balancing the strength between the EPO and FR fuses could furnish the hybrid system with the beneficial attribute of each.

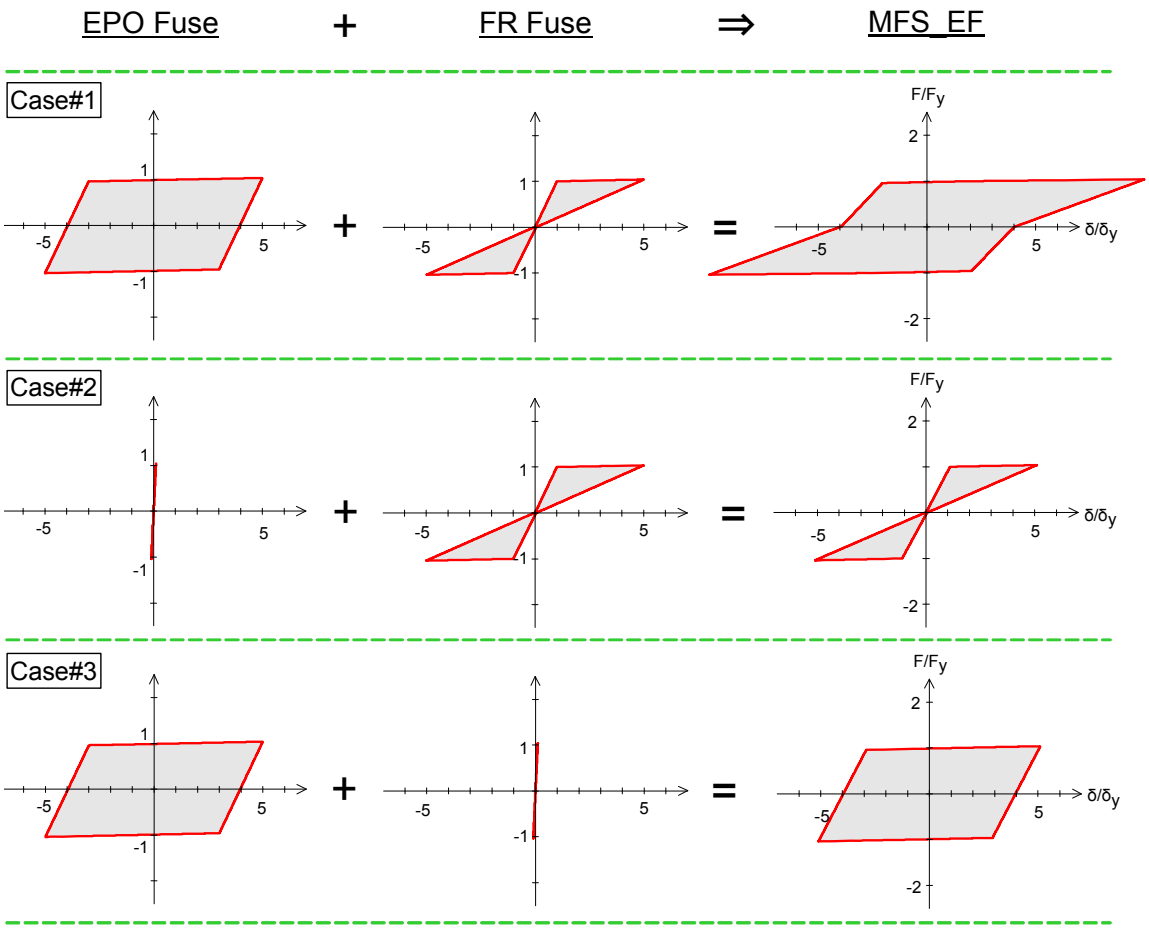

Figure 8.35 Hysteretic curves of three MFS_EF scenarios when μ=5

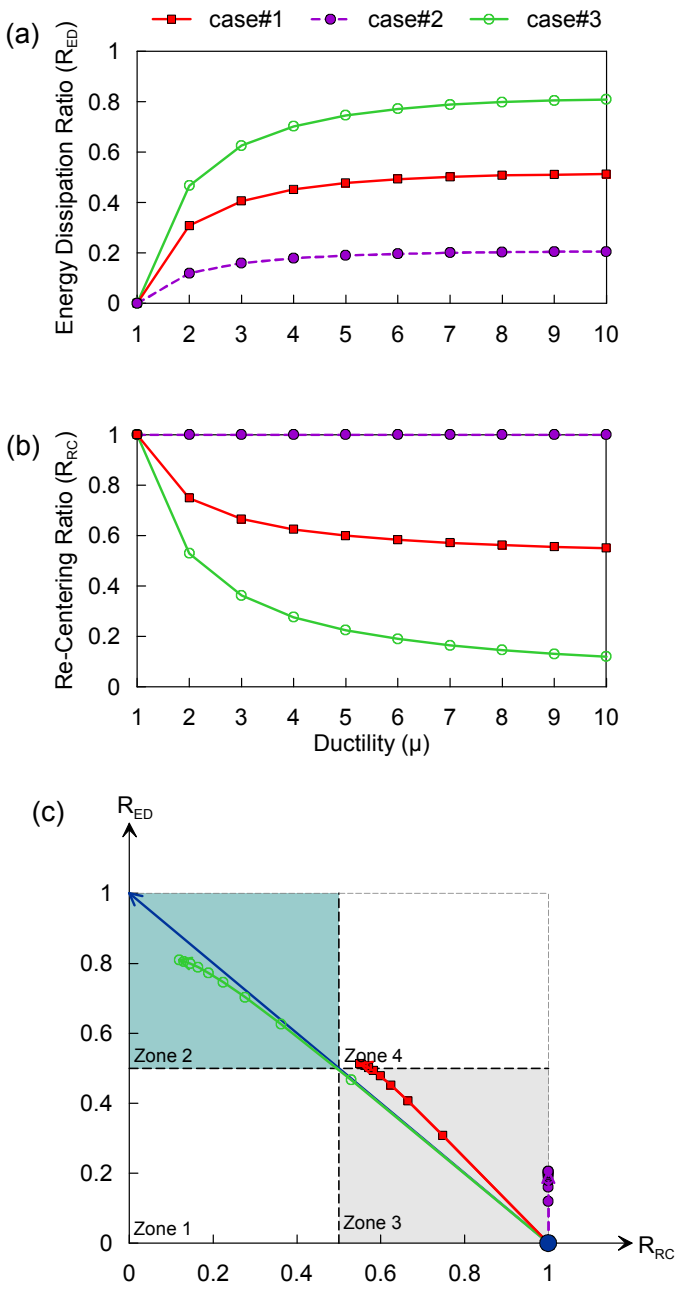

Figure 8.36 Performance comparison for the three MFS_ES systems: (a) R_{ED} vs μ; (b) R_{RC} vs μ; (c) R_{ED} vs R_{RC}

8.5.3 MFS_SF system

The final MFS system considers a combination of the SDP and FR fuse mechanism and is termed MFS_SF. In like fashion, Table 8.9 lists three different MFS_SF scenarios considering the strength difference between the two different fuses. The Numerical model construction follows the procedure described in Section 8.5.1and 8.4.3.

Table 8.9 Different MFS_SF cases considered

Case ID	Strength of SDP	Strength of FR
1	F_y	F_y
2	$10*F_y$	F_y
3	F_y	$10*F_y$

As expected, case#2 and case#3 are dominated by the FR fuse and the SDP fuse respectively. When a balanced design strategy is implemented (case#1), its overall performance is enhanced as well. For example, its re-centering capability is greatly improved compared with the SDP-dominated case (case#3), and its energy dissipation ratio is also slightly increased compared with the FR-dominated case. As such, it is still located in the re-centering zone (zone 3). Consistent with the findings during the analyses of the MFP_SF and MFS_EF systems, the observations in this section substantiate that the optimal seismic-resistant attributes of the balanced design strategy when implemented in the MFS_SF system. Indeed, this design philosophy needs be advanced in design practice.

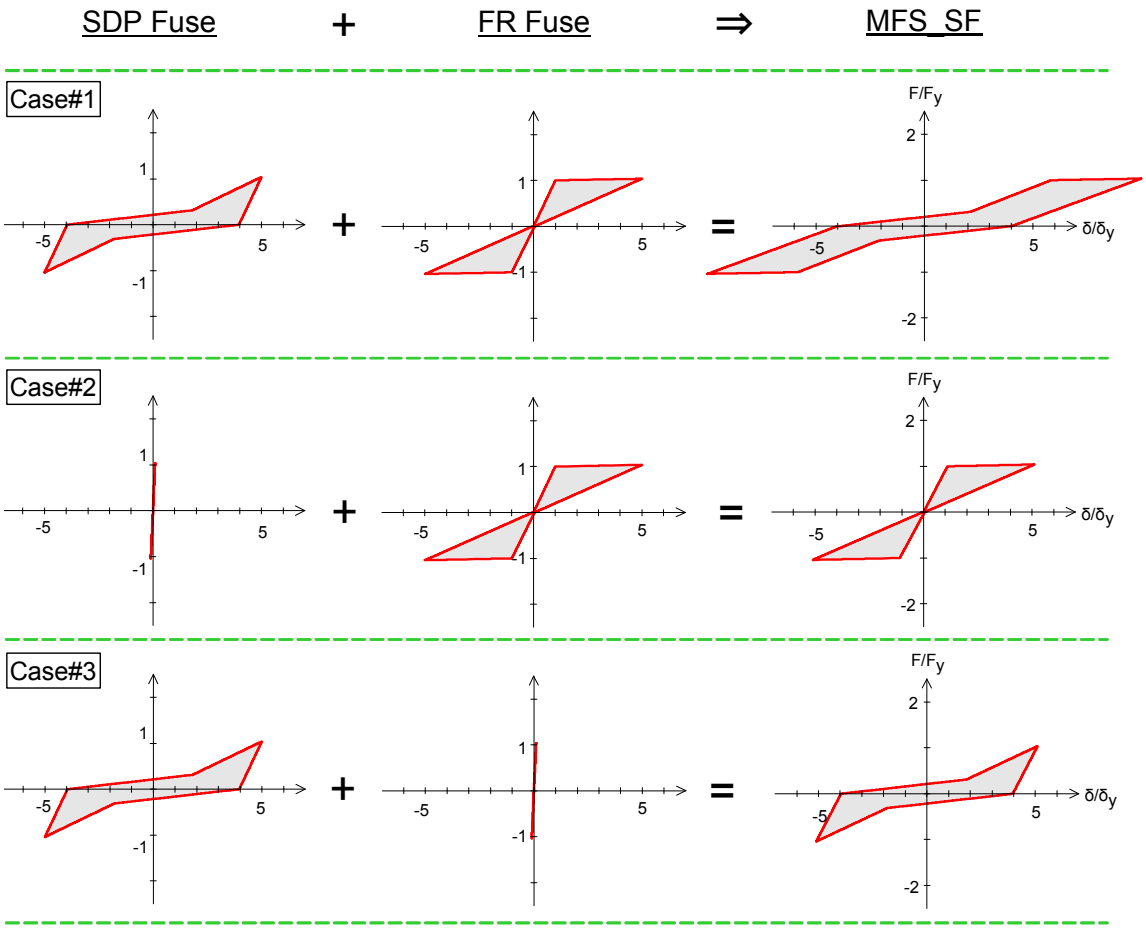

Figure 8.37 Hysteretic curves of three MFS_SF scenarios when μ=5

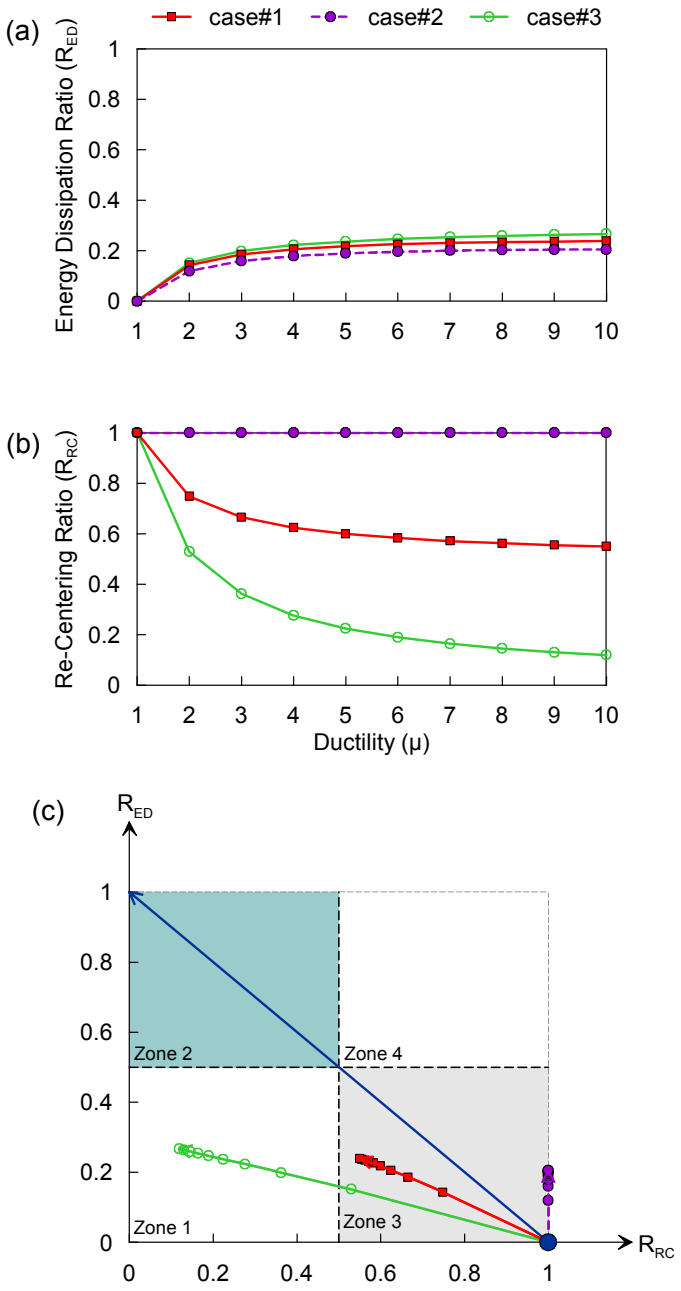

Figure 8.38 Performance comparison among three MFS_SF systems: (a) R_{ED} vs μ; (b) R_{RC} vs μ; (c) R_{ED} vs R_{RC}

8.6 Test-2 Experimental Data

The preceding sections have illustrated the efficiency of the established R_{ED}-R_{RC} diagram for characterizing an inelastic system's hysteretic performance. The goal of this section is to assess and compare the performances of the frame-wall-building models of Test-2 via this diagram. During Test-2, several frame-wall-foundation models were subjected to quasi-static cyclic loading, including the sFRD (Figure 5.12), sBD (Figure 5.16), and aFRD (Figure 7.8) models. Thus, the R_{ED} and R_{RC} of each model can be easily computed. Although the sSHD model has not been subjected to cyclic loading, the results of the SW fuse component cyclic test (Figure 5.6) are used herein to represent the performance of the sSHD model since the SW carries at the most of the lateral load based on the sBD's results (Figure 5.17c).

The models of Test-2 are essential multiple-fuse systems. In particular, the sFRD, sSHD, and aFRD models can be characterized as the parallel (MFP) system since the fuse elements considered in each model are kinematically consistent in deformation. For example, the SW and column footing in the sFRD and aFRD models share the same displacement demand since the beam is fairly rigid. Similarly, the deformation of the SW and column fuse in the sSHD model is kinematically coupled as well. The sBD system, however, is considered as a combination of MFP and MFS. In this system, the SW fuse and footing or the column fuse and footing share the same force demand which forms a series system. On the other hand, the SW and column components need to deform compatibly since the beam is fairly rigid, which creates a parallel mechanism.

Part (a) and (b) of Figure 8.39 show the plots of the R_{ED} and R_{RC} as functions of the achieved drift ratio (DR) observed in each model, respectively. Second-order polynomial trend line is added for each scatter plot. It shows that the sSHD model observes the largest R_{ED} and the smallest R_{RC} among all the models. As a result, this design configuration falls into zone 2 (energy dissipation prone zone). In contrast, when rocking foundation component has become the dominant inelastic element, as indicated in FRD models, their R_{RC} remain constantly high (>0.8) under all events; however, they observe the lowest R_{ED} (<0.2) for most of the cases. Consequently, this type of structural configuration belongs to zone 3 (re-centering prone zone). Also, it should be noted that the building asymmetry has negligible impact on the hysteretic performances of the FRD models since the sFRD and aFRD models observe nearly identical R_{RC} and R_{ED} response.

When a balanced design strategy is implemented (sBD), its R_{RC} is significantly improved when compared with the sSHD model. In the meantime, it has a better R_{ED} performance than the sFRD. As a result, this system is characterized as a re-centering system with improved energy dissipation capacity as it is located at zone 3. This observation is also consistent with the results of the numerical analyses in that, for a foundation rocking type system, balancing the strength between the fuses in parallel or series can furnish the system with the advantageous benefits from both and eventually improve the system's overall seismic performance.

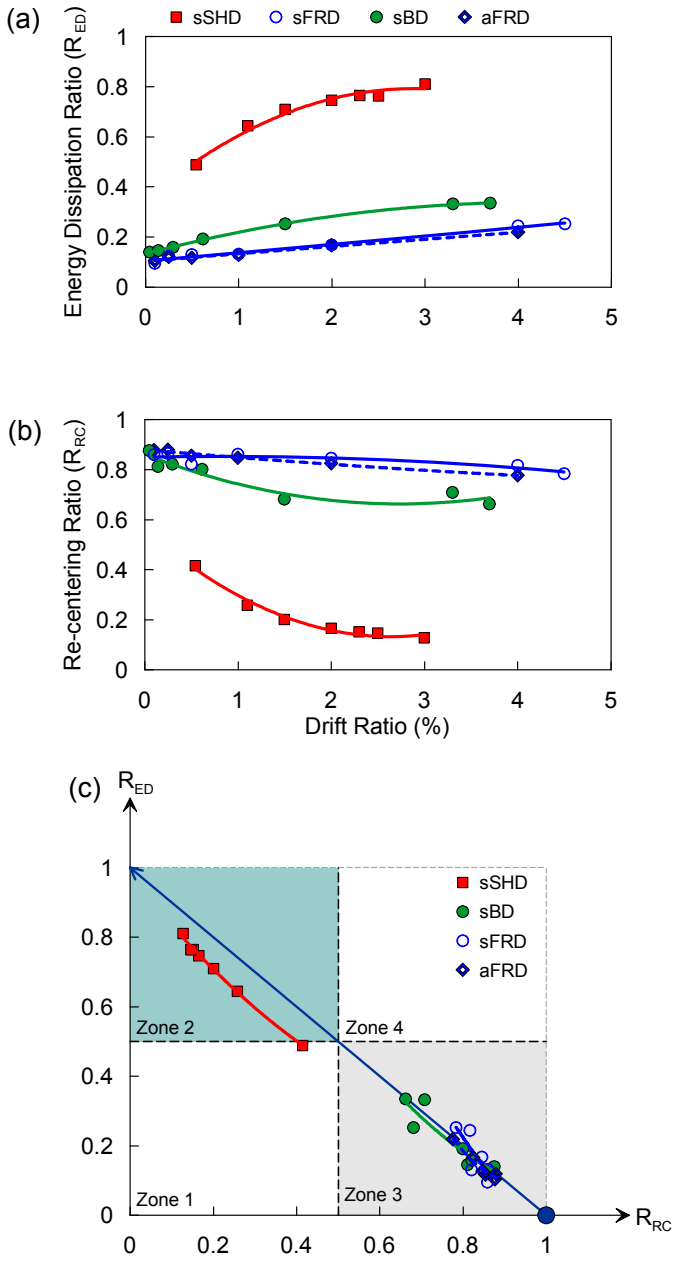

Figure 8.39 Performance comparison among four frame-wall-foundation models of Test-2: (a) R_{ED} vs DR; (b) R_{RC} vs DR; (c) R_{ED} vs R_{RC}

8.7 Conclusions and Limitations

8.7.1 Concluding Remarks

In this chapter, two parameters of an inelastic structural system, energy dissipation ratio (R_{ED}) and re-centering ratio (R_{RC}), are proposed and defined based upon the hysteretic curve. The key goal of this chapter is to establish a relation between these two parameters, and importantly, to utilize this diagram to characterize hysteretic performances of several simplified inelastic structural systems. The simplified systems are constructed by one single fuse or multiple fuse elements placed either in parallel or in series and numerically studied in the *OpenSees* program. The considered inelastic fuse mechanisms include Elastic Plastic with Overstrength (EPO), Stiffness Degradation and Pinching (SDP), and Foundation Rocking (FR). The systematic parametric studies result in the following conclusions:

- A system with an EPO fuse mechanism is characterized as an efficient energy dissipation system. However, as the post-yield stiffness ratio increases, its hysteretic performance gradually becomes unfavorable. The SDP fuse mechanism, on the other hand, consistently observes unfavorable hysteretic performance since it is always located at zone 1. However, when the displacement pinching factor decreases or the strength pinching factor increases, its performance will be enhanced. In addition, the investigated re-centering FR fuse mechanism has an inherently low R_{ED}.

- For a non-FR hybrid structural system (e.g., MFP_ES and MFS_ES), it is advised to implement the EPO fuse mechanism instead of the SDP since it could improve the system's energy dissipation capacity. However, for a FR-related hybrid system, such as the examined MFP_EF, MFP_SF, MFS_EF, MFS_SF systems, balancing the strength between the rocking foundation and the structural fuse (EPO or SDP) could furnish the system with the beneficial attribute of each fuse and eventually enhance the overall hysteretic performance compared with other single fuse dominated systems.
- With the aid of the R_{ED}-R_{RC} plot, the sBD model of Test-2 demonstrated its seismic-resistant advantages over the other model configurations (sSHD and sFRD), namely it attained a strong energy dissipation capacity and inherent re-centering characteristics concurrently.

8.7.2 Limitations

Although analyzing the established R_{ED}-R_{RC} correlation has demonstrated potential to characterize the beneficial response attributes if inelastic systems, this strategy should not be regarded as the sole method or unique criteria to judge an inelastic structural system's seismic performance. For a complete evaluation process, one should also consider other factors that would significantly affect the system's seismic performance and might not be reflected by correlating. For example, the strength and the actual dissipated hysteretic energy, which are not captured through this diagram, still play an important role in seismic design. This could explain why walls with an SDP inelastic

mechanism have emerged as an important type of seismic-resisting element in practice, despite the fact that it falls into the unfavorable zone of the R_{ED}-R_{RC} plot. In addition, the R_{ED}-R_{RC} correlation diagram in its present form is not able to consider the detrimental impacts of seismic response, such as residual settlements for foundation rocking systems. In this context, the strategy presented herein simply provides a new perspective to shed light on the hysteretic performance, and it should not be used alone for a complete seismic analysis.

Chapter 9

Conclusions and Future Work

9.1 Motivation and Scope

To date, numerous component- and system-level experimental studies have illustrated that foundation rocking can advantageously provide an isolation mechanism, energy dissipation, and re-centering of building-foundation systems. Likewise, within the framework of performance-based earthquake engineering, structural components are strategically designed to behave inelastically such as structural fuses, providing dissipation of seismic energy. These structural fuses, however, are intended to be damaged during a design earthquake and as a result will leave a structure with some level of residual distortion. By augmenting a system's response with the re-centering and energy dissipation potential of a rocking foundation, this work hypothesizes that the seismic performance of the building-foundation system can be greatly improved.

To advance this concept, experimental data is needed to understand how rocking foundations will dynamically interact with inelastic structural components. To this end, the present study is conducted with three distinct, yet complementary tasks: (1)

investigating the seismic performance of moment frame-foundation systems with varying levels of foundation yield moment, (2) investigating the seismic performance of frame-wall-foundation structural systems with varying levels of foundation yield moment as well as structural symmetry, and (3) investigating the relation between the energy dissipation and re-centering capability of inelastic systems with multiple fuses, including rocking foundations, placed in parallel or series. The first two tasks of the present study are completed by performing two large-scale laboratory experiments at centrifuge scale, and are referred to as Test-1 and Test-2, respectively. The last aspect is conducted via systematic numerical analyses in *OpenSees*.

For each test program, three fundamental model configurations were constructed considering the strength difference between the rocking foundation and the structural fuse. The first system is termed a **Structural Hinging Dominated** (SHD) system wherein the capacity of the rocking foundation is significantly larger than that of the structural fuse. This reflects a traditional fixed-base design approach. In contrast, the second case is termed a **Foundation Rocking Dominated** (FRD) system in which the foundation element has much lower strength compared with that of the structural fuse. The last system is termed a **Balanced Design** (BD) system. In this design configuration, the rocking foundation and the structural fuse are expected to yield at approximately the same base shear level.

9.2 Major Findings

9.2.1 Test-1 Experimental Findings

Test-1 was focused on moment-resisting frame building models resting on rocking shallow foundations. Three-dimensional two-story-one-bay models of each type of system, namely SHD, FRD and BD, were constructed and tested at a 30-g centrifuge scale. All models were supported on overconsolidated clay (undrained shear strength s_u=70 kPa) and were subjected to a similar sequence of six earthquake motions. The main goal of this test was to experimentally investigate the dynamic interaction between rocking foundations and structural fuses in a moment frame-foundation system. From these tests, the following major findings emerge:

- The BD model observes negligible permanent rotations of the rocking footing and the structural fuse. Compared with the SHD model, its peak seismic demand, including roof drift, structural fuse rotation, and base shear are also significantly lower. In addition, the total energy dissipated within this system is observed to be distributed fairly well between the structural fuses and rocking footings.
- For the FRD model, energy dissipation is dominated by the foundation rocking (>95%). The ductility demands on the structural components are significantly reduced. The moment-rotation hysteretic response of the rocking footing does not show significant loss in yield moment; however, it does show significant degradation in rotational stiffness.

- The SHD model experienced significant transient and residual deformation demands in the structural fuses under high amplitude motions. Its footings did observe some nonlinearity, but the rotation demand remained low even during strong shaking. All tested models observed negligible settlement, despite the fact that significant footing uplift did occur for the FRD model.

9.2.2 Test-2 Experimental Findings

During Test-2, three types of 2-dimensional two-story-two-bay frame-wall structural systems founded on surface footings were constructed and tested in a 30-g centrifuge environment. Similar to Test-1, these models were designed to achieve the behaviors of the SHD, FRD and BD system response. Each model type was constructed with a geometrically symmetric and asymmetric layout, resulting in six models in total. To properly differentiate the symmetric and asymmetric model type, a prefix of "s" or "a" is used in each model acronym. All models were founded on dry Nevada sand with a relative density of 90% and subjected to a sequence of twelve earthquake motions. Three models, aFRD, sFRD, and sBD, were additionally subjected to a sequence of quasi-static cyclic loading of increasing amplitude. The goal of Test-2 was twofold: (1) evaluate the dynamic interaction between structural fuses and rocking footings, particularly when the structural fuses are located within the shear wall (SW); (2) investigate the effect of axial load variation induced by seismic action and building asymmetry on the seismic response of the rocking footing and the entire building-foundation system.

The following major findings particular to the **symmetric** models emerge from this test series:

- The global hysteretic response of the sFRD and sBD systems are fairly ductile and stable. Notably, the load-carrying capacities of both models do not descend appreciably even at large roof drift ratios of 3.5%.
- During the sequence of earthquake motions, the sSHD model observes the largest peak roof accelerations, base shear demand, and residual deformation. In contrast, the sFRD model experiences considerably lower force and acceleration demands; however, it does observe a significantly larger peak roof drift.
- Settlements normalized by the footing length are larger in both the SW and column footings of the sFRD model than that of the sBD.
- In the sSHD and sFRD model, the majority of the energy is dissipated in the SW fuse and the rocking foundations, respectively. In the sBD model, however, dissipated energy is well distributed between the superstructure inelastic components and the rocking footings under moderate and high intensity earthquake excitations.

The following major findings, particular to the **asymmetric** models emerge from these tests:

- The interior rocking footing of the aFRD model observes a significant axial load reduction when the model is loaded towards its strong direction (towards the SW). This reduction leads to a highly asymmetric moment-

rotation hysteresis of the rocking footing, with a "bend-over" behavior. Furthermore, the asymmetry combined with the axial load fluctuation leads to a highly asymmetric system-level load-carrying response, depending on if the model is pushed towards or away from the SW of the aFRD model.

- All asymmetric models observe smaller peak roof accelerations and peak base shear demands compared with those of its symmetric counterparts particularly in their weak (away from SW) loading direction. The peak roof drift demands, however, are slightly larger in the asymmetric models.
- Placing the SW in the center, geometrically symmetric within the frame-wall-foundation system, helps to minimize residual deformations. However, it is noted that the fluctuations in axial load, which are pronounced for the asymmetric structures, do not significantly influence the relative energy dissipated by inelastic superstructure and substructure components, irrespective of motion intensity.

9.2.3 Findings of the Numerical Analyses

The goal of the numerical analyses were to investigate the relation between the energy dissipation and re-centering capability of inelastic systems constructed with a pair of fuses, including rocking foundations, placed in parallel or series. Using the hysteretic curve, two parameters, the energy dissipation ratio (R_{ED}) and the re-centering ratio (R_{RC}), are proposed to quantify the abilities of inelastic systems to dissipate hysteretic energy and recover from peak transient displacements, respectively. These two parameters are

not independent variables, yet they are inherently related. As a result, analyzing the inelastic system while correlating these two parameters could provide additional insight into its seismic performance.

The examined inelastic systems consider the behavior of the following fuse mechanisms: elastic plastic with overstrength (EPO), stiffness degradation and pinching (SDP), and foundation rocking (FR). The following major findings emerge from the numerical study:

- A system dominated by the EPO fuse mechanism is characterized as an efficient energy dissipation system as its R_{ED}-R_{RC} relation falls into the energy dissipation prone zone. The SDP fuse mechanism, on the other hand, observes unfavorable performance since it is highly likely located in the unfavorable zone.
- For an inelastic system with foundation rocking, balancing the strength between the rocking foundation and the structural fuse could furnish the system with the beneficial attributes of each inelastic fuse and eventually enhance the overall performance compared with single-fuse-dominated scenarios.
- With the aid of the R_{ED}-R_{RC} correlation, the sBD model constructed in Test-2 demonstrates its seismic advantages over the other model configurations (sSHD and sFRD), namely significant energy dissipation capacity and inherent re-centering characteristics concurrently.

9.3 Research Impact

Seismic soil-foundation-structure-interaction has received much attention in recent years; however, experimental studies thus far have yet to systematically integrate the effects of footing rocking with inelastic multi-degree-of-freedom building-foundation systems. The research effort of this dissertation addresses this issue from three distinct, yet complementary aspects. The primary impacts of this work are the following:

- Experimental data regarding the seismic response of building-foundation systems with and without foundation rocking is comprehensively documented. Observations from the tests greatly advance the understanding of how rocking foundations dynamically interacting with yielding structural elements in a system in various seismic-resistant structural configurations. Moreover, this benchmark experimental database, which incorporates inelastic structural and foundation behavior, will be highly useful for calibrating numerical models in the future. The data from these tests have been archived within the Network for Earthquake Engineering Simulation (NEES) database (DOI for Test-1: 10.4231/D3QJ77Z1R[1]; DOI for Test-2: 10.4231/D3NG4GR9C[2];).
- These tests significantly increase confidence regarding the merits of using rocking foundations as a viable inelastic fuse in seismic design.
- The tests and numerical studies systematically demonstrate that the balanced design strategy could enable the inelastic system to acquire the

[1] http://nees.org/warehouse/experiment/2886/project/732
[2] http://nees.org/warehouse/experiment/4940/project/732

beneficial attributes of each inelastic mechanism and ultimately enhance the system's seismic performance.

- Finally, the work proposes a pair of terms for characterizing two important attributes of seismic response, namely the energy dissipation ratio (R_{ED}) and the re-centering ratio (R_{RC}). The correlation between R_{ED}-R_{RC} is demonstrated as a utility for a designer to assess the seismic performance of a multi-fuse system.

9.4 Future Work

Additional efforts are needed in the future to extend and strengthen the understanding of the merits of a balanced design strategy, which incorporates the foundation rocking mechanism. Recommendations for future research include:

- Numerical simulations and in particular parametric studies are warranted considering the constructed building-foundation models as a baseline. These tests only produced a limited amount of data with limited earthquake events. Therefore, following validation of a numerical model, an extensive numerical study is warranted to consider various motion characteristics. In addition, parametric studies considering various fuse locations, characteristics, model geometries, mass distributions, soil and footing details should be considered.
- The merits of this concept should be considered for medium- and high-rise building-foundation systems as well. The current efforts are focused on

low-rise building-foundation systems; therefore, the findings may not be applicable to medium- and high-rise buildings. As such, future studies should attempt to investigate the benefits of foundation rocking on taller building systems, either experimentally or numerically.

- Examine the effects of vertical and bi-directional shaking on the system's response. Research and field evidence indicate that the vertical component of near-fault ground motions may be more severe than the horizontal component. However, the consequence of considering only vertical shaking or coupled with horizontal shaking has observed limited study, and therefore warrants further study.
- Extend the study to consider a variety of soil conditions. The soil environments considered in these tests were uniform and competent. In reality, however, the geologic media is far more complicated, and possibly less competent, such as liquefiable and reduced-strength soils. Thus, the effects of poor soil conditions on the structure and rocking footing response warrant systematic study. Furthermore, the effects of ground treatment methods, which may be used to improve soil conditions, may be of interest.
- Advance and improve the application of the R_{ED}-R_{RC} correlation. Although this diagram shows its efficiency to characterize the seismic performance of an inelastic system in the current study, it was exercised with only a handful of hysteretic systems and a maximum of a two-fuse configuration. Therefore, further numerical studies on multiple-fuse

systems (e.g., typical building systems with more than two fuses) or using experimental data of other inelastic SHD systems to populate this correlation would help advance its adoption in practice. In addition, this diagram does not allude to the direct detrimental impacts on the system, such as footing residual settlements.

9.5 Considerations for Future Centrifuge Tests

These tests incorporated multiple inelastic elements, structural components, various geologic media, and both 2-dimensional and 3-dimensional test structures. As in any test program, it is useful to synthesize the learning regarding the design and execution of the tests themselves, for future centrifuge tests. Subsequent tests, particularly should inelastic structural components be desired may consider the following:

- Improvement of the method for determining permanent displacements. New technologies, such as laser, target based, or imaging methods may be appealing for monitoring permanent displacements of inelastic structural systems in the centrifuge environment. Using conventional linear potentiometers mounted on external reference frames proves challenging due to the harsh environment of the centrifuge, shaking of the reference frame, mechanical slip at connectors, etc.
- Direct measurement of forces at footing components would be ideal to capture their static and dynamic forces. The present research utilized pairs of strain gages- though this results in discrete measurements at the column

or wall base, given the importance of the footing force history, a direct multi-axis force measurement as near to the footing base as possible would be appealing.

Bibliography

Abrams, D. P. (1987). "Influence of axial force variations on flexural behavior of reinforced concrete columns." *ACI structural journal*, 84(3), 246-254.

ACI 318 (2011). *Building Code Requirements for Structural Concrete and Commentary (ACI 318-11)*. American Concrete Institute, MI.

AISC (2011). *Steel Construction Manual, 14th Edition*. American Institute of Steel Construction, Chicago, IL.

Ajrab, J. J., Pekcan, G., and Mander, J. B. (2004). "Rocking wall-frame structures with supplemental tendon systems." ASCE, *Journal of Structural Engineering*, 130(6), 895-903.

Alavi, B. and Krawinkler, H. (2004). "Strengthening of moment-resisting frame structures against near-fault ground motion effects." *Earthquake Engineering and Structural Dynamics*, 33(6), 707-722.

Algie, T. B., Pender, M. J., Orense, R. P., and Wotherspoon, L. M. (2010). "Dynamic field testing of shallow foundations subject to rocking." *New Zealand Society for Earthquake Engineering Conference*, Paper No. 15, Wellington, New Zealand, March 26-28.

Allotey, N. K., and El Naggar, M. H. (2008). "An investigation into the Winkler modeling of the cyclic response of rigid footings." *Soil Dynamics and Earthquake Engineering*, 28(1), 44–57.

Anastasopoulos, I., Gazetas, G., Loli, M., Apostolou, M., and Gerolymos, N. (2010). "Soil failure can be used for seismic protection of structures." *Bulletin Earthquake Engineering*, 8(2), 309–326.

Anastasopoulos, I., Kourkoulis,R., Gelagoti, F., Papadopoulos, E. (2012). "Rocking Response of SDOF Systems on Shallow Improved Sand: an Experimental Study." *Soil Dynamics and Earthquake Engineering*, 40,15–33.

Anastasopoulos, I., Loli, M., Georgarakos, T., and Drosos.,V. (2013). "Shaking Table Testing of Rocking-Isolated Bridge Pier on Sand." *Journal of Earthquake Engineering* 17(1), 1-32.

American Society of Civil Engineers (2006). *Seismic rehabilitation of existing buildings*. ASCE 41-06, ASCE/Structural Engineering Institute, Reston, VA.

American Society of Civil Engineers (2010). *Minimum Design Loads for Buildings and Other Structures*. ASCE 7-10, ASCE/Structural Engineering Institute, Reston, VA.

Bartlett, P. E. (1976). *Foundation rocking on a clay soil*. ME thesis, Report number 154, School of Engineering, University of Auckland, New Zealand.

Balendra, T., Swaddiwudhipong, S., Quek, S. T., and Lee, S. L. (1984). "Free vibration of asymmetric shear wall-frame buildings." *Earthquake Engineering and Structural Dynamics*, 12(5), 629-650.

Black, C. J., Makris, N., and Aiken, I. D. (2004). "Component testing, seismic evaluation and characterization of buckling-restrained braces." *ASCE Journal of Structural Engineering*, 130(6), 880-894.

Buckle, I. G. and Mayes, R. L. (1990). "Seismic isolation: history, application, and performance-a world view." *Earthquake spectra*, 6(2), 161-201.

Carbonari, S., Dezi, F., and Leoni, G. (2012). "Nonlinear seismic behavior of wall-frame dual systems accounting for soil–structure interaction." *Earthquake Engineering and Structural Dynamics*, 41(12), 1651-1672.

Chang, B. J., Raychowdhury, P., Hutchinson, T. C., Thomas, J., Gajan, S., and Kutter, B. L. (2007). "Evaluation of the seismic performance of combined frame-wall-foundation structural systems through centrifuge testing." *In the Proceedings of the 4th International Conference on Earthquake Geotechnical Engineering (ICEGE)*, Thessaloniki, Greece, 25-28 June, Paper No. 1497.

Chatzigogos, C. T., Pecker, A., and Salençon, J. (2009). "Macroelement modeling of shallow foundations." *Soil Dynamics and Earthquake Engineering*, 29(5), 765–781.

Chen, X. C. and Lai, Y. M. (2003). "Seismic response of bridge piers on elasto-plastic Winkler foundation allowed to uplift." *Journal of sound and vibration*, 266(5), 957-965.

Chopra, A. K. and Goel, R. K. (2004). "A modal pushover analysis procedure to estimate seismic demands for unsymmetric-plan buildings." *Earthquake Engineering and Structural Dynamics*, 33(8), 903-927.

Chopra, A. K. (2007). *Dynamics of structures: Theory and applications to earthquake engineering*, Prentice Hall, Upper Saddle River, NJ.

Christopoulos, C., Filiatrault, A., Folz, B., and Uang, C. M. (2002). "Post-Tensioned Energy Dissipating Connections for Moment-Resisting Steel Frames." *ASCE Journal of Structural Engineering*, 128(9), 1111-1120.

Christopoulos, C., Tremblay, R., Kim, H.-J., and Lacerte, M. (2008). "Self-Centering Energy Dissipative Bracing System for the Seismic Resistance of Structures: Development and Validation." *ASCE Journal of Structural Engineering*, 134(1), 96-107.

Christopoulos, C., Filiatrault, A., Uang, C.-M., and Folz, B. (2002). "Posttensioned energy dissipating connections for moment-resisting steel frames." *ASCE Journal of Structural Engineering*, 128(9), 1111-1120.

Clough, R. W. and Johnston, S. B. (1966). "Effect of stiffness degradation on earthquake ductility requirements." *Transaction of Japan Earthquake Engineering Symposium*, Tokyo, Japan, 195-198.

Clough, R. W. and Huckelbridge, A. A. (1977). "Preliminary Experimental Study of Seismic Uplift of a Steel Frame." *Earthquake Engineering Research Center (EERC) Report No. UCB/EERC-77- 22*.

Clough, R. W. and Penzien, J. (1993). *Dynamics of Structures*, 2nd ed., McGraw Hill, New York, NY.

Como, M., De Stefano, M., and Ramasco, R. (2003) "Effects of column axial force–bending moment interaction on inelastic seismic response of steel frames." *Earthquake Engineering and Structural D*ynamics, 32(12), 1833-1852.

Deng, L. (2012). *Centrifuge Modeling, Numerical Analyses, and Displacement-Based Design of Rocking Foundations*. PhD Dissertation, Department of Civil and Environmental Engineering, University of California, Davis, CA.

Deng, L. and Kutter, B. L. (2012). "Characterization of rocking shallow foundation using centrifuge model tests." *Earthquake Engineering and Structural Dynamics*, 41(5), 1043–1060.

Deng, L., Kutter, B. L., and Kunnath, S. K. (2012a). "Centrifuge modeling of bridge systems designed for rocking foundations." *ASCE Journal of Geotechnical Geoenvironmental Engineering*, 138(3), 335-344.

Deng, L., Kutter, B. L., and Kunnath, S. K. (2012b). "Probabilistic seismic performance of rocking-foundation and hinging-column bridges." *Earthquake Spectra*, 28(4), 1423-1446.

Driver, R. G., Kulak, G. L., Kennedy, D. L., and Elwi, A. E. (1998). "Cyclic test of four-story steel plate shear wall." *ASCE Journal of Structural Engineering*, 124(2), 112-120.

Drosos, V., Georgarakos, T., Loli, M., Anastasopoulos, I., Zarzouras, O., Gazetas, G. (2012). "Soil-Foundation-Structure Interaction with Mobilization of Bearing Capacity: An Experimental Study on Sand." *ASCE Journal of Geotechnical Geoenvironmental Engineering*, 138(11), 1369-1386.

Eatherton, M., Hajjar, J., Ma, X., Krawinkler, H., and Deierlein, G. (2010). "Seismic Design and Behavior of Steel Frames with Controlled Rocking-Part I: Concepts and Quasi-Static Subassembly Testing," *Proceedings of the ASCE/SEI Structures Congress 2010*, Orlando, FL, May 12-15.

El Ganainy, H. and El Naggar, M. H. (2009). "Efficient 3D nonlinear Winkler model for shallow foundations." *Soil Dynamics and Earthquake Engineering*, 29(8), 1236–1248.

Esmaeily, A. and Xiao, Y. (2005). "Behavior of reinforced concrete columns under variable axial loads: analysis." *ACI structural journal*, 102(5), 736-744.

Espinoza, A. and Mahin, S. A. (2006). "Rocking of bridge piers subjected to multidirectional earthquake excitation." *Proc. 5th National Seismic Conference on Bridge and Highways*, September 18-20, 2006. San Francisco, CA.

Figini, R., Paolucci, R., and Chatzigogos, C. T. (2012). "A macro-element model for non-linear soil-shallow foundation-structure interaction under seismic loads: theoretical development and experimental validation on large scale tests." *Earthquake Engineering and Structural Dynamics*, 41(3), 475–493.

Gajan, S., Kutter, B. L., Phalen, J. D., Hutchinson, T. C., and Martin, G. R. (2005). "Centrifuge modeling of load-deformation behavior of rocking shallow foundations." *Soil Dynamics and Earthquake Engineering*, 25, 773–783.

Gajan, S. and Kutter, B. L. (2008). "Capacity, settlement, and energy dissipation of shallow footings subjected to rocking." *ASCE Journal of Geotechnical Geoenvironmental Engineering*, 134(8), 1129-1141.

Gajan, S. and Kutter, B. L. (2009a). "Contact interface model for shallow foundations subjected to combined cyclic loading." *ASCE Journal of Geotechnical Geoenvironmental Engineering*, 135(3), 407–419.

Gajan, S. and Kutter, B. L. (2009b). "Effects of moment-to-shear ratio on combined cyclic load-displacement behavior of shallow foundations from centrifuge experiments." ASCE *Journal of Geotechnical and Geoenvironmental Engineering*, 135(8), 1044-1055.

Gazetas, G. (1991). “Foundation vibrations.” In “Foundation Engineering Handbook, 2nd edition”, H. Y. Fang, Ed., Kluwer/Springer, Chapter 15, 553-593.

Gelagoti, F., Kourkoulis, R., Anastasopoulos, I., Gazetas, G. (2012a). “Rocking isolation of low-rise frame structures founded on isolated footings.” *Earthquake Engineering and Structural Dynamics*, 41(7), 1177-1197.

Gelagoti, F., Kourkoulis, R., Anastasopoulos, I., Gazetas, G. (2012b). “Rocking-isolated frame structures: Margins of safety against toppling collapse and simplified design approach.” *Soil Dynamics and Earthquake Engineering*, 32(1):87–102.

Hakhamaneshi, M., Kutter, B. L., Hutchinson, T. C., and Liu, W. (2011). “Compatible soil and structure yielding to improve system performance.” *Rep. No. UCD/CGMDR-11/07*, Center for Geotechnical Modeling, Univ. of California, Davis, CA.

Hakhamaneshi, M., Kutter, B. L., Deng, L., Hutchinson, T. C. and Liu, W. (2012). “New findings from centrifuge modeling of rocking shallow foundations in clayey ground.” *Proceedings of ASCE 2012 Geo-congress*, Oakland, March 25-29.

Hakhamaneshi, M., Gavras, A. G., Wilson D. W., Kutter, B. L., Liu, W., and Hutchinson, T. C. (2014). “Effects of footing shape on the settlement of rectangular and I-shaped rocking shallow foundations.” *8th International Conference Physical Modelling in Geotechnics*, Perth, Australia, January 14-17.

Harden, C. W. and Hutchinson, T. C. (2009). “Beam-on-nonlinear-Winkler-foundation modeling of shallow, rocking-dominated footings.” *Earthquake Spectra*, 25(2), 277-300.

Holden, T, Restrepo, J. I., and Mander, J. B. (2003). “Seismic Response of Precast Reinforced and Prestressed Concrete Walls.” *ASCE Journal of Structural Engineering*, 129(3), 286-296.

Housner, G. W. (1963). “The behavior of inverted pendulum structures during earthquakes.” *Bulletin of the Seismological Society of America*, 53(2), 403–417.

Hung, H. H., Liu, K. Y., Ho, T. H., and Chang, K .C. (2011). “An experimental study on the rocking response of bridge piers with spread footing foundations.” *Earthquake Engineering and Structural Dynamics*, 40(7), 749-769.

Ibarra, L. F., Medina, R. A., and Krawinkler, H. (2005). “Hysteretic models that incorporate strength and stiffness deterioration.” *Earthquake Engineering and Structural Dynamics*, 34(12), 1489-1511.

Ikenaga, M., Nagae, T., Nakashima, M., and Suita, K. (2006). “Development of Column Bases Having Self-Centering and Damping Capability”. *Proceedings of the Fifth*

International Conference on Behaviour of Steel Structures in Seismic Areas STESSA 2006, Yokohama, Japan, August 14-17.

Johnson, K. J. (2012). *Characterization of test results of rocking foundations using a multi-linear hysteretic model*. MS Report, Department of Civil and Environmental Engineering, University of California, Davis, CA.

Kam, W. Y., Pampanin, S., and Elwood, K. (2011). Seismic performance of reinforced concrete buildings in the 22 February Christchurch (Lyttelton) earthquake. *Bulletin of the New Zealand Society for Earthquake Engineering*, 44(4), 239-278.

Kelley, J. and Tsztoo, D. (1977). "Earthquake Simulation Testing of a Stepping Frame with Energy-Absorbing Devices", *Report No. EERC 77-17*, Earthquake Engineering Research Center, College of Engineering, University of California, Berkeley.

Kilar, V. and Fajfar, P. (1997). "Simple push-over analysis of asymmetric buildings." *Earthquake Engineering and Structural Dynamics*, 26(2), 233-249.

Kourkoulis, R., Gelagoti, F., and Anastasopoulos., I. (2012). "Rocking Isolation of Frames on Isolated Footings: Design Insights and Limitations." *Journal of Earthquake Engineering*, 16(3), 374-400.

Kurama, Y., Sause, R., Pessiki, S., and Lu, L. W. (1999). "Lateral load behavior and seismic design of unbonded post-tensioned precast concrete walls." *ACI Structural Journal*, 96(4), 622-632.

Kurama, Y. C. and Shen, Q. (2004). "Posttensioned Hybrid Coupled Walls under Lateral Loads," *ASCE Journal of Structural Engineering*, 130(2), 297-309.

Kutter, B. L. (1995). "Recent advances in centrifuge modeling of seismic shaking." *Proc., 3rd Int. Conf. on Recent Advances in Geotechnical Earthquake Engineering and Soil Dynamics*, Vol. 2, Univ. of Missouri, Rolla, MO, 927–942.

Liu, W., Hakhamaneshi, M., Kutter, B. L., and Hutchinson, T. C. (2011). "Compatible soil and structure yielding to improve system performance." *Rep. No. UCD/CGMDR-11/07*, Center for Geotechnical Modeling, Univ. of California, Davis, CA.

Liu, W., Hutchinson, T. C., Hakhamaneshi, M., and Kutter, B. L. (2012). "Numerical parametric study on inelastic foundation-building models with presence of rocking foundation." *15th World Conference on Earthquake Engineering*, Lisbon, Portugal, September 24-28.

Liu, W., Hutchinson, T. C., Kutter, B. L., Hakhamaneshi, M., and Gavras, A. G. (2013a). "Balancing the Beneficial Contributions of Foundation Rocking and Structural Yielding to Improve Structural Seismic Resilience." *4th ECCOMAS Thematic*

Conference on Computational Methods in Structural Dynamics and Earthquake Engineering, Kos Island, Greece, June 12-14.

Liu, W., Hutchinson, T. C., Kutter, B. L., Hakhamaneshi, M., Aschheim, M., and Kunnath, S. (2013b). "Demonstration of Compatible Yielding between Soil-Foundation and Superstructure Components." *ASCE Journal of Structural Engineering*, 139(8), 1408-1420.

Liu, W., Gavras, A.G., Hakhamaneshi, M., Kutter, B. L. and Hutchinson, T. C. (2013c). "Compatible soil and structure yielding to improve system performance." Centrifuge Data Report for Test Series MAH03, *Report No. UCD/CGMDR-13/12*, Center for Geotechnical Modeling, University of California, Davis.

Liu, W., Hutchinson, T. C., Gavras, A. G., Kutter, B. L., and Hakhamaneshi, M. (201Xa). "Seismic Behavior of Frame-Wall-Rocking Foundation Systems-Part I: Test Program and Slow Cyclic Test Results." *ASCE Journal of Structural Engineering*, (submittal).

Liu, W., Hutchinson, T. C., Gavras, A. G., Kutter, B. L., and Hakhamaneshi, M. (201Xb). "Seismic Behavior of Frame-Wall-Rocking Foundation Systems-Part II: Shake Table Testing Results." *ASCE Journal of Structural Engineering*, (submittal).

Liu, W., Hutchinson, T. C., Kutter, B. L., Gavras, A. G., and Hakhamaneshi, M. (201Xc). "Effect of Seismic-Induced Axial Load Fluctuation on Asymmetric Wall-Frame-Rocking Foundation Systems." *Earthquake Engineering and Structural Dynamics*, (submittal).

Luco, J. E. and Wong, H. L. (1987). "Seismic response of foundations embedded in a layered half-space." *Earthquake engineering and structural dynamics*, 15(2), 233-247.

Ma, X., Eatherton, M., Hajjar, J., Krawinkler, H., and Deierlein, G. (2010). "Seismic Design and Behavior of Steel Frames with Controlled Rocking-Part II: Large Scale Shake Table Testing and System Collapse Analysis," *Proceedings of the ASCE/SEI Structures Congress 2010*, Orlando, FL, May 12-15.

Marriott, D., Pampanin, S., Bull, D., and Palermo, A. (2008). "Dynamic testing of precast, post-tensioned rocking wall systems with alternative dissipating solutions." *Bulletin of the New Zealand Society for Earthquake Engineering*, 41(2):90–103.

Maugeri, M., Musumeci, G., Novità, D., Taylor, C. A. (2000). "Shaking table test of failure of a shallow foundation subjected to an eccentric load." *Soil Dynamics and Earthquake Engineering*, 20(5), 435-444.

Mazzoni, S., McKenna, F., Scott, M. H., and Fevens, G. L. (2009). *Open System for Earthquake Engineering Simulation User Command-Language Manual*, Pacific Earthquake Engineering Research Center, Univ. of California, Berkeley, CA <http://opensees.berkeley.edu/>.

Mergos, P. E. and Kawashima, K. (2005). "Rocking isolation of a typical bridge pier on spread foundation." *Journal of Earthquake Engineering*, 9(Sup 2), 395–414.

Menegotto, M., and Pinto, P. E. (1973). "Method of analysis of cyclically loaded RC plane frames including changes in geometry and nonelastic behavior of elements under normal force and bending." *Proc., IABSE Symposium on Resistance and Ultimate Deformability of Structures Acted on by Well-Defined Repeated Loads*, Final report, 112–123, Lisbon, Portugal.

Midorikawa, M., Azuhata, T., Ishihara, T., and Wada, A. (2006). "Shaking table tests on seismic response of steel braced frames with column uplift." *Earthquake Engineering and Structural Dynamics*, 35(14), 1767-1785.

Moroni, M. O., Sarrazin, M., & Soto, P. (2012). Behavior of Instrumented Base-Isolated Structures during the 27 February 2010 Chile Earthquake. *Earthquake Spectra*, 28(S1), S407-S424.

Mylonakis, G., Nikolaou, S., and Gazetas, G. (2006). "Footing under seismic loading: Analysis and design issues with emphasis on bridge foundations." *Soil Dynamics and Earthquake Engineering*, 26(9), 824–853.

Nakaki, D. K., and Hart, G. C. (1987). "Uplifting response of structures subjected to earthquake motions." *Rep. No. 2.1-3, U.S.-Japan Coordinated Program for Masonry Building Research*, Ewing/Kariotis/ Englekirk and Hart, Los Angeles.

Negro, P., Paolucci, R., Pedretti, S., and Faccioli, E. (2000). "Large-scale soil-structure interaction experiments on sand under cyclic loading." *Proc., 12th World Conf. on Earthquake Engineering*, Paper No. 1191, Auckland, New Zealand, January 30-February 4.

Nilson, A, H., Darwin, D., Dolan, C. W. (2004) *Design of concrete structures* (No. 13th Edition), New York, NY: Mcgraw-Hill.

Pacific Earthquake Engineering Research Center (PEER), 2012. <http://peer.berkeley.edu>

Palermo, A., Pampanin, S., and Calvi, G. M. (2005). "Concept and Development of Hybrid Solutions for Seismic Resistant Bridge Systems." *Journal of Earthquake Engineering*, 9(6), 899-921.

Paolucci, R., Shirato, M., and Yilmaz, M. T. (2008). "Seismic behavior of shallow foundations: Shaking table experiments vs numerical modeling." *Earthquake Engineering and Structural Dynamics*, 37(4), 577–595.

Panagiotidou, A. I., Gazetas, G., and Gerolymos, N. (2012). "Pushover and Seismic Response of Foundations on Stiff Clay: Analysis with P-Delta Effects." *Earthquake Spectra*, 28(4), 1589-1618.

Panagiotou, M., and Restrepo, J. I. (2009). "Dual-Plastic Hinge Design Concept for Reducing Higher-Mode Effects on High-Rise Cantilever Wall Buildings." *Earthquake Engineering and Structural Dynamics*, 38 (12), 1359-1380.

Paulay, T. and Priestley, M. J. N. (1992). *Seismic design of reinforced concrete and masonry buildings*, Wiley, New York.

Pecker,A., andChatzigogos,C.T. (2010). "Non linear soil structure interaction: impact on the seismic response of structures." Earthquake engineering in Europe, geotechnical, geological, and earthquake engineering, Vol. 17, 79–103, M. Garevski and A. Ansal, eds., Springer, New York.

Pecker, A., Paolucci, R., Chatzigogos, C., Correia, A. A., and Figini, R. (2014). "The role of non-linear dynamic soil-foundation interaction on the seismic response of structures." *Bulletin of Earthquake Engineering (In Press)*.

Phalen, J. D. (2003). *Physical modeling of the soil–foundation interaction of spread footings subjected to lateral cyclic loading*. MS Thesis, University of California, Davis, CA.

Pollino, M. and Bruneau, M. (2008). "Analytical and Experimental Investigation of a Controlled Rocking Approach for Seismic Protection of Bridge Steel Truss Piers." *Technical Report MCEER-08-0003*.

Pollino, M., Sabzehzar, S., Qu, B., and Mosqueda, G. (2013). "Research Needs for Seismic Rehabilitation of Sub-standard Buildings using Stiff Rocking Cores." *In the proceedings of ASCE 2013 Structures Congress*, Pittsburgh, Page 1683-1693, May 2-4.

Priestley, M. J. N. and Tao, J. R. T. (1993). "Seismic Response of Precast Prestressed Concrete Frames with Partially Debonded Tendons." *PCI Journal*, 38(1), 58-69.

Psycharis, I. N. (1981). *Dynamic behavior of rocking structures allowed to uplift*. PhD thesis, California Institute of Technology.

Raychowdhury, P. (2008). *Nonlinear Winkler-based Shallow Foundation Model for Performance Assessment of Seismically Loaded Structures*. PhD thesis, Department of Structural Engineering, University of California, San Diego.

Raychowdhury, P., Hutchinson T. C. (2009). "Performance evaluation of a nonlinear Winkler-based shallow foundation model using centrifuge test results." *Earthquake Engineering and Structural Dynamics*, 38 (5), 679-698.

Raychowdhury, P., Hutchinson T.C. (2011). "Performance of seismically loaded shearwalls on nonlinear shallow foundations." *International Journal for Numerical and Analytical Methods in Geomechanics*, 35 (7), 846-858.

Restrepo, J. I., and Rahman, A. (2007). "Seismic performance of self-centering structural walls incorporating energy dissipators." ASCE, *Journal of Structural Engineering* 133(11), 1560-1570.

Reyes, J. C. and Chopra, A. K. (2011). "Evaluation of three-dimensional modal pushover analysis for unsymmetric-plan buildings subjected to two components of ground motion." *Earthquake Engineering and Structural Dynamics*, 40(13), 1475-1494.

Ricles, J. M., Sause, R., Garlock, and Zhao, C. (2001). "Posttensioned Seismic-Resistant Connections for Steel Frames." *ASCE Journal of Structural Engineering*, 127(2), 113-121.

Rosebrook, K. R., and Kutter, B. L. (2001a). "Soil-foundation-structure interaction: Shallow foundations." *Rep. No. UCD/CGMDR-01/09*, Univ. of California, Davis, CA.

Rosebrook, K. R., and Kutter, B. L. (2001b). "Soil-foundation-structure interaction: Shallow foundations." *Rep. No. UCD/CGMDR-01/10*, Univ. of California, Davis, CA.

Rosebrook, K. R., and Kutter, B. L. (2001c). "Soil-foundation-structure interaction: Shallow foundations." *Rep. No. UCD/CGMDR-01/11*, Univ. of California, Davis, CA.

Rutenberg, A., Tso, W. K., Heidebrecht, A. C. (1977). "*Dynamic properties of asymmetric wall-frame structures*." *Earthquake Engineering and Structural Dynamics*, 5(1), 41-51.

Saad, A., Sanders, D. H., and Buckle, I. G. (2012). "Impact of Rocking Foundations on Horizontally Curved Bridge Systems Subjected to Seismic Loading." *Proc. Structures Congress 2012*, ASCE, Chicago, IL, March 29-31.

Saadeghvaziri, M. A. (1997). "Nonlinear response and modelling of RC columns subjected to varying axial load." *Engineering Structures*, 19(6), 417-424.

Schofield, A. N. (1980). Cambridge geotechnical centrifuge operations. *Geotechnique*, 30(3), 227-268.

Scott, M. H. and Fenves, G. L. (2006). "Plastic hinge integration methods for force-based beam–column elements." *ASCE Journal of Structural Engineering*, 132(2), 244-252.

Scott, R. F. (1983). Centrifuge model testing at Caltech. *International Journal of Soil Dynamics and Earthquake Engineering*, 2(4), 188-198.

Shenton III, H. W., Dinehart, D. W., and Elliott, T. E. (1998). "Stiffness and energy degradation of wood frame shear walls." *Canadian Journal of Civil Engineering*, 25(3), 412-423.

Shirato, M., Kouno, T., Asai, R., Nakani, S., Fukui, J., and Paolucci, R. (2008). "Large-scale experiments on nonlinear behavior of shallow foundations subjected to large earthquakes." *Soils and Foundations*, 48(5), 673–692.

Sittipunt, C. and Wood, S. L. (1995). "Influence of web reinforcement on the cyclic response of structural walls." *ACI Structural Journal*, 92(6), 745-756.

Spencer, B. F., Dyke, S. J., Sain, M. K., and Carlson, J. (1997). "Phenomenological model for magnetorheological dampers." *ASCE Journal of Engineering Mechanics*, 123(3), 230-238.

Stanton, J., Stone, W., and Cheok, G. S. (1993). "A Hybrid Reinforced Precast Frame for Seismic Regions." *PCI Journal*, 42(2), 20-32.

Stewart, J. P., Seed, R. B., and Fenves, G. L. (1999). "Seismic soil-structure interaction in buildings. II: Empirical findings." *ASCE Journal of Geotechnical Geoenvironmental Engineering*, 125(1), 38–48.

Taylor, C. A., and Crewe, A. J. (1996). "Shaking table tests of simple direct foundations." *Proc., 11th World Conf. on Earthquake Engineering*. Paper No. 2048, Acapulco, Mexico, June 23-28.

Taylor, P. W., Bartlett, P. E., Weissing, P. R. (1981). "Foundation rocking under earthquake loading." *Proceedings of the 10th International Conference on Soil Mechanics and Foundation Engineering*, vol. 3, Page 313–322, Stockholm, June 15-19.

Takamatsu, T., Tamai, H., Yamanishi, T., and Matsuo, A. (2006). "Self-Centering Performance of Non-Slip-Type Exposed Column Base" *Proceedings of the Fifth International Conference on Behaviour of Steel Structures in Seismic Areas (STESSA)*, Yokohama, Japan, August 14-17.

Thomas, J. M., Gajan, S., and Kutter, B. L. (2006). "Soil-foundation structure interaction: Shallow foundations." *Centrifuge Data Rep. for test series JMT01, Rep. No. UCD/CGMDR*, Center for Geotechnical Modeling, Univ. of California, Davis, Calif.

Toranzo, L. A., Restrepo, J. I., Mander, J. B., and Carr, A. J. (2009). "Shake-Table Tests of Confined-Masonry Rocking Walls with Supplementary Hysteretic Damping." *Journal of Earthquake Engineering*, 13(6), 882-898.

Tremblay, R., Poirier, L. P., Bouaanani, N., Leclerc, M., Rene, V., Fronteddu, L., and Rivest, S. (2008). "Innovative Viscously Damped Rocking Braced Steel Frames." *Proceedings of the 14th World Conference on Earthquake Engineering*, Beijing, China, October 12-17.

Tremblay, R., Lacerte, M., and Christopoulos, C. (2008). "Seismic response of multistory buildings with self-centering energy dissipative steel braces." ASCE *Journal of structural engineering*, 134(1), 108-120.

Trombetta, N. W., Mason, H. B., Chen, Z., Hutchinson, T. C., Bray, J. D., and Kutter, B. L. (2013). "Nonlinear dynamic foundation and frame structure response observed in geotechnical centrifuge experiments." *Soil Dynamics and Earthquake Engineering*, 50, 117–133.

Trombetta, N. W., Mason, H. B., Hutchinson, T. C., Zupan, J. D., Bray, J. D., and Kutter, B. L. (2014). "Nonlinear soil-foundation-structure and structure-soil-structure interaction: centrifuge test observations." ASCE *Journal of Geotechnical and Geoenvironmental Engineering*, (in press).

Veletsos, A. S. and Meek, J. W. (1974). "Dynamic behaviour of building-foundation systems." *Earthquake Engineering and Structural Dynamics*, 3(2), 121-138.

Wiessing, P. R. (1979). *Foundation rocking on sand*. ME thesis, Report number 203, School of Engineering, the University of Auckland, New Zealand.

Yim, C. S., Chopra, A. K., and Penzien, J. (1980). "Rocking response of rigid blocks to earthquakes." *Earthquake Engineering and Structural Dynamics*, 8(6), 565-587.

Yim, C. S., and Chopra, A. K. (1984). "Earthquake response of structures with partial uplift on Winkler foundation." *Earthquake Engineering and Structural Dynamics*, 12(2), 263–281.

Appendix A

OpenSees Input Files for Numerical Models

A.1 BD Model of Test-1

A.1.1 Main Tcl File

```
#--------------------------------------------------------------------
---------------------
# MAH02 2-story model: 2D 2-Story with Balanced Design (2011-10-24)
(One Frame)
# This script is intended to validate the centrifuge model's seismic
performance
#--------------------------------------------------------------------
---------------------
#
# Unit System: N, m, sec, prototype scale.
# Note: Node and element numbering, please refer to the figure
created by Grapher
#


#1. SET UP----------------------------------------------------------
---
wipe;                                # clear opensees model
model basic -ndm 2 -ndf 3;           # 2 dimensions, 3 dof per node
set su 60;
set dmp1 0.08;          # Damping ratio for 1st mode
set dmp2 0.08;
```

```
set su [expr $su*1000];           # update su
set G [expr 260*$su];       # clay shear Modulus
set q_ult [expr 5.141593*$su];    # Ultimate bearing capacity
set Rk 5;        # stiffness intensity ratio
set Re 0.1;# End length ratio
set Se 0.02;     # spring spacing
set crad 60;               # radition damping

set dataDir Results3;                  # set up name of data
directory
file mkdir $dataDir;              # Create data directory called
Results in the same directory as the file itself
set Nscale 1.0;                   # Centrifuge scale
(prototype/model)
set N1     $Nscale;             # scaling with N (length, time etc)
set N2     pow($Nscale,2.0);      # scaling with N^2(i.e. Area,
shear, axial force etc.)
set N3     pow($Nscale,3.0);      # scaling with N^3(i.e. Mass,
bending moment etc.)
set N4     pow($Nscale,4.0);      # scaling with N^3(i.e. Moment of
Inertia etc.)


#2. Global Parameters Input & Derivation----------------------------
--------------------------
#2.1 Global Parameters Input (mass & geometry)----------------------
--------------------------
set M_PL   [expr 0.395*$N3];      # mass of Aluminum plate (kg)
set M1_BM  [expr 1.584*$N3];      # mass of first floor (kg)
set M1_LD  [expr 0.191*$N3];      # mass of leading block (kg)
set M2_BM  [expr 0.73*$N3];       # mass of second floor (kg)
set M_CL1  [expr 0.24875*$N3];    # mass of first floor single
column(kg)
set M_CL2  [expr 0.08435*$N3];    # mass of second floor single
column (kg)
set M_ftg  [expr 0.46*$N3];       # mass of single footing

set M1     [expr ($M1_LD*2+$M1_BM+$M_PL)*2];       # total mass for
first floor
set M2     [expr ($M2_BM+$M_PL)*2];                # total mass for
second floor

set H1     [expr 0.2*$N1];        # First story height (m)
set H2_1   [expr 0.0222*$N1];     # Second story first part height
(m)
set H2_2   [expr 0.0127*$N1];     # Second story second part height
(m)
set H2_3   [expr 0.1251*$N1];     # Second story second part height
(m)
set H2     [expr $H1+$H2_1];      # the nodal height (m)
set H3     [expr $H2+$H2_2];      # the nodal height (m)
set H4     [expr $H3+$H2_3];      # the top nodal height (m)
```

```
set L1_1   [expr 0.0378*$N1];     # first story beam first part
length (m)
set L1_2   [expr 0.1479*$N1];     # first story beam second part
length (m)
set L1_3   [expr 0.1*$N1];        # first story beam third part
length (m)
set L1     $L1_1;                 # nodal horiz. location (m)
set L2     [expr $L1_1+$L1_2];    # nodal horiz. location (m)
set L3     [expr $L2+$L1_3];      # nodal horiz. location (m)
set L4     [expr $L3+$L1_3];      # nodal horiz. location (m)
set L5     [expr $L4+$L1_2];      # nodal horiz. location (m)
set L6     [expr $L5+$L1_1];      # nodal horiz. location (m)

set g 9.81;            # Gravitational Acceleration (m/s^-2)
set EAl 6.895e10;      # Aluminum Young's Modulus (6.895e10 Pa)
set rho 2700;          # Aluminum density (kg/m^3)
set PI 3.1415926;


#2.2 Cross-Section Parameters ----------------------------------
------------
set A_col1       [expr 4.429e-4*$N2];        # first story column
area (m^2)
set I_col1       [expr 9.081e-8*$N4];        # first story column
moment of inertia (m^4)

set A_col2       [expr 2.014e-4*$N2];        # second story column
area (m^2)
set I_col2       [expr 0.88e-8*$N4];         # second story column
moment of inertia (m^4)

set A_bm1_1      [expr 3.825e-4*$N2];        # first story beam
first part area (m^2)
set I_bm1_1      [expr 5.649e-8*$N4];        # first story beam
first part moment of inertia (m^4)
set A_bm1_2      [expr 8.664e-4*$N2];        # first story beam
second part area (m^2)
set I_bm1_2      [expr 19.547e-8*$N4];       # first story beam
second part moment of inertia (m^4)
set A_bm1_3      [expr 10.576e-4*$N2];       # first story beam
third part area (m^2)
set I_bm1_3      [expr 26.697e-8*$N4];       # first story beam
third part moment of inertia (m^4)

set A_bm2_1      [expr 3.825e-4*$N2];        # first story beam
first part area (m^2)
set I_bm2_1      [expr 4.208e-8*$N4];        # first story beam
first part moment of inertia (m^4)
set A_bm2_2      [expr 4.832e-4*$N2];        # first story beam
second part area (m^2)
```

```
set I_bm2_2      [expr 5.568e-8*$N4];        # first story beam
second part moment of inertia (m^4)

#3. Model Construction-----------------------------------------------
----------------------------
#3.1 Nodes' coordinate
node 1 0 0;
node 2 0 $H1;
node 3 0 $H1;
node 4 0 $H2;
node 5 0 $H3;
node 6 0 $H4;
node 7 0 $H4;
node 8 $L1 $H1;
node 9 $L2 $H1;
node 10 $L2 $H4;
node 11 $L3 $H1;
node 12 $L3 $H4;
node 13 $L4 $H1;
node 14 $L4 $H4;
node 15 $L5 $H1;
node 16 $L6 0;
node 17 $L6 $H1;
node 18 $L6 $H1;
node 19 $L6 $H2;
node 20 $L6 $H3;
node 21 $L6 $H4;
node 22 $L6 $H4;

node 23 0 [expr $H2+0.0127/8];
node 24 0 [expr $H2+0.0127/8*4];
node 25 0 [expr $H2+0.0127/8*7];

node 26 $L6 [expr $H2+0.0127/8];
node 27 $L6 [expr $H2+0.0127/8*4];
node 28 $L6 [expr $H2+0.0127/8*7];


#3.3 Construct Pin Connections & Equal DOF
equalDOF 2 3 1 2;
equalDOF 6 7 1 2;
equalDOF 17 18 1 2;
equalDOF 21 22 1 2;

#3.4 Assign Mass
mass 3 [expr $M1_BM/10] [expr $M1_BM/10] 1.0e-9;
mass 8 [expr $M1_BM/10+$M1_LD] [expr $M1_BM/10+$M1_LD] 1.0e-9;
mass 9 [expr $M1_BM/5+$M_PL/3] [expr $M1_BM/5+$M_PL/3] 1.0e-9;
mass 11 [expr $M1_BM/5+$M_PL/3] [expr $M1_BM/5+$M_PL/3] 1.0e-9;
mass 13 [expr $M1_BM/5+$M_PL/3] [expr $M1_BM/5+$M_PL/3] 1.0e-9;
mass 15 [expr $M1_BM/10+$M1_LD] [expr $M1_BM/10+$M1_LD] 1.0e-9;
mass 18 [expr $M1_BM/10] [expr $M1_BM/10] 1.0e-9;
```

```
mass 7 [expr $M2_BM/8] [expr $M2_BM/8] 1.0e-9;
mass 10 [expr $M2_BM/4+$M_PL/3] [expr $M2_BM/4+$M_PL/3] 1.0e-9;
mass 12 [expr $M2_BM/4+$M_PL/3] [expr $M2_BM/4+$M_PL/3] 1.0e-9;
mass 14 [expr $M2_BM/4+$M_PL/3] [expr $M2_BM/4+$M_PL/3] 1.0e-9;
mass 22 [expr $M2_BM/8] [expr $M2_BM/8] 1.0e-9;


#4. Element Construction-----------------------------------------
------------------------------
#4.1 Geometric Tag number assignment-----------------------------
----------------------------------------
set ColTransfTag 1;                     # associate a tag to column
transformation
set BeamTransfTag 2;                    # associate a tag to beam
transformation
geomTransf Corotational $ColTransfTag;        # Corotational (other
options: PDelta, Linear )
geomTransf Corotational $BeamTransfTag;       # Corotational

#4.2 Define elastic column elements------------------------------
--------------
element elasticBeamColumn 1 1 2 $A_col1 $EAl $I_col1 $ColTransfTag;
      # first story column (left)
element elasticBeamColumn 2 3 4 $A_col2 $EAl $I_col2 $ColTransfTag;
      # second story column btm part (left)
element elasticBeamColumn 4 5 6 $A_col2 $EAl $I_col2 $ColTransfTag;
      # second story column btm part (left)

element elasticBeamColumn 15 16 17 $A_col1 $EAl $I_col1
$ColTransfTag;         # first story column (right)
element elasticBeamColumn 16 18 19 $A_col2 $EAl $I_col2
$ColTransfTag;         # second story column btm part (right)
element elasticBeamColumn 18 20 21 $A_col2 $EAl $I_col2
$ColTransfTag;         # second story column btm part (right)

#4.3 Define nonlinear fuse elements with fiber section----------
--------------------------------
source Fuse_section.tcl
element nonlinearBeamColumn 3 4 23 5 $fuseFiberTag1 $ColTransfTag;
      # other options: nonlinearBeamColumn
element nonlinearBeamColumn 17 23 24 5 $fuseFiberTag2 $ColTransfTag;
element nonlinearBeamColumn 19 24 25 5 $fuseFiberTag2 $ColTransfTag;
element nonlinearBeamColumn 20 25 5 5 $fuseFiberTag2 $ColTransfTag;


element nonlinearBeamColumn 21 19 26 5 $fuseFiberTag1 $ColTransfTag;
element nonlinearBeamColumn 22 26 27 5 $fuseFiberTag2 $ColTransfTag;
element nonlinearBeamColumn 23 27 28 5 $fuseFiberTag2 $ColTransfTag;
element nonlinearBeamColumn 24 28 20 5 $fuseFiberTag2 $ColTransfTag;
```

```
#4.4 Define Elastic Beam Elements----------------------------------
-------------
element elasticBeamColumn 5 3 8 $A_bm1_1 $EAl $I_bm1_1
$BeamTransfTag;        # First story beam first part
element elasticBeamColumn 6 8 9 $A_bm1_2 $EAl $I_bm1_2
$BeamTransfTag;        # First story beam second part
element elasticBeamColumn 7 9 11 $A_bm1_3 $EAl $I_bm1_3
$BeamTransfTag;        # First story beam third part
element elasticBeamColumn 8 11 13 $A_bm1_3 $EAl $I_bm1_3
$BeamTransfTag;  # First story beam third part
element elasticBeamColumn 9 13 15 $A_bm1_2 $EAl $I_bm1_2
$BeamTransfTag;  # First story beam second part
element elasticBeamColumn 10 15 18 $A_bm1_1 $EAl $I_bm1_1
$BeamTransfTag;  # First story beam first part

element elasticBeamColumn 11 7 10 $A_bm2_1 $EAl $I_bm2_1
$BeamTransfTag;  # Second story beam first part
element elasticBeamColumn 12 10 12 $A_bm2_2 $EAl $I_bm2_2
$BeamTransfTag;  # Second story beam second part
element elasticBeamColumn 13 12 14 $A_bm2_2 $EAl $I_bm2_2
$BeamTransfTag;  # Second story beam second part
element elasticBeamColumn 14 14 22 $A_bm2_1 $EAl $I_bm2_1
$BeamTransfTag;  # Second story beam first part


#4.5 Generate foundation-------------------------------------------
-----------------
set Niu 0.4;                # clay Possion's ratio
set cohesion $su;# cohesion
set gamma [expr 544455/$N1]; # unit weight
set phi 0;                  # frictional angle (radian)

set L_ftg [expr 0.107*$N1];  # Footing length
set W_ftg [expr 0.176*$N1];  # Footing width
set T_ftg [expr 0.00953*$N1];     # Footing thickness
set D_ftg [expr 0.0*$N1];    # Footing embedment
set Ef 68950000000;          # Footing Young's Modulus
set Beta 0.0;                # Footing inclination angle


set TP 0.01;                # tension capacity of qzsimple2 spring
set Wgt [expr 745.79*$N2];  # Total vertical load acting on each
footing

set Q_ult [expr $q_ult*$L_ftg*$W_ftg];
      # ultimate vertical load
set P_ult [expr 1.0*$N2];
set T_ult [expr $Wgt*tan(0.5*$phi)+$cohesion*$L_ftg*$W_ftg];
      # sliding capacity
set Kv [expr $G*$L_ftg/(1-
$Niu)*(0.73+1.54*pow(($W_ftg/$L_ftg),0.75))];      # Vertical
initial stiffness
```

```
set Kh [expr $G*$L_ftg/(1-$Niu)*(2+2.5*pow(($W_ftg/$L_ftg),0.85))];
      # Horizontal initial stiffness

set su0 [expr $su/1000];

set filename "foundation_$su0.txt";
set fileId [open $filename "w"]
puts $fileId "SoilProp 1 $cohesion $phi $gamma $G $Niu $crad $TP";
puts $fileId "CapSoil $Q_ult $P_ult $T_ult $Kv $Kh";
puts $fileId "FootProp $L_ftg $W_ftg $T_ftg $D_ftg $Ef $Wgt $Beta";
puts $fileId "MeshProp $Rk $Re $Se";
close $fileId;


ShallowFoundationGen 1 1 "foundation_$su0.txt" 5;
ShallowFoundationGen 2 16 "foundation_$su0.txt" 5;

source Foundation_1.tcl
source Foundation_2.tcl

for {set ii 1001} {$ii<=1057} {incr ii 1} {
      mass $ii [expr $M_ftg/57] [expr $M_ftg/57] 1.0e-9;
}

for {set ii 2001} {$ii<=2057} {incr ii 1} {
      mass $ii [expr $M_ftg/57] [expr $M_ftg/57] 1.0e-9;
}


puts "Model are built"

#5. Eigenvalue Analysis-----------------------------------------
-----------------------------------------------------------------
---------
#puts "The scaled natural periods are:"
set mt 6;                    # number of modes
eigen frequency $mt
set lambdax [eigen $mt]
for {set i 1} {$i<=$mt} {incr i 1} {
set lambda [lindex $lambdax [expr $i-1]]
set omega [expr pow($lambda,0.5)]
set omega$i $omega;
set Tn [expr 2*30.0*$PI/$omega]
#puts "T$i=$Tn sec"
puts "omega$i=$omega HZ"
}

#6. Define RECORDERS --------------------------------------------
--------------
```

```
recorder Node -file $dataDir/SSDisp.out -time -node 1 2 11 6 12 16 -
dof 1 2 3 disp;             # Superstructure disp. at each floor
level
recorder Node -file $dataDir/FtgDisp.out -time -node $endFootNodeL_1
[expr ($endFootNodeL_1+$endFootNodeR_1)/2] $endFootNodeR_1
$endFootNodeL_2 [expr ($endFootNodeL_2+$endFootNodeR_2)/2]
$endFootNodeR_2 -dof 1 2 3 disp;             # Superstructure disp.
at each floor level

recorder Element -file $dataDir/eleglobal.out -time -ele 1 15 3 4 17
18 globalForce;
recorder Node -file $dataDir/NodeAcc.out -time -node 11 12 1 100001
3 7 -dof 1 2 3 accel;
recorder Node -file $dataDir/NodeReac.out -time -node 5 20 1 11 6 7
-dof 1 2 3 reaction;
recorder Element -file $dataDir/Ftg1_force.out -time -ele
$endSprEleL_1 $midSprEle_1 $endSprEleR_1 [expr $endSprEleR_1+1]
[expr $endSprEleR_1+2] force;
recorder Element -file $dataDir/Ftg2_force.out -time -ele
$endSprEleL_2 $midSprEle_2 $endSprEleR_2 [expr $endSprEleR_2+1]
[expr $endSprEleR_2+2] force;


#7. Dead Load application (uniform distributed load acting on the
beams)
set q1 [expr $M1*30.0*$g/$L6/2];        # uniform distributed load
acting on first floor beam
set q2 [expr $M2*30.0*$g/$L6/2];        # uniform distributed load
acting on second floor beam

set W_LD [expr $M1_LD*30.0*$g];         # Lead mass weight
set W_ftg [expr $M_ftg*30.0*$g];        # footing weight

set P_col1 [expr 0.5*$M_CL1*30.0*$g];   # Half weight of first floor
single column
set P_col2 [expr 0.5*$M_CL2*30.0*$g];   # Half weight of second
floor single column

#puts "P_col2=$P_col2";

set P_ftg [expr $W_ftg+$P_col1];  # vertical static load acting on
footing
pattern Plain 1 Linear {
   eleLoad -ele 5 -type -beamUniform -$q1;
   eleLoad -ele 6 -type -beamUniform -$q1;
   eleLoad -ele 7 -type -beamUniform -$q1;
   eleLoad -ele 8 -type -beamUniform -$q1;
   eleLoad -ele 9 -type -beamUniform -$q1;
   eleLoad -ele 10 -type -beamUniform -$q1;
   eleLoad -ele 11 -type -beamUniform -$q2;
   eleLoad -ele 12 -type -beamUniform -$q2;
   eleLoad -ele 13 -type -beamUniform -$q2;
```

```
   eleLoad -ele 14 -type -beamUniform -$q2;
load 1 0. -$P_ftg 0. 0. 0. 0.0;
load 2 0. -$P_col1 0. 0. 0. 0.0;
load 5 0. -$P_col2 0. 0. 0. 0.0;
load 6 0. -$P_col2 0. 0. 0. 0.0;
load 8 0. -$W_LD 0. 0. 0. 0.0;
load 15 0. -$W_LD 0. 0. 0. 0.0;
load 16 0. -$P_ftg 0. 0. 0. 0.0;
load 17 0. -$P_col1 0. 0. 0. 0.0;
load 20 0. -$P_col2 0. 0. 0. 0.0;
load 21 0. -$P_col2 0. 0. 0. 0.0;
}

# Gravity-analysis parameters -- load-controlled static analysis
set Tol 1.0e-6;              # convergence tolerance for test
constraints Transformation;             # how it handles boundary
conditions
numberer RCM;                # renumber dof's to minimize band-width
(optimization), if you want to
system BandGeneral;          # how to store and solve the system of
equations in the analysis
test EnergyIncr $Tol 1;           # determine if convergence has
been achieved at the end of an iteration step
algorithm Newton;            # use Newton's solution algorithm:
updates tangent stiffness at every iteration
set NstepGravity 400;              # apply gravity in 10 steps
set DGravity [expr 1./$NstepGravity];   # first load increment;
integrator LoadControl $DGravity; # determine the next time step for
an analysis
analysis Static;             # define type of analysis static or
transient
analyze $NstepGravity;       # apply gravity
# ------------------------------------------------- maintain
constant gravity loads and reset time to zero
loadConst -time 0.0
puts "static analysis is done."


set w1 $omega1;
set w2 $omega2;

set a0 [expr 2*$w1*$w2*(-$dmp1*$w2+$dmp2*$w1)/(pow($w1,2.0)-
pow($w2,2.0))];        # damping matrix coefficient
set a1 [expr 2*($dmp1*$w1-$dmp2*$w2)/(pow($w1,2.0)-pow($w2,2.0))];
           # damping matrix coefficient

puts "a0=$a0";
puts "a1=$a1";

#10. DYNAMIC Ground-Motion Analysis -------------------------------
----------------------------
# CREATE LOAD PATTERN
```

```
#
#        # The damping matrix D is specified as a combination of
stiffness and mass-proportional damping matrices:
#        # D = $alphaM * M + $betaK * Kcurrent +$betaKinit * Kinit +
$betaKcomm * KlastCommit
#        # The mass and stiffness matrices are defined as:
#        # M:  mass matrix used to calculate Rayleigh Damping
#        # Kcurrent: stiffness matrix at current state determination
used to calculate Rayleigh Damping
#        # Kinit: stiffness matrix at initial state determination
used to calculate Rayleigh Damping
#        # KlastCommit: stiffness matrix at last-committed state
determination used to calculate Rayleigh Damping
#
# rayleigh $alphaM $betaK $betaKinit $betaKcomm
#set accelSeries "Series -dt [expr 0.007324/30.0] -filePath
C_GZ0.4FFacc.txt -factor [expr 30.0*$g]";         # define
acceleration vector from file (dt=0.005 is $glevel"
set accelSeries "Series -dt [expr 0.007324/30.0] -filePath
motion_gen/motion.txt -factor [expr 30.0*$g]";
pattern UniformExcitation 2 1 -accel $accelSeries;
# define where and how (pattern tag, dof) acceleration is applied
rayleigh $a0 0. 0. $a1;      # set damping based on first eigen mode
(on initial stiffness)

set step 4;
#
# Create the EQ Analysis
#wipeAnalysis;                                # clear previously-
define analysis parameters
constraints Transformation;                        # how it handles
boundary conditions
numberer Plain;                              # renumber dof's to
minimize band-width (optimization), if you want to
system BandGeneral;                            # how to store and
solve the system of equations in the analysis
test EnergyIncr 1.0e-9 100 5;                 # determine if
convergence has been achieved at the end of an iteration step
algorithm Newton;                             # use NewtonLineSearch
algorithm
integrator Newmark 0.5 0.25 ;                 # determine the next
time step for an analysis
#integrator HHT 1.0;
#integrator TRBDF2;
analysis Transient;                           # define type of
analysis: time-dependent

set Nsteps [expr 4096*$step];
set dt [expr 0.007324/$step/30.0];

analyze $Nsteps $dt;
puts "------------SF0.2 motion is done!------------";
```

```
analyze $Nsteps $dt;
puts "------------GZ0.2 motion is done!------------";
analyze $Nsteps $dt;
puts "------------GZ0.4 motion is done!------------";
analyze $Nsteps $dt;
puts "------------GZ0.7 motion is done!------------";
analyze $Nsteps $dt;
puts "------------GZ1.0 motion is done!------------";
analyze $Nsteps $dt;
puts "------------SF0.4 motion is done!------------";
```

A.1.2 Fuse Tcl File

```
# Create fiber section for structural fuse
# 1.0 Fuse section material property
set EAl_0        [expr  9.65e10];       # Aluminum Young's Modulus
set fy [expr 1.99e8];        # Aluminum yielding stress
set betta 0.035;       # strain hardening ratio
set Al_MatTag 10;      # Aluminum material tag
uniaxialMaterial Steel02 $Al_MatTag $fy $EAl_0 $betta 20 0.5 0.15;
      # Formulate unaxial material for Aluminum


#2.0 Fuse geometry information
set FuseLg_min    [expr 5.588e-3*$N1];        # Fuse length (m)---
0.22in=5.588mm  0.26in=6.604mm
set FuseLg_max   [expr 19.05e-3*$N1];        # Fuse length (m)---
0.22in
set FuseTk       [expr 3.175e-3*$N1];        # Fuse thickness of
one strip (m)---1/8 in
set FuseWd       [expr 19.05e-3*$N1];        # Fuse width (m)---3/4
in

set FuseLg_mid   [expr ($FuseLg_max+$FuseLg_min)/2];
set FuseLg1      [expr ($FuseLg_max+$FuseLg_mid)/2];
set FuseLg2      $FuseLg_min;

#3.0 Formulate fiber section

set fuseFiberTag1 21;             # assign fuse fiber section tage
(wider portion)

section Fiber $fuseFiberTag1 {

    # Create the Aluminum fibers at two strips
    patch rect $Al_MatTag 12 6 [expr -$FuseLg1/2] [expr -$FuseWd/2]
[expr $FuseLg1/2] [expr -$FuseWd/2+$FuseTk]
    patch rect $Al_MatTag 12 6 [expr -$FuseLg1/2] [expr $FuseWd/2-
$FuseTk] [expr $FuseLg1/2] [expr $FuseWd/2]

}

set fuseFiberTag2 22;       # assign fuse fiber section tage
(narrower portion)

section Fiber $fuseFiberTag2 {

    # Create the Aluminum fibers at two strips
    patch rect $Al_MatTag 12 6 [expr -$FuseLg2/2] [expr -$FuseWd/2]
[expr $FuseLg2/2] [expr -$FuseWd/2+$FuseTk]
    patch rect $Al_MatTag 12 6 [expr -$FuseLg2/2] [expr $FuseWd/2-
$FuseTk] [expr $FuseLg2/2] [expr $FuseWd/2]}
```

A.1.3 Foundation Tcl File

```
##########################################################################
##################
#
#
# This is an intermediate file generated by the command
ShallowFoundationGen.        #
# Source it after the ShallowFoundationGen command.
#
# Use this file to check shallow foundation nodes, elements,  fixity
details         #
# ShallowFoundationGen.cpp is developed by Prishati Raychowdhury
(UCSD)              #
#
#
##########################################################################
##################


 # Foundation Tag =1
 # Foundation Base Condition Tag =5

 #node   $NodeTag  $Xcoord  $Ycoord
 node  1001  -0.0535 0
 node  100001 -0.0535 0
 node  1002  -0.05243 0
 node  100002 -0.05243 0
 node  1003  -0.05136 0
 node  100003 -0.05136 0
 node  1004  -0.05029 0
 node  100004 -0.05029 0
 node  1005  -0.04922 0
 node  100005 -0.04922 0
 node  1006  -0.04815 0
 node  100006 -0.04815 0
 node  1007  -0.04708 0
 node  100007 -0.04708 0
 node  1008  -0.04601 0
 node  100008 -0.04601 0
 node  1009  -0.04494 0
 node  100009 -0.04494 0
 node  1010  -0.04387 0
 node  100010 -0.04387 0
 node  1011  -0.0428 0
 node  100011 -0.0428 0
 node  1012  -0.04066 0
 node  100012 -0.04066 0
 node  1013  -0.03852 0
 node  100013 -0.03852 0
 node  1014  -0.03638 0
```

```
node  100014 -0.03638 0
node  1015  -0.03424 0
node  100015 -0.03424 0
node  1016  -0.0321 0
node  100016 -0.0321 0
node  1017  -0.02996 0
node  100017 -0.02996 0
node  1018  -0.02782 0
node  100018 -0.02782 0
node  1019  -0.02568 0
node  100019 -0.02568 0
node  1020  -0.02354 0
node  100020 -0.02354 0
node  1021  -0.0214 0
node  100021 -0.0214 0
node  1022  -0.01926 0
node  100022 -0.01926 0
node  1023  -0.01712 0
node  100023 -0.01712 0
node  1024  -0.01498 0
node  100024 -0.01498 0
node  1025  -0.01284 0
node  100025 -0.01284 0
node  1026  -0.0107 0
node  100026 -0.0107 0
node  1027  -0.00856 0
node  100027 -0.00856 0
node  1028  -0.00642 0
node  100028 -0.00642 0
node  1029  -0.00428 0
node  100029 -0.00428 0
node  1030  -0.00214 0
node  100030 -0.00214 0
node  1031  6.93889e-018 0
node  100031 6.93889e-018 0
node  1032  0.00214 0
node  100032 0.00214 0
node  1033  0.00428 0
node  100033 0.00428 0
node  1034  0.00642 0
node  100034 0.00642 0
node  1035  0.00856 0
node  100035 0.00856 0
node  1036  0.0107 0
node  100036 0.0107 0
node  1037  0.01284 0
node  100037 0.01284 0
node  1038  0.01498 0
node  100038 0.01498 0
node  1039  0.01712 0
node  100039 0.01712 0
node  1040  0.01926 0
```

```
node  100040 0.01926 0
node  1041  0.0214 0
node  100041 0.0214 0
node  1042  0.02354 0
node  100042 0.02354 0
node  1043  0.02568 0
node  100043 0.02568 0
node  1044  0.02782 0
node  100044 0.02782 0
node  1045  0.02996 0
node  100045 0.02996 0
node  1046  0.0321 0
node  100046 0.0321 0
node  1047  0.03424 0
node  100047 0.03424 0
node  1048  0.03638 0
node  100048 0.03638 0
node  1049  0.03852 0
node  100049 0.03852 0
node  1050  0.04066 0
node  100050 0.04066 0
node  1051  0.0428 0
node  100051 0.0428 0
node  1052  0.04387 0
node  100052 0.04387 0
node  1053  0.04494 0
node  100053 0.04494 0
node  1054  0.04601 0
node  100054 0.04601 0
node  1055  0.04708 0
node  100055 0.04708 0
node  1056  0.04815 0
node  100056 0.04815 0
node  1057  0.04922 0
node  100057 0.04922 0
node  1058  0.05029 0
node  100058 0.05029 0
node  1059  0.05136 0
node  100059 0.05136 0
node  1060  0.05243 0
node  100060 0.05243 0
node  1061  0.0535 0
node  100061 0.0535 0
node  100062 0.0535 0
node  100063 0.0535 0

#equalDOF $rNodeTag $cNodeTag $dof1 $dof2 $dof3
equalDOF 1  1031 1 2 3

#Materials for shallow foundation
```

```
 #uniaxialMaterial  QzSimple2  $matTag  $SoilType  $Qult-end-extreme
$z50-end  <TpSoil>  <CradSoil>
 uniaxialMaterial  QzSimple2 101  1 29.0479 0.000133036 0.01 60

 #uniaxialMaterial  QzSimple2  $matTag  $SoilType  $Qult-end  $z50-
end  <TpSoil>  <CradSoil>
 uniaxialMaterial  QzSimple2 102  1 58.0959 0.000133036 0.01 60

 #uniaxialMaterial  QzSimple2  $matTag  $SoilType  $Qult-mid  $z50-
mid  <TpSoil>  <CradSoil>
 uniaxialMaterial  QzSimple2 103  1 116.192 0.00066518 0.01 60

 #uniaxialMaterial  PySimple2  $matTag  $SoilType  $Pp  $xp50  Cd
<CradSoil>
 uniaxialMaterial  PySimple2 105  1 1 4.94403e-007 0.1 60

 #uniaxialMaterial  TzSimple2  $matTag  $SoilType  $Tult  $xt50
<CradSoil>
 uniaxialMaterial  TzSimple2 106  1 1129.92 0.000558636 0.1 60

 #Vertical spring element connectivity
 #element   zeroLength  $eleTag  $iNode  $jNode  -mat$matTag  -dir
$dir
 element   zeroLength 100001  100001  1001 -mat 101   -dir  2
 element   zeroLength 100002  100002  1002 -mat 102   -dir  2
 element   zeroLength 100003  100003  1003 -mat 102   -dir  2
 element   zeroLength 100004  100004  1004 -mat 102   -dir  2
 element   zeroLength 100005  100005  1005 -mat 102   -dir  2
 element   zeroLength 100006  100006  1006 -mat 102   -dir  2
 element   zeroLength 100007  100007  1007 -mat 102   -dir  2
 element   zeroLength 100008  100008  1008 -mat 102   -dir  2
 element   zeroLength 100009  100009  1009 -mat 102   -dir  2
 element   zeroLength 100010  100010  1010 -mat 102   -dir  2
 element   zeroLength 100011  100011  1011 -mat 103   -dir  2
 element   zeroLength 100012  100012  1012 -mat 103   -dir  2
 element   zeroLength 100013  100013  1013 -mat 103   -dir  2
 element   zeroLength 100014  100014  1014 -mat 103   -dir  2
 element   zeroLength 100015  100015  1015 -mat 103   -dir  2
 element   zeroLength 100016  100016  1016 -mat 103   -dir  2
 element   zeroLength 100017  100017  1017 -mat 103   -dir  2
 element   zeroLength 100018  100018  1018 -mat 103   -dir  2
 element   zeroLength 100019  100019  1019 -mat 103   -dir  2
 element   zeroLength 100020  100020  1020 -mat 103   -dir  2
 element   zeroLength 100021  100021  1021 -mat 103   -dir  2
 element   zeroLength 100022  100022  1022 -mat 103   -dir  2
 element   zeroLength 100023  100023  1023 -mat 103   -dir  2
 element   zeroLength 100024  100024  1024 -mat 103   -dir  2
 element   zeroLength 100025  100025  1025 -mat 103   -dir  2
 element   zeroLength 100026  100026  1026 -mat 103   -dir  2
 element   zeroLength 100027  100027  1027 -mat 103   -dir  2
 element   zeroLength 100028  100028  1028 -mat 103   -dir  2
 element   zeroLength 100029  100029  1029 -mat 103   -dir  2
```

```
 element   zeroLength 100030  100030  1030 -mat 103   -dir  2
 element   zeroLength 100031  100031  1031 -mat 103   -dir  2
 element   zeroLength 100032  100032  1032 -mat 103   -dir  2
 element   zeroLength 100033  100033  1033 -mat 103   -dir  2
 element   zeroLength 100034  100034  1034 -mat 103   -dir  2
 element   zeroLength 100035  100035  1035 -mat 103   -dir  2
 element   zeroLength 100036  100036  1036 -mat 103   -dir  2
 element   zeroLength 100037  100037  1037 -mat 103   -dir  2
 element   zeroLength 100038  100038  1038 -mat 103   -dir  2
 element   zeroLength 100039  100039  1039 -mat 103   -dir  2
 element   zeroLength 100040  100040  1040 -mat 103   -dir  2
 element   zeroLength 100041  100041  1041 -mat 103   -dir  2
 element   zeroLength 100042  100042  1042 -mat 103   -dir  2
 element   zeroLength 100043  100043  1043 -mat 103   -dir  2
 element   zeroLength 100044  100044  1044 -mat 103   -dir  2
 element   zeroLength 100045  100045  1045 -mat 103   -dir  2
 element   zeroLength 100046  100046  1046 -mat 103   -dir  2
 element   zeroLength 100047  100047  1047 -mat 103   -dir  2
 element   zeroLength 100048  100048  1048 -mat 103   -dir  2
 element   zeroLength 100049  100049  1049 -mat 103   -dir  2
 element   zeroLength 100050  100050  1050 -mat 103   -dir  2
 element   zeroLength 100051  100051  1051 -mat 103   -dir  2
 element   zeroLength 100052  100052  1052 -mat 102   -dir  2
 element   zeroLength 100053  100053  1053 -mat 102   -dir  2
 element   zeroLength 100054  100054  1054 -mat 102   -dir  2
 element   zeroLength 100055  100055  1055 -mat 102   -dir  2
 element   zeroLength 100056  100056  1056 -mat 102   -dir  2
 element   zeroLength 100057  100057  1057 -mat 102   -dir  2
 element   zeroLength 100058  100058  1058 -mat 102   -dir  2
 element   zeroLength 100059  100059  1059 -mat 102   -dir  2
 element   zeroLength 100060  100060  1060 -mat 102   -dir  2
 element   zeroLength 100061  100061  1061 -mat 101   -dir  2

 #Horizontal spring element connectivity
 #element   zeroLength  $eleTag  $iNode  $jNode  -mat$matTag  -dir
$dir
 element   zeroLength 100062  1061  100062 -mat 105   -dir  1
 element   zeroLength 100063  1061  100063 -mat 106   -dir  1

 # geomTransf Linear $transfTag <-jntOffset $dXi $dYi $dXj $dYj>
 geomTransf Linear  10

 #foundation element connectivity
 #element   elasticBeamColumn  $eleTag  $iNode  $jNode  $A  $E  $Iz
$transfTag
 element elasticBeamColumn 1001 1001  1002 0.00167728 6.895e+010
1.26943e-008 10
 element elasticBeamColumn 1002 1002  1003 0.00167728 6.895e+010
1.26943e-008 10
 element elasticBeamColumn 1003 1003  1004 0.00167728 6.895e+010
1.26943e-008 10
```

```
 element elasticBeamColumn 1004 1004  1005 0.00167728 6.895e+010
1.26943e-008 10
 element elasticBeamColumn 1005 1005  1006 0.00167728 6.895e+010
1.26943e-008 10
 element elasticBeamColumn 1006 1006  1007 0.00167728 6.895e+010
1.26943e-008 10
 element elasticBeamColumn 1007 1007  1008 0.00167728 6.895e+010
1.26943e-008 10
 element elasticBeamColumn 1008 1008  1009 0.00167728 6.895e+010
1.26943e-008 10
 element elasticBeamColumn 1009 1009  1010 0.00167728 6.895e+010
1.26943e-008 10
 element elasticBeamColumn 1010 1010  1011 0.00167728 6.895e+010
1.26943e-008 10
 element elasticBeamColumn 1011 1011  1012 0.00167728 6.895e+010
1.26943e-008 10
 element elasticBeamColumn 1012 1012  1013 0.00167728 6.895e+010
1.26943e-008 10
 element elasticBeamColumn 1013 1013  1014 0.00167728 6.895e+010
1.26943e-008 10
 element elasticBeamColumn 1014 1014  1015 0.00167728 6.895e+010
1.26943e-008 10
 element elasticBeamColumn 1015 1015  1016 0.00167728 6.895e+010
1.26943e-008 10
 element elasticBeamColumn 1016 1016  1017 0.00167728 6.895e+010
1.26943e-008 10
 element elasticBeamColumn 1017 1017  1018 0.00167728 6.895e+010
1.26943e-008 10
 element elasticBeamColumn 1018 1018  1019 0.00167728 6.895e+010
1.26943e-008 10
 element elasticBeamColumn 1019 1019  1020 0.00167728 6.895e+010
1.26943e-008 10
 element elasticBeamColumn 1020 1020  1021 0.00167728 6.895e+010
1.26943e-008 10
 element elasticBeamColumn 1021 1021  1022 0.00167728 6.895e+010
1.26943e-008 10
 element elasticBeamColumn 1022 1022  1023 0.00167728 6.895e+010
1.26943e-008 10
 element elasticBeamColumn 1023 1023  1024 0.00167728 6.895e+010
1.26943e-008 10
 element elasticBeamColumn 1024 1024  1025 0.00167728 6.895e+010
1.26943e-008 10
 element elasticBeamColumn 1025 1025  1026 0.00167728 6.895e+010
1.26943e-008 10
 element elasticBeamColumn 1026 1026  1027 0.00167728 6.895e+010
1.26943e-008 10
 element elasticBeamColumn 1027 1027  1028 0.00167728 6.895e+010
1.26943e-008 10
 element elasticBeamColumn 1028 1028  1029 0.00167728 6.895e+010
1.26943e-008 10
 element elasticBeamColumn 1029 1029  1030 0.00167728 6.895e+010
1.26943e-008 10
```

```
 element elasticBeamColumn 1030 1030  1031 0.00167728 6.895e+010
1.26943e-008 10
 element elasticBeamColumn 1031 1031  1032 0.00167728 6.895e+010
1.26943e-008 10
 element elasticBeamColumn 1032 1032  1033 0.00167728 6.895e+010
1.26943e-008 10
 element elasticBeamColumn 1033 1033  1034 0.00167728 6.895e+010
1.26943e-008 10
 element elasticBeamColumn 1034 1034  1035 0.00167728 6.895e+010
1.26943e-008 10
 element elasticBeamColumn 1035 1035  1036 0.00167728 6.895e+010
1.26943e-008 10
 element elasticBeamColumn 1036 1036  1037 0.00167728 6.895e+010
1.26943e-008 10
 element elasticBeamColumn 1037 1037  1038 0.00167728 6.895e+010
1.26943e-008 10
 element elasticBeamColumn 1038 1038  1039 0.00167728 6.895e+010
1.26943e-008 10
 element elasticBeamColumn 1039 1039  1040 0.00167728 6.895e+010
1.26943e-008 10
 element elasticBeamColumn 1040 1040  1041 0.00167728 6.895e+010
1.26943e-008 10
 element elasticBeamColumn 1041 1041  1042 0.00167728 6.895e+010
1.26943e-008 10
 element elasticBeamColumn 1042 1042  1043 0.00167728 6.895e+010
1.26943e-008 10
 element elasticBeamColumn 1043 1043  1044 0.00167728 6.895e+010
1.26943e-008 10
 element elasticBeamColumn 1044 1044  1045 0.00167728 6.895e+010
1.26943e-008 10
 element elasticBeamColumn 1045 1045  1046 0.00167728 6.895e+010
1.26943e-008 10
 element elasticBeamColumn 1046 1046  1047 0.00167728 6.895e+010
1.26943e-008 10
 element elasticBeamColumn 1047 1047  1048 0.00167728 6.895e+010
1.26943e-008 10
 element elasticBeamColumn 1048 1048  1049 0.00167728 6.895e+010
1.26943e-008 10
 element elasticBeamColumn 1049 1049  1050 0.00167728 6.895e+010
1.26943e-008 10
 element elasticBeamColumn 1050 1050  1051 0.00167728 6.895e+010
1.26943e-008 10
 element elasticBeamColumn 1051 1051  1052 0.00167728 6.895e+010
1.26943e-008 10
 element elasticBeamColumn 1052 1052  1053 0.00167728 6.895e+010
1.26943e-008 10
 element elasticBeamColumn 1053 1053  1054 0.00167728 6.895e+010
1.26943e-008 10
 element elasticBeamColumn 1054 1054  1055 0.00167728 6.895e+010
1.26943e-008 10
 element elasticBeamColumn 1055 1055  1056 0.00167728 6.895e+010
1.26943e-008 10
```

```
 element elasticBeamColumn 1056 1056  1057 0.00167728 6.895e+010
1.26943e-008 10
 element elasticBeamColumn 1057 1057  1058 0.00167728 6.895e+010
1.26943e-008 10
 element elasticBeamColumn 1058 1058  1059 0.00167728 6.895e+010
1.26943e-008 10
 element elasticBeamColumn 1059 1059  1060 0.00167728 6.895e+010
1.26943e-008 10
 element elasticBeamColumn 1060 1060  1061 0.00167728 6.895e+010
1.26943e-008 10

 #fixity
 fix  100001 1 1 1
 fix  100002 1 1 1
 fix  100003 1 1 1
 fix  100004 1 1 1
 fix  100005 1 1 1
 fix  100006 1 1 1
 fix  100007 1 1 1
 fix  100008 1 1 1
 fix  100009 1 1 1
 fix  100010 1 1 1
 fix  100011 1 1 1
 fix  100012 1 1 1
 fix  100013 1 1 1
 fix  100014 1 1 1
 fix  100015 1 1 1
 fix  100016 1 1 1
 fix  100017 1 1 1
 fix  100018 1 1 1
 fix  100019 1 1 1
 fix  100020 1 1 1
 fix  100021 1 1 1
 fix  100022 1 1 1
 fix  100023 1 1 1
 fix  100024 1 1 1
 fix  100025 1 1 1
 fix  100026 1 1 1
 fix  100027 1 1 1
 fix  100028 1 1 1
 fix  100029 1 1 1
 fix  100030 1 1 1
 fix  100031 1 1 1
 fix  100032 1 1 1
 fix  100033 1 1 1
 fix  100034 1 1 1
 fix  100035 1 1 1
 fix  100036 1 1 1
 fix  100037 1 1 1
 fix  100038 1 1 1
 fix  100039 1 1 1
 fix  100040 1 1 1
```

```
fix  100041 1 1 1
fix  100042 1 1 1
fix  100043 1 1 1
fix  100044 1 1 1
fix  100045 1 1 1
fix  100046 1 1 1
fix  100047 1 1 1
fix  100048 1 1 1
fix  100049 1 1 1
fix  100050 1 1 1
fix  100051 1 1 1
fix  100052 1 1 1
fix  100053 1 1 1
fix  100054 1 1 1
fix  100055 1 1 1
fix  100056 1 1 1
fix  100057 1 1 1
fix  100058 1 1 1
fix  100059 1 1 1
fix  100060 1 1 1
fix  100061 1 1 1
fix  100062 1 1 1
fix  100063 1 1 1

set endFootNodeL_1   1001
set endFootNodeR_1   1061
set endSprEleL_1   100001
set endSprEleR_1   100061
set midSprEle_1   100031
```

A.2 Modeling of Simplified Inelastic Systems in Chapter 8

A.2.1 MFP_ES System

```
#-------------------------------------------------------------------------
---------------------
# SDOF system re-centering vs energy dissipation: (2013-10-07)
#-------------------------------------------------------------------------
---------------------
#System Type: MFP_ES
# Unit System: N, m, sec, prototype scale.

#
#

#1. SET UP-----------------------------------------------------------
---
for {set miu 2} {$miu <=10} {incr miu 1} {
wipe;                                # clear opensees model
model basic -ndm 2 -ndf 3;           # 2 dimensions, 3 dof per node
set dataDir Results_$miu;                  # set up name of data
directory

file mkdir $dataDir;                 # Create data directory called
Results in the same directory as the file itself


#2. Model Construction----------------------------------------------
-----------------------------
#2.1 Nodes' coordinate
node 1 0 0;
node 2 0 0;



#2.3 Assign Mass
mass 2 1 1 1;


#3. Element Construction-------------------------------------------
-------------------------------
#3.1 Geometric Tag number assignment-------------------------------
-------------------------------
set TransfTag 1;                     # associate a tag to column
transformation
geomTransf Linear $TransfTag;        # Corotational (other options:
pdelta, Linear )
```

```
#3.2 Key Parameters-------------------------------------------------
--------------

set Fy2 100;
set Dy2 0.01;
set b 0.01;
#################################################################
set Pinch_D 0.7;
set Pinch_F 0.3;
set beta 0;
#################################################################


#3.3 Uniaxial material
set matTag3 3;
#uniaxialMaterial Hysteretic $matTag $s1p $e1p $s2p $e2p <$s3p $e3p>
$s1n $e1n $s2n $e2n <$s3n $e3n> $pinchX $pinchY $damage1 $damage2
<$beta>
uniaxialMaterial Hysteretic $matTag3 $Fy2 $Dy2 [expr (1+4*$b)*$Fy2]
[expr 5*$Dy2] 0 [expr 15*$Dy2] -$Fy2 -$Dy2 [expr -(1+4*$b)*$Fy2]
[expr -5*$Dy2] 0 [expr -15*$Dy2] $Pinch_D $Pinch_F 0 0 $beta;


#3.4 material #1: EPP behavior
set matTag1 1;


set Fy1 [expr $Fy2];
set Dy1 [expr $Dy2];

set Dy min($Dy1,$Dy2);

#uniaxialMaterial Steel01 $matTag $Fy $E0 $b <$a1 $a2 $a3 $a4>
uniaxialMaterial Steel01 $matTag1 $Fy1 [expr $Fy1/$Dy1] $b;

#3.5 Fuse in Parallel
set matTagPR1 5;
uniaxialMaterial Parallel $matTagPR1 $matTag1 $matTag3;


#3.6 Define elastic column elements---------------------------------
--------------

element zeroLength 1 1 2 -mat $matTagPR1 -dir 1;




#fixity
fix 1 1 1 1;
fix 2 0 1 1;
```

```
puts "Model is built"


#4. Define RECORDERS ----------------------------------------------
--------------

recorder Node -file $dataDir/SSDisp.out -time -node 1 2 -dof 1 2 3
disp;            # Superstructure disp. at each floor level
recorder Element -file $dataDir/eleglobal.out -time -ele 1 force;
recorder Node -file $dataDir/reaction.out -time -node 1 -dof 1 2 3
reaction;


#5. Cyclic ANALYSIS-----------------------------------------------
-------------------------------------------------------------
#  -------------------------------------------------------------
---------------------------------
#

set IDctrlNode 2;            # node where displacement is read for
displacement control
set IDctrlDOF 1;             # degree of freedom of displacement
read for displacement contro
set Dmax [expr 5];           # maximum displacement of pushover.
push to 10% drift.
set Dincr [expr 0.001*$Dy];       # displacement increment for
pushover. you want this to be very small, but not too small to slow
down the analysis

# create load pattern for lateral pushover load
pattern Plain 1 Linear {                # define load pattern --
generalized
      load 2 1 0.0 0.0 0.0 0.0 0.0;     # define lateral load in
static lateral analysis
}


constraints Plain;
numberer Plain;
system BandGeneral;
set Tol 1.e-8;                        # Convergence Test: tolerance
set maxNumIter 10;                # Convergence Test: maximum number
of iterations that will be performed before "failure to converge" is
returned
set printFlag 0;                # Convergence Test: flag used to
print information on convergence (optional)        # 1: print
information on each step;
set TestType EnergyIncr;     # Convergence-test type NormDispIncr,
EnergyIncr
test $TestType $Tol $maxNumIter $printFlag;
set algorithmType Newton
```

```
algorithm $algorithmType;
integrator DisplacementControl $IDctrlNode $IDctrlDOF $Dincr;
analysis Static;
analyze [expr $miu*1000];

integrator DisplacementControl $IDctrlNode $IDctrlDOF [expr -$Dincr];
analyze [expr $miu*2000];

integrator DisplacementControl  $IDctrlNode   $IDctrlDOF $Dincr;
analyze [expr $miu*2000];

integrator DisplacementControl $IDctrlNode $IDctrlDOF [expr -$Dincr];
analyze [expr $miu*2000];

puts "The analysis of miu=$miu is completed!"}
```

A.2.2 MFS_ES System

```
#-------------------------------------------------------------------
--------------------
# SDOF system re-centering vs energy dissipation: (2013-10-07)
#-------------------------------------------------------------------
--------------------
#System Type: MFS_ES
# Unit System: N, m, sec, prototype scale.

#
#

#1. SET UP---------------------------------------------------------
---
for {set miu 2} {$miu <=10} {incr miu 1} {
wipe;                                # clear opensees model
model basic -ndm 2 -ndf 3;           # 2 dimensions, 3 dof per node
set dataDir Results_$miu;                  # set up name of data
directory

file mkdir $dataDir;                 # Create data directory called
Results in the same directory as the file itself


#2. Model Construction---------------------------------------------
-----------------------------
#2.1 Nodes' coordinate
node 1 0 0;
node 2 0 0;



#2.3 Assign Mass
mass 2 1 1 1;


#3. Element Construction------------------------------------------
-------------------------------
#3.1 Geometric Tag number assignment------------------------------
-------------------------------
set TransfTag 1;                     # associate a tag to column
transformation
geomTransf Linear $TransfTag;        # Corotational (other options:
pdelta, Linear )

#3.2 Key Parameters-----------------------------------------------
--------------

set Fy2 100;
set Dy2 0.01;
```

```
set b 0.01;
#################################################################
set Pinch_D 0.7;
set Pinch_F 0.3;
set beta 0;
#################################################################


#3.3 Uniaxial material
set matTag3 3;
#uniaxialMaterial Hysteretic $matTag $s1p $e1p $s2p $e2p <$s3p $e3p>
$s1n $e1n $s2n $e2n <$s3n $e3n> $pinchX $pinchY $damage1 $damage2
<$beta>
uniaxialMaterial Hysteretic $matTag3 $Fy2 $Dy2 [expr (1+4*$b)*$Fy2]
[expr 5*$Dy2] 0 [expr 15*$Dy2] -$Fy2 -$Dy2 [expr -(1+4*$b)*$Fy2]
[expr -5*$Dy2] 0 [expr -15*$Dy2] $Pinch_D $Pinch_F 0 0 $beta;


#3.4 material #1: EPP behavior
set matTag1 1;


set Fy1 [expr $Fy2];
set Dy1 [expr $Dy2];

set Dy min($Dy1,$Dy2);

#uniaxialMaterial Steel01 $matTag $Fy $E0 $b <$a1 $a2 $a3 $a4>
uniaxialMaterial Steel01 $matTag1 $Fy1 [expr $Fy1/$Dy1] $b;

#3.5 Fuse in Parallel
set matTagPR1 5;
uniaxialMaterial Series $matTagPR1 $matTag1 $matTag3;


#3.6 Define elastic column elements--------------------------------
--------------

element zeroLength 1 1 2 -mat $matTagPR1 -dir 1;




#fixity
fix 1 1 1 1;
fix 2 0 1 1;

puts "Model is built"


#4. Define RECORDERS -----------------------------------------------
--------------
```

```
recorder Node -file $dataDir/SSDisp.out -time -node 1 2 -dof 1 2 3
disp;            # Superstructure disp. at each floor level
recorder Element -file $dataDir/eleglobal.out -time -ele 1 force;
recorder Node -file $dataDir/reaction.out -time -node 1 -dof 1 2 3
reaction;


#5. Cyclic ANALYSIS-------------------------------------------------
-------------------------------------------------------------
#  -----------------------------------------------------------------
---------------------------------
#

set IDctrlNode 2;            # node where displacement is read for
displacement control
set IDctrlDOF 1;             # degree of freedom of displacement
read for displacement contro
set Dmax [expr 5];           # maximum displacement of pushover.
push to 10% drift.
set Dincr [expr 0.001*$Dy];       # displacement increment for
pushover. you want this to be very small, but not too small to slow
down the analysis

# create load pattern for lateral pushover load
pattern Plain 1 Linear {                # define load pattern --
generalized
      load 2 1 0.0 0.0 0.0 0.0 0.0;     # define lateral load in
static lateral analysis
}


constraints Plain;
numberer Plain;
system BandGeneral;
set Tol 1.e-8;                        # Convergence Test: tolerance
set maxNumIter 10;                 # Convergence Test: maximum number
of iterations that will be performed before "failure to converge" is
returned
set printFlag 0;                # Convergence Test: flag used to
print information on convergence (optional)        # 1: print
information on each step;
set TestType EnergyIncr;     # Convergence-test type NormDispIncr,
EnergyIncr
test $TestType $Tol $maxNumIter $printFlag;
set algorithmType Newton
algorithm $algorithmType;
integrator DisplacementControl $IDctrlNode $IDctrlDOF $Dincr;
analysis Static;
analyze [expr $miu*1000];

integrator DisplacementControl $IDctrlNode $IDctrlDOF [expr -$Dincr];
```

```
analyze [expr $miu*2000];

integrator DisplacementControl  $IDctrlNode   $IDctrlDOF $Dincr;
analyze [expr $miu*2000];

integrator DisplacementControl $IDctrlNode $IDctrlDOF [expr -$Dincr];
analyze [expr $miu*2000];

puts "The analysis of miu=$miu is completed!"}
```